Dissertation zur Erlangung des akademischen Grades eines Doktors der Naturwissenschaften.

Remnant Planetesimals and their Collisional Fragments: Physical Characterization from Thermal–Infrared Observations

vorgelegt von

Michael Mommert

2013

Eingereicht und verteidigt im Fachbereich Geowissenschaften der Freien Universität Berlin. Angefertigt am Institut für Planetenforschung des Deutschen Zentrums für Luft- und Raumfahrt e.V. (DLR) in Berlin-Adlershof.

Begutachtet von
Prof. Dr. Ralf Jaumann (Freie Universität Berlin, DLR Berlin)
Prof. Dr. Stephan van Gasselt (Freie Universität Berlin)

Tag der Disputation: 26. Juni 2013

Selbstständigkeitserklärung

Hiermit erkläre ich, die vorliegende Arbeit selbstständig und ohne Zuhilfenahme von nicht gekennzeichneten Hilfsmitteln erstellt zu haben.
Vorab veröffentlichte Ergebnisse sind als solche gekennzeichnet; Zuarbeiten von Co–Autoren sind entsprechend hervorgehoben und werden nur dann erwähnt, wenn sie für das Verständnis der Arbeit nötig sind.

Berlin, 12. März 2013

Michael Mommert

Abstract

In this work I have investigated the physical properties of near–Earth objects (NEOs) and trans–Neptunian objects (TNOs), two small–body populations at the focus of current Solar System research. TNOs are pristine icy objects that reside beyond the orbit of Neptune. NEOs are physically evolved objects with orbits that, at times, bring them close to the Earth. Both populations formed from the same disk of planetesimals, the building blocks of the planets, representing different stages of evolution: TNOs may be the least altered population of remnant planetesimals, while NEOs are fragments that have formed through collisions, analogous to pebbles forming from rocks in a stream–bed. Dynamical models suggest that most NEOs originate from main–belt asteroids, which orbit between Mars and Jupiter, but some appear to be of cometary origin. I have investigated whether the predictions concerning the origin of NEOs are consistent with their observed physical properties. I have focused on a possible cometary origin for some NEOs: scattered TNOs can enter the NEO population as short–period comets, where they become indistinguishable from asteroidal NEOs after cessation of their activity.

Physical properties of NEOs and TNOs have been derived in the framework of the "*ExploreNEOs*" (Trilling et al. 2010) and "*TNOs are Cool!*" (Müller et al. 2010) programs, which obtained space–based thermal–infrared observations of NEOs and TNOs, respectively, using the Spitzer Space Telescope and the Herschel Space Observatory. Both programs study physical ensemble properties and the properties of individual objects. An important aspect of my work has been the derivation of diameters and albedos from *ExploreNEOs* and *TNOs are Cool!* observations using asteroid thermal models.

I have compared albedos of NEOs derived from *ExploreNEOs* data and albedos of their parent populations in the main belt and short–period comets; albedo distributions of the parent populations have been derived from literature data on the basis of dynamical model predictions. In general, the results of the comparison agree with predictions from dynamical models, except for a lack of low–albedo objects among the NEOs. I have found that $(5 \pm 3)\%$ of all NEOs in a size–limited sample have a cometary origin. In the course of the latter analysis, I have shown that one of the largest NEOs, (3552) Don Quixote, is in fact an active comet currently in the process of evolving into an asteroid. The example of Don Quixote suggests that the presence of volatiles and cometary activity in the NEO population are more common than expected.

As a contribution to the *TNOs are Cool!* program, I have investigated the physical properties of a representative sample of Plutinos, a TNO subpopulation. I have found no significant correlation between the albedos of TNOs and their taxonomic type classifications, according to Barucci et al. (2005). I have found that the presence of ices on the surfaces of TNOs does not necessarily give rise to higher albedos. However, I have observed that TNOs with diameters larger than 900 km are likely to have surface ices, and those larger than 1200 km have extraordinarily high albedos. Based on their size and albedo distributions, I have identified those TNO subpopulations, from which the short–period comets are most likely the originate.

In conclusion, the physical property comparisons in this work support the inferences from dynamical models regarding connections between different Solar System small–body populations.

Zusammenfassung

In der vorliegenden Arbeit untersuchte ich die physikalischen Eigenschaften erdnaher (NEOs) und transneptunischer Objekte (TNOs), Populationen kleiner Körper im Brennpunkt der aktuellen Sonnensystemforschung. TNOs sind ursprüngliche, eisige Körper, deren Bahnen außerhalb der des Neptuns liegen. NEOs sind physikalisch weiter entwickelte Körper mit Bahnen, die sie der Erde nahe bringen können. Beide Populationen entwickelten sich aus den gleichen Planetesimalen und stellen unterschiedliche Entwicklungsphasen dieser Planetenbausteine dar: TNOs könnten die Überreste einer ursprünglichen Population von Planetesimalen darstellen, während NEOs deren Bruchstücke sind, die durch Kollisionen in ähnlicher Weise entstanden sind, wie Kiesel aus größeren Steinen durch Kollisionen und Abrieb. Dynamische Modelle deuten darauf hin, dass die meisten NEOs von den Hauptgürtelasteroiden, die zwischen Mars und Jupiter die Sonne umkreisen, abstammen; andere scheinen von Kometen abzustammen. Ich habe die Vorhersagen dieser Modelle bezüglich des Ursprungs der NEOs anhand deren physikalischen Eigenschaften untersucht. Dabei habe ich mich auf einen möglichen kometären Ursprung einiger NEOs konzentriert: dynamisch instabile TNOs können in die erdnahe Population als aktive kurzperiodische Kometen eintreten, wo sie nach Beendigung ihrer Aktivität von den Asteroiden kaum noch zu unterscheiden sind.

Die physikalischen Eigenschaften von NEOs und TNOs wurden im Rahmen der "*ExploreNEOs*" (Trilling et al. 2010) und "*TNOs are Cool!*" (Müller et al. 2010) Programme bestimmt, in welchen weltraumgestützte Beobachtungen unter Verwendung des Spitzer Space Telescope und des Herschel Space Observatory durchgeführt wurden. Beide Programme erforschen die physikalischen Ensemble–Eigenschaften im Allgemeinen und einzelne Objekte im Besonderen. Ein wichtiger Anteil meiner Arbeit bestand in der Bestimmung von Durchmessern und Albedos aus den Beobachtungsdaten mittels thermischer Modelle für Asteroiden.

Basierend auf "*ExploreNEOs*"–Daten verglich ich die Albedo–Eigenschaften der NEOs mit denen ihrer Quell–Populationen im Asteroiden–Hauptgürtel und den Kometen. Im Allgemeinen stimmen die Albedo–Verteilungen mit den Vorhersagen überein, es wurde jedoch ein Mangel an NEOs mit niedrigen Albedos sichtbar. Ich konnte zeigen, dass $(5 \pm 3)\%$ aller NEOs in einer Durchmesser–begrenzten Population kometären Ursprungs sind. Im Rahmen dieser Untersuchung stellte sich heraus, dass einer der größten NEOs, (3552) Don Quixote, in Wirklichkeit ein aktiver Komet ist, der sich momentan im Entwicklungssprozess hin zu einem Asteroiden befindet. Das Beispiel Don Quixotes weist darauf hin, dass die Gegenwart flüchtiger Verbindungen und kometäre Aktivität in der NEO–Population häufiger anzutreffen sein könnten, als angenommen.

In einem Beitrag zum "*TNOs are Cool!*" Programm habe ich die physikalischen Eigenschaften einer repräsentativen Auswahl von Plutinos, einer TNO–Untergruppierung, untersucht. Ein Vergleich der Albedos von TNOs mit ihrer taxonomischen Klassifizierung nach Barucci et al. (2005) erbrachte keine signifikante Korrelation. Die Gegenwart von Oberflächeneis auf TNOs hat nicht zwingend eine hohe Albedo zur Folge. Jedoch habe ich festgestellt, dass TNOs mit Durchmessern größer als 900 km wahrscheinlich zumindest teilweise mit Eis bedeckt sind und dass solche TNOs, die größer als 1200 km sind, außerordentlich hohe Albedos besitzen. Basierend auf Größen– und Albedo–Verteilungen, konnte ich diejenigen TNO–Untergruppierungen identifizieren, die am wahrscheinlichsten zu den Quellen der kurzperiodischen Kometen zählen.

Abschließend unterstützt der Vergleich der physikalischen Eigenschaften der verschiedenen Kleinkörperpopulationen die Vorhersagen dynamischer Modelle zu deren Wechselwirkung.

Für Katja.

Contents

List of Figures

List of Tables

Chapter 1

Introduction

The vast majority of objects in the Solar System has significantly smaller diameters than the 8 planets. The existence and spatial distribution of the "small bodies" are indicative for the formation and evolution of the Solar System, which formed $\sim$4.5 *Gyrs ago from a rotating molecular cloud of gas and dust into a primordial disk of planetesimals (see Section 1.1.2.2). The small bodies we observe today in the Solar System are the remnants of the planetesimal disk, some of which might even be examples of remnant planetesimals; others are much smaller and clearly show signs of physical evolution as a result of collisions.*

Small bodies are not evenly distributed in the Solar System. Outside the orbit of Neptune, a population of large, pristine objects, the trans–Neptunian objects (TNOs), exists, some of which might have barely evolved since the early ages of the Solar System. The main asteroid belt between the orbits of Mars and Jupiter is mostly made up from the collisional fragments of planetesimals. The orbits of objects in this region are perturbed by the close encounters with planets or other dynamical effects, bringing them to the near–Earth object (NEOs) population. NEOs are physically and dynamically evolved, whereas TNOs are among the most pristine objects in the Solar System. The dynamical distributions and the physical ensemble properties of both of these populations put strong constraints on the formation and dynamical evolution of the Solar System.

As part of this work, I examine links between the TNOs and the main belt asteroids, and the NEOs. Most NEOs are collisional fragments from the asteroid main belt. However, short–period comets, originating in the TNO region, can end up in near–Earth space, where they become dead or dormant comets after the depletion of their volatile inventories.

In the following sections, I give an introduction to the dynamical properties and orbital distributions of Solar System small bodies, including the interactions between the individual populations, and discuss their physical properties.

1.1 Small Bodies in the Solar System

As of March 1, 2013, the Solar System inventory counts 8 planets and 611530 small bodies, comprising asteroids and comets, according to the Minor Planet Center (Minor Planet Center Observations Database), which collects and evaluates observations of small bodies and provides ephemerides for all known small bodies. New small bodies are discovered continuously. Most of the small bodies are members of one of the main populations, four of which that are important in the scope of this work, are introduced in the following sections. Other populations are mentioned and only briefly discussed.

After a historical introduction, the asteroid main belt is briefly introduced; it is only indirectly related to this work, but important for the understanding of the orbital dynamics of small bodies. The near–Earth objects (NEOs) and trans–Neptunian objects (TNOs) are the main subjects of this work and are discussed in more detail. Eventually, comets are introduced and their link to the other small body populations is discussed. Figure 1.1 shows a graphical representation of the radial distribution of the small bodies of the Solar System and their most important mutual interactions.

Throughout this work, the term "small body" is used as an umbrella term for all types of Solar System objects that are neither planet nor moon. For a brief outline of some basic concepts of celestial mechanics, I refer to Section A.1.

1.1.1 Historical Introduction

Comets were the first–known type of Solar System small bodies, although their nature has been a miracle until rather recently (Whipple 1950). Bright comets with large comae and tails can be observed with the naked eye; recorded observations date back into ancient times. The discovery of the first asteroid, (1) Ceres, dates back to 1801. Initially, Ceres was considered another planet orbiting the Sun between the orbits of Mars and Jupiter, although it was not possible to resolve its disk in telescopic observations, which was the case for the previously known planets. It was deduced that Ceres must be much smaller than the other planets. In the following years, the increasing number of discoveries in the region between Mars and Jupiter, and the discovery of the planet Neptune in 1846, led the astronomical community to decide to restrict the term planet to those 8 objects that are large enough to be resolved in contemporary telescopes. All other non–resolvable objects were degraded to the newly created object class of the "asteroids", Greek for "star–like object" (see Davies et al. 2008, for a historical review), due to their non–resolvable nature. The number of known small bodies increased rapidly in the late 19–th century as a result of larger telescopes and the newly conceived photographic techniques. In 1930, Pluto was discovered, which was the most distant object in the Solar System at that time, and

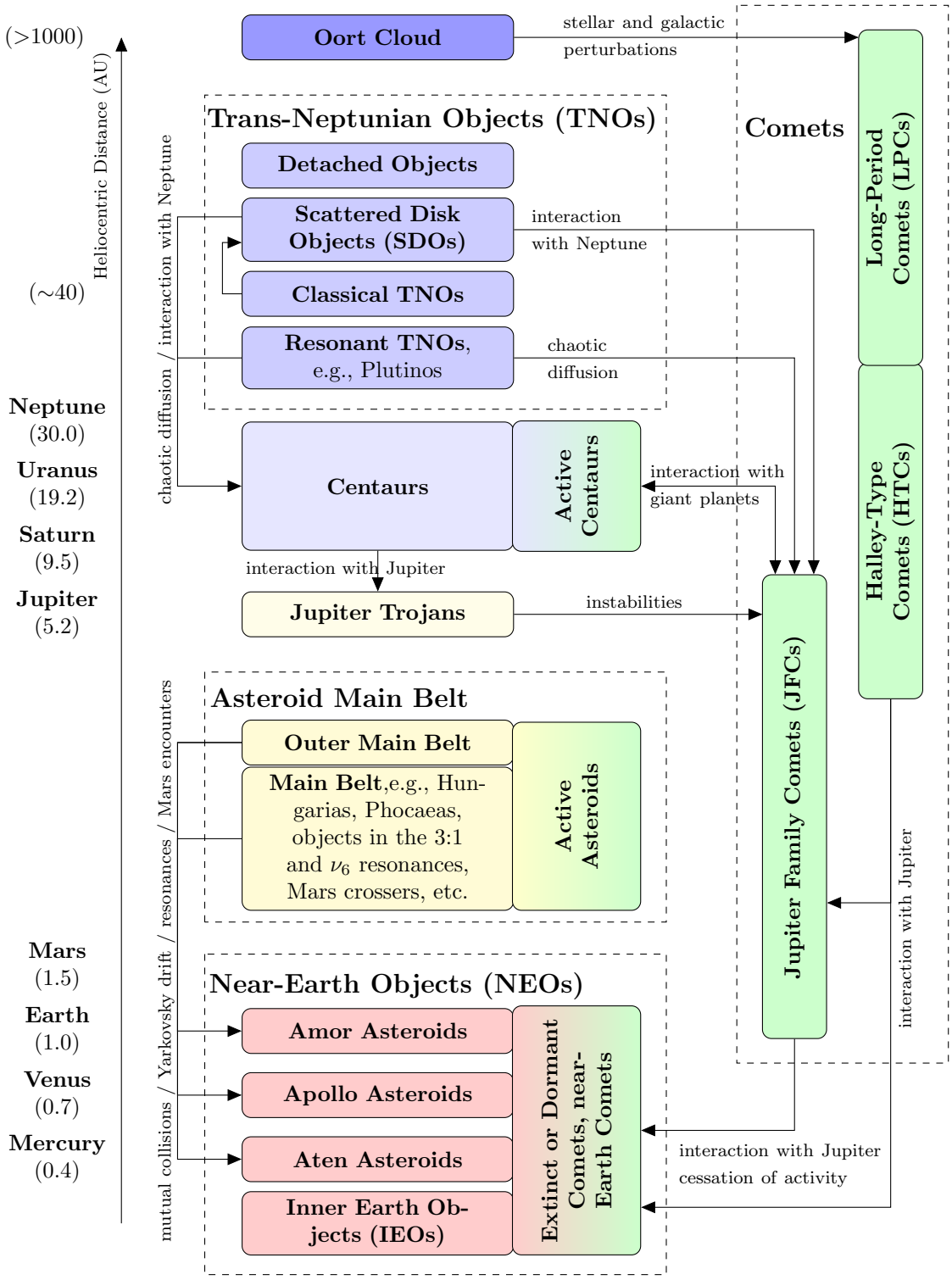

Figure 1.1 Schematic overview of the distribution of small body populations in the Solar System, and their mutual interactions. Note that the paths are only possibilities; the probability of an object impacting a planet or the Sun, or even escaping the Solar System usually exceeds the probability of any of the shown paths. Distances are not to scale. For a detailed description, cf. Sections 1.1.2–1.1.5.

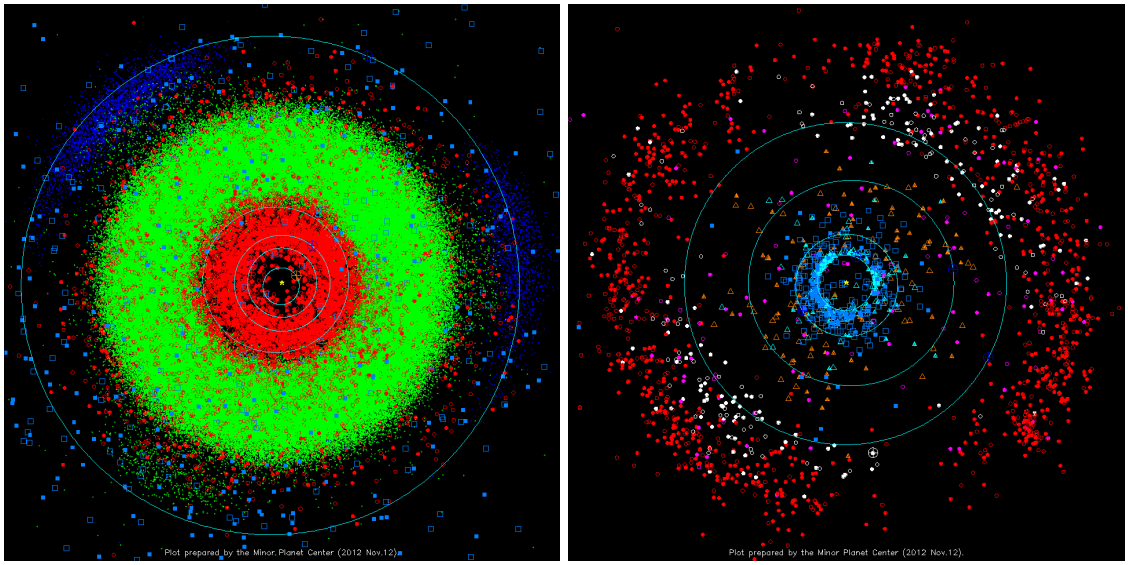

Figure 1.2 Locations of the known Solar System bodies as of November 12, 2012, in the inner (left) and outer (right) Solar System. Large circles depict the orbits of the planets. Points of different color and shape refer to different object types. In the left plot, green and red symbols depict main belt and near–Earth asteroids, respectively. In the right plot, classical TNOs and Plutinos are shown as red and white symbols, respectively. Both plots were produced by Gareth Williams/MPC.

counted as the 9th planet. Despite its rather small size, Pluto's diameter is roughly two–third the diameter of the Moon, its status as a planet was undisputed until the discovery of other small bodies with distances even larger than Pluto's in the 1990s. In 2006, the International Astronomical Union (IAU) declared Pluto a small body[1], and a member of the newly discovered trans–Neptunian population of small bodies, limiting the number of planets in the Solar System to 8.

1.1.2 The Asteroid Main Belt

The term "asteroid main belt" or simply "asteroid belt" appeared in the early 1850s describing the accumulation of asteroids with orbits between the planets Mars and Jupiter (cf. Figures 1.1 and 1.2). The belt's population comprises more than 95% of the currently known small bodies in the Solar System (as of November 2012, Minor Planet Center Observations Database). Their vast number allows for the exploration of dynamical effects using statistical methods that would not be possible from the small number of planets in the Solar System.

[1] According to Resolution 5A of the IAU General Assembly 2006 in Prague, a planet is a celestial object that (1) orbits the Sun, (2) is in hydro–static equilibrium, and (3) has cleared the neighborhood around its orbit. All Solar System objects that are not planets or satellites (or the Sun, apparently), are collectively referred to as "Solar System small bodies". Objects that meet the first two but not the third criterion, like Pluto, are also referred to as a "dwarf planet".

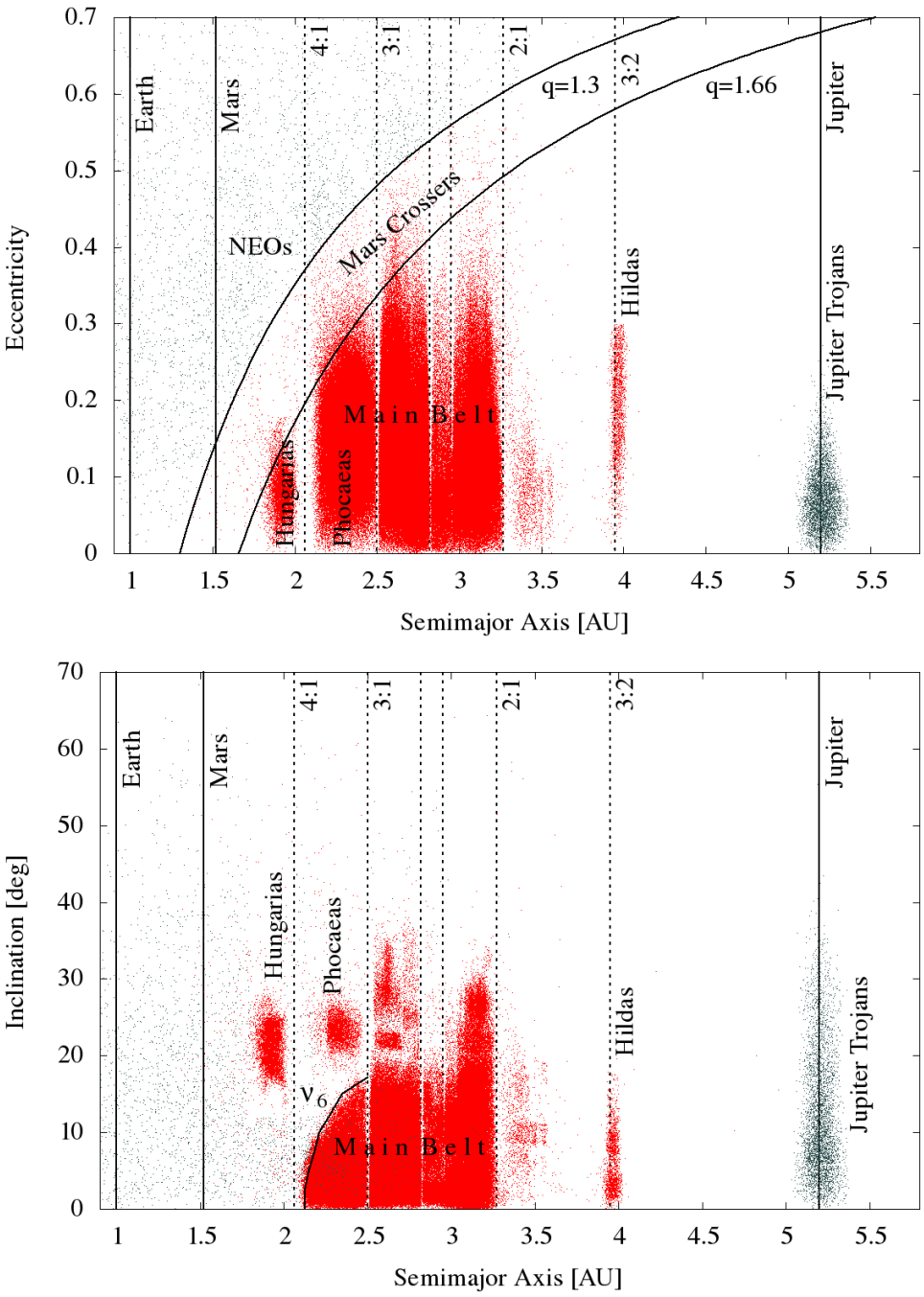

Figure 1.3 Overview of the dynamical structure of the asteroid main belt, showing the distribution in e–a (**top**) and i–a space (**bottom**). Red and grey dots represent members of the main belt and adjacent asteroid populations, respectively. The positions of planets are indicated by vertical dashed lines, dotted vertical lines represent the positions of major mean motion resonances. Curves in the top plot indicate orbits of equivalent perihelion distance, which separate the main belt from the near–Earth population and define the Mars–crossing subpopulation. The curved line in the bottom plot represents the ν_6 secular resonance (see text). Both plots have been generated from MPC data as of May 4, 2012.

1.1.2.1 Dynamical Structure

The dynamical structure of the asteroid main belt can be explored by plotting the eccentricity, e, or inclination, i, of its constituents as a function of semimajor axis, a, as shown in Figure 1.3. The massive accumulation of main belt asteroids between semimajor axes of 1.7 and 4 AU, i.e., well between the orbits of Mars and Jupiter, is obvious from both plots. The plots show that main belt asteroids are not homogeneously distributed in a–e and a–i-space: the so called "Kirkwood gaps", appear at certain values of a where only very few objects are found (Kirkwood 1866, 1869). The Kirkwood gaps are the result of "mean motion resonances" (MMR, cf. Section A.1.3.2) that occur at semimajor axes where the ratio of the orbital period of a test particle and the orbital period of Jupiter form a simple integer ratio. MMRs can lead to extreme orbital stability or chaotic behavior (see Section A.1.3.2). The locations and period ratios of the most important MMRs of the main belt are displayed in Figure 1.3. An important example is the 3:1 MMR, which constantly ejects main belt objects into near–Earth orbits (see Section 1.1.3.2). Secular resonances (see Section A.1.3.2), like the ν_6 resonance[2] with Saturn, which occurs when the mean precession rates of the longitudes of perihelia of the asteroids and of Saturn are equal to each other, also work as feeding mechanism for the NEO population. Asteroids that are caught in the ν_6 resonance have their eccentricities pumped up until they become Mars crossers and eventually NEOs. The location of this resonance is a strong function of a and i, but depends only weakly on e (Morbidelli and Henrard 1991, see also Figure 1.3). In some cases resonances can lead to an improved stability, as discussed in Section A.1.3.2. For instance, the Hilda asteroid group occupies the 3:2 mean motion resonance with Jupiter, in which close encounters with Jupiter are precluded, improving the stability of their orbits. The orbits of Hildas can be stable on timescales of $\geq$4 Gyrs (Brož and Vokrouhlický 2008).

Adjacent to the outer main belt are the "Jupiter Trojans", a group of asteroids that are in 1:1 mean motion resonance with Jupiter. Most of its members librate on tadpole orbits around the "Lagrangian Points" L4 and L5, points of stability in the three–body problem that are located in an angular distance of 60° leading (L4) and trailing (L5) the position of Jupiter on its orbit. Jupiter Trojans are not regarded members of the main belt, and they are not of significant importance for this work. Trojan asteroid populations have also been found in other planets (see the Minor Planet Center List of Trojan Minor Planets), including Neptune, Mars, and Earth.

The inner edge of the main belt is defined in terms of perihelion distance with respect to the orbit of Mars. The two curves in the upper panel of Figure 1.3 indicate lines of equal perihelion distance $q = a(1-e) = 1.3$ ($\sim$ Mars' perihelion distance) and 1.66 (Mars'

[2]The ν_6 secular resonance occurs when the precession frequency of the asteroid's longitude of perihelion is equal to the "sixth frequency of the planetary system" (Laskar 1990), which can usually be identified with the mean precession frequency of Saturn's longitude of perihelion (Morbidelli et al. 2002; Nesvorný et al. 2002).

aphelion distance), respectively. Objects with perihelion distances $1.3 \leq q \leq 1.66$ are denoted "Mars crossers", since they are gravitationally influenced by Mars and are able to cross its orbit. Those asteroids with $q \leq 1.3$ are considered members of the near–Earth object population (cf. Section 1.1.3), although this definition is somewhat arbitrary. Outer main belt objects have $a \geq 2.8$ AU (Bottke et al. 2002b).

Main belt asteroids with similar orbits are grouped together, like the "Hungaria" and "Phocaea" asteroid groups; both groups are named after their prototype asteroids: (434) Hungaria and (25) Phocaea, respectively. Hungarias are dynamically separated from the bulk of the main belt population by the cleared 4:1 mean motion resonance and their high inclinations (Figure 1.3, bottom), which they share with the Phocaeas. Phocaeas are separated from the rest of the main belt by the ν_6 resonance. A number of other subgroups in the main belt population exists, which will not be further addressed here. An intriguing phenomenon are the "asteroid families", groups of asteroids that share nearly the same proper orbital elements (see Section A.1.2.4) despite their spatial scattering. Asteroid families are believed to be collisional remnants of a common parent body (see, e.g., Hirayama 1918).

1.1.2.2 Origin and Evolution

Originally, it was hypothesized that the members of the asteroid main belt are debris of a planet that formed between the orbits of Mars and Jupiter and has been destroyed in a collision or due to the gravitational influence of Jupiter. However, dynamical simulations show that no planet could have formed in the region of the asteroid belt due to strong gravitational perturbations of Jupiter (Petit et al. 2001).

Instead, it is now believed that the constituents of the main belt are the leftovers from the formation of the planets (for a review, see Bottke et al. 2002a). The Solar System formed from a large molecular cloud consisting of gas and dust. After the gravitational collapse of the cloud, it reshaped into a disk as a result of the interplay between the conservation of angular momentum and the self–gravity of its constituents. Gas and dust particles stuck together, formed larger particles of the sizes in the μm, cm and finally km range. The central bulge of the disk formed the proto–Sun. The largest conglomerates in the disk are called "planetesimals", being the building blocks of the planets. In the region of the asteroid main belt the gravitational influence of Jupiter, which formed early, was too strong and prevented the formation of a planet. Today's main belt asteroids are the leftovers of the planetesimals in this region. Mutual collisions of the planetesimals have destroyed most of them, producing smaller debris, which we now observe as asteroids. The largest asteroids, (1) Ceres, (2) Pallas, and (4) Vesta may actually be remnant planetesimals.

Asteroids have altered significantly since the early age of the Solar System: their sizes and shapes have been altered in collisions, their internal mixing has changed as a result of their thermal evolution, mostly influenced by radiogenic heating, and their surfaces have evolved due to cratering, impacts of micrometeorites, and space–weathering (see Section 1.2.4). Furthermore, their orbits have changed due to the interaction with planets and dynamical resonances in the course of the migration of the giant planets (cf. Section 1.1.4.2), which led to the ejection of more than 99% of the asteroids in the main belt. Hence, the asteroids observed today make up less than 1% of the number of asteroids in the primordial belt (Petit et al. 2001). Eccentricities and inclinations of the remaining asteroids have been pumped up, increasing the degree of mixing between the different taxonomic types as a function of heliocentric distance.

The current dynamical evolution of main belt asteroids is governed by the "production" of main belt asteroids in the course of mutual collisions, and their escape from the main belt due to dynamical effects like resonances, planetary perturbations or collisions. Most asteroids that leave the main belt are ejected from the Solar System, collide with the Sun or a planet. Few asteroids end up in other asteroid populations, like the near–Earth object population (cf. Figure 1.1 and Section 1.1.3), which is the most important population of main belt asteroid descendants. Bottke et al. (2002b) have identified a number of main belt subpopulations (Mars crossing asteroids, Hungarias, Phocaeas, and outer main belt asteroids) and dynamical resonances (3:1 mean motion resonances, ν_6 secular resonance) as the main drainages to the NEO population. The transport of main belt asteroids to the NEO population is driven by a variety of resonances that increase the orbital eccentricities of these asteroids, leading them into resonances (ν_6, 3:1) or into Mars–crossing orbits, from where they get injected onto near–Earth orbits (Morbidelli et al. 2002; Nesvorný et al. 2002). Furthermore, mutual collisions of main belt asteroids can be involved as well: driven by the size–dependent Yarkovsky drag[3] collisional debris can dynamically evolve into a resonance or a planetary encounter and end up in near–Earth space.

1.1.3 Near-Earth Objects (NEOs)

The discovery of asteroid (433) Eros in 1898 showed that asteroids can come close to the Earth. In the following decades, a growing number of the later so–called "near–Earth asteroids" has been discovered. In this work, I use the term "near–Earth objects", which includes near–Earth asteroids and comets that move on near–Earth orbits. NEOs have

[3]The Yarkovsky drag (Öpik 1951) is a force exerted on small bodies that is caused by the anisotropic emission of thermal photons. The rotation of small bodies leads to a cooling of its surface on the night side. The surface temperature, and hence the emission of thermal photons, is higher near the evening terminator compared to the morning terminator. The emission of thermal photons exerts a transfer of momentum on the body. The resulting force is directed, due to the anisotropic emission of photons. The magnitude of the Yarkovsky force depends on the thermal properties of the body, its size, and albedo. Small bodies and low–albedo bodies experience strong Yarkovsky drags. See Bottke et al. (2002c) for a full discussion of the Yarkovsky force.

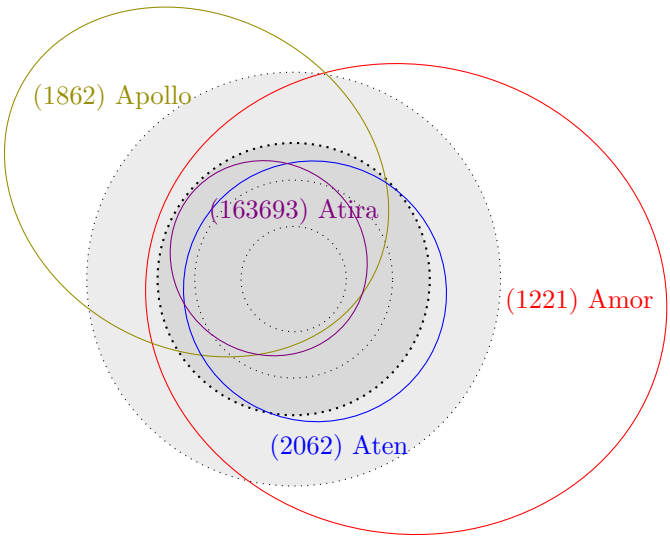

Figure 1.4 Dynamical classification of NEOs. The orbits of the terrestrial planets are shown as dotted circles (for the sake of simplicity disregarding their eccentricity and orientation in space). Earth's orbit is highlighted in bold. The four asteroids of which the orbits are plotted are the prototypes of the respective dynamical types of NEOs. For a detailed description, cf. Section 1.1.3.

orbits that take them close to the Earth; they are defined as having $q \leq 1.3$, which means that their perihelion is inside the orbit of Mars, which is somewhat arbitrary, but common use.

1.1.3.1 Orbital Classification

The population of near–Earth asteroids is unstable; the average dynamical lifetime of NEOs is $\sim 10^7$ yrs (Morbidelli and Gladman 1998). Hence, the NEO classification scheme is based on a momentary snapshot of the currently observed population, rather than on profound dynamical distinctions between the individual classes. According to the classification scheme of Shoemaker et al. (1979), which is still commonly used, the NEO population can be divided into 3 different dynamical groups, named after their respective prototypes. The classification is mainly based on the perihelion distances of Mars ($q \sim 1.3$) and the Earth ($q = 0.983$), and the aphelion distance of the Earth ($Q = 1.017$). A fourth dynamical group, the IEOs, was added later to the scheme. In the order of decreasing average semimajor axis, the different types are (cf. Figure 1.4):

Amor ($a > 1$ AU, $1.017 < q < 1.3$ AU), objects outside Earth's orbit that come close to Earth, but do not cross its orbit; the gravitational attraction of the Earth can influence the orbit of Amor–type NEOs. (433) Eros is an Amor–type NEO.

Apollo ($a > 1$ AU, $q < 1.017$ AU) are objects that spend most of their time outside

Earth's orbit, but are able to cross it. Their orbits are likely to be changed by Earth's gravitational field in close encounters.

Aten ($a < 1$ AU, $Q > 0.983$ AU), objects that spend most of their time inside Earth's orbit and are able to cross it. Like Apollo NEOs, Aten's are likely to be influenced by Earth during close encounters.

Inner Earth Object (IEO) or **Atira** asteroids ($a < 1$ AU, $Q < 0.983$ AU) are objects that spend their whole lifetime inside Earth's orbit. Their proximity to the Sun hampers their discovery significantly.

The relative composition of the known NEO population as of November 2012, according to the Minor Planet Center Observations Database, is: 42.0% Amors, 49.6% Apollos, 7.7% Atens, and 0.2% IEOs.

1.1.3.2 Origin and Evolution

The average dynamical lifetime of NEOs is $\sim 10^7$ yrs (Morbidelli and Gladman 1998), which is short compared to the age of the Solar System (4.5×10^9 yrs). At the end of their dynamical lifetime, most NEOs are ejected from the Solar System, or collide with a planet or the Sun, as a result of encounters with the terrestrial planets or due to resonances. Despite the relative short lifetime of individual NEOs, the overall number of NEOs is believed to be steady with time, which was derived from lunar crater statistics (Grieve and Shoemaker 1994). The existence of the NEO population requires continuous replenishment. Sources of replenishment have been found in the main asteroid belt (see Section 1.1.2) and the comets (see Section 1.1.5) (Bottke et al. 2002b). According to a de–biased, magnitude–limited model of the NEO population (Bottke et al. 2002b) the NEO population obtained 37% and 23% of its constituents from the 3:1 mean motion and ν_6 secular resonance, 25%, 8% and 6% from the Mars crossing, outer main belt and Jupiter family comet[4] populations, respectively. The Mars crossing population includes members of the Phocaea and Hungaria asteroid groups.

1.1.3.3 Impact Hazard

As a consequence of the proximity of NEOs to the Earth, some of them pose an impact hazard. NEOs with orbits that cross Earth's orbit are referred to as "potentially hazardous asteroids" (PHAs). PHAs are defined as having a minimum orbit intersection distance with Earth ($MOID$) of 0.05 AU or less, and an absolute magnitude (H) of 22 mag or brighter, according to the JPL Near Earth Object Program Website. The magnitude limit

[4]The study by Bottke et al. (2002b) takes only the Jupiter family comets into account, disregarding contributions by the long–period comet population, due to the lack of observations of such objects in near–Earth space. However, a contribution of HTCs and LPCs to the NEO population is anticipated.

can be roughly translated into a diameter of 140 m or larger. As of March 1, 2013, 1381 PHAs are known, making up 14% of the known NEO population.

In order to address the NEO impact hazard, the U.S. Congress mandated NASA to compose the Spaceguard Survey Report (1992). The "United States House Committee on Science, Space and Technology" mandated NASA in 1994 to identify and catalog 90% of all NEOs and comets with diameters of 1 km and larger within the next 10 yrs. Mainzer et al. (2011b) have declared this goal to be met and estimate the number of NEOs with diameters of 1 km and larger to be 981±19. In 2005, the "George E. Brown, Jr. Near-Earth Object Survey Act" assigned NASA to detect 90% all NEOs with diameters of 140 m and larger. A 140 m–sized asteroid impacting Earth is able to cause damage on a regional scale, whereas a 1 km–sized NEO is capable of causing global damage (Defending Planet Earth 2010). In the course of both mandates, a number of NEO survey programs have been initiated, including the successful LINEAR program (Viggh et al. 1998), the Catalina Sky Survey (Catalina Sky Survey Website), and the "Panoramic Survey Telescope and Rapid Response System" (Pan-STARRS, PanSTARRS Website). For more information on the NEO impact hazard, see Morrison et al. (2002).

1.1.4 Trans–Neptunian Objects (TNOs)

Small bodies spending most of their orbits outside the orbit of Neptune are referred to as "trans–Neptunian objects" (TNOs). Formally, their semimajor axes, a, are required to be larger than that of Neptune, a_{N}, $a > a_{\mathrm{N}}$ (Gladman et al. 2008). TNOs represent the most distant known objects in the Solar System.

The existence of a trans–Neptunian population has not been proven until the discovery of the object (15760) 1992 QB1 (Jewitt et al. 1992). There were speculations about the existence of such a population of minor planets even before the discovery of Pluto (see Davies et al. 2008, for a historical discussion)[5]. The speculations were motivated by the persistent occurrence of short–period comets moving close to the ecliptic plane, suggesting the existence of an ecliptic annulus of cometary nuclei outside the orbit of Neptune. The first quantitative analyses of such a presumed population were carried out by Edgeworth (1949) and Kuiper (1951). Although Edgeworth published his work first, the annulus of the trans–Neptunian region is often referred to as the "Kuiper belt". In order to avoid the naming issue, the member objects are usually referred to as trans–Neptunian objects.

1992 QB1 was discovered as a result of one of a number of dedicated surveys. Many discoveries followed, so that as of March 1, 2013, the known trans–Neptunian population comprises 1632 objects, 883 of which have reasonable orbit determinations (see below).

[5]After its discovery, Pluto was considered a planet. In fact, it was the first known member of the TNO population, which later led to its demotion (see Section 1.1.1).

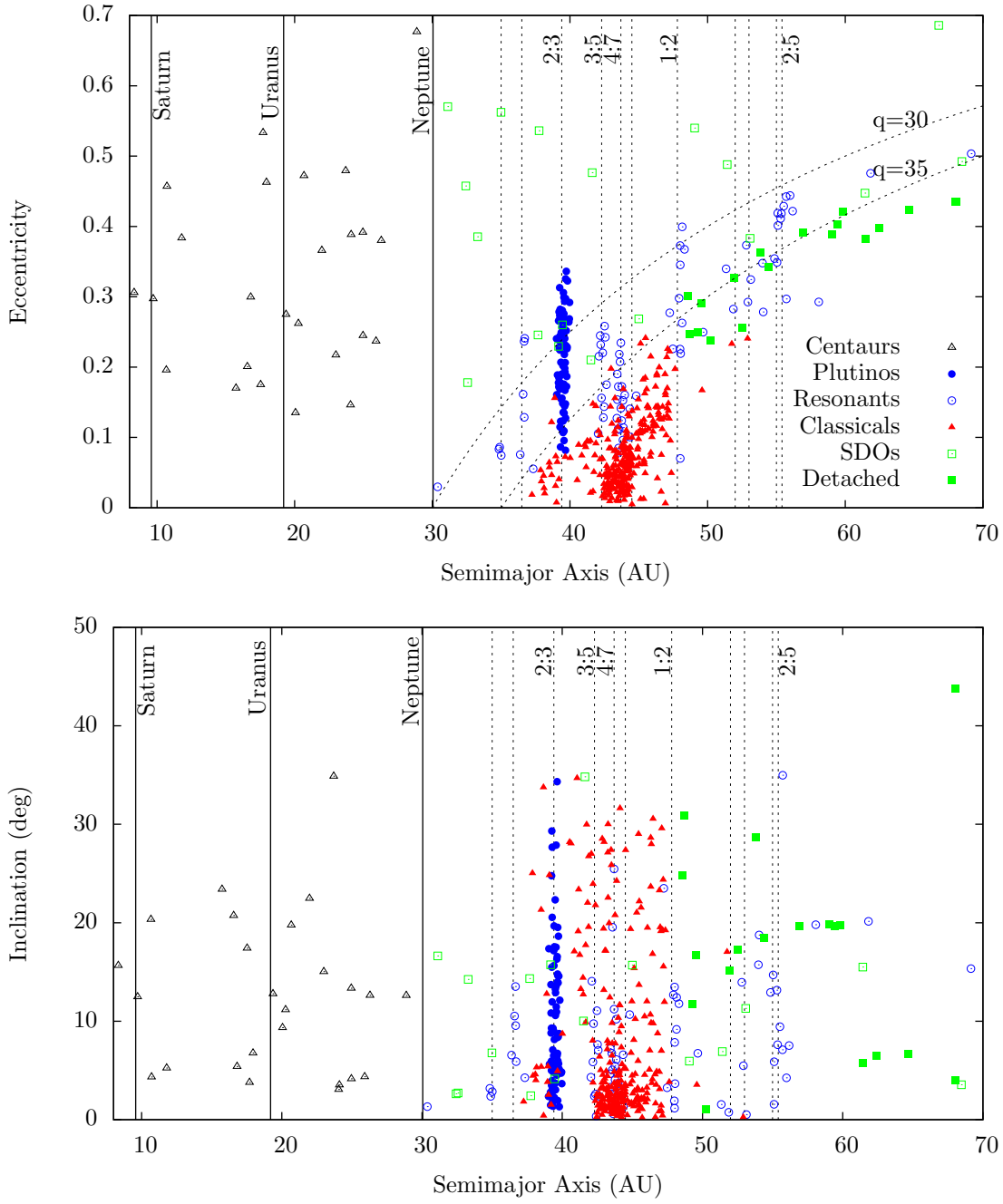

Figure 1.5 TNO classifications in eccentricity versus semimajor axis (**top**) and inclination versus semimajor axis (**bottom**) plots. The symbols have the same meaning in both plots; the key is given in the top plot. The classification of TNOs follows Gladman et al. (2008). The positions of the outer planets and the most important mean–motion resonances, as well as two lines indicating curves of equal perihelion distances $q = a(1 - e)$ are shown. Most of the objects with semimajor axes greater than 70 AU, which are not shown in the plots, are SDOs and detached objects.

1.1.4.1 Dynamical Structure

The dynamical structure of the trans–Neptunian region is different from that of the asteroid main belt, as can be seen in Figure 1.5. The investigation of its dynamical structure is still subject to current research. Note that the large semimajor axes of TNOs require their orbital periods to be of the order of a hundred years and more. Consequentially, only small orbital arcs have been observed in all TNOs, compromising the accuracy of their orbit determinations. Even the length of Pluto's observed arc is only $\sim$145°, including observations from more than 8 decades. Gladman et al. (2008) argue that TNOs have to be observed over at least three oppositions, i.e., 3 years, to be able to determine proper orbits for them.

The classification of TNOs into subclasses has been attempted in Elliot et al. (2005) and Gladman et al. (2008), leading to similar classifications with slightly different definitions. In this work, I apply the classification scheme defined by Gladman et al. (2008), which is based on numerical simulations of the orbit of each object over 10 million years, taking into account uncertainties of the orbital elements. Little is known about the dynamical origin and evolution of TNOs. Hence, the classification scheme is based on the current orbital situation and provides information on the short–term dynamics rather than guesses on the past or future orbital evolution of the objects.

The TNO subpopulations are introduced below, in the order of increasing average semimajor axes. Figure 1.5 plots the distributions of the individual subtypes in e–a and i–a space, respectively.

Centaurs are objects moving between the giant planets. Strictly speaking, they are not members of the TNO population, since, by definition, they have a semimajor axis a smaller than that of Neptune ($a < a_N$) (cf. Figure 1.5). However, they are listed here since they are tightly dynamically linked to the TNO population, being a transition stage of TNOs before they (1) escape the Solar System, (2) impact one of the giant planets, or (3) enter the inner Solar System as short–period comets (cf. Section 1.1.5). The Centaurs are mainly replenished from the scattered disk population, but also from other TNO subpopulations like the Plutinos. The orbital evolution of Centaurs is characterized by close encounters with the giant planets resulting in a chaotic dynamical behavior (Levison and Duncan 1997) and relatively short lifetimes of one to several hundred Myrs with a median of 9 Myrs (Tiscareno and Malhotra 2003, and references therein). Some Centaurs, like (2060) Chiron (Luu and Jewitt 1990; Hahn and Bailey 1990), have been observed to show cometary activity, underlining their transitional character.

Resonant Objects are TNOs whose orbits are in resonance with that of Neptune (for a discussion of orbital resonances, see Appendix A.1.3.2). The largest subgroup of resonant objects, containing 90% of all known resonant TNOs as of March 1, 2013

(MPC), are the "Plutinos". Plutinos are TNOs in 2:3 mean motion resonance with Neptune (Melita and Brunini 2000). They are named after their prototype, former planet Pluto. Plutinos have semimajor axes of ∼39.5 AU. 27% of the Plutinos are believed to have dynamical lifetimes of the order of the age of the Solar System (Tiscareno and Malhotra 2009). Plutinos that are ejected from the population are likely to end up in the Centaur and JFC population (Duncan et al. 1995; Morbidelli 1997; di Sisto et al. 2010). The Plutino population is most likely the result of a resonant capture mechanism: the outward migration of Neptune, as explained by the Nice model (see Section 1.1.4.2), led to the capture of small bodies in its 2:3 mean motion resonance, where they were locked (Malhotra 1993) and transported outward to their current orbits. As a consequence of the migration, the eccentricities and inclinations of Plutinos are pumped up. Plutinos are depicted as white symbols in Figure 1.2. Other noteworthy resonant populations populate the 4:7 (at $a \sim 43.7$ AU), 3:5 (∼42.3 AU) and 1:2 MMRs (∼47.8 AU), the members of the latter are often referred to as "Twotinos". The Twotino population is considered the outer edge of the Kuiper belt (see Figure 1.5).

Scattered Disk Objects (SDOs) are defined as those TNOs that are actively scattering off Neptune (Gladman et al. 2008; Duncan and Levison 1997). They are identified using numerical simulations: those objects whose semimajor axes vary more than 1.5 AU in a 10^6 yrs dynamical model integration are classified as scattered disk objects (Gladman et al. 2008). SDOs cover a wide range of semimajor axes: they can be found within the Centaur region ($a > 30$ AU), as well as outside the classical Kuiper belt ($a > 50$ AU). The scattered disk population is likely to be replenished by the classical Kuiper belt objects (Duncan and Levison 1997), namely the hot classicals that have high inclinations (see, e.g., Fraser et al. 2010). In the long term, SDOs evolve onto Centaur orbits and finally end up as short–period comets (Levison and Duncan 1997; Horner et al. 2003), or they are ejected from the Solar System in the course of close approaches with the giant planet.

Detached Objects are non–scattering TNOs with large eccentricities ($e > 0.24$) and usually large semimajor axes with $a < 2000$ AU. Despite their large semimajor axes, they are still close enough to the Sun to be untouched from influences from outside the Solar System (Gladman et al. 2008). An example for a detached object is (90377) Sedna, which is currently the object with the largest known aphelion distance ($Q = 937$ AU, $q = 76$ AU). The mechanisms that led to the formation of the detached population are the subject of current research and not yet understood.

Classicals (formally: Classical Kuiper belt objects) make up 55% of all known TNOs as of March 1, 2013 (MPC). They are roughly distributed in a torus between 39 and 48 AU from the Sun in the ecliptic plane (red symbols in Figure 1.2). Classicals are those

TNOs that do not fall into any one of the aforementioned categories (Gladman et al. 2008). The classical Kuiper belt can be subdivided into a main classical belt, an inner ($a < 39.4$ AU), as well as an outer belt ($a > 48.4$ AU). The main belt population can be again split into a dynamically "hot" and a "cold" subpopulation with inclinations $i > 5°$ and $i < 5°$ (see Figure 1.5 and Gladman et al. 2008; Petit et al. 2011), respectively. The adjective "hot" refers to the higher inclinations of these objects. Although there is no dynamical basis for such a separation, both subpopulations show significant differences: cold classicals have higher albedos (Brucker et al. 2009), redder surfaces (Trujillo and Brown 2002b), and are more likely to have companions (Noll et al. 2008) than hot classicals. These observations suggest that the classical main belt is made up from two overlapping populations. Morbidelli et al. (2008) suggest that cold classicals might have formed where they are today, whereas the hot classicals might have been pushed into their current orbits in the course of the migration of the giant planets (see below). This evolution would also explain the excitation of their eccentricities and inclinations, as observed today.

1.1.4.2 Origin and Evolution

The existence of a trans–Neptunian population puts strict constraints on formation and evolution models of the Solar System. In the last two decades, a number of models have emerged to explain the existence and structure of the Kuiper belt (for a review see Morbidelli et al. (2008)).

The origin and evolution of the Kuiper belt is believed to be tightly connected to the migration of the giant planets, which is predicted by the "Nice[6] model" (Gomes et al. 2005; Morbidelli et al. 2005; Tsiganis et al. 2005). According to this model, the giant planets were originally on nearly circular orbits with heliocentric distances of 5.5–14 AU (today, Jupiter's and Neptune's semimajor axes are 5.2 and 30 AU, respectively). A planetesimal disk is assumed to lie outside the orbits of the giant planets. Gravitational interaction of the giant planets with the planetesimal disk leads to a transport of angular momentum towards the planetesimals. As a result of the transfer, the orbits of the planets move outwards and planetesimals are ejected from the Solar System. After 350–1100 Myrs, the orbits of Jupiter and Saturn have changed in such a way that they cross their mutual 1:2 mean motion resonance, exciting the orbits of the planets so that their orbits are quasi–chaotic for a few million years. During that time, the planetesimal disk destabilizes and its constituents are scattered all over the Solar System. The remaining planetesimals are able to damp the excitation of the giant planets, which find themselves very close to the orbits where they are observed today.

The outcome of the Nice model agrees with a number of observational facts: it reproduces the coarse structure of the Kuiper belt and the orbits of the giant planets; fur-

[6]The Nice model is named after the French city Nice, where it has been conceived.

thermore, the stirring of the planetesimal disk provides explanations for a brief period of high influx of small bodies into the inner Solar System (the "late–heavy bombardment"), and the existence of the Oort cloud (see Section 1.1.5.2). For a full discussion of the Nice model and its implications for the origin of the Kuiper belt, see Morbidelli et al. (2008).

1.1.5 Comets

Comets are icy objects that originate from the outskirts of the Solar System, i.e., in the Kuiper belt (see Section 1.1.4) and the hypothetical Oort cloud (see below). Together with the TNOs, they represent the most pristine objects in the Solar System (Morbidelli 2005). Comets that enter the inner Solar System show cometary activity as a result of the sublimation of their surface ices.

1.1.5.1 Dynamical Structure

The comet population can be subdivided according to their dynamical properties, in particular their orbital periods and Tisserand parameters with respect to Jupiter, T_J (the Tisserand parameter is a dynamical quantity indicative of the interaction of a body with a planet; see Section A.1.3.1 for a full discussion of the parameter):

Short–period comets are also referred to as Jupiter family comets (JFCs) and have orbital periods of less than 20 yrs and $2 \leq T_J \leq 3$, which makes them strongly tied to the gravitational influence of Jupiter. JFCs usually have low inclinations, which, together with their short orbital periods, suggest an origin in the Kuiper belt (Levison and Duncan 1997).

Long–period comets (LPCs) have orbital periods longer than 200 yrs and $T_J < 2.0$. LPCs have $a > 35$ AU, and one third of them even has $a \sim 20000$ AU (Weissman 1996). The inclinations of LPCs are nearly isotropically distributed, which, together with their long periods, suggests an origin in the Oort cloud (see below).

Halley type comets (HTCs) have periods between 20 and 200 yrs and $T_J < 2.0$. HTCs have $a \sim$ 10–30 AU and can be considered the short–period tail of the LPCs (Weissman 1996).

Active asteroids or "main belt comets" (MBCs) are main belt asteroids that show, usually sporadic, activity. They are dynamically unrelated to all other types of comets and have been discovered rather recently (Hsieh and Jewitt 2006). The reason of their activity is manifold: sublimation of surface ices, excavation of surface material as the result of a recent impact, rotational instability or thermal fracture (for a discussion of different mechanisms, see Jewitt 2012). Orbits of active asteroids barely differ from the nearly circular orbits of most main belt asteroids. Most active asteroids have been observed in the outer main belt.

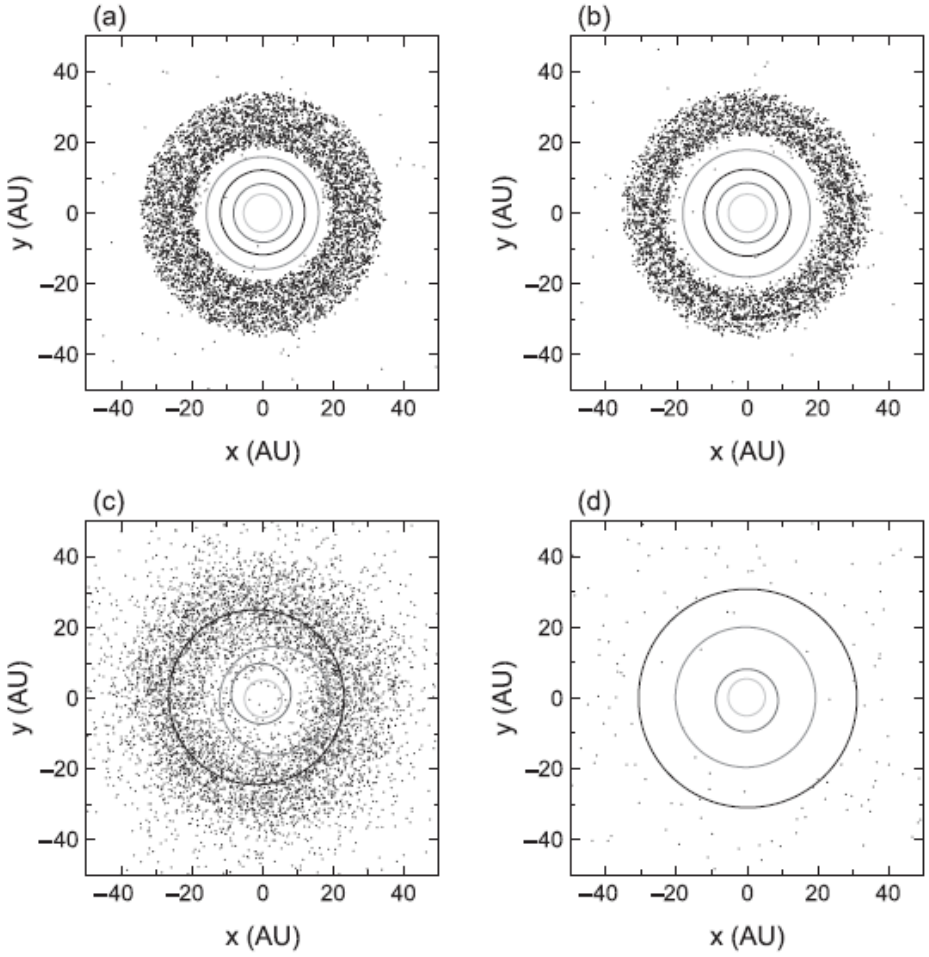

Figure 1.6 Four stages in the evolution of the outer Solar System according to the Nice model (see text, as well as Gomes et al. 2005; Morbidelli et al. 2005; Tsiganis et al. 2005). **(a)** Original structure of the outer Solar System: the giant planets are on orbits much closer to the Sun than today, and surrounded by the remnants of the planetesimal disk. **(b)** Dynamical friction leads to a transfer of linear momentum from the planets to the disk. The motion of the planets slows down, increasing their semimajor axes.**(c)** Jupiter and Saturn cross their mutual 1:2 mean motion resonance, leading to a quasi–chaotic behavior of the giant planets, in the course of which planetesimals are scattered from their disk basically anywhere in the Solar System. **(d)** Most of the mass has been removed from the planetesimal disk. The remaining bodies, forming the scattered disk and classical Kuiper belt populations, have damped the outward migration of the giant planets, which are now on orbits very similar to their observed orbits. Illustration taken from Morbidelli et al. (2008).

1.1.5.2 Origin and Evolution

The significant differences in the orbital periods between short–period and long–period comets suggests two distinct origins for both populations:

- From the nearly isotropic distribution of the long–period comets and their orbital periods, Oort (1950) concluded the existence of a spherically symmetric reservoir of cometary nuclei in a distance of 50000 to 150000 AU from the Sun. LPCs and HTCs can be removed from the Oort cloud by stellar and/or galactic perturbations (Weissman 1996; Levison et al. 2001). So far, the existence of the Oort cloud is only a hypothesis; not a single Oort cloud objects has been discovered, which is the result of its vast distance. Nevertheless, its existence is considered assured.

- The short periods of JFCs, and the fact that their orbital planes are close to the ecliptic, suggests an origin of these objects in a region much closer than the Oort cloud and close to the ecliptic. Numerical simulations by Duncan and Levison (1997), as well as Levison and Duncan (1997), showed that SDOs are a likely source of short–period comets. Furthermore, the Centaurs (Tiscareno and Malhotra 2003), resonant TNO populations (Morbidelli 1997; di Sisto et al. 2010, have identified the Plutinos to be a possible source of JFCs), and the Jupiter Trojans (Levison et al. 1997) have been identified as sources of the short–period comets. Inversely, numerical simulations of Horner et al. (2004) suggest that short–period comets are able to become Centaurs, as well. The simulations of Levison and Duncan (1997) show that comets that are scattered inward from the trans–Neptunian region are under the dynamical control of only one planet at any time, with a Tisserand parameter of roughly 3 with respect to this planet. The comet scatters randomly inward or outward, but its eccentricity is restricted to a maximum value of $\sim$0.25, which is a result of the Tisserand parameter being locked at $\sim$3. Thus, the comet can only be handed over to the planet interior or exterior of the current one, until Jupiter is reached, where eccentricities of 1 are possible, which ejects the comet from the Solar System.
  Short–period comets are expected to show activity for $\sim$12000 yrs, and the number of extinct comets, having ceased their activity, is estimated to be 3.5 times the number of currently active JFCs (Levison and Duncan 1997). Extinct (and also active) comets can end up in the NEO population (Bottke et al. 2002b). In the long term, i.e., after the median dynamical lifetime of 4.5×10^7 yrs, most comets are ejected from the Solar System or impact a planet (Levison and Duncan 1997) or the Sun (Bailey et al. 1992). Comets are believed to be a major source of water and organic material present on the Earth (Hartogh et al. 2011; Irvine 1998).

1.2 Physical Properties of Small Bodies

The small bodies of the Solar System have all formed from the remnants of the same disk of planetesimals. Nevertheless, an enormous variety can be observed in the physical properties of small bodies from different populations, but also within the same population, providing insights into evolutionary differences.
In this section, the basic physical properties of small bodies are introduced, and methods that are used to deduce them are outlined and discussed. Differences between the members of the individual populations are highlighted.

1.2.1 Brightness

Small bodies are usually too small and/or too far away to be optically resolved[7] using telescopic observations, producing only star–like images on the detector. Nevertheless, optical observations, measuring the disk–integrated amount of solar light reflected from the object's surface, are a most efficient way to reveal the physical properties of small bodies. In the following, I provide a brief introduction into the basic concepts of astronomical brightness measurements.

1.2.1.1 Apparent Magnitude

The observed brightness, or "apparent magnitude", of an object is mainly a function of its size and surface albedo (see Section 1.2.2.1), and the observation geometry between the Sun, the observer and the object (see Section A.1.1). The historic magnitude scale is the common means to describe brightness in most fields of astronomy. The magnitude unit is a relative measure to describe the brightness difference between to objects, m_1 and m_2, in terms of their fluxes, F_1 and F_2, respectively, as

$$m_1 - m_2 = -2.5 \log_{10} (F_1/F_2) , \tag{1.1}$$

meaning that a difference in brightness of five magnitude units equals a flux ratio of one hundred. The magnitude scale is calibrated using measurements of calibration stars. Note that as a result of the minus sign in Equation 1.1, objects with lower magnitudes have higher fluxes, and therefore are brighter.

1.2.1.2 Color Information

The apparent magnitude is a wavelength–dependent parameter, since the solar spectrum, and the reflectance spectrum of the target, are non–uniform. This property can be used

[7] Resolved observations of the surfaces of small bodies are only possible for the largest specimen. Examples are the main belt asteroids (1) Ceres and (4) Vesta, as well as the trans–Neptunian object (134340) Pluto, which have all been observed by the Hubble Space Telescope. Interferometric observations of small bodies are planned for the future (Li et al. 2011).

to obtain coarse spectral information on the target by using color filters that constrain the spectral transmissivity. Examples are the widely used V–band ($\sim$0.55 μm) and R–band ($\sim$0.66 μm) filters[8] of the Johnson UBVRI photometric system (Johnson and Morgan 1953), resulting in apparent magnitudes V and R, respectively. Coarse spectral slopes can be expressed by so–called "color indices", which represent the difference in magnitude between two bands. For instance, a color index $V - R = 0.5$ means that the V–magnitude of an object is 0.5 mag higher (fainter in V) than its R–band magnitude and, hence, the object has a reddish color. The following discussions of the object brightness are presented in V–band magnitudes. All relations are equally valid for any other photometric band.

1.2.1.3 Absolute Magnitude and Phase Curve

In order to be able to compare the apparent magnitudes $V = V(\alpha, r, \Delta)$ of two observations, the magnitudes have to be normalized to the same geometry and aspect angles. Aspect effects (lightcurve effects, see Section 1.2.3) have to be taken account of by either averaging observations to determine the average brightness, or by correcting the measured brightness, if the lightcurve is known. In order to correct for the observational geometry, two steps are necessary. Firstly, the heliocentric distance r and the distance from the observer Δ of the target have to be normalized to a distance of 1 astronomical unit (AU, see Section A.1.1), resulting in the "reduced magnitude", $V(\alpha, 1, 1)$

$$V(\alpha, 1, 1) = V(\alpha, r, \Delta) - 5 \log r\Delta, \tag{1.2}$$

with r and Δ given in AU. Secondly, the reduced magnitude has to be corrected for the solar phase angle, α (see Section A.1.1). Objects observed at low solar phase angles appear to be brighter than those with high α, in the same way as the disk–integrated brightness of the Moon is higher at low phase angles. The geometry and phase angle–corrected magnitude is called the "absolute magnitude"[9], H, which equals the apparent magnitude of a target body observed in 1 AU distance from the Sun and the observer, respectively, with a solar phase angle of zero (Bowell et al. 1989)

$$H = V(\alpha, 1, 1) + 2.5 \log \left[(1 - G)\, \phi_1(\alpha) + G\, \phi_2(\alpha) \right], \tag{1.3}$$

with the "slope parameter", G, and the phase functions $\phi_1(\alpha)$ and $\phi_2(\alpha)$. The slope parameter G describes the gradient of the phase curve and is scaled in such a way that

[8] The widespread use of the V and R–band filters has not only historical reasons. The V–band filter transmission curve allows for the most energetic part of the solar spectrum to pass, making it suitable for objects of neutral color that are illuminated by the Sun. The R–band filter allows for transmission of the reflected light of reddish objects, which are quite frequent among small bodies. Furthermore, modern CCD detectors have their best sensitivity characteristics in the red regime.

[9] Magnitudes used in this work are mainly V–band magnitudes. Hence, H usually refers to the absolute magnitude in the V–band, H_V, if not mentioned otherwise.

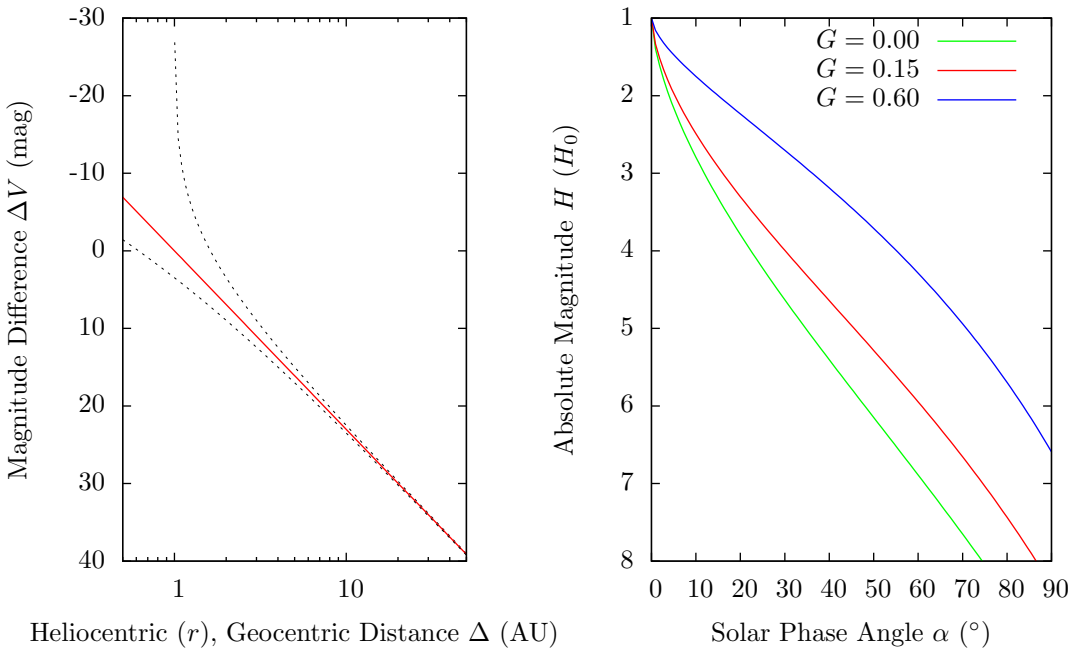

Figure 1.7 Effects of heliocentric and geocentric distance (left panel), and solar phase angle (right panel) on the apparent magnitude, according to Equations 1.2 and 1.3, respectively. **Left**. The red line shows the effect of the distance of an object from the Sun and the observer on its apparent magnitude, assuming the case $r = \Delta$, which is a good approximation for objects that are far from the Sun (e.g., TNOs). For objects closer to the Sun (e.g., NEOs), r and Δ are significantly different; the dotted lines limit the possible values for this case, assuming $|r - \Delta| = 1$ (the object is in opposition). The baseline of this plot is that the apparent magnitude of any object is a strong function of its distance from the Sun. Note that Jupiter ($H = -9.4$ mag) would have an apparent magnitude of only $V = 7.6$ mag if it would be placed at the outer edge of the Kuiper belt ($r = \Delta = 50$ AU). **Right**. The right panel shows a set of arbitrary phase functions for different values of G. $G = 0.15$ is the standard value that is used if no information on the phase curve is available (Tedesco 1990). The apparent brightness of a body drops significantly with α; hence, an insufficient determination of G introduces significant uncertainty.

$G \approx 0$ applies for steep phase curves (low–albedo bodies, generally) and $G \approx 1$ applies for shallow phase curves (high—albedo bodies). For a definition of the phase functions, see Bowell et al. (1989). H and G are obtained by fitting the reduced magnitudes at different phase angles α to Equation 1.3 (see Figure 1.7). The H–G formalism has been introduced to properly describe the magnitude of an atmosphere–less body with the smallest possible number of parameters. Note that Equation 1.3 is only an empirical relation without physical justification that may fail for some objects, whereas Equation 1.2 is based on physical principles.

The absolute magnitude H is sometimes referred to as the "intrinsic brightness" of an object, since it is independent of variable factors like distance or phase.

Properly measured values of H and G are available only for a limited number of

small bodies. If no measured value is available, $G = 0.15$ is usually adopted, which is suggested by Tedesco (1990) based on photometry of main belt asteroids. The largest database of H magnitudes is the Minor Planet Center Observations Database, determined from astrometric observations with only limited photometric accuracy. It has often been criticized that no uncertainties are provided with the MPC H magnitudes. Several works (e.g., Pravec et al. (2012); Romanishin and Tegler (2005); Benecchi et al. (2011)) show that MPC H magnitudes can deviate significantly from properly measured H magnitudes.

1.2.1.4 Observational Bias

Small body discovery surveys, most of which are performed using observations in the optical (e.g., Petit et al. 2008), are subject to observational bias. The bias leads to the incompleteness of the known small body populations compared to the total populations, and is caused by multiple effects: (1) bias introduced by the observation geometry, (2) the limiting magnitude of the survey telescope, and (3) the physical properties of the objects. The limiting magnitude (2) is a function of the telescope's aperture, detector sensitivity, and the observing conditions; objects fainter than the limiting magnitude are undiscoverable. The observation geometry (1), i.e., the distance from the Sun and the observer, as well as the solar phase angle of the object, impacts the detectability of small bodies via Equations 1.2 and 1.3; farther objects and objects with high phase angles are harder to detect. Finally, the physical properties of the objects (3) impact their detectability: the discovery of small and low–albedo objects[10] is biased against compared to large and high–albedo objects (this is a consequence of Equation 1.4).

1.2.2 Size and Albedo

Despite being the most basic physical parameter, the sizes of only few small bodies have actually been measured. The main reason is that these objects are generally too small and/or too distant to be optically resolved. However, it is possible to estimate the diameter of a small body from the measurement of its absolute magnitude H, assuming its albedo. The relation between the three parameters is explained in the following.

1.2.2.1 Albedo

The albedo of a material describes its ability to reflect light. The "geometric albedo", is defined as the ratio of the actual target brightness compared to that of a perfect diffusely reflecting ("Lambertian", see Section 3.1) disk with the same cross section and at zero phase angle. The geometric albedo is wavelength dependent, since the object's reflectance

[10] Low–albedo objects are only biased against in optical observations. In the thermal infrared, the albedo barely affects the emission and hence detectability. This is taken advantage of in thermal–infrared surveys like IRAS (Matson et al. 1989) and NEOWISE (see Section 2.3 and Mainzer et al. 2011b).

spectrum is not uniform. The most commonly used geometric albedo is the V–band albedo, p_V.

If the geometric albedo p_V and the absolute magnitude H are known, one can derive the diameter, d, of the object measured in km as

$$d = 2/\sqrt{p_V} \cdot 10^{1/5(V_\odot - H)} \cdot \delta = \frac{1329}{\sqrt{p_V}} 10^{-H/5} \text{ using } V_\odot = -26.76 \text{ mag}, \tag{1.4}$$

with the absolute magnitude, H, the V–magnitude of the Sun, $V_\odot$, and a numerical constant, δ, which equals 1 AU expressed in km. The value 1329 is introduced in Tedesco et al. (1992), assuming $V_\odot = -26.76$ mag. The relation is derived by integrating the amount of reflected solar light from the surface of the body over its illuminated portion. Equation 1.4 is graphically represented in Figure 1.8.

The bolometric Bond albedo, A, is the albedo of the object integrated over the entire electromagnetic spectrum. The bolometric Bond albedo describes the total energy fraction that is reflected from a surface. Note that the bolometric Bond albedo is not equal to the geometric albedo, p_V. A can be approximated as A_V, the bond albedo integrated over the visible wavelength regime, since the largest part of the Sun's spectral emission is in this regime. A_V can be described as a function of p_V and the phase integral, q, as described in the H–G magnitude system (Bowell et al. 1989, also see Section 1.2.1):

$$A \cong A_V = q \cdot p_V, \text{ with} \tag{1.5}$$

$$q = 0.290 + 0.684 \cdot G, \tag{1.6}$$

with the photometric slope parameter G.

1.2.2.2 Effective Diameter

The diameter derived from disk–integrated photometric data is an "effective diameter", representing the diameter of a circle that is equivalent in area to the object's real shape projected on the plane of the sky, which can lead to deviations between the effective diameter and the real dimensions of an object. In the following, the term "diameter" always refers to the "effective diameter", if not mentioned otherwise.

1.2.2.3 Size and Luminosity Distributions

Size distributions of small body populations are useful means to constrain their origin and evolution. The size distribution is the result of accretion mechanisms in the planetesimal disk and subsequent collisions (Dohnanyi 1969; Petit et al. 2008). One distinguishes between differential and cumulative size distributions. The "differential size distribution" returns the number of objects, N, that have a diameter of d, $N(d)$. Dohnanyi (1969) shows that the differential size distribution can be sufficiently approximated by a simple

power law relation $N(d) \propto d^{-q}$, with the power–law slope[11], q. The size distribution can also be expressed as a "cumulative size distribution",

$$N(>d) = \int_{>d} N(\bar{d})\ d\bar{d} \propto d^{-(q-1)}, \tag{1.7}$$

which gives the total number of objects with diameter d or larger. Dohnanyi (1969) derives $q = 2.5$ for a collisionally relaxed steady–state population. Lower values than 2.5 describe a shallower size distribution in which collisional grinding dominates, whereas higher values of q describe a steeper size distribution in which collisional grinding is less efficient and material strength dominates. Size distribution slopes and "kinks" in the size distributions, the latter of which are transition zones in which the slope changes, provide important constraints for the accretional and collisional evolution of small body populations (see, e.g., Kenyon et al. 2008).

The derivation of size distributions requires size measurements, which are non–trivial (see above). More easy to measure are "cumulative luminosity distributions" that give the total number of objects brighter than a specific absolute magnitude, H:

$$N(<H) \propto 10^{\alpha H}. \tag{1.8}$$

Assuming a fixed albedo for all objects, the size and luminosity distribution are directly linked by $\alpha = (q-1)/5$ (see, e.g., Fraser et al. 2008, for a discussion). Luminosity distributions are derived from optical surveys and require sophisticated de–biasing of the observations (see, e.g., Petit et al. 2008).

Consequentially, small body surveys are incomplete, revealing only a fraction of the actual total population, which distorts the ensemble properties and has to be corrected for. The "de–biasing" of small body surveys is a complex task that requires knowledge of the technical details of the survey and dynamical models of the observed small body population (e.g., Bottke et al. 2002b; Gladman et al. 2012; Petit et al. 2008). Proper de–biasing allows for the compensation of the observational bias and enables deductions on the total population.

Observational Methods. The most efficient way of measuring a body's diameter and albedo is from thermal–infrared observations and thermal models (see Chapter 3). Other methods that provide even more accurate sizes and albedos are either more expensive (in–situ measurements by spacecraft) or require extraordinary circumstances (occultation measurements).

[11] In order to minimize confusion with the phase integral (q), I clarify in the following whether the slope parameter or the size distribution slope is meant.

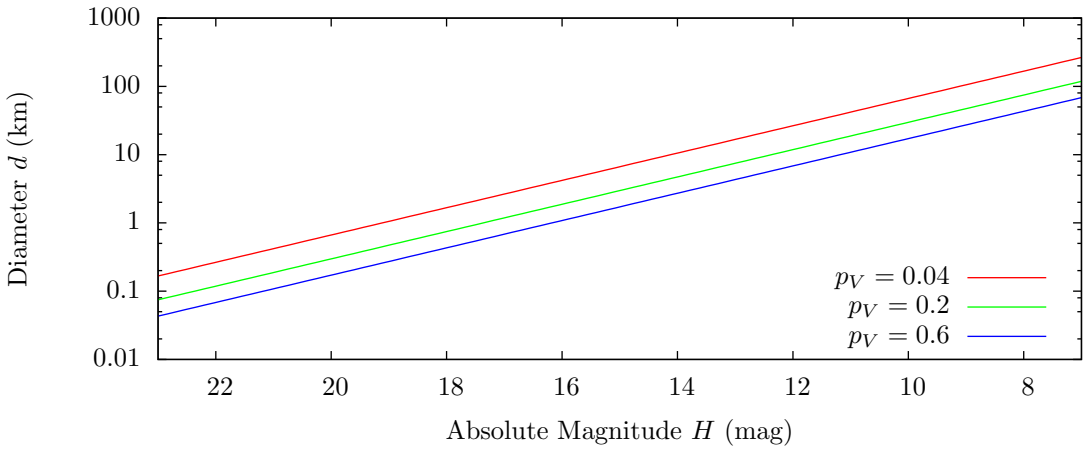

Figure 1.8 Graphical representation of Equation 1.4, showing the diameter as a function of the absolute magnitude for different albedos.

Observational Results. The sizes of small bodies cover several orders of magnitudes, from centimeters to more than 2000 km. The largest specimen of the NEO, main belt and TNO populations have diameters of ∼32 km ((1036) Ganymed, Tedesco et al. 1992), ∼950 km ((1) Ceres, Thomas et al. 2005) and ∼2300 km ((134340) Pluto and (136199) Eris, Young et al. 2007; Sicardy et al. 2011), respectively. The smallest known members of the NEO and TNO populations have diameters of the order of 10 m and 10 km, respectively.

The albedo basically depends on the taxonomic type (see Section 1.2.4), and hence the mineralogical composition, of the object. Albedo values range from 0.02 for dark carbonaceous objects up to ∼0.6 for objects mainly made of silicates. However, greater values are possible. Large TNOs have been found to have extremely high albedos (e.g., ∼0.85 for Eris, Santos-Sanz et al. 2012). Even albedos exceeding unity (1.41 for Saturn's moon Enceladus, Verbiscer et al. 2005) are physically possible. An albedo gradient can be observed in the asteroid main belt: the inner regions mainly consist of relatively high–albedo S–type asteroids, whereas the outer regions are dominated by low–albedo C–type asteroids (e.g., Masiero et al. 2011). The separation between the two types is believed to be a remnant feature of the primordial planetesimal disk; the water–rich carbonaceous C–type asteroids are likely to have formed further from the Sun than the rocky S–type asteroids. Since NEOs are replenished from source regions in the asteroid main belt and the comet populations, they show a dispersed albedo distribution. Morbidelli et al. (2002) estimate 17% of all NEOs with $H < 20$ mag to have albedos low enough to be regarded as C–type asteroids. The albedos of cometary nuclei are distinctively low. Lamy et al. (2004) lists measured albedos of cometary nuclei of different types of comets, all of which have $p_V \leq 0.06$.

1.2.3 Lightcurve Effects – Rotation, Shape and Binarity

All small bodies rotate. The angular momentum of the bodies has been acquired from the planetesimal disk, has built up in collisions, or from interaction and re–emission of solar radiation (the YORP effect, see Rubincam 2000). Spin periods of small bodies can be as short as a couple of minutes or as long as a month. Small NEOs and main belt asteroids ($0.15 < d < 10$ km) show an excess of both fast and slow spinning objects relative to a random distribution of spin periods, as well as a so–called "spin barrier": asteroids with diameters in this size range and larger have periods larger than 2 h, only smaller objects can rotate faster. The spin barrier is believed to be caused by the fact that many asteroids are rubble piles (see Section 1.2.6) that disintegrate if they spin too fast. Smaller objects, however, are thought of as monolithic objects that are held together by material strength, being able to rotate even faster.

As a result of the rotation, disk–integrated remote observations are subject to recurring brightness variations that are summarized as "lightcurve effects". The variation in brightness is caused by the irregular shape of the body, surface albedo variations, or the existence of a companion, which are discussed in the following.

For a discussion of the impact of the rotational properties on the thermal properties, see Section 1.2.7.

1.2.3.1 Shape

As shown in Figure 1.9, small bodies usually have irregular shapes, which is most likely a result of their collisional nature. There is a trend for larger objects to deviate less from ablated spherical hydrostatic equilibrium figures, since their self–gravity is stronger than the material strength, leading to a preference for less elongated shapes (Tanga et al. 2009).

1.2.3.2 Binarity

In 1996, the flyby of the Galileo spacecraft, heading for Jupiter, revealed the existence of a companion of the main belt asteroid (243) Ida, the first known asteroid satellite. Lightcurve studies had hinted at the existence of satellites before that. Later, precise optical lightcurve measurements have revealed a large number of small bodies throughout the whole Solar System to have satellites, referred to as "binary bodies". The existence of companions puts constraints on formation and evolutionary models of small bodies, and allows for the derivation of the mean density of the bodies, using Kepler's third law, which can be translated into the mass if the size of the bodies is known.

Binaries can form from rubble pile bodies (see Section 1.2.6) by disintegration caused by spin–up and subsequent accretion (Walsh et al. 2008), or from tidal forces during close encounters with planets (Bottke and Melosh 1996a,b). Significantly smaller companions are likely to have been captured gravitationally by the main body. Other formation

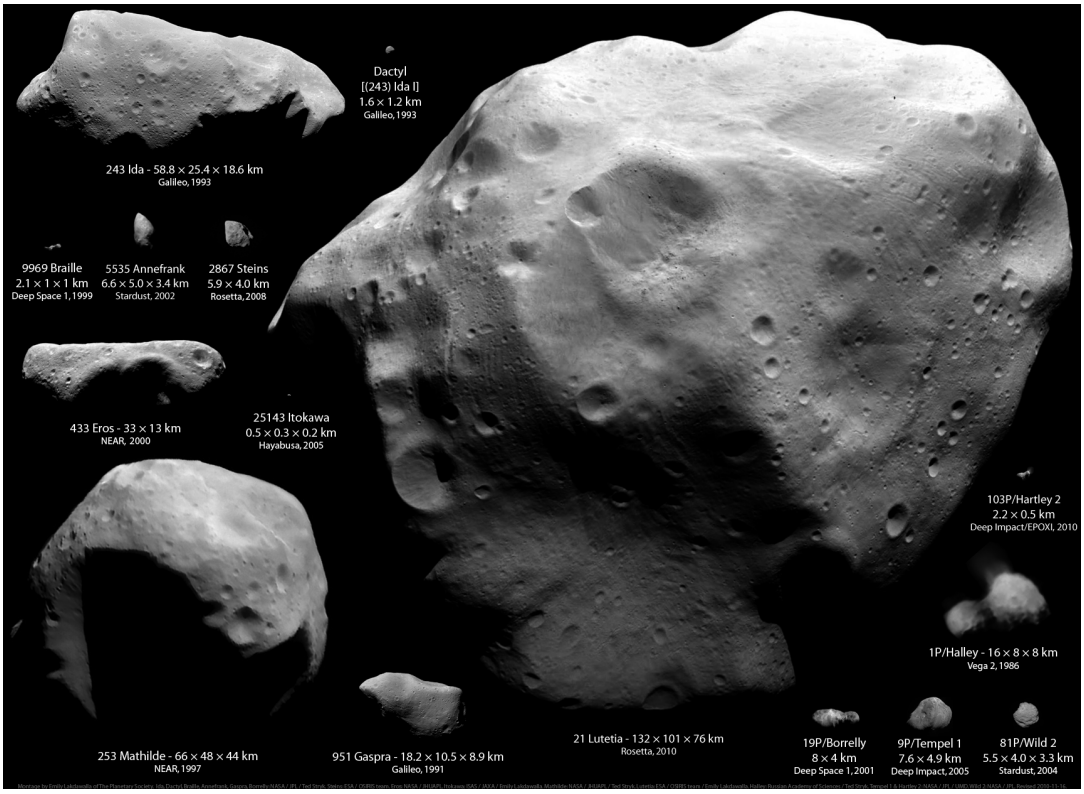

Figure 1.9 Asteroids and cometary nuclei visited by spacecraft as of November 2010. Images are to scale. The collage reveals a variety in sizes and shapes among the objects. Eros and Itokawa are NEOs, the five objects in the lower right corner are cometary nuclei, and the other objects are main belt asteroids. *Montage by Emily Lakdawalla. Ida, Dactyl, Braille, Annefrank, Gaspra, Borrelly: NASA/JPL/Ted Stryk. Steins: ESA/OSIRIS team. Eros: NASA/JHUAPL. Itokawa: ISAS/JAXA/Emily Lakdawalla. Mathilde: NASA/JHUAPL/Ted Stryk. Lutetia: ESA/OSIRIS team/Emily Lakdawalla. Halley: Russian Academy of Sciences/Ted Stryk. Tempel 1, Hartley 2: NASA/JPL/UMD. Wild 2: NASA/JPL*

scenarios include collisional fission and formation from cratering ejecta (Weidenschilling et al. 1989; Merline et al. 2002).

Observational Methods. Lightcurves can be determined by collecting large amounts of precise, time–resolved photometric data. Lightcurves allow for the determination of the rotational period and for deductions on the coarse shape of the body. Observations performed under various aspect angles allow for lightcurve inversion techniques to be applied, which synthesize a shape model of the object (Kaasalainen et al. 2002). Lightcurve inversion techniques can be applied to NEOs and MBA, but not to TNOs, since their large distances limit the range of possible aspect angles. The same technique can be used for the discovery of companions. The combination of optical lightcurve data with thermal–infrared data allows for an investigation of albedo variations on the surface of the body: since low–albedo surface patches emit heat, the thermal–infrared and optical lightcurves are anti–correlated, which is not the case if the lightcurve is dominated by the shape of the body.

1.2.4 Taxonomy

1.2.4.1 NEOs and Main Belt Asteroids

Spectroscopic analyses in the visible and near–infrared wavelength regimes combined with albedo measurements allow for drawing conclusions on the mineralogical composition of small bodies. This kind of analysis also enables a linking between distanced small bodies and meteorites found on Earth. The taxonomies of NEOs and MBAs are identical, since the same object types can be found in both populations (Binzel et al. 2002). The Bus-DeMeo classification scheme (DeMeo et al. 2009), which is based on the schemes by Bus and Binzel (2002a) and Tholen (1984) is applied throughout this work. Figure 1.10 gives an overview on the average spectra of the individual types and complexes. Generally, albedo alone allows for a distinction between the main complexes:

C–complex: carbonaceous, or C–type, bodies have small positive (or negative for B–types) spectral slopes and shallow, if any, absorption bands (DeMeo et al. 2009). They have low albedos ($p_V \leq 0.10$) and are the most abundant type of asteroid in the outer main belt region (Bus and Binzel 2002a). C–type spectra are similar to those of carbonaceous chondrites, i.e., C–type asteroids are most likely the parent bodies of this primitive type of meteorite (Burbine et al. 2002).

S–complex: silicaceous, or S–type, bodies show absorption features at 1 and 2 μm (DeMeo et al. 2009) and have albedos p_V that usually range between 0.1 and 0.25. S–type asteroids dominate the inner main belt (Bus and Binzel 2002a) and that part of the near–Earth population that has been classified (Stuart and Binzel 2004). The

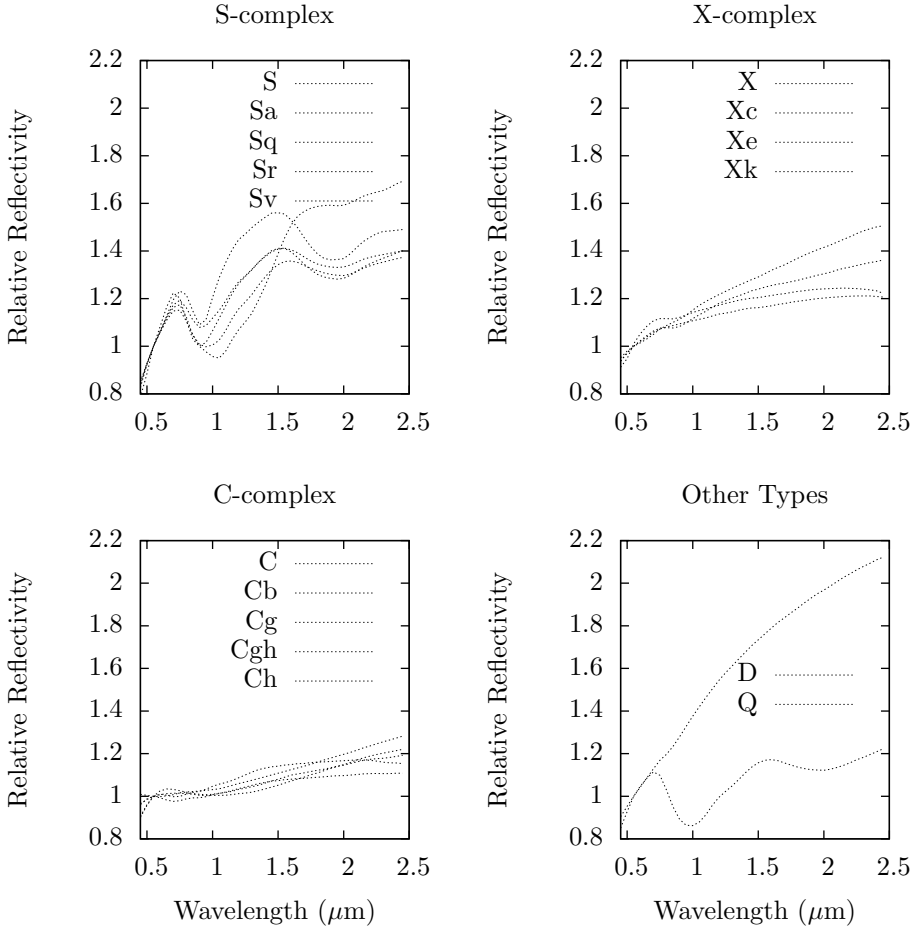

Figure 1.10 Averaged sample spectra of the Bus–DeMeo taxonomy scheme (DeMeo et al. 2009). The plots show the relative reflectivity of different spectral types of asteroids as a function of wavelength. The three main complexes shown are the C, S and X–complex. The spectra of D and Q–type asteroids are given for comparison. Descriptions of the individual complexes and types are given in the text. Spectral data were taken from `http://smass.mit.edu/busdemeoclass.html` (accessed November 2012).

high frequency of S–type asteroids in near–Earth space suggests a link to the most frequent types of meteorites, the ordinary chondrites. However, S–type asteroids are spectrally redder than ordinary chondrites and tend to have weaker absorption bands (Burbine et al. 2002). The discrepancy has been resolved using results of the "Hayabusa" mission to the S–type asteroid (25143) Itokawa (Nakamura et al. 2011). It could be shown that a surface altering process called "space weathering", involving impacts by micro–meteorites, solar wind and cosmic particles, leads to a change of the asteroid's surface, which is removed during its atmospheric entry, leaving the meteoritic material to be invisible below the asteroid's surface.

X–complex: X–complex bodies have medium to high spectral slopes and display either small or no spectral features (DeMeo et al. 2009). Objects belonging to this type cannot be unambiguously interpreted in terms of mineralogy or taxonomy based on their spectra alone. However, the members of the X–complex can be subdivided into three other classifications, E, M and P, depending on their albedo: E–type asteroids have high albedos between 0.10 and 0.50 and are possibly linked to enstatite meteorites; M–types have intermediate albedos of 0.10 to 0.20 and are possibly linked to metallic meteorites; P-types have low albedos smaller than 0.10. No meteorite analog for the latter type is known (Clark et al. 2004). The lack of albedo measurements for most X–type asteroids leaves the majority of the members of this group as being unclassified.

The exact definitions of the individual types can be found in DeMeo et al. (2009) and Bus and Binzel (2002a). Differences between the subtypes in the individual complexes are subtle and only of minor interest in the scope of this work. Two further spectral types, which are not members of any of the aforementioned complexes, are 'D–type' and 'Q–type' asteroids. D–types generally have featureless spectra with extremely steep slopes (DeMeo et al. 2009), making them appear reddish, and have low albedos ($0.02 \leq p_V \leq 0.07$). D–type asteroids are abundant in the outer main belt and the Jupiter Trojan population (Hicks et al. 2000). Q–type asteroids show a distinct 1 μm absorption feature (DeMeo et al. 2009) and have albedos similar to those of S–type asteroids. They are believed to be unweathered S–type asteroids, having been resurfaced, due to close encounters with a planet (Binzel et al. 2010).

Although a variety of other taxonomic types exists, most of the observed NEOs and main belt asteroids fit into one of the above complexes. Taxonomic types are determined from spectroscopic observations in the near and mid–infrared. For a review of the methods, see Bus et al. (2002). Albedo measurements can be used to constrain the taxonomic type to a small number of types, but usually cannot constrain the types entirely.

1.2.4.2 TNOs

The taxonomic scheme introduced above cannot be applied to TNOs, since their spectra do not match those found in asteroids. Tegler and Romanishin (1998) used broadband color information to find that the TNO population comprises two distinct subpopulations: one consists of objects of mostly neutral color while the other consists of the reddest objects known in the Solar System. Barucci et al. (2005) elaborated on this work and created a TNO taxonomy based on broadband photometry and spectroscopic analysis, consisting of the two groups mentioned above and two intermediate types. The taxonomy distinguishes between objects with neutral–greyish ("BB") and extremely red color indices ("RR"), as well as two intermediate types, "BR" and "IR". The individual types can be associated with spectral slopes and the absorption band depths. All BB–type TNOs seem to have icy surfaces (Barucci et al. 2011), often including H_2O ice (Fulchignoni et al. 2008), although ices can be present on the surfaces of the other types, as well. In contrast, no ices have been unambiguously identified on IR–type TNOs. RR–type TNOs are among the reddest objects in the Solar System. Their red color usually originates from titan or triton tholins, molecules that have been formed by solar ultraviolet irradiation from simple organic compounds such as methane. For a full discussion of the individual TNO types, see Fulchignoni et al. (2008). The lack of albedo data for TNOs has so far precluded an investigation of possible associations of the different taxonomic types with geometric albedos. This is done as part of this work in Section 5.3.

1.2.5 Surface Roughness and Other Surface Properties

1.2.5.1 NEOs and Main Belt Asteroids

Observations of small bodies show images of their surfaces. Hence, knowledge about the surface properties are necessary to properly interpret observational data. Space missions offer the best way to examine small body surfaces in great detail. Figures 1.9 and 1.11 show a small selection of the variety of small body surfaces. The top panel in Figure 1.11 shows close–up images of the surface of (433) Eros, one of the largest NEOs, taken by the NEAR–Shoemaker mission (Cheng et al. 1997; Cheng 2002). Craters of all sizes and boulders are ubiquitous on Eros' surface, both being remnants of impacts, leading to a high degree of surface roughness. "Surface Roughness" describes the degree of roughness of a surface, referring to macro–porosities like craters, rather than micro–porosities. Surface roughness gives rise to shadowing and beaming effects, as introduced in Section 1.2.7. Deep layers of "regolith" (< 100 m) have been found to cover most of the surface of Eros. Regolith is a heterogeneous mix of dust and rocky material, which is most likely retained impact ejecta being loosely layered on the surface (Scheeres et al. 2002). The existence of regolith on large asteroids, the Moon and other large bodies has been known long since. It was a surprise to find patches of regolith on smaller objects like Itokawa (see below),

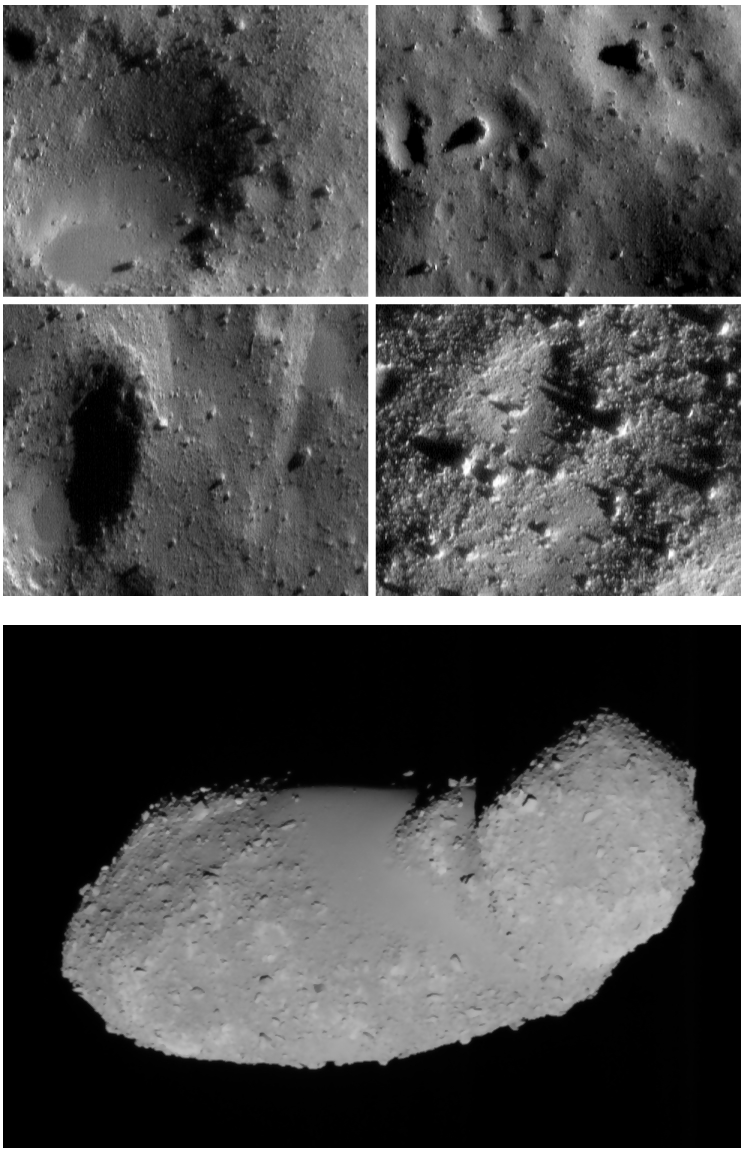

Figure 1.11 Close–up images of the surfaces of NEOs Eros (top) and Itokawa (bottom), taken by the spacecraft missions NEAR–Shoemaker (NASA, 2001) and Hayabusa (JAXA, 2005), respectively. The four Eros images show, from upper left to lower right, its bouldered surface at increasing resolution. The images in the upper row and lower row are about 550 m and 230 m across, respectively. Eros' surface is covered with craters of different sizes (compare also Figure 1.9), regolith, and boulders. The image of Itokawa (bottom) shows the whole body with its dimensions of $540 \times 270 \times 210$ m, i.e., at comparable resolution to the images of Eros. Itokawa's surface shows no craters at all, but two distinct features: part of the surface seems to be smoothly covered by fine regolith, whereas the rest seems to be rocky without any trace of regolith. Eros image data: Johns Hopkins University Applied Physics Laboratory, NASA; Itokawa image data: JAXA.

which was believed to lose all its ejecta due to its low escape velocity and self–gravity. The existence of regolith suggests the surface material to be rather porous and of low internal strength leading to the production of little ejecta (e.g., Holsapple et al. 2002). Eros, being an S–type asteroid, has a surface composition that is consistent with that of ordinary chondrites. The surface material may have been melted or differentiated partially, but not fully.

The surface properties of the small NEO (25143) Itokawa differ significantly from those of the larger Eros. Itokawa was visited by the JAXA mission "Hayabusa" in 2005 that took images of its surface (Fujiwara et al. 2006). The bottom panel of Figure 1.11 shows an intriguing dichotomy between smooth patches covered by regolith and rough, rocky regions virtually free of regolith. Hence, the degree of surface roughness can vary even on the small scale of Itokawa's surface. The accumulation of regolith in certain areas has been suggested to be a result of the interplay between the rotation of Itokawa and its irregular gravitational attraction (Miyamoto et al. 2006).

Eros and Itokawa, as well as spacecraft mission targets in the main belt, show a huge variety in their surface properties, in terms of the degree of surface roughness, coverage by regolith, and crater distribution. Ices are unlikely to be found on the surface of NEOs, due to their proximity to the Sun, whereas main belt asteroids are able to maintain ices in the top few meters of their surfaces for billions of years (Schorghofer 2008).

For a discussion of the impact of the surface roughness on the thermal properties of small bodies, see Section 1.2.7.

1.2.5.2 TNOs

So far, no TNO has been visited by space missions[12]. Hence, all available data on the surface properties have been deduced from remote imaging and spectroscopic observations. Due to their remoteness, TNOs have much lower surface temperatures compared to MBAs and NEOs ($\sim 30 - 50$ K), which allows for the presence of volatiles in the form of ices, among which are, water (H_2O), Methanol (CH_3OH), Methane (CH_4), and Nitrogen (N_2) (Barucci et al. 2008, 2011, and references therein). An intriguing fact is that ices are likely to be found on the largest TNOs, but unlikely on the smaller ones: Schaller and Brown (2007) have shown that the strong gravitational field of a large TNO helps to retain volatiles on the object, forming an icy surface layer. Such an effect can also explain the high albedos observed in large TNOs, which is investigated and discussed in Section 5.3.

[12]The NASA "New Horizons" mission (New Horizons Mission Website) arriving at Pluto in 2014 will be the first mission to a TNO. After examining the geomorphology of Pluto and its satellites, as well as Pluto's atmosphere, New Horizons will continue its mission to another TNO which is yet to be decided upon.

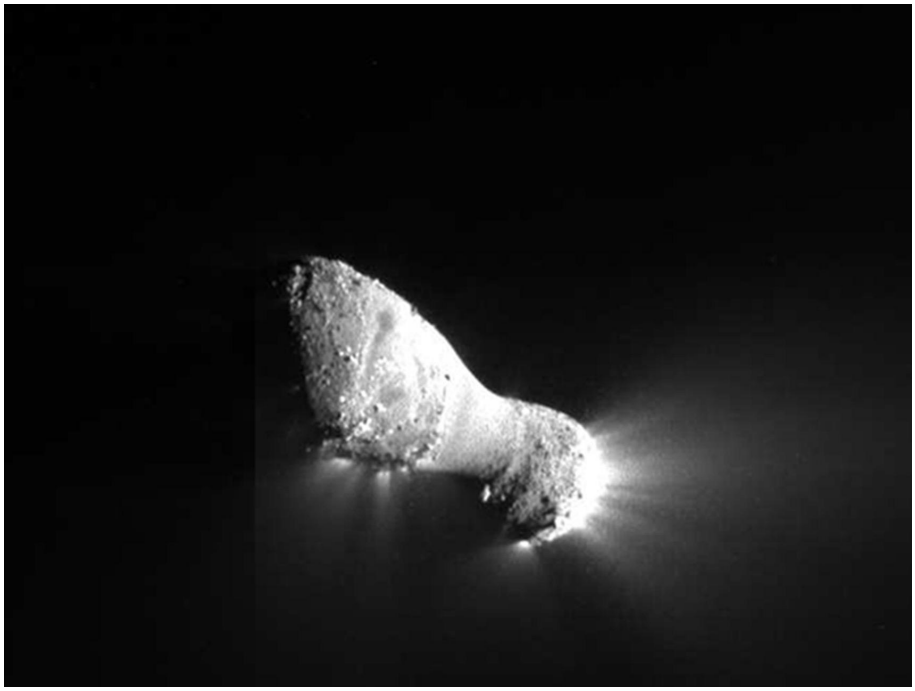

Figure 1.12 Image of the nucleus of comet 103/P Hartley (Hartley 2). Jets emerge from the ends of the peanut–shaped nucleus, where the surface appears to be rocky. The center section of the nucleus is covered by fluffy, regolith–like material. Image courtesy: NASA.

1.2.5.3 Comets

Comets were believed to be "dirty snowballs"(Whipple 1950), meaning a "conglomerate of ices ... combined in a conglomerate with meteoric materials". This concept was able to explain most of the observed features in comets. However, spacecraft flying by a number of comets in the last decades led to a revision of the dirty snowball picture. After the visit of the Giotto spacecraft to comet Halley in 1986, comets are rather seen as "snowy dirtballs" (Keller 1989), meaning a rocky, asteroid–like nucleus with icy inclusions on its surface and in its interior. Refractory particles that are launched from the surface can survive for a long time, explaining meteor streams that are on the same trails as known comets. Later visits of the cometary nuclei of Tempel 1 and Hartley 2 by the DEEP IMPACT/EPOXI spacecraft supported this hypothesis (A'Hearn and the DEEP IMPACT Team 2011). The surface of the peanut–shaped nucleus of Hartley 2 (cf. Figure 1.12) turned out to be rocky at its ends, where most of the cometary activity takes places, and to be covered with fluffy material, similar to regolith, in its center section. The fluffy material is believed to be refractory material that has been launched from the surface and fallen back due to the gravitational attraction of the nucleus.

1.2.6 Internal Structure and Bulk Density

The internal structure of small bodies is diagnostic of their formation. The largest objects have partially differentiated interiors similar to planets and larger moons, whereas the smaller objects can be divided in two groups: "monolithic" and "rubble–pile" bodies. Monolithic bodies are mainly made up from one large rocky body, being held together by material strength. Rubble–piles are conglomerates of a large number of smaller rocks, or even gravel–like material, that is held together by the self–gravity of its constituents. Both types of objects have significantly different mean densities: monolithic bodies have mean densities close to the density of solid rock, whereas rubble–pile bodies have significantly lower densities, as a result of void spaces in their interior, which is referred to as "macro–porosity". Monolithic bodies can be thought of as single pieces of debris from asteroid collisions, whereas rubble–piles are conglomerates of debris (Michel et al. 2001).

Observational Methods. The mean or bulk density, ρ, of small bodies also significantly depends on the individual densities of the material they are made up from: solid rock, ices, and metals have densities of $\sim$2–4, $\sim$1, and $\geq$6 g cm^{-3}, respectively (see, e.g., Mueller 2007, for an overview). The internal composition of small bodies can be deduced from measurements of the bulk density and density variations, which can both be detected as irregularities in the gravitational field of the body by orbiting spacecraft. A more efficient method that is restricted to binary bodies, makes use of Kepler's third law to determine the bulk density of the system. Determinations of the diameter of the main object allows for the computation of its mass as $\rho(\pi d^2)/6 = M$, if the mass of the secondary can be neglected; otherwise, correction terms have to be applied.

Observational Results. The asteroid rendezvous missions NEAR–Shoemaker and Hayabusa have revealed the monolithic and rubble–pile nature of the NEOs (433) Eros and (25143) Itokawa, respectively. Mass and diameter determinations of other NEOs and main belt asteroids show that low–porosity objects are rare. The interiors of most objects are heavily fractured or even rubble–piles (Britt et al. 2002). The bulk densities of TNOs span a wide range from $\sim$0.5 to nearly 3 g cm^{-3} (Barucci et al. 2008), corresponding to an internal mix of rock and ice. The existence of TNOs with $\rho < 1.0$ g cm^{-3} suggests a high degree of porosity. The bulk densities of cometary nuclei are estimated to lie within the range 0.5–1.2 g cm^{-3}, most of which are probably rubble piles with inclusions of ices (Weissman et al. 2004).

1.2.7 Thermal Properties

Thermal Inertia. The thermal evolution of small bodies is important for the understanding of the evolution of their surfaces, especially with respect to the presence of volatiles and ices. The surface temperatures of small bodies are mainly constrained by

their heliocentric distances, their albedo, and surface properties, as described in Section 3.1. As a result of the rotation of small bodies, part of their surface crosses the terminator and enters the night side of the body. Here, the surface temperature does not drop instantaneously to zero, as assumed by the thermal models introduced in Chapter 3, but decreases rather gradually, which is the result of the non–vanishing "thermal inertia" of the surface material. The thermal inertia describes the rate at which a material cools off (heats up) in the absence (presence) of heating. Thermal inertia is a material property and hence a function of the material's density, ρ, heat capacity, κ, and its specific heat, c_V:

$$\Gamma = \sqrt{\kappa \rho c_V}.$$

A full derivation of the thermal inertia and a discussion of its effects is given in Spencer et al. (1989). Thermal inertia is given in units of J $s^{-1/2}$ K^{-1} m^{-2}, which is usually abbreviated as "SI", meaning that the value is expressed in SI units. High–thermal inertia materials take a long time to heat up and to radiate their energy into space; a low thermal inertia material changes its temperature more rapidly. The effect of thermal inertia on the diurnal temperature variation is shown in Figure 1.13.

Typical values of thermal inertia are ∼400 SI for loose sand (Mellon et al. 2000), ∼2000 SI for a block of water ice (Mueller 2007, and references therein), and ∼2500 SI for bare rock (Jakosky 1986). Thermal inertia is diagnostic of the presence of regolith on the surface of small bodies. Measurements of the thermal inertia of regolith on Mars and the Moon revealed values of $\Gamma = 30$ SI (Putzig et al. 2005), and $\Gamma = 50$ SI (e.g., Spencer et al. 1989; Winter and Krupp 1971), respectively.

Thermal inertia can be derived from in–situ measurements of the surface temperature as a function of time. A more practicable method involves the application of thermophysical models (see a brief discussion in Section 3.5) on combined thermal–infrared and optical observation data.

Delbo' et al. (2007) found the average thermal inertia of NEOs to be ∼200 SI. Furthermore, they found a clear trend for smaller objects to have higher thermal inertia, presumably due to the exposure of bare rock and the fact that less regolith is present on their surfaces. Main belt asteroids have been found to cover a huge range of thermal inertia, 5–1000 SI (references in Delbo' et al. 2007), with the largest specimen having a rather low thermal inertia, presumably due to the presence of regolith. The thermal inertia of TNOs is significantly lower compared to those found on NEOs or main belt bodies. For instance, Müller et al. (2010) find $\Gamma \leq 25$ SI for a sample of 7 TNOs and Centaurs. The low thermal inertia is the result of a drop of the thermal conductivity and heat capacity at low temperatures. A detailed explanation of the physical principles of this effect is given in Spencer et al. (1989).

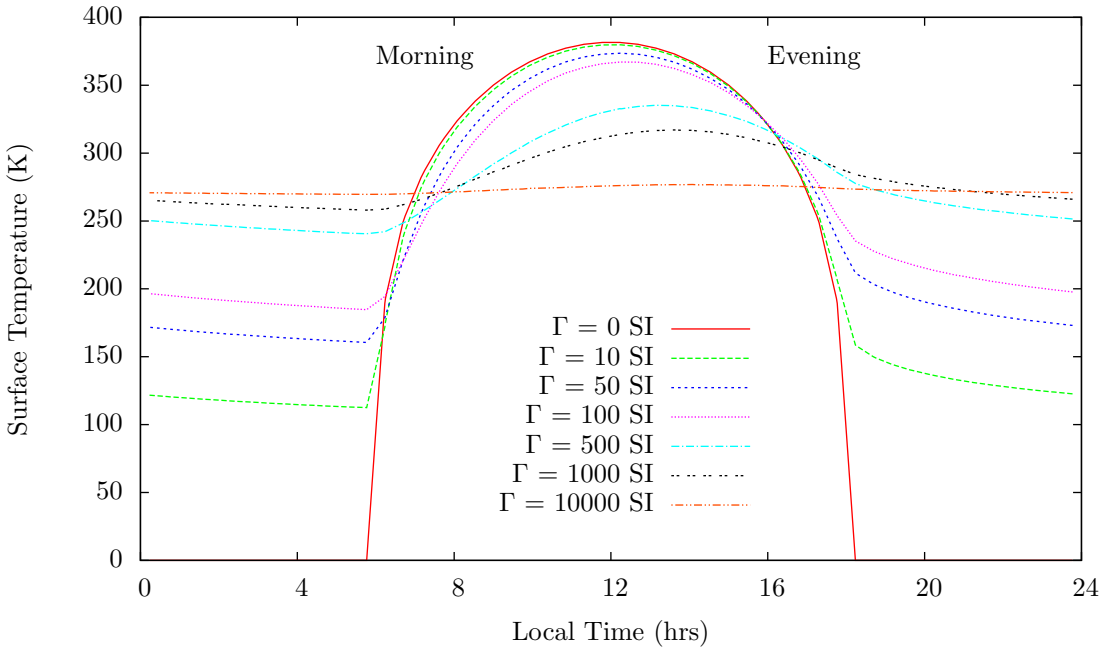

Figure 1.13 The effect of thermal inertia on the diurnal temperature curve of a spherical, rotating body. Each line gives the temperature at an arbitrary position on the equator as a function of its local time and for different thermal inertias, Γ. The local time is normalized in such a way as to have the Sun passing the zenith at noon (12). From the distribution of the temperature curves it is obvious that for increasing Γ, the amplitude of the curves decrease, and that the peak temperatures shift towards the "afternoon". The extreme cases, $\Gamma = 0$ SI and $\Gamma = 10000$ SI, show the highest and lowest temperature amplitudes, respectively, and are equivalent to the STM and FRM temperature distributions introduced in Chapter 3.

Spin Properties. The impact of the thermal inertia on the thermal properties of a body is directly linked to its spin properties. The spin period determines the duration during which an individual surface element absorbs sunlight; the thermal inertia determines how quick the element changes its temperature.

The spin axis orientation, often reduced to the subsolar latitude, i.e., the latitude of that location on the body where the Sun is in the zenith, also impacts the insolation of an individual surface element via the solar incidence angle. Note that for a subsolar latitude of 0, the Sun is in the equatorial plane of the body, whereas for subsolar latitudes of $\pm 90°$, the Sun is above one of the poles. In the latter case, the thermal inertia of an individual surface element becomes obsolete, since each surface element is exposed to the same amount of sunlight at any time; the surface temperature of each surface element is then invariable.

Surface Roughness Effects (Beaming). The surface roughness also impacts the effective temperature on the surface of a body as a function of the local solar incidence angle. Consider a single surface element with high roughness, for instance, represented by a deep crater[13]: with the Sun near the local zenith (low angle with respect to the surface normal), the crater absorbs and stores more thermal energy due to its larger surface area compared to a smooth surface and the mutual heating of facing surface elements. The effective surface temperature is higher compared to that of a smooth surface. With the Sun near the local horizon (large angle with respect to the surface normal), surface elements of the crater are shadowed and less energy is absorbed. Furthermore, due to the conservation of energy, less energy is radiated into directions that draw large angles with the surface normal.
Hence, the distribution of thermal emission is anisotropic; a directional preference of the thermal emission from a rough surface element towards its surface normal exists, which is referred to as "beaming" or "infrared beaming". The effect on the thermal emission of a (nearly) spherical small body is such that the measured surface temperature is higher in each point compared to that of a smooth body. The discrepancy is largest in the subsolar point, for which the direction to the Sun coincides with the surface normal. The beaming effect can be approximated with the beaming parameter (η) in the thermal modeling of small bodies (see Sections 3.2.2, 3.2.4, and 3.5).

[13] A crater is the most simple approximation of a rough surface; the same reasoning can be applied to the picture of large boulders that face each other, or any other rough surface.

1.3 Motivation and Scope of this Work

In the previous sections, I introduced and discussed the properties of individual Solar System small body populations and their mutual interactions. Despite the physical and dynamical differences between members of the individual populations, all small bodies are descendants from the original planetesimal disk and have evolved in different ways.
In this section, I discuss the motivation behind this work, and the relevance of the results of this work to our understanding of the Solar System.

1.3.1 "ExploreNEOs", "TNOs are Cool!" and the Big Picture of Small Bodies in the Solar System

This work was enabled by the simultaneous realization of the *ExploreNEOs* and *TNOs are Cool!* projects, which are introduced in detail in Sections 2.2.3 and 2.4.3, respectively. The two programs perform space–based thermal–infrared observations of NEOs and TNOs, utilizing the Spitzer Space Telescope and Herschel Space Observatory, respectively. The aims and methods of both programs are similar: thermal models (see Chapter 3) are used to obtain diameter and albedo estimates from the observed thermal–infrared measurements, from which ensemble properties of both populations are deduced. Similarities in the objectives and methods of both programs allow for logistic and methodical synergies. The scientific outcome of a combination of both fields is appealing in itself, as demonstrated in the following.

The Big Picture: From Rocks to Pebbles...

TNOs and comets are among the most pristine objects in the Solar System. Their compositions and physical properties are believed to be similar to those of the earliest bodies that formed in the original planetesimal disk, from which the planets have formed. Dynamical simulations suggest that some TNO subpopulations are likely to be sources of short–period comets (see Section 1.1.5.2). Given the large heliocentric distances of TNOs and the small number of known TNOs, little is known about their compositional and physical properties. The diameters and albedos derived within the *TNOs are Cool!* program more than double the number of TNOs with measured physical properties.

NEOs are the remnants of collisions in the primordial planetesimal disk and are physically and dynamically highly evolved. Their proximity to the Earth makes them easily accessible targets for space missions, but also poses an impact hazard to our planet. At the beginning of this work, measured physical properties existed for less than 100 NEOs. The *ExploreNEOs* program has measured the diameters and albedos of ∼600 NEOs. The program has contributed to our knowledge of the physical ensemble properties of NEOs, which are important for understanding the evolution of this population and for the mitigation of future impact hazards posed by NEOs.

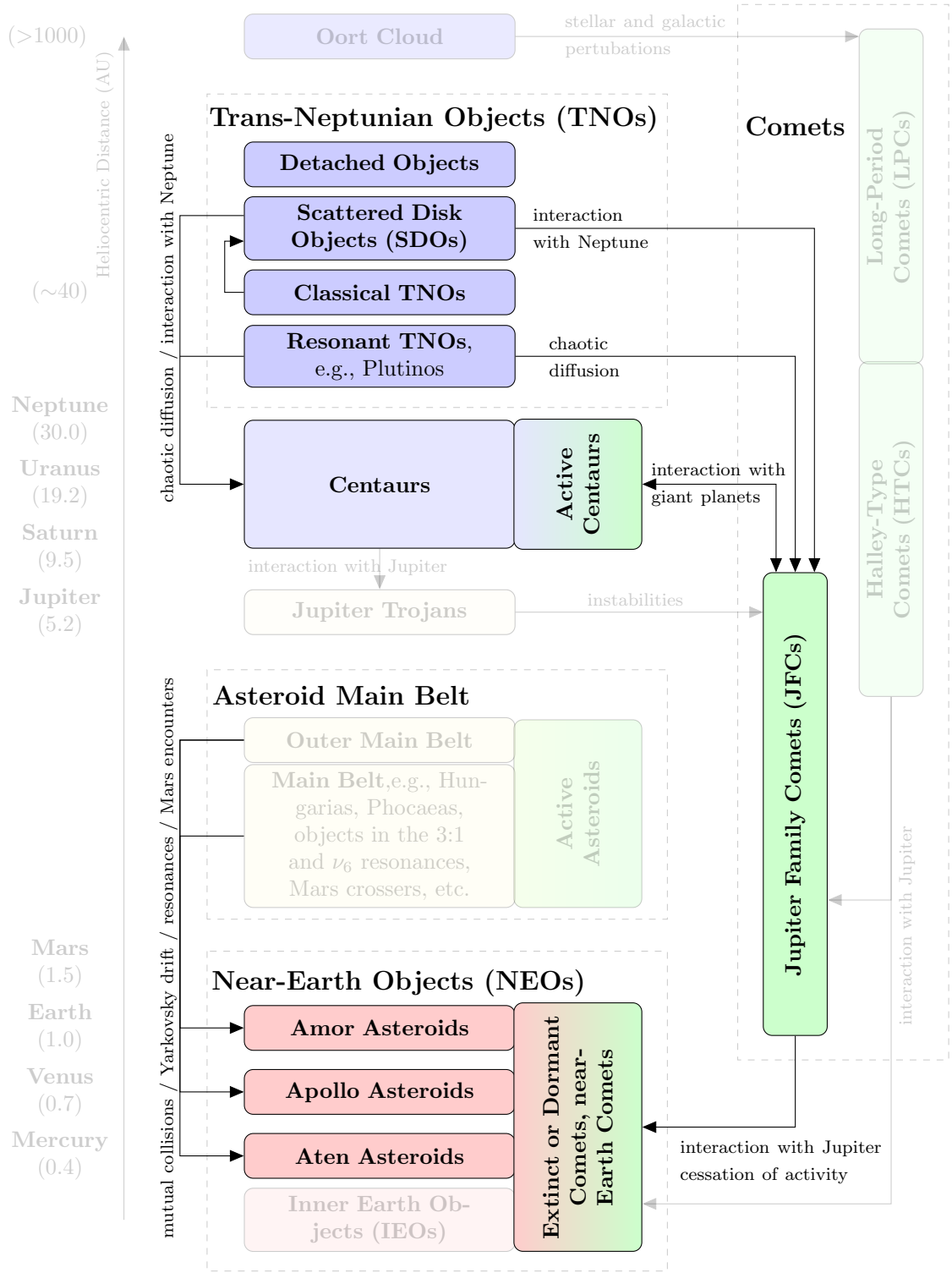

Figure 1.14 This flowchart highlights the populations of small bodies and their mutual interactions that are investigated as part of this work (see text). I focus on three aspects: (1) the comparison of the physical properties of NEOs and their source populations in the asteroid main belt and the short–period comets, (2) the identification of the source regions of the short–period comets in the TNO and Centaur populations, based on their physical properties, and (3) the investigation of the direct link between the TNOs and the NEOs via the short–period comets. This sketch is a modified version of Figure 1.1 on page 3.

This work benefits from the dramatic increase in the numbers of NEOs and TNOs with measured diameters and albedos afforded by the *TNOs are Cool!* and *ExploreNEOs* programs. The larger number of TNOs with measured properties allows for a detailed analysis of their ensemble properties, their dynamical links, and even their progenitors: the evolution of planetesimal remnants (TNOs and large main belt asteroids) to their highly evolved collisional fragments (NEOs) resembles the picture of rocks that turn into pebbles. *In much the same way the properties of rocks in a streambed allow for deductions on the nature of events upstream, the NEO population provides us with valuable clues to the nature and evolution of its source populations* (here, the main belt asteroids and the trans–Neptunian objects).

By combining the results of the TNOs are Cool! and ExploreNEOs programs, this work provides a test, based on the measurement of physical properties, for the proposed transport mechanisms into the NEO population, namely the transition of TNOs and Centaurs via the short–period comets into the NEO population, as sketched in Figure 1.14.

1.3.2 Scope of this Work

The workload of the *TNOs are Cool!* and *ExploreNEOs* programs is shared among the collaborating team members (see Sections 2.2.3 and 2.4.3). I have chosen my tasks in both programs in such a way as to contribute to the understanding of the evolutionary processes and dynamical mechanisms mentioned above.

The specific aims of this work are divided into primary and secondary aims as presented in the following.

1.3.2.1 Primary Aims

This work mainly focuses on *finding evidence in the physical properties of both the NEOs and the TNOs for the transport mechanisms suggested by dynamical simulations* (see Figure 1.14). Specifically, this includes:

- The comparison of the albedo properties of NEOs and objects in their respective source populations suggested by dynamical models (see Section 4.1).
- The investigation of the fraction of NEOs that is of cometary origin (see Section 4.2).
- The detailed analysis of NEO (3552) Don Quixote, which I show to display cometary activity in *ExploreNEOs* image data (see Section 4.3). Don Quixote is currently in transition from being a comet to becoming an asteroid–like extinct or dead comet, and provides evidence for a direct transport mechanism from the TNO region to the NEO population.

- The investigation of the size and albedo distributions of the known TNO subpopulations. The comparison of the TNO size and albedo distributions with those of the short–period comets provides constraints on the source populations of these comets (see Section 5.2).

1.3.2.2 Secondary Aims

Based on the results of the *TNOs are Cool!* program, I also investigate the ensemble properties of TNOs, which includes:

- The physical characterization of a representative sample of the Plutino subpopulation, which is a possible contributor to the short–period comet population (see Section 5.1).
- The investigation of a possible correlation between the color–based TNO taxonomy, as well as the presence of surface ices, with the measured albedos (see Section 5.3).

In Appendix B, I present results of related work, including an assessment of the accuracy of the *ExploreNEOs* results and a comparison of the *ExploreNEOs* results with those of the NEOWISE program (see Section B.1), an investigation of the uncertainty estimates of thermal models (see Section B.2), and work on a re–analysis of all TNO and Centaur observations performed with the Spitzer MIPS instrument in support of the *TNOs are Cool!* program (see Section B.3).

In this work, the results from two sophisticated space–based observation programs are combined to investigate the physical properties of the near–Earth and trans–Neptunian object populations and seek physical evidence for dynamical transport models that suggest a direct link between them.

Chapter 2

Observations of Small Bodies

Most of the available knowledge about the physical properties and dynamical parameters of small bodies stem from remote observations in different wavelength regimes of the electromagnetic spectrum, investigating different physical and chemical properties. Observations of small bodies differ only slightly from those of other astronomical targets.

In the following sections, I provide an introduction in the observation of small bodies in the optical and thermal–infrared wavelength ranges. I introduce the two space–based observatories with which the observations used in this work were performed: the "Spitzer Space Telescope" and the "Herschel Space Observatory". The specifications and capabilities of the instruments of both observatories are briefly discussed. Furthermore, I present the two programs in the course of which the observations were performed that lead to the results of this work. I briefly introduce the "Wide–field Infrared Survey Explorer" (WISE) and its asteroid survey program "NEOWISE", results of which are utilized in this work.

Note that I was not involved in the processing of the observational data; flux densities were derived from the Spitzer and Herschel observations by members of ExploreNEOs and TNOs are Cool! teams, respectively.

2.1 Observations in Different Wavelength Regimes

Astronomical observations are performed in nearly all wavelength ranges. The most important wavelength ranges for the observation of small bodies of the Solar System are the optical and infrared regimes, which are dominated by reflected solar light and thermal emission, respectively.
In the following sections, I briefly outline the concepts of observations in the optical, and then discuss the caveats of observations in the thermal–infrared.
For a brief introduction into observational concepts, image processing, and analysis techniques, cf. Section A.2.

2.1.1 Observations in the Optical

The optical light covers that portion of the electromagnetic spectrum that is accessible to the human eye, in terms of wavelength: $\sim$0.4 to 0.75 μm.

Optical observations of small bodies measure the amount of reflected solar light, as discussed in Section 1.2.1. Observations are usually carried out using ground–based telescopes. State–of–the–art telescopes are equipped with detectors that are highly sensitive over a broad wavelength range, but especially in the red, i.e., at wavelengths longer than $\sim$0.6 μm. The largest available telescopes have mirror diameters of 10 m (e.g., the Keck[1] telescopes) or 8 m (e.g., the Very Large Telescope[2]), which are necessary for the observation of faint objects. For brighter objects (<23 mag), smaller telescopes with mirror diameters of $\sim$4 m are usually sufficient to obtain useful observational data. Observations in the optical are used to perform astrometry, photometry, spectroscopy, but also to perform discovery surveys.

Observations of Solar System bodies differ from other astronomical observations only in the fact that Solar System objects have proper motions that are perceptible on the timescale of a single night or less. The rotation of the Earth leads to an apparent motion of any extra–terrestrial object with respect to the local horizon, requiring tracking. In the case of Solar System bodies, this motion is superimposed by the proper motion of the body relative to the observer, which requires additional tracking capabilities from the observatory. In the case of NEOs, which are closest to the Earth, tracking rates up to $1'$/min and even more may be required. Main belt asteroids and TNOs move slower, the proper motion of the latter is mostly dominated by the motion of the observer relative to the target. Hence, the target's motion relative to the sky background can be used to constrain its distance from the observer.

Observations in the optical have not been conducted as part of this work. However, especially the albedo results obtained in this work rely heavily on the accuracy of optical observations (see Section 3.6 for a discussion).

[1] `http://keckobservatory.org/`
[2] `https://www.eso.org/vlt`

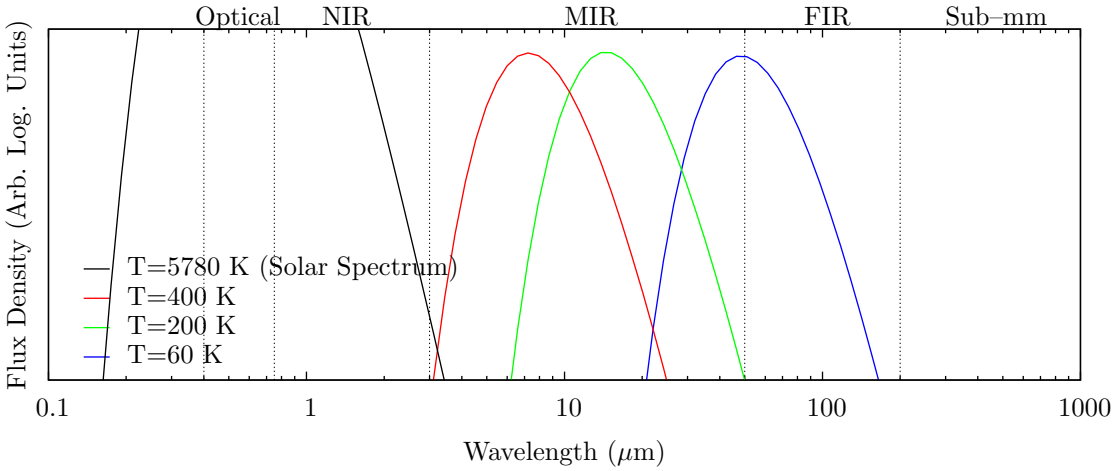

Figure 2.1 Comparison of normalized black body spectra. The three spectra on the right show emission spectra of bodies at temperatures of 400, 200, and 60 K from the left to the right. The leftmost spectrum is that of a black body at a temperature of 5780 K, which is the mean temperature of the surface of the Sun. All but the latter spectrum are normalized to the same height. For comparison, the ranges of the optical and individual infrared regimes are shown as well. According to Wien's displacement law, the emission maxima of the spectra shift to longer wavelengths with decreasing temperature. The temperatures of the spectra plotted here refer to typical temperatures on the surfaces of NEOs (400 K), main belt asteroids (200 K), and TNOs (60 K). The details of thermal emission of small bodies in the Solar System is discussed in Chapter 3.

2.1.2 Observations in the Thermal–Infrared

The infrared wavelength range of the electromagnetic spectrum starts at 0.75 μm, adjacent to the optical regime. Typically, one distinguishes between the near–infrared (NIR, 0.75–3.0 μm), mid–infrared (MIR, 3–50 μm) and far–infrared (FIR, 50–200 μm) regimes. At longer wavelengths than 200 μm the sub–millimeter regime begins. Figure 2.1 shows that the NIR is dominated by reflected solar light, whereas the MIR and the FIR are dominated by the thermal emission of black bodies with typical small body temperatures. The figure also shows that the different types of small bodies have to be observed in different infrared wavelength ranges, which is discussed in detail in Sections 3.7.1 and 3.7.2.

The brightness of objects in the infrared regime is usually given in flux density units instead of magnitude units, which has the advantage of being instrument–independent. Flux densities are given in SI–units of W m^{-2} Hz^{-1} or W m^{-2} μm^{-1}. In both units, the flux densities of most small bodies are impractically small. Hence, the unit of choice is borrowed from radio astronomy: one "Jansky" (Jy), named after radio astronomy pioneer Karl Jansky, is defined as 10^{-26} W m^{-2} Hz^{-1}. Since the usage of wavelengths, λ, instead of frequency, ν, is more common in infrared astronomy, fluxes, F, given in SI units can be

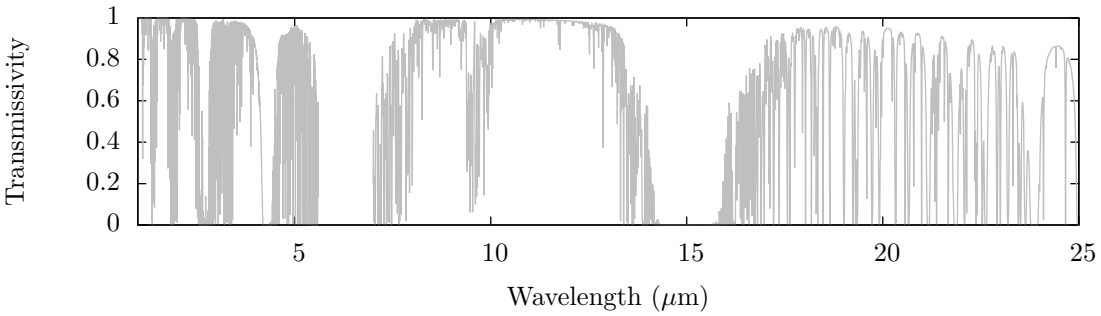

Figure 2.2 Infrared transmissivity of the atmosphere at the site of NASA's Infrared Telescope Facility (IRTF) on Mauna Kea, Hawai'i. The plots shows that the atmosphere is highly opaque in the infrared wavelength ranges. Observations are possible only in narrow bands. The depths of the absorption bands are subject to fluctuations, depending on the water vapor content in the atmosphere. Data from Lord (1992) and the Gemini Observatory.

converted into Janskys using the following relation

$$F(\mathrm{mJy}) = 3.335640952{\cdot}10^{14} \times \lambda^2 \times F(\mathrm{W\ m^{-2}\ \mu m^{-1}}), \tag{2.1}$$

which is based on the general relation $\nu F_\nu = \lambda F_\lambda$. The typical order of magnitude of flux densities of small bodies is 10^{-3} Jy = 1 mJy; some close NEOs or large main belt asteroids, however, can easily reach flux densities of several Jy.

Thermal–infrared observations require the cooling of all telescope and detector parts to minimize contaminations. Furthermore, infrared detectors have to be cooled to temperatures of the order of 1 K in order to minimize thermal noise and maximize the detector sensitivity. Ground–based thermal–infrared observations are furthermore compromised by Earth's atmosphere, which is highly opaque in most IR wavelengths (cf. Figure 2.2). The opacity is due to absorption bands of molecules like H_2O and CO_2. The depth of the bands depends on the water vapor content in the atmosphere and is therefore subject to fluctuations that have to be corrected for. Hence, thermal–infrared observations are only possible from the ground where the water vapor content is low and observing conditions are favorable. NASA's Infrared Telescope Facility (IRTF) is located on Mauna Kea, Hawai'i, where the conditions are adequate for infrared observations (see Figure 2.2). The observatory provides a 3.0 m telescope with imaging (MIRSI, 2–28 μm) and spectroscopy (SpeX, 0.8–5.4μm) capabilities. IRTF observations are utilized in Section 4.3.

Observations using longer wavelengths cannot be performed from the ground, since the thermal background radiation of the atmosphere exceeds the emission of most extra–terrestrial objects. Such observations can only be performed by space–based observatories and with sufficient cooling.

2.1.2.1 Space–Based Infrared Observations

Due to the lack of an ambient atmosphere, space–based observatories provide perfect conditions for infrared observations. Active cooling, however, is still necessary for observations at most wavelengths. The sensitivity of space–based infrared observatories is significantly better compared to ground–based telescopes, given the more favorable conditions; however, space–based observatories suffer from other effects, including thermal emission from zodiacal dust[3] and galactic cirrus[4], but still provide the best conditions to perform observations in the infrared.

The first infrared space telescope, the "Infrared Astronomical Satellite" (IRAS), was launched in 1983 and surveyed 96% of the whole sky in its four bands centered at 12, 25, 60, and 100 μm, during its 10 months lifetime. IRAS observed a total of 2228 asteroids and more than 25 comets (Tedesco et al. 2002); it discovered 3 new asteroids and 6 comets. The "IRAS Asteroid and Comet Survey" (Matson et al. 1989; Tedesco et al. 1992) was the largest, most uniform and least biased survey ever conducted of asteroids and comets till that time.

The huge success of the IRAS mission and the necessity for a mid and far–infrared observatory in a number of astronomical fields forwarded the design of follow–up missions. Two infrared space observatories have been utilized in the course of this work: NASA's "Spitzer Space Telescope" and ESA's "Herschel Space Observatory", which are introduced in the following sections. The "Wide–field Infrared Survey Explorer" (WISE, Wright et al. 2010), results of which have been used in this work, is also briefly introduced in the following.

[3]Zodiacal dust refers to low–density clouds of dust particles that mainly extend in the ecliptic plane. Zodiacal light is visible in the optical and thermal–infrared, as a result of reflected solar light and thermal emission, respectively. The dust particles are produced from active and dormant comets (Nesvorný et al. 2010).

[4]Galactic cirrus are clouds of molecular gases and dust that are heated by the integrated emission of all the stars in the galaxy. Their emission is mostly thermal and most obvious in the infrared wavelengths.

2.2 The Spitzer Space Telescope

The Spitzer Space Telescope is the fourth of NASA's Great Observatories, which were developed to conduct space–borne astronomical observations over a wide range of the electromagnetic spectrum. Spitzer was designed for imaging and spectroscopy of astronomical objects in the near to far–infrared.
In this section, I introduce Spitzer, which was utilized for thermal–infrared observations of NEOs and TNOs as part of this work. I give a brief outline of the spacecraft design and its scientific instruments, one of which, the IRAC photometer, has been extensively used for this work. In the discussion of the instruments, I focus on the relevant specifications and issues. Finally, the "ExploreNEOs" program is introduced.
In Section B.3, I briefly introduce the MIPSKBOs project, which provides additional observations of TNOs and Centaurs that are used in this work and in combination with the TNOs are Cool! program.

2.2.1 Spitzer Overview

The Spitzer Space Telescope (Werner et al. 2004; Gehrz et al. 2007), formerly known as the "Space Infrared Telescope Facility" (SIRTF), was launched on August 25, 2003, to its Earth–trailing solar orbit. Spitzer is named in honor of the American astronomer Lyman Spitzer (1914–1997), who was one of the first to conceive the idea of space–based observatories. Spitzer consists of a 85 cm diameter mirror telescope and three scientific instruments for imaging and spectroscopy in the near to far–infrared. During its cryogenic operation phase, all optical and scientific instruments had to be cooled to temperatures as low as 5.5 K. The nominal (cold) mission phase ended with the depletion of the liquid helium cryogen on May 15, 2009, over 5 years after launch. The "warm" mission phase, with the telescope and instruments only passively cooled to about 35 K, started in late July 2009 and continues as of this writing. A full description of the spacecraft and the individual instruments is given in the Warm Spitzer Observer's Manual (2012), the Spitzer Observer's Manual (2007), and the Spitzer Space Telescope Handbook (2011).

2.2.1.1 Spacecraft Design

Figure 2.3 shows the Spitzer spacecraft design. The observatory, with a total length of $\sim$4 m and a diameter of $\sim$2 m, consists of three main components:

- the spacecraft bus, providing telecommunications, attitude control and computer systems for both data handling and telescope control;
- the cryogenic telescope assembly (CTA), including the telescope, scientific instruments and the helium tank;

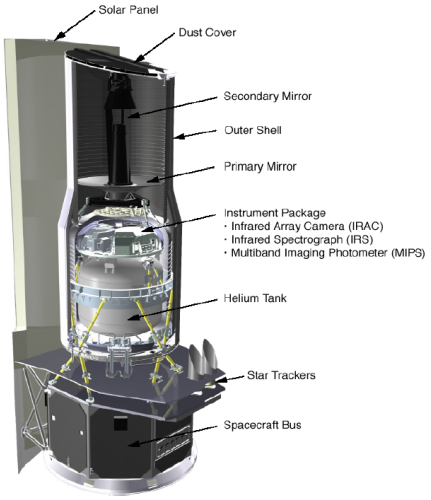

Figure 2.3 An overview of the different components of the Spitzer spacecraft. Image adapted from Spitzer Space Telescope Handbook (2011).

- the solar panel, supplying the spacecraft with energy and serving as a shielding for solar light.

Passive cooling of the telescope and instruments is provided by the solar panel, which works as a shield for insolation. In order to take full advantage of the shielding, Spitzer is subject to rigid pointing constraints: the telescope can only observe objects with solar elongations between 82.5° and 120° to prevent sunlight from heating the telescope aperture or the spacecraft bus (cf. Figure 2.4). For additional active cooling during the cryogenic part of the mission, liquid helium was evaporated. The CTA is thermally shielded from both the spacecraft bus and solar panel to minimize thermal conduction.

Spitzer's telescope is a 85 cm diameter mirror Ritchey-Chrétien design telescope, with a focal length of 10.2 m (focal ratio f/12). The primary mirror is entirely made from Beryllium, which offers an excellent strength–to–weight ratio and a reproducible cryogenic behavior. Spitzer's pointing is accurate within $<0.5''$ (1σ) and stable within $<0.1''$ (1σ) for 200 s. Its maximum tracking rate is $1.0''$ s^{-1}, which is fast enough to track most NEOs.

2.2.1.2 Spitzer's Orbit

Spitzer moves on an Earth–trailing orbit around the Sun (cf. Figure 2.5). Its distance to the Earth is ∼1.1 AU as of November 2012, steadily increasing at a rate of ∼0.12 AU/yr. The large distance from the Earth offers the advantage of minimizing the heating of the spacecraft from the thermal radiation of the Earth and the Moon, and minimizes the projected area of both in the plane of the sky. The disadvantage of Spitzer's increasing distance to the Earth is the gradually weakening of its radio signals, which will at one point disable communication with the spacecraft.

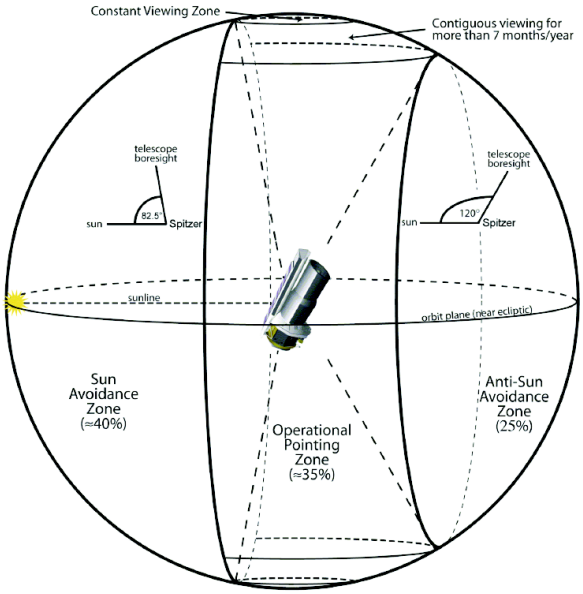

Figure 2.4 Illustration of Spitzer's pointing constraints. Spitzer's orientation in space is constrained to have the solar panel pointing towards the Sun in order to ensure both energy supply and passive cooling by the heat shield. Thus, only 35% of the whole sky can be observed with Spitzer at a time. However, during one Spitzer orbit, the whole sky is accessible. Image adapted from the Spitzer Observer's Manual (2007).

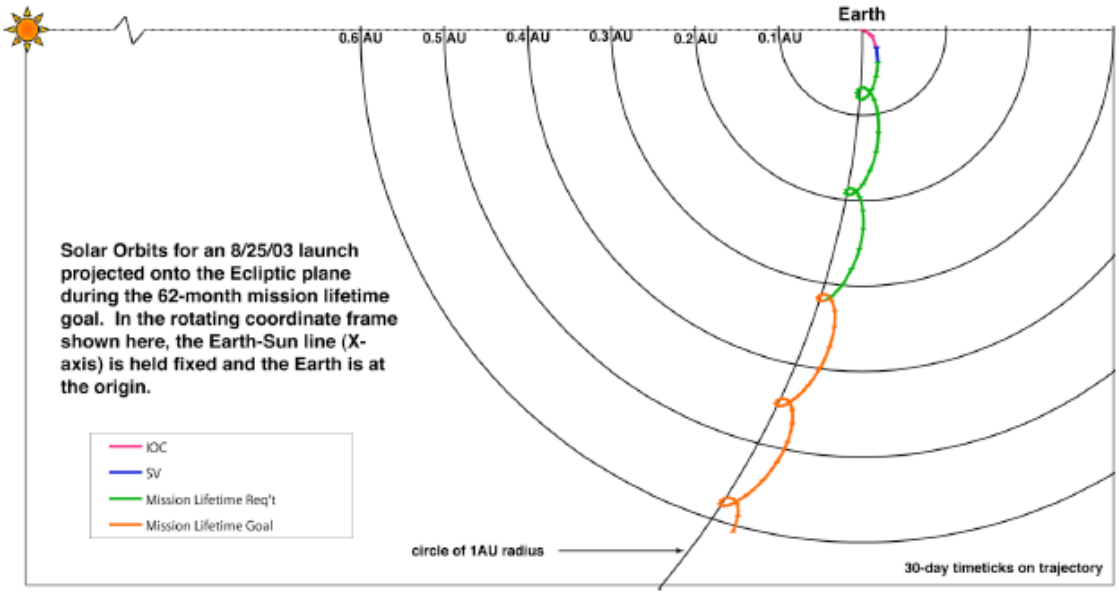

Figure 2.5 Illustration of Spitzer's orbit in a coordinate frame co–rotating with Earth's motion around the Sun at the end of its cryogenic mission phase. The orbit is also slightly inclined with respect to the ecliptic. IOC (In–Orbit Checkout phase) and SV (Science Verification phase) denote commissioning mission phases. Image adapted from the Spitzer Observer's Manual (2007).

2.2.1.3 Spitzer Data Products

Spitzer observation data are processed using a default pipeline, resulting in different types of calibrated data products that are accessible from the Spitzer Heritage Archive. The different available data products are outlined below.

Raw Data (Level 0) are entirely unprocessed and provided in a standard FITS[5] file format.

Calibration Data contain files that are used in the calibration of the higher–level data products. Usually calibration data are not provided to the observer, but they can be requested separately.

BCD (Level 1) passed through the automated pipeline to an extent where most instrument artifacts are removed. Furthermore, the pixel value scale has been absolutely calibrated into physical units (MJy/sr = 10^{-17} erg s^{-1} cm^{-2} Hz^{-1} sr^{-1}). BCD stands for Basic Calibrated Data. BCD are the primary data product for the observer. Along with the BCD come a number of ancillary files that contain additional information on the reduced data.

PBCD (Level 2) are the final products of the automated Spitzer pipeline. PBCD, or post–BCD, feature refined telescope pointing and mosaicked images.

The *ExploreNEOs* program uses Level 1 data, as described in Section 2.2.3. Each Spitzer observation is assigned an "Astronomical Observation Request" (AOR) key that allows for unambiguous identification of the observation.

2.2.1.4 Spitzer's Warm Mission – "Warm Spitzer"

Spitzer depleted its cryogen on May 15, 2009. Without active cooling, the CTA and telescope gradually heated up towards their new equilibrium temperature. All of Spitzer's long–wavelength detectors, in all of its three scientific instruments (see below), became unusable as the observatory warmed up, due to saturation by the elevated dark current[6]. The two shortest–wavelength detectors of the IRAC instrument (see Section 2.2.2.1) are not prone to significant dark currents and perform well at the new equilibrium temperature. Thermal emission from the mirror of the Spitzer telescope is higher at the new temperature (∼28 K), but has little effect at the 3.6 and 4.5 μm channels of the IRAC instrument.

[5]Flexible Image Transport System (FITS) is the standard file format for astronomical data. It contains a header, providing information on the observations, and stores image data in arrays.

[6]The dark current is caused by thermal excitation of the electrons in the detector material and leads to additional image noise. At high temperatures, the noise leads to a rapid saturation of the image pixels, precluding useful measurements.

As of March 2013, Spitzer is operating in its 9–th cycle of observations. Based on the results from the 2012 NASA Senior Review, Spitzer operations are planned through at least September of 2014, enabling a 10–th cycle of observations.

2.2.2 Scientific Instruments

Spitzer provides three scientific instruments that are capable of imaging and spectroscopic analysis ranging from the near to the far infrared. The three instruments, IRAC, MIPS, and IRS, are introduced in the following. The focus of the following discussion will be put on IRAC, which was utilized for observations of NEOs, as part of this work.

2.2.2.1 The InfraRed Array Camera (IRAC)

Originally, the "InfraRed Array Camera" (IRAC, Fazio et al. 2004) provided dual–band imaging in four different mid–infrared bands. The camera observed two fields on the sky plane that are separated by a gap of $1.5'$. The two adjacent fields enabled the instrument to image simultaneously at 3.6 (channel 1) and 5.8 μm (channel 3), or at 4.5 (channel 2) and 8.0 μm (channel 4). The IRAC detector unit consists of four detector arrays, two InSb (Indium Antimodite) (channel 1 and 2) detectors, and two Si:As (Silicon Arsenic) detectors (channel 3 and 4). The telescope beam is picked up at two locations in the focal plane of the telescope and split by a beam splitter into two separate beams that pass filters before arriving at the detector surfaces.

As a result of the transition to Spitzer's warm mission, IRAC channels 3 and 4 ceased operation: the high thermal noise in both bands impedes further observations. As of this writing, IRAC Channels 1 and 2 are still fully operational. Measurements of both bands are used in this work. Technical specifications and characteristics of the two remaining IRAC channels are listed in Table 2.1 and discussed in the following. The information were distilled from the Spitzer Space Telescope Handbook (2011), Warm Spitzer Observer's Manual (2012) and the IRAC Instrument Handbook (2012), which should be consulted for more information.

- The instrument point–spread function (PSF) full width half maximum (FWHM) (see Section A.2.1.1 for an introduction of both terms) of both channels are about the same size as the pixels and therefore under–sampled with respect to the Nyquist theorem (see Section A.2.1.1), leading to a loss of image information. However, this loss can be compensated for by using dithering during the observations, allowing for super–resolution observations.

- The spectral response of the channel 1 and 2 filters and detectors is illustrated in Figure 2.6. The effective wavelengths differ slightly from the mnemonic wavelengths. Calibrated IRAC flux densities are based on a nominal spectrum of the

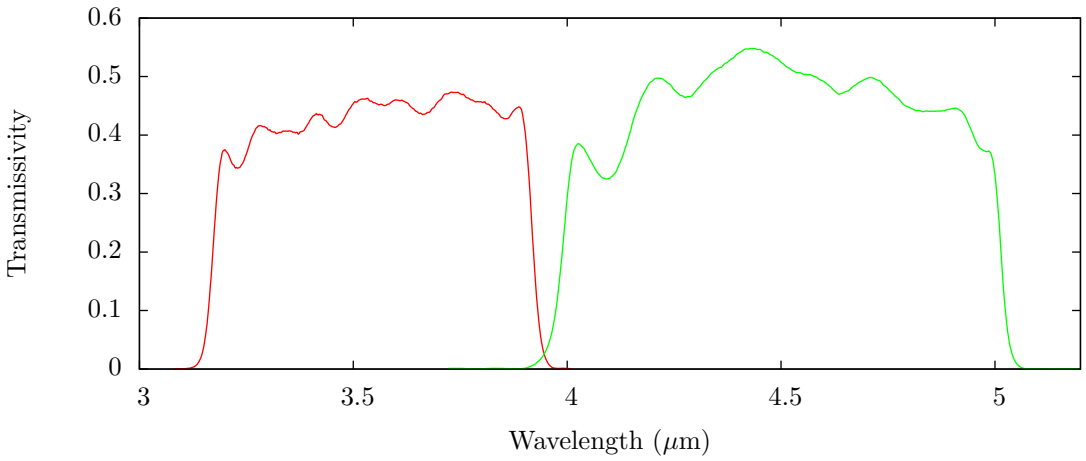

Figure 2.6 Spectral response function of IRAC's channel 1 and 2, averaged over the entire detector area. Data from the NASA/IPAC Infrared Science Archive (`http://irsa.ipac.caltech.edu/data/SPITZER/docs/irac/calibrationfiles/spectralresponse/`, accessed in January 2013).

form $f_{\mathrm{nom}}(\lambda) \propto \lambda^{-1}$ (see Section A.2.2.2). Using this nominal spectrum, Table 2.1 lists color correction coefficients based on black body spectra with temperatures that can be found on NEO surfaces. Color correction becomes significant for temperatures lower than 200 K.

- IRAC's stray–light behavior is well understood. Bright sources just outside the field of view can produce distinctive ghost images on the imaging array, which are caused by reflections at the array covers or the filter. The stray–light avoidance zones are well–determined (IRAC Instrument Handbook 2012).

- Other image artifacts are caused by IRAC's electronics, like the "column pull-down" effect and the "muxbleed" effect, which are present in IRAC Channels 1 and 2. The column pull-down effect is caused by saturated or nearly–saturated pixels that influence the pixel values in that column where they are located. The effect can be partially corrected for. Muxbleed, or Multiplexer bleed, causes a horizontal bleeding emerging from bright sources, hot pixels, and pixels that were hit by cosmic rays.

- As a result of the transition from Spitzer's cryogenic to its warm mission phase, changes had to be applied to the IRAC instrument setup, including adjustments to the instrument's voltages. The gradual heating of the instrument led to changes in the detector sensitivity and noise properties, requiring re-calibrations of the instrument. The performance of IRAC in its warm phase, the detector array has reached an equilibrium temperature of 28.7 K, is still excellent. The comparison between IRAC performances during the cryogenic and warm mission phases (cf. Table 2.1) clearly shows the reduced sensitivity of warm IRAC. On average, sensitivity has

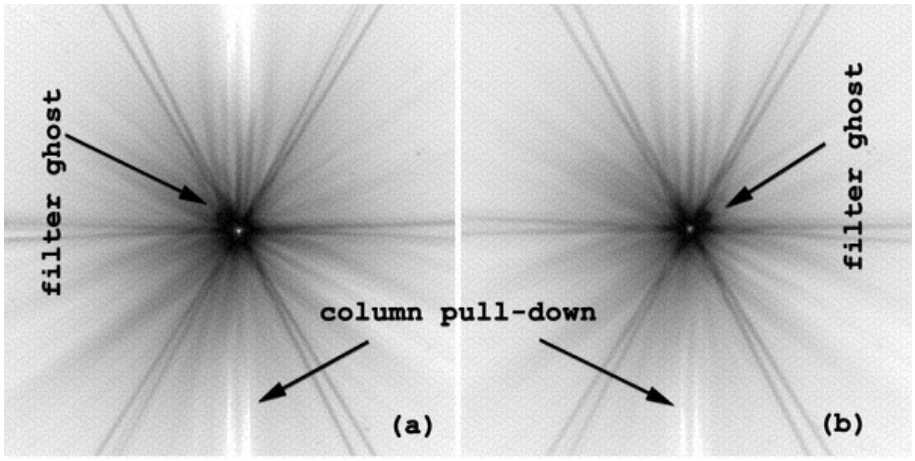

Figure 2.7 IRAC's channel 1 (**left**) and 2 (**right**) high–SNR point spread functions (PSFs) with inverted logarithmic scaling. Both PSFs were constructed from in–flight observational data to take into account pixel–to–pixel sensitivity variations. The resolution of the PSFs are improved to sub–pixel resolution using dithering routines. Image artifacts are labeled in the images and described in the text. Adapted from Marengo et al. (2009).

dropped by 10% and 5% for the 3.6 and 4.5 μm array, respectively. The absolute photometric calibration of both channels is stable and accurate within 4% for both channels, allowing for photometry results with a precision better than the order of 10^{-3} mag. There was no measurable loss in image quality compared to the cryogenic mission phase. IRAC supports all operations of the cryogenic mission and all planned warm mission science activities. For a full discussion of the performance of "warm IRAC" see Carey et al. (2010).

IRAC Observing Modes. IRAC offers four selectable frame times, 2, 12, 30 and 100 s, and a high dynamic range (HDR) option, which takes additional frames using shorter than the selected frame time, allowing for a larger dynamic range. Using the "moving cluster" option, multiple frames can be taken consecutively, which is especially useful for moving Solar System targets and allows for a user–defined dithering pattern.

2.2.2.2 The Multiband Imaging Photometer for Spitzer (MIPS)

The "Multiband Imaging Photometer for Spitzer" (MIPS, Rieke et al. 2004) provided broad–band imaging in three mid and far–infrared bands, centered at 24, 70 and 160 μm, as well as low–resolution spectroscopy in the wavelength range between 55 and 95 μm during Spitzer's cryogenic mission phase. The MIPS photometer was used for observations of TNOs and Centaurs, all of which are reprocessed in a consistent manner as part of the *MIPSKBOs* project (see Section B.3). For more information on the MIPS instrument, I refer to Section B.3.2 and the MIPS Instrument Handbook (2011).

Table 2.1. IRAC Detector Characteristics.

Parameter	Channel 1		Channel 2	
	Cryo	Warm	Cryo	Warm
Mnemonic Wavelength (μm)	3.6		4.5	
Effective Wavelength λ (μm)	3.550		4.493	
Bandpasses (μm)	3.2–4.0		4.0–5.0	
Field of View ($'$)	5.2×5.2		5.2×5.2	
Array Size (pixels)	256×256		256×256	
Projected Pixel Size ($''$)	1.2×1.2		1.2×1.2	
PSF Mean FWHM ($''$)	1.66		1.72	
Color Correction Coefficient for $T = 600$ K	1.0068		0.9961	
$T = 400$ K	1.0614		1.0240	
$T = 200$ K	1.5138		1.2929	
Read Noise for 2 s Frame Time (e^-)	11.8	12.1	13.0	9.1
30 s Frame Time (e^-)	7.8	7.5	8.6	7.5
100 s Frame Time (e^-)	8.4	7.9	9.2	7.9
PSS (1σ) for 2 s Frame Time (μJy)[1]	31	38	37	39
30 s Frame Time (μJy)	1.4	2.4	1.7	2.5
100 s Frame Time (μJy)	0.6	1.2	0.69	1.25

Note. — "Cryo" refers to the cryogenic mission phase, "Warm" to the warm mission phase. Values spanning both columns have not changed between both mission phases. Parameters during the cryogenic and warm mission phases were taken from the Spitzer Observer's Manual (2007) and the Warm Spitzer Observer's Manual (2012), respectively. The parameters are introduced in the text.

[1]PPS = Point Source Sensitivity; the point source flux that is necessary to trigger a signal that is at 1σ confidence level above the background noise level.

2.2.2.3 The InfraRed Spectrograph (IRS)

IRS (Houck et al. 2004) performs low and high–resolution spectroscopy at 5.2 to 38.0 μm, and at 9.9 to 37.2 μm, respectively. The instrument consists of four Si:As detectors. IRS has not been utilized in this work and is therefore not discussed any further.

2.2.3 "ExploreNEOs": The Warm Spitzer NEO Survey

The "The Warm Spitzer NEO Survey: Exploring the history of the inner Solar System and near Earth space" (*ExploreNEOs*) is a Spitzer Exploration Science Program that investigates the physical properties of the NEO population. *ExploreNEOs* was awarded 500 hrs of Spitzer observation time for the observation of ∼700 NEOs (Trilling et al. 2010) during Spitzer's warm mission phase. The program's principal investigator (PI) of the program is David E. Trilling, Northern Arizona University; the program's 19 co–investigators come from 11 different science institutes in 4 different countries. The Spitzer observations are supported by ground–based optical and spectroscopic observations that aim to improve the quality of absolute magnitude estimates and to enable taxonomic classifications of some of the sample targets, respectively; the auxiliary observations are beyond the scope of this work and I refer to Hagen et al. (2011) and Thomas et al. (2011) for more information. The Spitzer observations of the *ExploreNEOs* program were completed in November 2011, the data analysis is currently in progress.

2.2.3.1 Goals

The primary science goal of the *ExploreNEOs* program is the exploration of the history of near–Earth space by studying the physical properties of the NEO population as a whole, as well as those of individual objects. The specific aims of the program include:

- the *determination of the size distribution of sub–km sized NEOs*,
- an *assessment of the fraction of NEOs that have a cometary origin,* and
- the *investigation of the mixing of the NEO population based on a measurement of its albedo distribution.*

2.2.3.2 Data Acquisition

Using Warm Spitzer, the program is restricted to the use of IRAC's channels 1 and 2, providing imaging photometry at 3.6 and 4.5 μm.

Observation Planning. The ExploreNEOs target sample consists of optically pre–discovered NEOs that were selected based on Spitzer observability: all targets are required to meet the Spitzer solar elongation constraints (see Section 2.2.1.1), to have small positional uncertainties ($<150''$), and to have a proper motion not faster than $1''$ per second.

Furthermore, targets are only observed at times when their galactic latitude is larger than a predefined threshold, limiting the background confusion noise.

The finally observed *ExploreNEOs* sample contains 566 different NEOs, 8 of which were observed multiple times (so called "multi–visit targets") to assess systematics in the thermal modeling and lightcurve effects, and 4 of which have single–band data only. Some observations have failed due to background noise, some were saturated.

All observations aimed for SNR≥15. IRAC integration times are selected based on predicted target fluxes that are determined from thermal modeling, using H magnitudes and observation geometries as provided by the JPL Horizons Systems, accessed in 2008, and using an assumed albedo of 0.05, 0.2 and 0.4. In order to take into account the large uncertainties in the Horizons H magnitudes (Jurić et al. 2002; Pravec et al. 2012), magnitudinal offsets of 0, 0.3, and 0.6 mag are added to the provided magnitude. For each object, a visibility window of at least five consecutive days was selected for which SNR≥15 can be obtained with the shortest possible integration time and assuming the lowest possible flux estimate using the above method. For more details, see Trilling et al. (2010). *ExploreNEOs* observations were mainly planned by D. Trilling (Northern Arizona University), M. Mueller (now SRON, Netherlands) and J. Hora (CfA Harvard).

Observation Technique. Observations are performed in the Spitzer "moving cluster" mode: each AOR consists of a total of [9, 14, 10, 20] individual observations in each band with frame times of [12, 30, 100, 100] seconds, following a predefined dithering pattern, and yielding total integration times of [100, 400, 1000, and 2000] seconds for each channel. The dithered observations alternate between channel 1 and 2 to reduce the impact of lightcurve effects within the observation period and to maximize the relative motion, improving the background subtraction.

Data Reduction and Analysis. The reduction of the *ExploreNEOs* data is based on Level–1 BCD data that are downloaded from the Spitzer Heritage Archive (see Section 2.2.1.3) and reduced using the IRACproc software (Schuster et al. 2006). Mosaics of each AOR are constructed by aligning the dithered individual frames in the rest frame of the target, based on its projected motion. As a result of the dithering and outlier rejection during the mosaicking, background objects and cosmics are mostly removed. Flux densities are determined using aperture photometry. For a detailed discussion see Trilling et al. (2010). The *ExploreNEOs* data reduction is performed by J. Hora and H. Smith (both CfA Harvard).

Thermal Modeling Pipeline. Diameters and albedos are derived from the measured flux densities using a default and automatized pipeline that is based on the NEATM (see Section 3.2.4), using H magnitudes and geometrical data from the JPL Horizons Systems, accessed in 2008.

Warm Spitzer observations of NEOs, especially at 3.6 μm, suffer severely from contaminations by reflected solar light (see Section 3.7.1.1 for a discussion). This problem has been anticipated and a feasibility study prior to the start of the *ExploreNEOs* program (Trilling et al. 2008) has shown that the reflected solar light component in the measured flux densities can be approximately subtracted using an average reflectance ratio $RR_{\mathrm{IR/V}} = 1.4$ (Trilling et al. 2008, 2010; Harris et al. 2011). The method for the subtraction of the reflected solar light is described in Section 3.7.1.1. In some cases, all the measured flux density at 3.6 μm is reflected solar light, whereas the contribution to the 4.5 μm band is significantly smaller. The default modeling results are based on a fixed–η NEATM fit using the corrected 3.6[7] and 4.5 μm flux densities and a fixed relation $\eta(\alpha) = (0.013 \pm 0.004)\alpha + (0.91 \pm 0.17)$ (Wolters et al. 2008, see also Section 3.5), with α in degrees. Uncertainties in diameter and albedo are derived using the Monte–Carlo method described in Section 3.3. The default uncertainties in H and η are 0.3 mag and the uncertainty derived from the above equation, respectively. For a full discussion of the *ExploreNEOs* thermal modeling pipeline, see Trilling et al. (2010), Harris et al. (2011), and Mueller et al. (2011). The accuracy of the default *ExploreNEOs* thermal modeling pipeline has been tested in Harris et al. (2011), my contribution to which is described in Section B.1. The default *ExploreNEOs* thermal modeling pipeline has been created and is maintained by Michael Mueller (SRON, Netherlands).

2.2.3.3 Status

ExploreNEOs observations started in July, 2009, and ended in November, 2011. In total, 589 observations of 566 different NEOs have been conducted. Multiple observations of some objects are used to investigate lightcurve and aspect angle effects. As of this writing, 6 refereed publications have been published in the framework of the *ExploreNEOs* program (see Section C.1).

[7]The contribution of reflected solar light to the measured 3.6 μm flux density can make up a significant fraction. Hence, the corrected (i.e., thermal) 3.6 μm flux density is rather small, its SNR is significantly compromised. Consequentially, the SNR of the 3.6 μm flux density measurement is lower compared to that at 4.5 μm. The thermal modeling results are therefore mainly based on the 4.5 μm flux density, which has the higher SNR and an increased significance in the χ^2 fitting procedure (see Equation 3.6).

2.3 The Wide–field Infrared Survey Explorer

Mostly in parallel to the ExploreNEOs Spitzer observations, the Wide–field Infrared Survey Explorer (WISE, Wright et al. 2010) carried out an all–sky imaging survey in its four infrared bands. As part of its survey, WISE observed more than 100000 asteroids that are analyzed in the framework of the NEOWISE project (Mainzer et al. 2011a).

I was not involved in the NEOWISE program, but utilize some of its results in different parts of this work, which justifies a brief introduction of the WISE observatory and the NEOWISE project.

2.3.1 The WISE Mission

The WISE mission started in December 2009 and ended after the depletion of its solid hydrogen coolant and a post–cryogenic mission phase in February 2011. The primary WISE mission objectives included the observation of galaxies, brown dwarfs and other stars, as well as Solar System small bodies (Wright et al. 2010). The design of the WISE survey enabled it to discover new asteroids in the thermal infrared without being affected by the discovery bias against low–albedo objects, which affects optical surveys (see Section 1.2.1). As far as small Solar–System bodies are concerned, WISE was most sensitive to NEOs and main belt asteroids. The wavelength coverage largely precluded observations of colder objects in the outer Solar System.

WISE was equipped with a 40 cm mirror telescope, providing a $47'$ field of view with a plate scale of $2.75''$/pixel in each of its bands, centered at 3.5, 4.6, 12, and 22 μm; using on–board binning, the final maps have a resolution of $5.5''$ pixel^{-1}. The 2.85×2.00×1.73 m spacecraft was deployed on a Sun–synchronous polar orbit around the Earth, continuously scanning those parts of the sky with solar elongation of 90° with a cadence of 11 s. In the cryogenic part of the mission, the telescope and detectors were cooled down to 12 and 7.5 K, respectively. After 7.7 months of operation, the depletion of coolant in the secondary hydrogen tank led to a rise in the telescope and detector temperatures, forcing the 22 μm band to stop operation, and decreasing the sensitivity of the 12 μm band. The end of this "3–band cryogenic" mission phase was forced by the depletion of solid hydrogen in the primary tank in late September 2010, and followed by a four months "post-cryogenic" mission phase. See Wright et al. (2010) for more information on the WISE mission.

2.3.2 The NEOWISE Program

In total, NEOWISE (Mainzer et al. 2011a) has determined diameters and albedos of more than 100000 main belt asteroids (Masiero et al. 2011) and at least 584 NEOs; 135 NEOs of which were discovered by WISE. Diameters and albedos are derived using a NEATM–based thermal model (Mainzer et al. 2011b). Most of the NEOWISE thermal

model fits are floating–η fits, since data in more than one band were usually obtained. For single–band observations, a fixed $\eta = 1.35$ is adopted (Mainzer et al. 2011c). In the NEOWISE thermal modeling pipeline, spherical model asteroids are represented by sets of triangular facets, for each of which the surface temperature, the emitted flux density at a given wavelength, and the respective color correction coefficient is calculated. The two shortest–wavelength bands of WISE cover wavelength ranges similar to the Spitzer bands used by *ExploreNEOs*, and are hence subject to contamination by reflected solar light (see Section 3.7.1.1). The determination of the reflected solar light component uses a method similar to the one used in the *ExploreNEOs* program (see Section 3.7.1.1), using $RR_{\mathrm{IR/V}} = p_V/p_{IR}$, where $p_{IR} = p_{3.5} = p_{4.6}$ is the infrared albedo at 3.5 and 4.6 μm that can be measured from observations in at least two bands. If $RR_{\mathrm{IR/V}}$ cannot be derived from the observations, $RR_{\mathrm{IR/V}} = 1.6$ is adopted (Mainzer et al. 2011b,c).

NEOWISE results utilized in this work are mainly extracted from the publications of the NEOWISE team (e.g., Mainzer et al. 2011b; Masiero et al. 2011) and used in Sections 4.1, 4.2, and B.1. In Section 4.3, I make use of WISE observations extracted from the "WISE 3–Band Cryo Known Solar System Object Possible Association List" provided by the NASA/IPAC Infrared Science Archive/WISE Observations Database. The latest and most complete WISE data release is the Wide–Field Infrared Survey Explorer All–Sky Data Release.

2.4 The Herschel Space Observatory

The Herschel Space Observatory is the fourth "cornerstone" mission in ESA's Science Programme, and was designed for providing imaging and spectroscopic capabilities in the mid to far infrared, and into the sub–millimeter wavelengths. In the following sections, I introduce the Herschel spacecraft design and its scientific instruments, PACS, SPIRE, and HIFI. In the framework of the TNOs are Cool! program, PACS and SPIRE were utilized; however, only flux density measurements of PACS are used in this work. I have not been involved in the data processing of Herschel data, and will therefore keep the discussion brief and restrict it to the PACS photometer capabilities. At the end of this section, the TNOs are Cool! program is presented.

2.4.1 Herschel Overview

The Herschel Space Observatory (Pilbratt et al. 2010), formerly known as the "Far Infrared and Sub–millimetre Telescope" (FIRST), was launched on May 14, 2009, to its solar orbit. Herschel is named after the German–born British astronomer Sir Frederick William Herschel (1738–1822), who is widely considered the discoverer of infrared radiation (Herschel 1800). Herschel is the first space–based observatory that provides imaging and spectroscopy capabilities ranging from the mid–infrared to the sub–millimeter wavelengths. Active cooling using liquid helium is necessary to maintain the instrument operational, which limits Herschel's operational lifetime; its required lifetime was 3.5 yrs by design. As of the beginning of March 2013, all Herschel instruments are still fully operational. However, latest estimates of the actual lifetime expect a depletion of the coolant in late March 2013. A full description of the Herschel mission is given in the Herschel Observer's Manual (2012).

2.4.1.1 Spacecraft Design

The Herschel spacecraft is 7.5 m long and has a width of 4.0 m. Figure 2.8 shows the design of the spacecraft, which consists of two main components:

- the Payload Module (PLM), containing the Herschel telescope and the cryostat, which in turn comprises the liquid helium tank and the telescope's focal plane unit;
- the Service Module (SVM), which carries all spacecraft electronics and those parts of the instrument units that operate in an ambient temperature environment.

The detectors of the scientific instruments are cooled actively to temperatures ranging from 0.3 K to 10 K, in order to minimize thermal noise and to maximize the sensitivity. Herschel's telescope is cooled passively by the Sun shield to an equilibrium temperature of 70 to 80 K, constraining the pointing of the telescope to solar elongations between

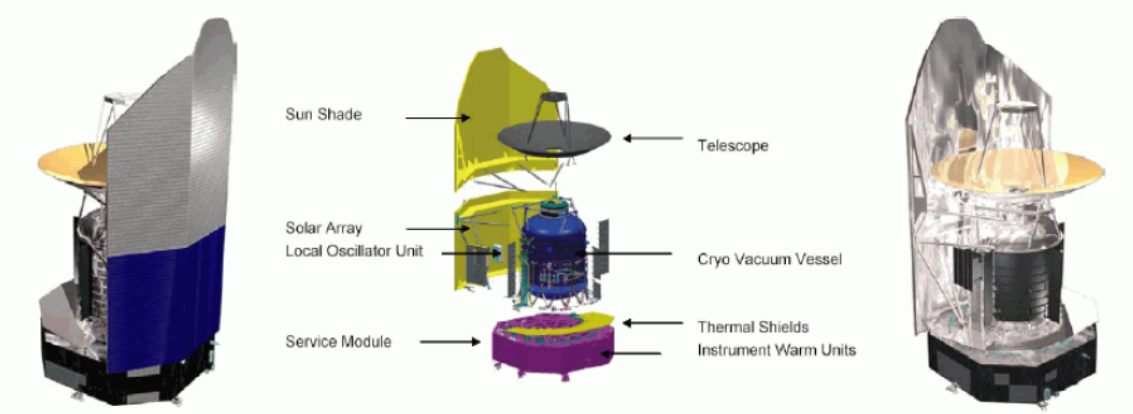

Figure 2.8 The Herschel spacecraft design. The Service Module is colored in violet, and the Sun shield is shown in yellow. All parts shown above the Service Module are part of the Payload Module. Image taken from the Herschel Observer's Manual (2012).

60.8° and 119.2°, which was later reduced to 60.8° and 110°, respectively, for nominal operations. The telescope is a traditional Cassegrain design with a primary mirror made of silicon carbide (SiC) with a diameter of 3.5 m, and a thickness of only ∼3 mm, being the largest telescope mirror ever deployed in space[8]. The telescope has a focal length of 28.5 m, and produces diffraction–limited images over a field of view of 0.5°, which roughly equals the size of the full Moon. Herschel's absolute pointing error was determined to be better than 1″ in nominal operation conditions.

2.4.1.2 Herschel's Orbit

Herschel has been inserted in its orbits around the second Lagrange point (L2) of the Sun–Earth system, which is located around 1.5 million km from the Earth in the anti–solar direction, about sixty days after its launch. The L2–orbit has the advantages of having the Earth close to Sun, not requiring additional pointing constraints, and a very stable thermal environment. It's disadvantages are the long distance for communications, and the unstable nature of L2–orbits, requiring regular orbit corrections.

2.4.1.3 Herschel Data Products

Herschel observations and service are coordinated by the Herschel Science Centre that also provides a number of software tools, one of which is HSpot, which can be used for the generation of Herschel observations (AORs). Observational data are provided by the Herschel Science Archive, 1–2 days after the downlink of the data. Initially, data can only be downloaded by the observer. After the proprietary period of 6 months (1 year in the early mission phase), data are publicly available. Herschel data products

[8]The size of the telescope was only restricted by the size of the launch vehicle.

are available in different stages of processing, provided by the HSC "Standard Product Generation software". The most important products to mention here are Level–0 and Level–1 data, which refer to raw telemetry as measured by the respective instrument, and calibrated data, respectively. The HSC provides a software tool, HIPE (Ott 2010), which is specifically designed for the reduction of Herschel observation data.

Herschel observing time is separated into two categories: Guaranteed Time (GT), which is assigned to the instrument consortia and makes up 32% of the whole observing time, and Open Time (OT), which is available to the scientific community. Due to the limited operational lifetime of Herschel, there have only been one call for OT key programmes and two calls for general OT proposals.

2.4.2 Scientific Instruments

Herschel has three scientific instruments that provide imaging and spectroscopic capabilities in the mid and far–infrared (PACS and SPIRE), as well as in the sub–millimeter wavelengths (SPIRE and HIFI).

In the following, the scientific instruments are briefly discussed. The focus is put on the imaging capabilities of PACS, on which some results of this work are based. SPIRE and HIFI are introduced briefly.

2.4.2.1 The Photodetector Array Camera and Spectrometer (PACS)

The Photodetector Array Camera and Spectrometer (PACS, Poglitsch et al. 2010) provides integral–field spectroscopy and imaging photometry in the 60–210 μm wavelength range. The spectrometer consists of two Ge:Ga photoconductor arrays (stressed and unstressed), 16×25 pixels, each, covering the wavelength range 55–210 μm. The spectrometer has not been used as part of this work and is therefore not discussed in more detail.

The PACS photometer allows for dual–band imaging in three bands, called the "blue", "green" and "red" band, using its two filled silicon bolometer arrays. Both bolometer arrays view the same field of the sky, allowing for simultaneous imaging in the red and the blue or green band, using dichroic beam splitters and respective filters.

Technical characteristics of the PACS photometer are listed in Table 2.2 and discussed in the following. Most of the information was extracted from Poglitsch et al. (2010) and the PACS Observer's Manual (2011), to which I refer for a more detailed discussion.

- The PACS PSF is well–sampled according to the Nyquist theorem (see Section A.2.1.1) in each of its three bands. The FWHM listed in Table 2.2 are derived for observation using the scan–map mode (see below) with a scan speed of 20″/s, which is the default value applied in *TNOs are Cool!* observations.

- The effective spectral response of the PACS filters and detectors is shown in Figure 2.9. Calibrated PACS flux densities are based on a constant energy spectrum of the

Table 2.2. PACS Photometer Characteristics.

Parameter	Blue Channel	Green Channel	Red Channel
Mnemonic = Effective Wavelength (μm)	70	100	160
Bandpasses (μm)	60–85	85–125	125–210
Field of View ($'$)	3.5×1.75		3.5×1.75
Array Size (pixels)	16×32		32×64
Projected Pixel Size ($''$)	3.2×3.2		6.4×6.4
PSF FWHM ($''$) at 20$''$/s scan speed	5.46×5.76	6.69×6.89	10.65×12.13
Color Correction Coefficient for $T = 100$ K	0.99	1.01	1.04
$T = 50$ K	0.98	0.99	1.01
$T = 20$ K	1.22	1.04	0.96
$T = 15$ K	1.61	1.16	0.99
Point–Source Sensitivity (5σ/1 hr, mJy)	4.4	5.1	9.8
Average Photometric Uncertainty (%)	±5	±5	±5

Note. — Data were extracted from the PACS Observer's Manual (2011) and Poglitsch et al. (2010).

form $f_{\rm nom}(\lambda) \propto \lambda^{-1}$ (see Section A.2.2.2). Effective wavelengths of the individual bands, which are chosen to be equal to the mnemonic wavelengths, as well as color correction coefficients, taken from Poglitsch et al. (2010), are listed in Table 2.2. The color correction coefficients are given for some typical TNO surface temperatures. It is obvious that color correction becomes significant in the blue band at temperatures $T < 50$ K.

- The point–source calibration uncertainties of PACS Level–1 data products has been assessed to be 3% in the blue and green band, and 5% in the red band (Müller et al. 2011).

- Sensitivities and mean photometric uncertainties listed in Table 2.2 are taken from Poglitsch et al. (2010) and were determined using the mini–scan–map mode (see below).

PACS Observing Modes. The PACS photometer offers three different observation modes: (1) point–source photometry using a chop–nod technique, (2) a scan–map mode, and (3) a scan–map mode providing simultaneous SPIRE observations. The chop–nod technique (1) uses a combination of mirror tilts to improve the background–removal. However, in the case of PACS, the technique has turned out to be significantly less sensitive than the scan–map technique, which has also been applied in most of the *TNOs are Cool!*

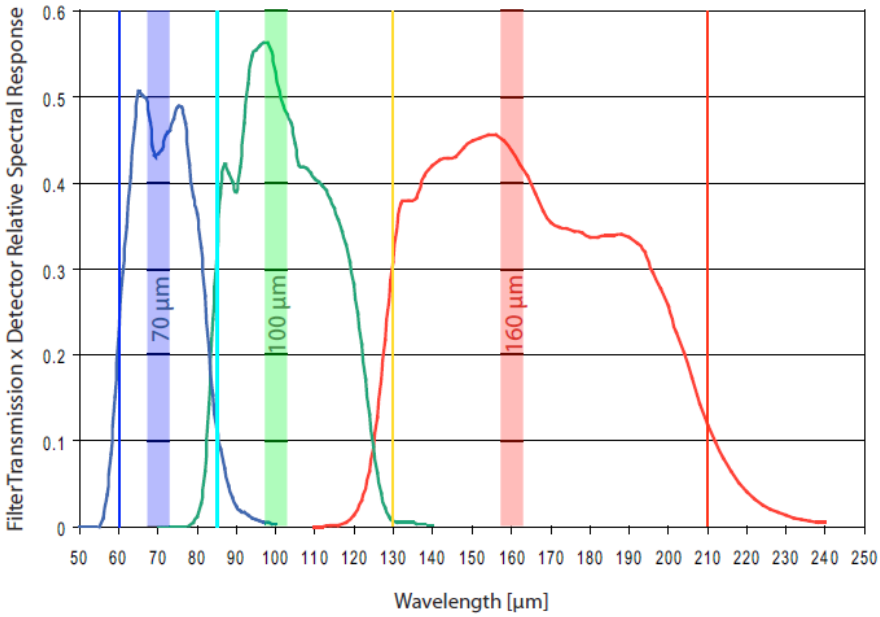

Figure 2.9 Effective spectral response of the PACS filters and detectors. Image adapted from Poglitsch et al. (2010).

PACS observations. The combined PACS/SPIRE mode, (3), was not applied in this work and is therefore not discussed.

In the scan–map mode, the Herschel spacecraft performs a number of continuous slews over the target region at a constant speed. The number of satellite scans, the scan leg length, the scan leg separation, as well as the scan directions relative to the sky background are freely selectable by the observer. Software routines are available in HIPE that produce a single map from all individual observations. A mini–scan–map mode with short scan leg lengths has been introduced for the use on point–sources. It provides better performance than the chop–nod technique in the same observing time.

2.4.2.2 The Spectral and Photometric Imaging REceiver (SPIRE)

The "Spectral and Photometric Imaging REceiver" (SPIRE, Griffin et al. 2010) consists of an imaging three–band photometer and a Fourier–transform spectrometer. The photometer performs broad–band photometry at roughly 250, 350 and 500 μm, and the spectrometer works in two overlapping bands, spanning from 194 μm (1550 GHz) to 671 μm (447 GHz). The photometer has been utilized in some observations of the *TNOs are Cool!* program, but not as part of this work. Hence, I skip the discussion of this instrument and refer to Griffin et al. (2010) for more information.

2.4.2.3 The Heterodyne Instrument for the Far–Infrared (HIFI)

The "Heterodyne Instrument for the Far–Infrared" (HIFI, de Graauw et al. 2010) performs spectroscopic observations in the sub–millimeter regime. The instrument comprises 7 heterodyne receivers, covering the 480–1250 GHz and the 1410–1910 GHz range. Expressed in wavelengths, the two ranges comprise wavelengths between 157 μm and 625 μm. HIFI has not been used in neither the *TNOs are Cool!* program, nor as part of this work. For information on HIFI, consult de Graauw et al. (2010).

2.4.3 "TNOs are Cool!": A Survey of the Trans–Neptunian Region

The Herschel Open Time Key Programme "*TNOs are Cool!*" (Müller et al. 2009) has been awarded 372 hrs of Herschel observing time for performing PACS and SPIRE observations of TNOs and Centaurs. Thermal modeling is applied to determine independent diameter and albedo estimates for all 132 sample targets, the largest ever sample of TNOs and Centaurs with measured physical properties. The principal investigator of the program is Thomas G. Müller, Max–Planck Institute for Extraterrestrial Physics (MPE); the project team includes 40 scientists from 20 institutes in 9 different countries. *TNOs are Cool!* is supported by a number of ground–based optical observation campaigns, performing astrometric and photometric observations in order to improve the orbits and absolute magnitudes of the sample targets, respectively. The observations of the *TNOs are Cool!* program are completed, the data analysis is in progress.

2.4.3.1 Goals

TNOs are Cool! has four major science goals:

1. The determination of the albedos and diameters of all 132 sample targets are used to constrain the *size distributions of TNOs and Centaurs*, as well as to investigate *correlations with the dynamical parameters and measured surface colors.*

2. The size measurements are used to *determine bulk densities* for 27 of the sample targets that are binaries.

3. Multi–wavelength observations are used to *constrain thermophysical properties* like the thermal inertia and the emissivity of the brightest targets.

4. Observations of the thermal lightcurves of some sample targets enable to *identify the nature of the observed lightcurve as a shape or albedo–effect* (see Section 1.2.3).

2.4.3.2 Data Acquisition

Observation Planning. The final *TNOs are Cool!* target sample comprises 132 objects in total, including 18 Centaurs, 45 classicals (33 hot and 12 cold ones), 43 resonants (29

of which are Plutinos), 13 scattered disk objects, 11 detached objects, and 2 moons of the giant planets. All targets were optically discovered prior to the Herschel observations, and were selected solely on the basis of Herschel observability, in terms of detector sensitivity and positional uncertainty (all targets have a 3σ positional uncertainty of $<10''$).

Frame times were chosen in such a way as to provide a SNR of 10 or higher in all three PACS bands, based on predicted flux densities that were derived using a thermal model. The predictions are based on the measured absolute magnitude, the predicted observation geometry, and an assumed albedo[9]. The average on–source integration time of the spacecraft amounts to 0.5 hrs per target.

Observation Technique. Most targets were observed using the mini–scan–map mode, few during the Science Demonstration Phase (SDP) with the point–source chop–nod mode. 10 of the sample targets were observed in the combined PACS/SPIRE mode (Fornasier 2013).

The PACS mini–scan–maps on which the flux density measurements for this work are based were taken in medium scan–speed ($20''$/s) mode, using a scan–leg length of $3'$ and 2–4 repetitions, in all three bands. Furthermore, follow–up observations (see Section A.2.1.1) were performed with a relative distance between the two target positions of 30–$50''$. Observations were mainly planned by T. Müller (MPE) and E. Vilenius (MPE).

Data Reduction and Analysis. The individual scan–maps, produced from level–0 raw data using an optimized HIPE pipeline, were mosaicked, as well as background–subtracted (see Section A.2.1.1, as well as Stansberry et al. 2008; Santos-Sanz et al. 2012; Mommert et al. 2012). Photometry was performed on the final background–subtracted maps using aperture photometry (see Section A.2.2.1) at the photocenter position of the target. Photometric uncertainties are estimated by random implantation of 200 artificial sources in the nearby sky background of the target (Santos-Sanz et al. 2012); the so–derived 1σ uncertainty is also given as an upper limit in the case of non–detections. The absolute accuracy of the photometry was found to be $\sim$5% for bright targets; in the faint regime (below 10 mJy) the accuracy of the 160 μm band is background–noise driven. The data reduction and analysis is mainly performed by C. Kiss (Konkoly Observatory, Hungary), A. Pal (Konkoly), P. Santos–Sanz (Obs. Paris Meudon/IAA Granada), and N. Szalai (Konkoly).

2.4.3.3 Status

The observations of the *TNOs are Cool!* program were completed in September 2012. Observations of the 132 TNOs, Centaurs and moons are available, but only $\sim$80 have been

[9]Most of the targets were assumed to have geometric albedos of 0.08. For objects with measured albedos, the measured values has been used.

reduced and published as of this writing. Additionally, thermal lightcurve observations have been obtained for (136108) Haumea, (20000) Varuna, (84922) 2003 VS2, and (208996) 2003 AZ84. As of March 2013, the *TNOs are Cool!* team has published its results in a total of 7 refereed publications, 3 of which were part of the Herschel Science Demonstration Phase (see Section C.1). More publications are in the pipeline.

Chapter 3

Thermal Modeling

The conclusions drawn in this work are mainly based on the results of thermal models. Thermal models simulate the temperature distribution on the surface of atmosphereless bodies and predict their thermal emission. Model fits to observed spectral energy distributions provide estimates of the most basic physical properties: diameter, d, and geometric albedo, p_V. Thermal models combine observational data from the optical and thermal–infrared.

In the course of this chapter, the basics of thermal modeling are discussed, and the most widely used thermal models, the standard thermal model (STM), the fast–rotating thermal model (FRM), and the near–Earth asteroid thermal model (NEATM), are reviewed. In this work, most thermal modeling results are obtained using the NEATM, which is widely accepted to be the most accurate and robust of the presented thermal models. Finally, the accuracy and limits of thermal models are discussed, as well as implications for the thermal modeling of NEOs and TNOs.

I am involved in the thermal modeling of flux densities derived from both the ExploreNEOs and the TNOs are Cool! programs and presented in this work. The model software utilized in the modeling is introduced in the following.

3.1 Thermal Emission of Atmosphereless Bodies

The following equations describing thermal emission are applicable to all atmosphereless bodies in the Solar System, irrespective of their size or distance to the Sun. The amount of solar flux $F_\odot$, that falls onto a body scales with its distance to the Sun, r (in AU), as

$$F_\odot = \frac{S_\odot}{r^2}, \tag{3.1}$$

with the Solar constant, $S_\odot = 1361$ W/m^2 (Kopp and Lean 2011), which is the amount of energy per unit area of the solar radiation integrated over the whole range of the electromagnetic spectrum at a distance of 1 AU from the Sun. The energy balance at the surface of a body,

$$F_\odot = F_{\text{refl}} + F_{\text{abs}}, \tag{3.2}$$

shows that part of the solar influx is being reflected, F_{refl}, and part is being absorbed, F_{abs}, leading to a heating of the surface. $F_{\text{refl}} = F_\odot \cdot A$, and accordingly $F_{\text{abs}} = F_\odot(1-A)$, with the bolometric Bond albedo, A (see Section 1.2.2).

Assuming an instantaneous thermal equilibrium between the incoming and outgoing amount of energy, the absorbed energy can be translated into a surface temperature using the Stefan-Boltzmann law,

$$F_{\text{abs}} = \epsilon\sigma T^4 = F_\odot(1-A) = \frac{S_\odot}{r^2}(1-A), \tag{3.3}$$

with the bolometric emissivity, ϵ, and the Stefan-Boltzmann constant, $\sigma = 5.67{\cdot}10^{-8}$ Wm^{-2} K^{-4}. The emissivity is a material constant, which equals unity for a black body and less for a real "grey" body. The surface temperature can then be derived as

$$T(\vec{x}) = \left[\frac{S_\odot(1-A)}{r^2\sigma\epsilon}\mu(\vec{x})\right]^{1/4}, \tag{3.4}$$

with the directional cosine $\mu(\vec{x})$ between the direction towards the Sun and the surface normal at the current position on the body, $\vec{x}$. The maximum surface temperature, where the surface normal is parallel to the direction towards the Sun and therefore $\mu = 1$, is called the "subsolar temperature", T_{SS}. The subsolar temperature occurs at the "subsolar point" in which the Sun is in the local zenith.

The thermal emission of a surface element of unit area at wavelength λ is described by Planck's law,

$$B_\lambda(T) = \frac{2hc^2}{\lambda^5}\frac{1}{\exp\left[hc/(\lambda k_B T)\right]-1}, \tag{3.5}$$

with the Planck constant h, the speed of light c, and the Boltzmann constant k_B. In the determination of the total emitted energy towards the observer, the surface of the object

is assumed to be that of a "Lambertian emitter", emitting diffuse light, i.e., there is no preferential direction of the emission. The thermal emission spectrum, or spectral energy distribution (SED), of the body is derived by integration of Equation 3.5 over the whole surface of the body, which has the effect of summing up the SEDs of the individual surface elements with their individual temperatures $T(\vec{x})$.

3.2 Basic Thermal Models

3.2.1 Model Parameters and the Modeling Routine

The basic idea of thermal modeling is to reproduce the spectral energy distribution (SED), represented by the thermal–infrared measurements of the observed body at different wavelengths, using a model SED. Figure 3.1 shows two examples. The model SED is constrained by the model parameters and the model specifications. The model specifications refer to simplifying assumptions of the individual model approaches presented in detail in Sections 3.2.2, 3.2.3, and 3.2.4.

Model Parameters

The model parameters can be split in two categories: input parameters and free model parameters.

Model Input Parameters. The input parameters are measured values that initialize the model and do not change in the course of the modeling process; there are: (1) the observation geometry, including the heliocentric distance, r, the distance to the observer, Δ, and the solar phase angle, α; (2) optical data, meaning the absolute magnitude, H, and the slope parameter, G; (3) the thermal–infrared data, in the form of measured flux densities, $F_{\mathrm{obs},i}$, at wavelength λ_i, and the respective uncertainties $\sigma_{\mathrm{obs},i}$, with the index of the measurement i.

Free Model Parameters. In order to fit the model SED to the observed one, the free model parameters are varied. The best–fit solution of the free model parameters represents the result of the thermal model. The number and nature of the free model parameters depend on the model of choice (see Sections 3.2.2, 3.2.3, and 3.2.4). The most obvious parameters that are varied in the fitting process are the diameter, d, and the geometric albedo, p_V. Both parameters are related to each other via $d = 1329 \cdot 10^{-H/5} / \sqrt{p_V}$ (Equation 1.4 on page 23), with the absolute magnitude, H, which leaves only one of the two parameters free and reduces the number of degrees of freedom of the fit problem.

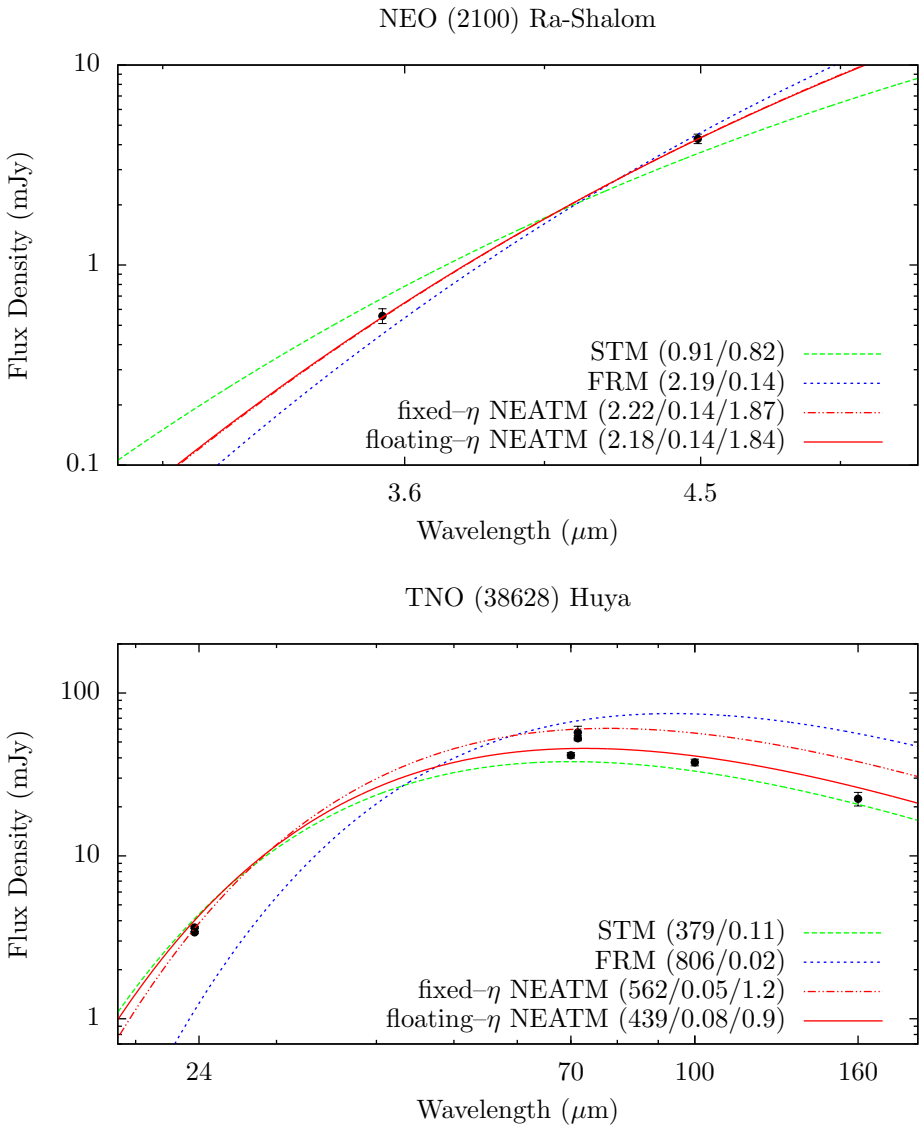

Figure 3.1 Model SEDs fitted to observations of two different objects using different thermal models (see Sections 3.2.2, 3.2.3, and 3.2.4). Black dots represent the measurements with respective error bars. The numbers in brackets after the model types give the respective model output parameters: diameter, geometric albedo, and η (when it was fitted to the data). **Top.** The NEO (2100) Ra-Shalom was observed in the framework of the *ExploreNEOs* program; its SED is constrained by two data points, which are both on the Wien slope of the Planck curve. The two NEATM models provide the best fit to the observations. The fixed η was derived from the linear $\eta(\alpha)$ relation found by Wolters et al. (2008). **Bottom.** The TNO (38628) Huya was observed by the *TNOs are Cool!* program; its SED covers a wide range including both wings of the Planck curve. In this case, the floating–η NEATM fit gives the best fit to the observations (Mommert et al. 2012). The coverage of both the Rayleigh and the Wien slopes constrains η sufficiently and enables a robust fit to the observations.

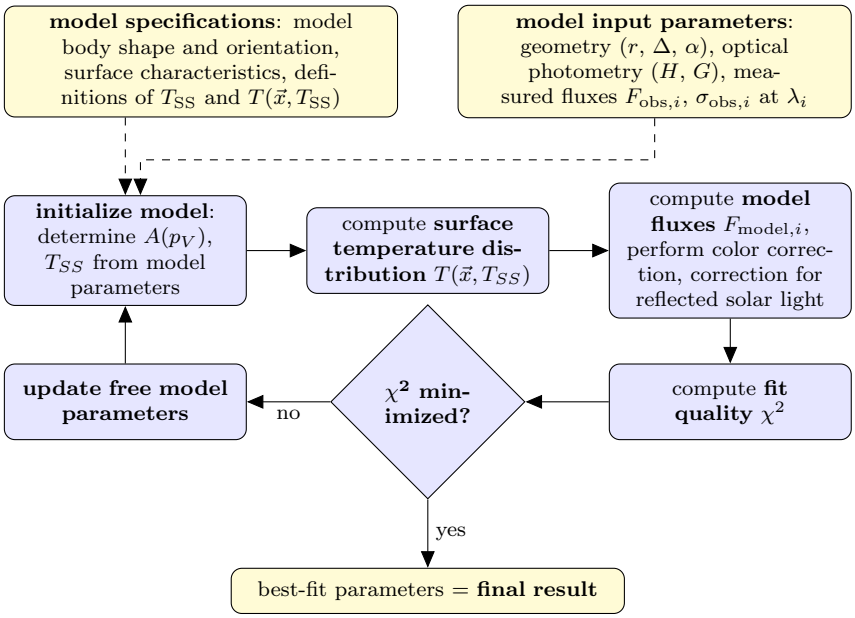

Figure 3.2 Thermal modeling flowchart. The sketch outlines the basic steps of thermal modeling, which are explained in Section 3.2. The model-specific parameters and specifications are discussed with the individual models.

Model Routine

In the following, a coarse outline, applicable to all of the below introduced thermal models, is given. For a graphical representation, see Figure 3.2.

Firstly, the model is initialized with the model input parameters and model specifications, as well as some default values for the free model parameters. In the same step, the bolometric Bond albedo, A, and the subsolar temperature, $T_{\rm SS}$, are computed. Using the specific model equations (introduced in Sections 3.2.2, 3.2.3, and 3.2.4), the surface temperature distribution and the flux densities of the model body are determined. The latter includes corrections of the measured flux densities for the instrument band–width (color correction, see Section A.2.2.2) and for reflected solar light (see Section 3.7.1.1), if necessary, based on the current set of free model parameters. The quality of the fit of the model SED to the observations is estimated using a χ^2 notation,

$$\chi^2 = \sum_i \left[\frac{F_{{\rm obs},i} - F_{{\rm model},i}}{\sigma_{{\rm obs},i}} \right]^2 , \tag{3.6}$$

where $F_{{\rm model},i}$ are the model fluxes at the same wavelengths λ_i as the observations. χ^2 is iteratively minimized to find the best–fit model SED. Note that Equation 3.6, as it is defined, weights each flux density measurements with its uncertainty; measurements with high signal–to–noise ratios (SNR) have a large impact on the shape of the model SED, whereas low–SNR measurements have litte impact on the model SED.

The implementation of the thermal model code utilized in this work is outlined in Section 3.4.

In the following sections, the most common thermal models are discussed and their equations are derived from the equations provided in Section 3.1.

3.2.2 The Standard Thermal Model (STM)

The "standard thermal model" (STM) (Morrison and Lebofsky 1979; Lebofsky et al. 1986, and references therein) was designed to derive diameters and albedos from single–wavelength observations of large main belt asteroids in the thermal infrared. It is based on the first radiometric models by Allen (1971), Matson (1971b), and Morrison (1973). The STM assumes the model body to

- be spherical (which is a good approximation for many large main belt asteroids),
- to rotate slowly or to be non–rotating ($P \to \infty$) and/or to have a vanishing thermal inertia ($\Gamma \to 0$), and to
- be observed at opposition ($\alpha = 0$, equivalent to a "full moon").

Mathematical Description. As a result of the first two assumptions, the surface is perfectly described by being in instantaneous thermal equilibrium with the insolation such that the temperature at the subsolar point is

$$T_{SS} = \left[\frac{S_\odot (1 - A)}{r^2 \eta \sigma \epsilon} \right]^{1/4}, \tag{3.7}$$

with the "beaming parameter" η and all other parameters as in Equation 3.4, from which this equation is derived. The beaming parameter allows for a modulation of the subsolar temperature and enables for a partial compensation of some of the simplifications of the STM compared to a real object, e.g., the infrared–beaming effect (see Section 1.2.7). Note that $\eta < 1$ increases the subsolar temperature, whereas $\eta > 1$ decreases it. A full discussion of the physical implications of the beaming parameter is given in Section 3.5. A comparison between diameters of main belt asteroids derived from occultation measurements and thermal modeling revealed significant discrepancies. The beaming parameter was introduced to partially compensate for effects that occur in "real" small bodies, like the beaming effect in a first–order approximation: Lebofsky et al. (1986) empirically calibrated the beaming parameter in their "refined STM" with $\eta = 0.756$ using diameters derived from occultation observations of (1) Ceres and (2) Pallas.

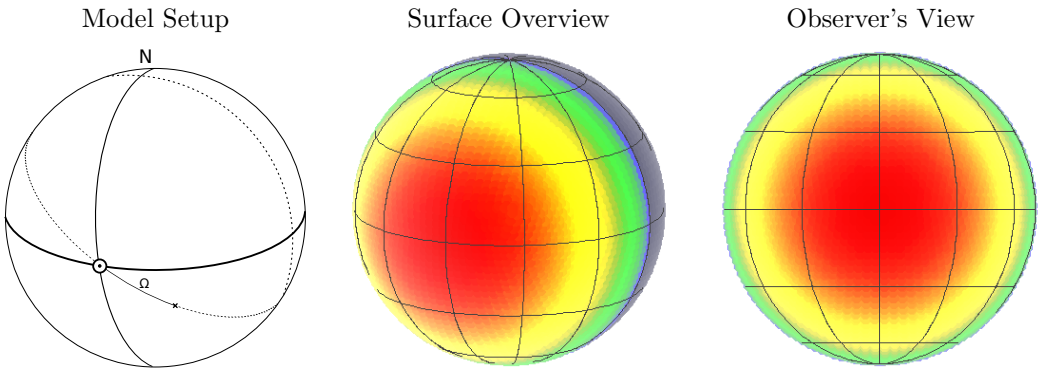

Figure 3.3 Illustration of the Standard Thermal Model (STM). **Left.** The sketch shows the spherical model body. Its northern pole is highlighted by "N", the equator is indicated by the thick horizontal curve. The subsolar point is depicted by the Sun symbol, $\odot$. The dotted curve at the top right of the sphere indicates the terminator, the division between day and night side of the body. In the STM, the temperature at any point on the surface (indicated by a cross) is a function of its angular distance to the subsolar point, Ω, indicated by the continuous portion of a great circle passing through both points (dotted curve). **Center.** The plot shows the surface temperature distribution produced by the STM using the same view as the model setup sketch to the left. The temperature distribution is described best as concentric isothermal circles that are centered on the subsolar point. The subsolar point, where the solar incidence is perpendicular to the surface, is the hottest point on the body. The temperature drops towards the terminator to zero. **Right.** The STM uses a fixed $\alpha = 0$, i.e., the observer always faces the subsolar point. The integration of Equation 3.9 is performed over that hemisphere that is centered on the subsolar point.

In each point of the surface with an angular distance Ω from the subsolar point, described by the angle between the solar incidence and the local zenith, the surface temperature is expressed by

$$T(\Omega) = \begin{cases} T_{SS}\cos(\Omega)^{1/4}, & \text{if } \Omega \leq \pi/2 \text{ (Sun above local horizon)} \\ 0, & \text{if } \Omega > \pi/2 \text{ (Sun below local horizon).} \end{cases} \tag{3.8}$$

The night side temperature of 0 K follows from the aforementioned assumptions; the night side emits no thermal radiation. A plot of an example STM temperature distribution is shown in Figure 3.3.

The model flux at wavelength λ follows from the combination of Equations 3.5 and 3.8 and integration over the body's surface A,

$$\begin{aligned} F_\lambda &= \frac{\epsilon}{\Delta^2}\int_A B_\lambda(T(\Omega))\cos(\Omega)dA \\ &= \frac{\epsilon d^2}{\Delta^2}\frac{\pi hc^2}{\lambda^5}\int_0^{\pi/2}\frac{\cos\Omega\sin\Omega\, d\Omega}{\exp\left[hc/(\lambda k_B T(\Omega))\right]-1}, \end{aligned} \tag{3.9}$$

with a correction for the distance of the observer, $1/\Delta^2$, and the emissivity of the object, ϵ. The model body's effective diameter is d.

Free Model Parameters. Designed for the application on single–band data, the STM has only one free model parameter that is used to fit the model SED to the observed SED: the model parameter can be chosen as either the diameter or the albedo, since both parameters are linked via $d = \frac{1329}{\sqrt{p_V}}10^{-H/5}$ (Equation 1.4 on page 23) to the absolute magnitude, H, and are therefore equally applicable as fitting parameters.

Linear Phase Correction. The STM assumes observations to have taken place during opposition ($\alpha = 0$), which is a useful approximation for TNOs and some main belt asteroids, but rarely the case for NEOs, giving rise to discrepancies: the model flux is derived by integration over that hemisphere that is centered at $\alpha = 0$, which does not necessarily match that part of the sphere that is actually illuminated (if $\alpha \neq 0$). Consequentially, the STM tends to overestimate the thermal flux emitted by the object, leading to an overestimation (underestimation) of the effective diameter (albedo). To correct for this effect, Lebofsky and Spencer (1989) apply a linear phase coefficient of 0.01 mag/°(Matson 1971a) to the observed thermal fluxes to approximately normalize them to zero phase angle.

Discussion. The STM was mainly applied in the determination of diameters and albedos of main belt asteroids that were observed by IRAS (see Section 2.1.2.1). Due to their large distances, main belt asteroids are usually observed at low phase angles, leading to minor deviations from the $\alpha = 0$ assumption, which could be compensated for by using the

linear phase coefficient correction. Observations of NEOs, however, usually take place at much larger solar phase angles, leading to significant discrepancies. The most significant disadvantage of the STM concerning all kinds of small bodies is its fixed value of the beaming parameter, η, leading to a limited degree of freedom in fitting the observed SED and thus compensating for thermal effects as discussed in Section 1.2.7. The NEATM (Section 3.2.4) represents an enhancement of the STM, compensating for both of the aforementioned disadvantages.

3.2.3 The Fast-Rotating Model (FRM)

The "fast–rotating model" (FRM Lebofsky and Spencer 1989) or "isothermal latitude model" (ILM) varies significantly in its model assumptions from the STM:

- The FRM model body is assumed to be spherical in shape,
- to spin rapidly ($P \to 0$) and/or to have a thermal inertia that is very high ($\Gamma \to \infty$), and
- to have the Sun in the equatorial plane.

Mathematical Description. The resulting temperature distribution of the FRM differs significantly from that of the STM. Owing to the aforementioned assumptions, the temperature distribution is only a function of latitude. Considering an isolatitudinal belt at latitude θ with a width of $d\theta$, the solar energy that is absorbed at the day side of the belt has to be re–emitted over the whole area of the belt:

$$\frac{(1-A)S_\odot}{r^2} \cdot \cos(\theta) \cdot \frac{d^2}{2} \cos(\theta)\ d\theta = \epsilon\sigma T^4 \cdot \pi \frac{d^2}{2} \cos(\theta)\ d\theta.$$

The above equation derives from Equation 3.3. The left–hand side describes the absorption of solar energy in the belt with a factor of $\cos(\theta)$ from the solar incidence angle at latitude θ, and a term $d^2/2\cos(\theta)\ d\theta$, which is the area element at latitude θ, including a factor of $\cos(\phi)$ for the solar incidence angle in longitude ϕ. The right–hand side describes the emission of energy over the entire belt with the area element $\pi\frac{d^2}{2}\cos(\theta)\ d\theta$ at latitude θ. The temperature distribution and subsolar temperature can be expressed as

$$T(\theta) = T_{SS}\cos(\theta)^{1/4}, \text{ and} \tag{3.10}$$

$$T_{SS} = \left[\frac{S_\odot(1-A)}{r^2\pi\sigma\epsilon}\right]^{1/4}, \text{ respectively,} \tag{3.11}$$

following the model setup in Figure 3.4, which also shows its surface temperature distribution. Similarly to Equation 3.9, the thermal flux per wavelength λ that is emitted from

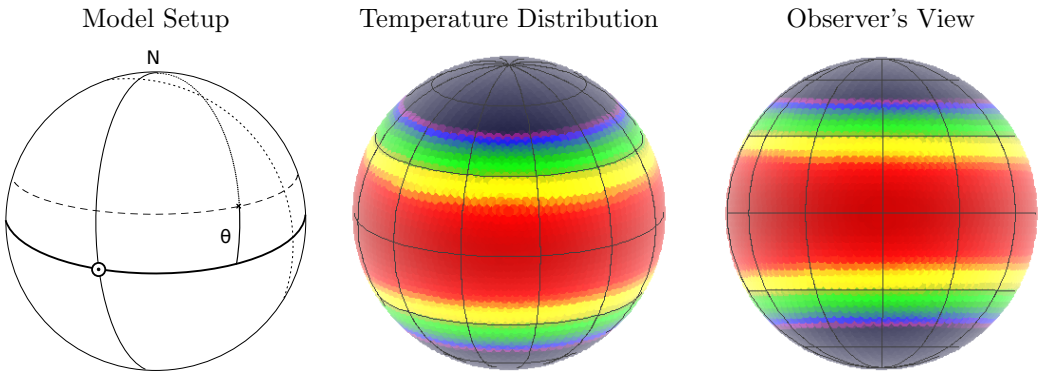

Figure 3.4 Illustration of the Fast Rotating Model (FRM). **Left.** The sketch shows the spherical model body. For a description of the different symbols and curves, cf. Figure 3.3. In the FRM, the surface temperature is a function of the latitude θ, only. **Center.** The FRM has isothermal latitudes. The surface temperature peaks at the equator and falls to zero towards the poles. **Right.** The observer sees a band–like temperature distribution on the model body. Phase angle has no effect on the observed temperature distribution as a result of the symmetry.

the observer–facing portion of the surface A results as

$$\begin{aligned} F_\lambda &= \frac{\epsilon}{\Delta^2} \int_A B_\lambda(T(\theta)) \cos(\theta) dA \\ &= \frac{\epsilon d^2}{\Delta^2} \frac{2hc^2}{\lambda^5} \int_0^{\pi/2} \frac{\cos(\theta)^2 \sin(\theta)\, d\theta}{\exp\left[hc/(\lambda k_B T(\theta))\right] - 1}. \end{aligned} \tag{3.12}$$

Free Model Parameters. As in the case of the STM, the FRM has only one free model parameter, which is either the diameter or albedo.

Discussion. The FRM was designed for the thermal modeling of fast–spinning objects or objects with high thermal inertia. The FRM fits the observational data properly only in a small number of cases (Delbo' 2004) and suffers from the fact that the color temperature of the model SED is fixed to the subsolar temperature, as in the case of the STM. In most observed objects, the model fits of the NEATM have proven to be superior to the FRM fits.

3.2.4 The Near–Earth Asteroid Thermal Model (NEATM)

The "near–Earth asteroid thermal model" (NEATM, Harris 1998) is the most commonly used asteroid thermal model and is also applied throughout this work. It was originally designed for the use on NEOs, but is applicable to all kinds of atmosphereless bodies in the Solar System. The model setup is based on the STM and shares its assumptions concerning the physical properties of the model body:

- the NEATM model body is spherical in shape,

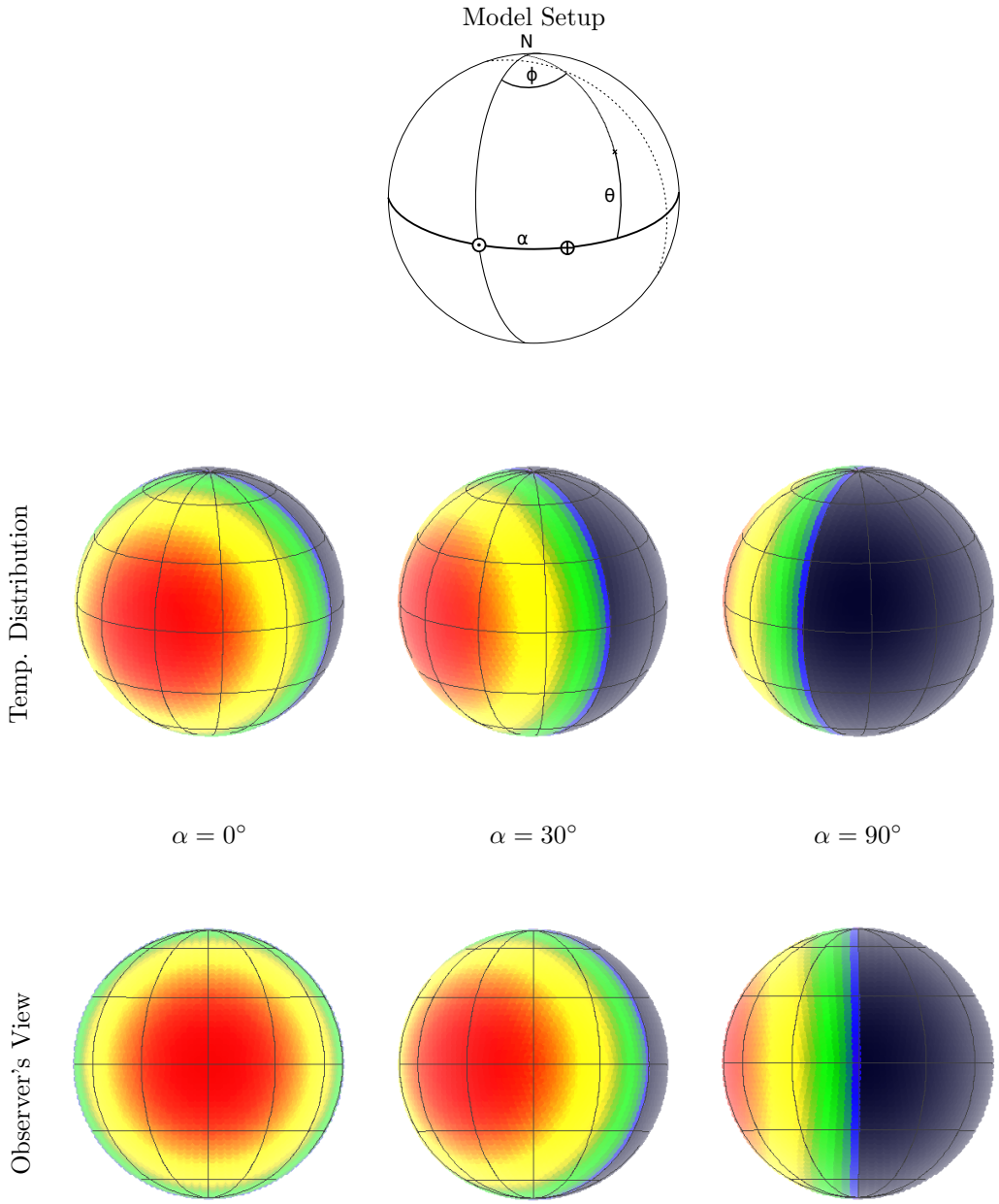

Figure 3.5 Illustration of the Near–Earth Asteroid Thermal Model (NEATM). **Top.** The sketch shows the definition of the longitudinal and latitudinal angles, ϕ and θ, respectively, for any point on the surface (indicated by a cross). The Earth symbol, $\oplus$, symbolizes the sub–observer point, meaning that point on the surface, where the observer is in the zenith. The solar phase angle α is the angular separation between the subsolar and sub–observer points along the equator. **Top Row.** The surface temperature distribution of the NEATM for different values of α, using the same view as the model setup sketch. All plots show the temperature drop towards the terminator. The temperature on the night side of the model body is defined as zero. **Bottom Row.** The observer's view of the temperature distribution for different values of α. In the case of $\alpha = 0$, the geometry of the temperature distribution is equal to that of the STM (Figure 3.3). For increasing values of α, the observer sees a larger portion of the non–illuminated and therefore cold night side of the model body.

- assumed to rotate slowly or to be non–rotating ($P \to \infty$), and/or to have a vanishing thermal inertia ($\Gamma \to 0$).

The differences of the NEATM compared to the STM are:

- the solar phase angle α is taken into account in the integration of the emitted flux density, and
- the use of η as a free fitting parameter.

Mathematical Description. The subsolar temperature, T_{SS}, of the NEATM equals that of the STM (Equation 3.7). The model is set up in such a way as to have both the subsolar and the sub–observer points on the equator, where $\theta = 0$. The subsolar point is located at $\phi = 0$, the sub–observer point at $\phi = \alpha$ (cf. Figure 3.5). The surface temperature of the NEATM is defined as:

$$T(\phi,\theta) = \begin{cases} T_{SS}\cos(\phi)^{1/4}\cos(\theta)^{1/4}, & \text{if}\cos(\phi)\cos(\theta) \geq 0 \text{ (Sun above local horizon)} \\ 0, & \text{otherwise (Sun below horizon).} \end{cases} \tag{3.13}$$

The integration of the emitted model thermal flux at wavelength λ takes into account the observation geometry by offsetting the hemisphere over which the temperature distribution is integrated by the amount of the solar phase angle α, leading to an additional factor of $\cos(\phi - \alpha)$ in the surface integral compared to Equation 3.9:

$$\begin{aligned} F_\lambda &= \frac{\epsilon}{\Delta^2}\int_{\theta=-\frac{\pi}{2}}^{\frac{\pi}{2}}\int_{\phi=-\frac{\pi}{2}+\alpha}^{\frac{\pi}{2}+\alpha} B_\lambda(T(\phi,\theta))\cos(\theta)\cos(\phi-\alpha)\; d\phi\; cos(\theta)\; d\theta \\ &= \frac{\epsilon d^2}{\Delta^2}\frac{hc^2}{\lambda^5}\int_{\theta=0}^{\frac{\pi}{2}}\int_{\phi=-\frac{\pi}{2}+\alpha}^{\frac{\pi}{2}+\alpha}\frac{\cos(\theta)^2\cos(\phi-\alpha)\; d\phi\; d\theta}{\exp\left[hc/(\lambda k_B T(\theta))\right]-1}. \end{aligned} \tag{3.14}$$

Free Model Parameters. In contrast to the STM and the FRM, the NEATM has two free model parameters: either the effective diameter, d, or the albedo, p_V, and the beaming parameter, η. As defined in Equation 3.7, η changes the color temperature of the model SED, offering one more degree of freedom in fitting the observed SED. η allows for a first–order approximation of complex thermal effects (see Section 1.2.7 for a introduction) on the surfaces of small bodies. The impact of the individual effects on η are the subject of Section 3.5.

In order to use η as a free–floating fitting parameter, the observed SED has to be constrained by at least 2 measured thermal flux densities. This approach is called a "floating–η" fit. If accurate measurements at only one wavelength are available, a fixed value of η has to be used, which is called a "fixed–η" fit. Usually, floating–η fits are more robust and return better results (see the more detailed discussion in Section 3.6).

Discussion. The NEATM, originally designed for the use on NEOs, has proven its applicability to all kinds of atmosphereless bodies in the Solar System (e.g., Müller et al. 2010; Trilling et al. 2010; Harris et al. 2011; Mainzer et al. 2011b) and its superiority over the results of the other thermal models. The main reason for the better agreement of the NEATM results with reality is caused by the use of η as a fitting parameter, significantly improving the agreement of the measured and modeled SEDs. Furthermore, the additional degree of freedom allows for a partial compensation of thermal effects like thermal inertia and/or infrared beaming (see Section 1.2.7).

Nevertheless, the NEATM is not flawless: the model assumes the thermal emission of the night side to be zero, which is not the case for a real body. The finite thermal inertia of the surface material leads to a residual emission from the night side, which is neglected in this model. Consequentially, the thermal model flux density is underestimated, resulting in an overestimation of the diameter and an underestimation of the albedo. This problem and the approach to a possible solution are the subject of Section 6.2.3.

3.3 Uncertainty Assessment

In order to address the question of the accuracy of thermal modeling results, a proper assessment of their uncertainties is necessary. An analytical uncertainty assessment of the output parameters of thermal models, e.g., using Gaussian error propagation, is extremely complicated due to the entanglement of the individual parameters, not only through Equation 1.4. A first step is taken in Section B.2.

A simpler and more intuitive way of assessing the uncertainties of the diameter, albedo, and, if used as a free model parameter, η, uses a Monte–Carlo approach: a large set of synthetic model bodies ($N \sim 1000$) with randomized input parameters are generated, each of which is then modeled, leading to a set of output parameters. Uncertainties are derived from the distributions of the output parameter ensembles. In the framework of NEATM fitting, the method was introduced by Mueller et al. (2011); more details are given below.

Randomization. The uncertainties of the input parameters are expected to be normally distributed. Hence, a routine is used that produces random numbers following a Gaussian distribution around a mean value with a pre–defined standard deviation. The mean of the distribution equals the nominal value of the respective parameter, and the 1σ standard deviation usually equals its 1σ uncertainty estimate.

Parameters that are randomized typically are the flux density measurements $F_{\mathrm{obs},i}$ and the absolute magnitude H of the target. In the case of a fixed–η fit, where η is used as a input parameter, η is randomized as well. In floating–η fits, η is one of the free model parameters and thus determined in the modeling process. No randomization is usually required for the geometric parameters, r, Δ, and α, the uncertainty of which is negligible.

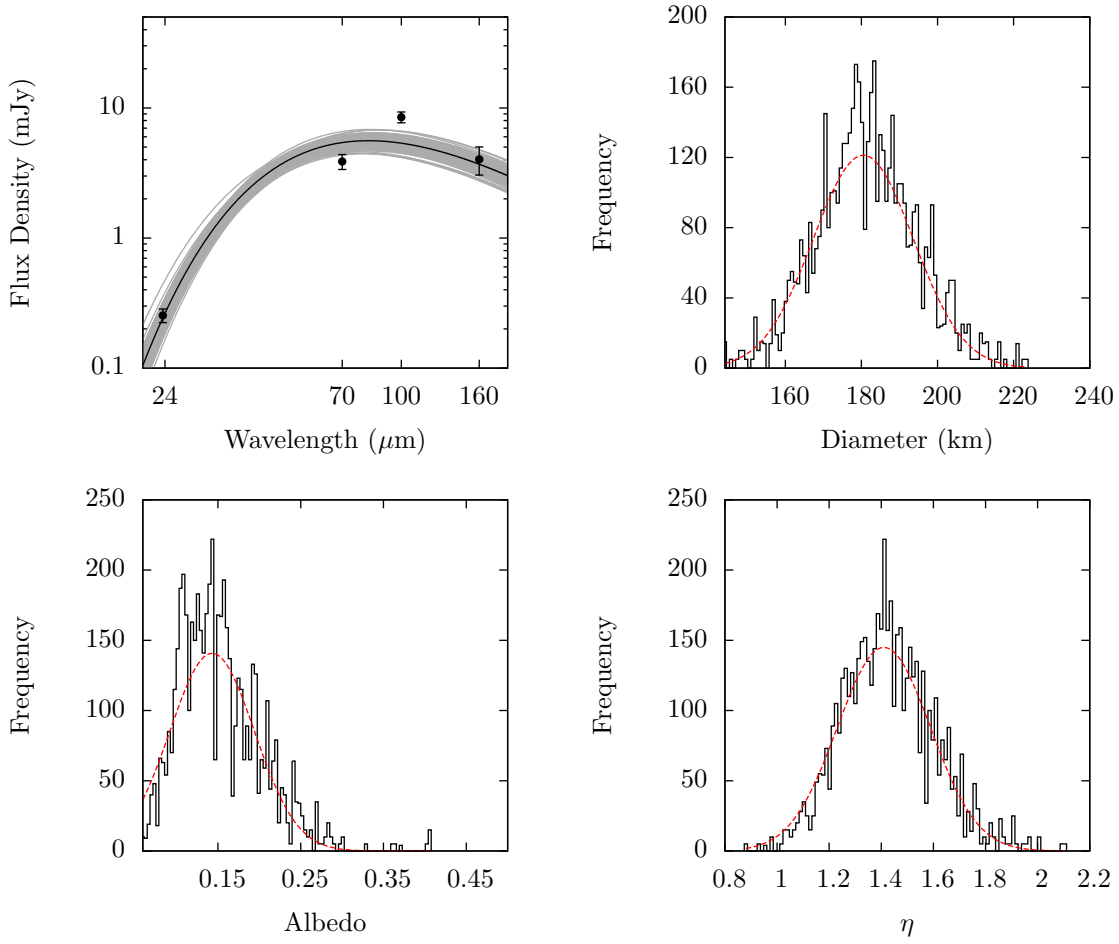

Figure 3.6 Illustration of the Monte–Carlo uncertainty assessment method. The top left plot shows the measured data points, the best–fit model of the nominal input parameters (black line) and the ensemble of synthetic model fits based on randomized input parameters (grey lines). The other three plots show the histograms of the output parameters, namely diameter, albedo and η. For comparison, a normal distribution (dashed red line) based on the results of the Monte-Carlo analysis has been plotted into each histogram: the agreement with the diameter and η histograms is good, whereas the albedo histogram is skewed. The modeled object is 2000 GN171; the results of the best–fit and the Monte–Carlo method are $d = 181.2^{+12.7}_{-12.5}$ km, $p_V = 0.14^{+0.06}_{-0.04}$, and $\eta = 1.41^{+0.19}_{-0.17}$ (Mommert et al. 2012).

Determination of the Uncertainties. After modeling each of the synthetic objects, the nominal result of each output parameter is determined as the median of the respective distribution, which usually agrees very well with the best–fit modeling results using the nominal input parameter. The uncertainties are derived as the values of the two outermost data points of that portion of the ensemble that includes 68.2% of the individual measurements that are closest to the median. This approach allows for the determination of asymmetric uncertainties, which are often encountered in albedo uncertainties. Note that this definition equals the definition of the standard deviation in the case of a symmetric distribution of the synthetic object parameters.

Example. Figure 3.6 shows an example of the results of the method. The top left panel shows the SEDs of the best–fit models of the nominal input data and of the ensemble of the randomized synthetic model bodies. The latter cover a broad range around the nominal best–fit model. The other panels show the diameter, albedo, and η histograms, respectively. While the diameter histogram shows a symmetric and close–to normal distribution, the albedo distribution is skewed. Hence, the diameter uncertainty is rather symmetric, whereas the albedo uncertainty is asymmetric. A better description of albedo uncertainties is suggested in Section B.2.

3.4 Model Implementation – The `model` Software

The structure of the thermal modeling software utilized in this work is based on the scheme presented in Section 3.2.1 and the flowchart in Figure 3.2 on page 73. The "`model`" code was implemented in a modular fashion, written in the programming language C, which provides excellent computation speed. `model` was written and debugged under RedHat Linux 6.4, using the gcc compiler (version 4.4.7), but has also been compiled and run on various other Linux systems.

Running `model`. The software uses a command–line interface, offering a large degree of flexibility. Model input parameters are provided in the form of an ASCII table file, the columns of which are: object name, geocentric distance, heliocentric distance, solar phase angle, absolute magnitude, slope parameter, wavelength, measured flux density, and its uncertainty. Multi–band observations of the same object are entered in the table one band per line, each line starting with the same object name, which allows the software to properly identify all observations of the same object. The necessary command–line arguments include the input filename and a flag for the desired thermal model (STM, FRM, NEATM) and the modeling approach (floating–η/fixed–η NEATM, default η/generic η STM, etc.). Optional arguments allow for a modification of preset model values like user–defined values of η, the limits of the allowed range of η, and the reflectance ratio $RR_{\mathrm{IR/V}}$, which is used in the correction for reflected solar light (see Section 3.7.1.1). Furthermore,

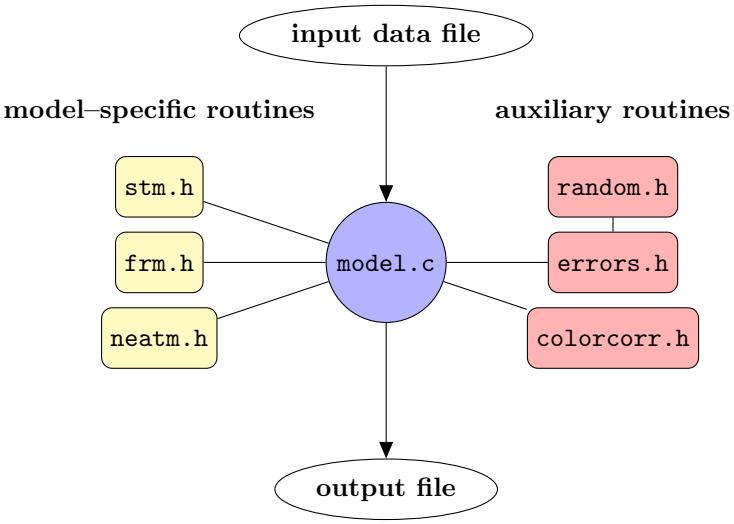

Figure 3.7 Schematic overview of the thermal modeling routine used in this work. For a detailed description, see Section 3.4.

command–line arguments for optional subroutines can be enabled like the filtering of the input data based on the SNR of the flux density measurements, plotting of the best–fit model SED, subtraction of reflected solar light, and on–the–fly color correction (see below).

Structure of `model`. The main routines of the `model` software are included in the file "`model.c`". Auxiliary routines, providing additional functionality and flexibility, are linked to `model.c` as C header files as shown in Figure 3.7. `model.c` contains subroutines for file access, data handling, as well as all basic fitting routines, and the χ^2 computation and comparison routines. Model input parameters are read from the input file and stored in a structure called `ASTEROID`, which contains the input parameters and free model parameters of all observations and all objects. Observations of the same object are grouped together using a pointer variable inherent to the `ASTEROID` structure that points to the next observation of the respective object or to the NULL pointer, if no further observations are available. The `ASTEROID` variable is passed to the subroutines of the `model` software and modified in each initialization step (cf. Figure 3.2). The advantage of this approach is that data with different observational geometries can be combined in the same thermal model, since parameters like the subsolar temperature can be derived for each epoch separately.

All model–specific routines like the computation of the surface temperature distribution and the thermal fluxes of the model body have been sourced out into C header files, namely `stm.h`, `frm.h`, and `neatm.h`. The model–specific routines are "called by reference", i.e., the necessary function of the desired model is passed as an input parameter to the fitting routines, improving the readability and flexibility of the code. Additional thermal models can be integrated into the existing code without the necessity to change the data handling or fitting routines. Other subroutines, like the uncertainty assessment

or the iterative color correction have been outsourced as well, improving the readability of the code.

`model` **Workflow.** After reading in the model input parameters, the `ASTEROID` variable is passed to the fitting routines. Subtraction of reflected solar light, if necessary, is performed after initialization of the `ASTEROID` structure. In the case of a STM, FRM or a fixed–η NEATM fit, only one fitting step has to be performed: the single free model parameter, d is used here, is varied to minimize χ^2 (Equation 3.6 on page 73). Iterative color correction coefficients are determined in each d–iteration step using a polynomial approximation[1], or are calculated on–the–fly, if desired. In the case of a floating–η NEATM fit, η is varied as well, introducing an additional fitting step. Each iteration in η requires a fit of d, making floating–η fits computationally more expensive than fixed–η and other model fits. After finding the best–fit free model parameters, the model SED as a function of the wavelength may be written in table format, covering the wavelength range of the measured bands, if desired. The best–fit model parameters are written in a file and printed on the screen.

The integration of the Planck equation (Equation 3.5 on page 70) is performed using the Romberg method (see Press et al. 1992), which provides excellent robustness and better precision than simple numerical integration algorithms. In order to find the minimum χ^2, a simple and robust bisection method is applied until a relative accuracy of $\epsilon = 10^{-3}$ in the respective parameter (d or η) is reached.

`model` **Results.** The results of `model` were checked against existing models, e.g., Trilling et al. (2008), Trilling et al. (2010), Delbo' et al. (2007) etc., as well as the default *Explore-NEOs* thermal modeling pipeline (see Section 2.2.3). The results typically agree in both diameter and albedo to within <1%. A comparison with the results of Trilling et al. (2010) and Mueller et al. (2011) reveals average fractional systematic discrepancies in diameter and albedo of 0.2% and 0.08%, respectively. The average fractional statistical discrepancies in diameter and albedo are both 0.2%. The discrepancies are mainly caused by the different adopted values of physical constants and the different numerical methods used in the implementation of the models.

The runtime of `model` depends on the number of objects and the number of observations per object: STM and FRM calculations, requiring only one fitting step, take only a few seconds, whereas a floating–η NEATM model can take up to 20 seconds per object if 5 or more observations are available. The uncertainty assessment is the most time–consuming function and can take up to several tens of minutes for a single object. The aforementioned

[1] Approximations of the color correction factors were determined by fitting polynomials of the 3–rd/4–th order to calculated color correction coefficients as a function of the subsolar temperature. The fit of the polynomials to the calculated coefficients, and also to the coefficients tabulated in the respective instrument handbooks, is very good. Typical deviations to properly calculated coefficients are <2%, leading to negligible deviations in the results. The advantage of this approach is the significantly shorter runtime of the model code.

runtimes were determined on a Quad–Core 3 GHz desktop computer with RedHat Linux 6.4 and 3.6 GBytes of RAM.

3.5 The Physical Meaning of the Beaming Parameter η

The beaming parameter η is a semi–empirical measure that has been introduced to modulate the subsolar temperature T_{SS} of the STM and the NEATM (Equation 3.7 on page 74). η varies the color temperature of the model SED (Equation 3.5 on page 70, Equation 3.9 on page 76, and Equation 3.14 on page 80): $\eta > 1$ decreases the subsolar temperature and shifts the model SED to longer wavelengths; accordingly, $\eta < 1$ increases the subsolar temperature. Variations in the color temperature of the measured SEDs are caused by a number of thermal effects like thermal inertia, spin properties, and the beaming effect (see Section 1.2.7), to which η provides a 0–th order correction. The variation of the model SED's color temperature allows for additional freedom in fitting real target SEDs, which explains the success of the NEATM over the other thermal models.

The different thermal effects are introduced in Section 1.2.7. In the following, the impact of the effects on η are qualitatively discussed.

- *Surface Roughness (Beaming Effect)*: A high degree of surface roughness gives rise to infrared beaming effects: at low (high) solar phase angles, the thermal–infrared emission is stronger (fainter) compared to that of a smooth surface (see Section 1.2.7), causing $\eta < 1$ ($\eta > 1$), respectively. Hence, the beaming effect leads to an increase of η with phase angle α.

- *Thermal inertia and spin period*: Thermal inertia leads to day–side surface temperatures that are lower than those derived from instantaneous thermal equilibrium, leading to $\eta > 1$. Vice versa, thermal inertia leads to night–side temperatures that are higher than assumed from thermal equilibrium. The impact of the spin period is similar to that of the thermal inertia: in the case of a fast–rotating body, the duration during which each surface element absorbs sunlight is short, which lowers the surface temperature ($\eta > 1$) on the day–side compared to an instantaneous thermal equilibrium. On the night–side, however, the surface elements cool down slower compared to a slow rotater; hence, the surface temperature is here higher compared to the thermal equilibrium case. Thus, the effects of thermal inertia and spin period on η are tightly linked.

- *Spin axis orientation*: Objects where the Sun is located in the spin axis (subsolar latitude of $\pm 90°$) have one hemisphere illuminated all the time, whereas the other hemisphere is dark all the time. In this case, the spin period and the thermal inertia have no effect, since the temperature in any point of the surface is fixed (this configuration is equal to a perfect STM–case). For subsolar latitudes lower than $90°$,

the situation is more complicated and highly depends on the thermal inertia and the spin period.

Note that in the case of a real body, all of the aforementioned effects are present at the same time. Thus, without additional information on the thermal and spin properties, it is impossible to make deductions on thermal inertia or surface roughness on the basis of η.

The special case of $\eta = 1$ is consistent with a body that is described by the assumptions of the STM or NEATM: a body with a smooth, zero–thermal–inertia surface. The complexity of the thermophysical problem prohibits the disentanglement of η into its individual contributions without additional information on the body. However, the thermophysical problem can be addressed in its (nearly) full complexity using a " thermophysical model". Thermophysical models take into account the real shape of the object, its spin axis orientation and period, as well as material and surface properties like the thermal inertia and surface roughness, respectively. The surface temperature distribution is derived by solving the heat conduction equation, the boundary conditions of which are given by the isothermal interior of the model body, and the insolation and emission of thermal energy from the surface. Detailed descriptions of thermophysical models can be found in Spencer et al. (1989); Lagerros (1996); Mueller (2007).

Using a thermophysical model, I explore the physically meaningful range of η. Taking into account the aforementioned physical parameters affecting η, flux densities of a high–η and a low–η case can be determined. The low–η (high–η) body is simulated by assuming a high (low) surface roughness, low (high) thermal inertia, and an orientation of the spin axis of the model body towards the observer (perpendicular to the line–of–sight). Thermal modeling of the two cases using a floating–η NEATM model results in a range of $0.6 \leq \eta \leq 2.7$, for $\alpha = 0$ (Spencer et al. (1989) and Delbo' (2004) obtain similar results). Values of η outside this range can be regarded unphysical, and respective model fits are likely to be unrealistic. Note that the above results were obtained for phase angle $\alpha = 0$. As shown below, η increases with phase angle, leading to an absolute upper limit of η for all phase angles $\alpha > 0$ of $\eta \leq \pi$, which is represented by the FRM (see Section 3.2.3).

An empirical correlation between η and the solar phase angle, α, has first been reported by Delbo' et al. (2003) ($\eta = 1.0$ for $\alpha < 45°$, $\eta = 1.4$ for $\alpha \geq 45°$) and later revised by Wolters et al. (2008) ($\eta = (0.013 \pm 0.004)\alpha + 0.91 \pm 0.17$) and Mainzer et al. (2011b) ($\eta = (0.00963 \pm 0.00015)\alpha + 0.761 \pm 0.009$). Qualitatively, η increases with α, which is a result of the beaming effect (see Section 1.2.7): rough surfaces emit more thermal radiation in the direction of the Sun ($\alpha = 0$) than smooth surfaces, but less so in other directions ($\alpha \gg 0$). Consequentially, η increases with α.

3.6 The Accuracy and Limits of Thermal Modeling

Thermal models use model assumptions that drastically simplify their formulation and computability at the cost of losing precision in the description of the body and the physics. A detailed mathematical analysis of the accuracy of thermal models is a very complex task, given the entanglement of the model's input and free model parameters. A straight–forward method using a Monte–Carlo approach is presented in Section 3.3.

In the following, I discuss some basic principles that allow for a lower–limit determination of the uncertainties.

Accuracy. The surface temperature of Solar System small bodies is only a weak function of their albedo. Thus, their thermal emission, is also a weak function of the albedo, but a strong function of the diameter (the flux density scales with d^2 in Equations 3.9, 3.12, and 3.14). On the other hand, the reflected solar light is proportional to the albedo. Hence, the thermal emission of a small body constrains its size; the diameter and optical light together constrain its albedo (Harris and Harris 1997, which follows from Equation 1.4 on page 23). Note that diameter uncertainties lead to additional uncertainties in albedo due to Equation 1.4. Using the aforementioned relation, the following estimates are legitimate:

- From Equations 3.9, 3.12, and 3.14, it follows that the thermal flux density, F, scales as $F \propto d^2$. Using Gaussian error propagation, one obtains

$$\frac{\sigma d}{d} \geq \frac{1}{2}\frac{\sigma F}{F}.$$

  Hence, a 20% uncertainty in the thermal flux accounts for a 10% uncertainty in diameter.

- Since the albedo is mainly constrained by the optical brightness, one can simplify Equation 1.4 to $p_V \propto 10^{-\frac{2}{5}H}$. As a rule–of–thumb: a change in H of 10% causes a simultaneous change in p_V of about 10% as well. Note that albedo uncertainties caused by uncertainties in H are on top of uncertainties introduced by the diameter. Hence, the aforementioned relation provides only a lower limit on the albedo uncertainty.

The accuracy of thermal models was tested against sophisticated thermophysical models. The approach uses a thermophysical model to produce thermal flux densities for virtual objects. The thermal model is applied to determine the physical properties of the virtual body and the results are compared with the input parameters of the thermophysical model. Wright (2007) has tested the accuracy of the NEATM using such a method. He found NEATM diameters to be accurate within 10% (RMS) for phase angles $\alpha \leq 60°$, even if the object is of elliptical shape. The accuracy decreases significantly for larger

phase angles. The diameters and albedos of the *ExploreNEOs* program were estimated to be accurate within 20% and 50%, respectively (Harris et al. 2011, also see Section B.1).

The accuracy of thermal models is also the subject of Section B.2.

Limits of Thermal Modeling. The applicability of thermal models is limited to bodies that do not have an atmosphere, since atmospheres significantly influence the absorption and storage of thermal energy, and thus lead to surface temperature distributions that differ from those of simple thermal models. For instance, thermal models fail for (134340) Pluto (see Mommert et al. 2012, and Section 5.1), which is known to have an atmosphere (Stern and Trafton 2008).

Naturally, the accuracy of thermal models is limited by the accuracy of the observational data. Low–SNR thermal flux density data are barely useful to constrain the physical properties of a body.

3.7 Thermal Modeling Caveats

In the following sections, caveats of the thermal modeling of NEOs and TNOs, both of which are investigated as part of this work, are discussed.

Note that I discuss in the following reflected solar light as a NEO–specific issue, which is the case in this work. Strictly speaking, reflected solar light affects thermal–infrared measurements for all types of small bodies, depending on the wavelengths in which the observations are performed. In the course of this work, only NEO observations are affected by reflected solar light.

3.7.1 Thermal Models for NEOs

NEOs stand out from the members of other small body populations due to their proximity to the Earth and the Sun, leading to two effects that have to be taken into account: reflected solar light and the effect of large solar phase angles.

3.7.1.1 Reflected Solar Light

Subsolar temperatures on NEO surfaces can reach and even exceed temperatures of 400 K. Figure 2.1 on page 45 shows that at high surface temperatures, the peak of the thermal emission is shifted to shorter wavelengths, such that the Wien slope (short–wavelength tail) of the SED of the NEO overlaps with the Rayleigh slope (long–wavelength tail) of the Sun's SED. Hence, thermal–infrared observations in the near and mid–infrared are contaminated by solar light that is reflected from the surface of the NEO; measured flux densities are the sum of a thermal and a reflected solar light component. Flux densities of the *ExploreNEOs* program, especially at 3.6 μm are significantly contaminated by reflected solar light (see Section 2.2.3). In order to properly disentangle the two components, the

shape of the object's reflectance spectrum has to be known, which is a function of its composition, or approximately its taxonomic type (see Section 1.2.4). Since measured reflectance spectra exist only for a limited number of NEOs, usually a fixed spectral slope is assumed: $RR_{\mathrm{IR/V}}$ describes the ratio of the reflectances in the optical and infrared wavelengths. As part of the *ExploreNEOs* program, a default value of $RR_{\mathrm{IR/V}} = 1.4$ has been adopted (Trilling et al. 2010; Harris et al. 2011), meaning that 40% more light is reflected in the infrared wavelengths than in the optical wavelengths. $RR_{\mathrm{IR/V}} = 1.4$ is derived from the spectra of S–type asteroids (Rivkin et al. 1997; Harris et al. 2009, see also Figure 1.10 on page 29), which are the most abundant among the NEOs. However, the slopes of the different taxonomic asteroid types cover a wide range; for instance, C–type asteroids have $RR_{\mathrm{IR/V}} \sim 1.2$. $RR_{\mathrm{IR/V}}$ is a coarse simplification of the physical reality, but offers a useful means to deal with the problem; see Section B.1 for an assessment of the accuracy of the thermal modeling results with respect to variations in $RR_{\mathrm{IR/V}}$.

The determination of the reflected light component at wavelength λ is introduced in the following. Firstly, the apparent magnitude of the NEO, m is derived from its absolute magnitude (see Equations 1.2 and 1.3 on page 20). Secondly, the flux density of the solar spectrum at λ, $F_{\odot}(\lambda)$, is extrapolated from a calibrated measurement at 3.6 μm (Rieke et al. 2008) and assuming the solar spectrum to follow that of a 5800 K black body. The fraction of solar light that is reflected by the surface of the NEO is derived from the apparent magnitude of the NEO and the magnitude of the Sun, $m_{\odot} = -26.74$ (see Section 1.2.1), using Equation 1.1 on page 19: $10^{-2/5(m-m_{\odot})}$. The contribution of reflected solar light at λ is then

$$F_{\odot}(\lambda) \times 10^{-2/5(m-m_{\odot})} \times RR_{\mathrm{IR/V}}.$$

3.7.1.2 Large Solar Phase Angles

The vicinity of NEOs to the Earth causes high values of the solar phase angle α. The larger α, the larger is that fraction of the surface of the NEO that faces the observer but is not illuminated by the Sun, emitting thermal emission that is neglected in most thermal models (see Wolters and Green 2009, and Section 6.2.3 for a discussion of the "NESTM"). Consequentially, the accuracy of thermal models decreases with increasing α. The NEATM has been shown to reproduce diameters better than 10% for $\alpha \leq 60°$ (Wright 2007). At higher values of α, however, the uncertainty increases rapidly.

The lack of night–side thermal emission in thermal models leads to an overestimation of the diameter. In Section 6.2.3, I present a thermal modeling approach that is designed to better describe the real situation.

3.7.2 Thermal Models for TNOs

The large distance of TNOs from the Sun and the Earth forces low values of the solar phase angle of a few degrees at most. The NEATM's ability to account for the phase angle is

not required in this case. However, a variable beaming parameter η has proven extremely useful to fit the SEDs of TNOs. Stansberry et al. (2008) have adopted a so called "hybrid STM", which is basically a STM–like thermal model using a variable η parameter.

3.7.2.1 Wavelength–Dependent Emissivity

Some large TNOs with detailed optical and thermal–infrared data over a wide range in wavelength show hints of a wavelength–dependence of the thermal emissivity, ϵ. Usually, a fixed value of the emissivity of $\epsilon = 0.9$ is applied to all kinds of small bodies, being based on laboratory measurements of silicate powder (Hovis and Callahan 1966). The variability is partially attributed to the effect that far–infrared wavelengths emerge from deeper surface layers that naturally have a lower temperature and therefore appear to be colder, or to have a lower emissivity. The effect has been observed in Pluto (Lellouch et al. 2011), revealing different trends for the emissivity of individual chemical components of Pluto's surface.

3.7.2.2 Phase Integral

The high albedos measured in some large TNOs require photometric slope parameters, G, that deviate significantly from the commonly adopted value of $G = 0.15$. Instead of the default phase integral, relating the albedos A and p_V (Equation 1.6 on page 23), a different relation is used in the case of TNOs (Vilenius et al. 2012; Mommert et al. 2012; Santos-Sanz et al. 2012) that is based on the measurement of the phase integral of icy satellites of the giant planets (Brucker et al. 2009), which are a better equivalent of TNOs than ice–free asteroids:

$$A \sim A_V = 0.336 p_V + 0.479. \tag{3.15}$$

3.7.2.3 Opposition Surge

Some TNOs have been observed to show an "opposition surge", a non–linear brightening of the order of $\sim$0.1 mag at very low phase angles ($\leq 0.2°$) (Belskaya et al. 2008). The opposition surge is at least partially caused by multiple reflections on facing surface elements, increasing the brightness in the direction of the Sun, which is also called the "opposition effect". The existence of the opposition surge has implications for the results of thermal models that make use of the absolute magnitude H, which is defined at $\alpha = 0$. Taking into account the impact of the opposition surge is necessary for proper thermal modeling results of TNOs. However, the bad quality of current optical TNO data (e.g., Romanishin and Tegler 2005; Benecchi et al. 2011, have found a systematic uncertainty of MPC H magnitudes of 0.3 mag) supersedes concerns about the impact of the opposition surge.

Chapter 4

"ExploreNEOs" Results

The following sections reflect my work on the physical characterization of near–Earth objects (NEOs) and the assessment of their origin (see Section 1.1.3.2). The results presented here are based on the Spitzer IRAC observations performed in the framework of the ExploreNEOs program (Section 2.2.3); some results have been submitted to peer–reviewed journals, as indicated.
The following topics are covered in this chapter:

- *The comparison of the physical properties of NEOs with those of their source populations in the main belt and the comets (see Section 4.1).*
- *The assessment of the fraction of NEOs that are of cometary origin, one of the main goals of the ExploreNEOs program (see Section 4.2).*
- *The investigation of evidence for cometary activity in NEO (3552) Don Quixote, one of the largest of the NEOs, from ExploreNEOs data. Don Quixote is most probably an example of a transitionary object evolving from being a comet to becoming an asteroid (see Section 4.3).*
- *The assessment of the reliability of the default ExploreNEOs thermal modeling pipeline results, including an investigation of the contributors to the uncertainties, and a direct comparison of the results of the ExploreNEOs and NEOWISE programs. Since the results of both analyses are related to, but not crucial for the conclusions of this work, they are presented in Appendix B.1.*

The integration of the results presented here into our picture of the Solar System is discussed in Section 6.1.

4.1 Comparing the Physical Properties of NEOs and their Source Populations

The short–lived NEO population is constantly replenished by objects coming from its source populations, as a result of different dynamical mechanisms (see Section 1.1.3). The most important source populations have been identified by Bottke et al. (2002b) to lie within the main asteroid belt and the Jupiter family comets ("JFCs"). The individual main belt source populations in the order of ascending average semimajor axis are: the Hungarias ("HUN"), the ν_6 secular resonance ("ν_6"), the Phocaeas ("PHO"), the Mars crossing population ("MC"), the 3:1 mean motion resonance ("3:1"), and the outer main belt ("OB"); see Section 1.1.2.1 for information on the individual populations. Bottke et al. (2002b) have used sophisticated dynamical simulations to set up a de–biased model of the NEO population, based on NEO discoveries and re–discoveries of the Spacewatch program (Rabinowitz 1994). From their model they derive the probability that NEOs populating discrete cells in $[a,e,i]$–space originate from one of the aforementioned source populations, P_i, where i is the respective source population. Bottke et al. (2002b) is presently considered the most realistic description of the distribution of the NEO population and its mechanisms of replenishment. Their work is based on purely dynamical considerations.

The members of the asteroid main belt are known to show a gradient in their albedos: objects from the inner regions of the main belt are more likely to be intermediate to high–albedo S–type asteroids, whereas the members of the outer belt are more likely to be dark C–type asteroids (e.g., Masiero et al. 2011, see also Section 1.2.2). Hence, the albedo distributions of the individual NEO source populations should be reflected in the NEO population.

In the following, I investigate the albedo properties of NEOs coming from the aforementioned source populations, based on the probabilities provided by Bottke et al. (2002b) and the diameters and albedos derived by the default *ExploreNEOs* thermal modeling pipeline. I compare the measured albedos in the NEO population with model predictions and measured albedos of the respective source populations to find physical evidence for a connection between NEOs and the proposed source populations.

4.1.1 Prerequisites

4.1.1.1 NEO Albedos

The proper identification of the source population of a specific NEO is hampered by the fact that its origin can only be described in a probabilistic sense. For the determination of the albedo properties, namely the average albedo and the albedo distribution, of NEOs originating from a specific source population I use two distinct approaches:

1. "Offspring Samples": I group NEOs into "offspring" samples that include those objects that are most likely to come from the same source population (i): each NEO is assigned to that source population i where $P_i > 0.3$. I derive the average albedo and respective uncertainty for each offspring sample using the arithmetic average and the standard deviation. The above definition of the offspring sample ensures an identification in a conservative sense; the threshold probability of 30%, which is selected somewhat arbitrarily, includes all objects that have a reasonable probability to stem from the respective source population. However, the relatively low threshold also allows for the inclusion of objects that actually originate from a different source population[1]. The implications of this ambiguity and a comparison with a sample defined with $P_i \geq 0.5$ are discussed below.

2. "Weighted Average": The weighted average albedo, $\langle p_V^i \rangle$, and respective weighted standard deviation, $\sigma_{p_V}^i$, over all objects j, are determined for each source population i using

$$\langle p_V^i \rangle = \frac{\sum_j P_{i,j} \cdot p_V^j}{\sum_j P_{i,j}}, \quad \sigma_{p_V}^i = \sqrt{\frac{\sum_j P_{i,j} (p_V^j - \langle p_V^i \rangle)^2}{\sum_j P_{i,j}}}$$

   This approach takes into account all NEOs with measured albedos, ensuring large number statistics. The weighting guarantees that NEOs with larger probabilities P_i have a larger impact on the resulting average albedo.

Note that calculated standard deviations using the aforementioned definitions are mainly driven by the albedo scatter inherent to the respective sample. Hence, the standard deviation should be seen as a measure for the magnitude of the scatter.

4.1.1.2 Model Predictions

The model predictions for the average albedos and albedo distributions of NEOs coming from the individual source populations are based on calculations by Morbidelli et al. (2002), who have used the same model of the NEO distribution as here (Bottke et al. 2002b). Morbidelli et al. (2002) determine the relative contributions of the individual source populations to 5 different albedo bins (their Table 3). I utilize their predictions in two ways: (1) the model prediction average albedo of the respective offspring population is calculated by summing up the contributions to the different albedo bins of each individual source population, and (2) the model prediction albedo distributions are represented by the contributions of the individual source populations to the albedo bins[2]. The utilized albedo bins have their boundaries at 0, 0.089, 0.112, 0.355, and 0.526 (Morbidelli et al. 2002).

[1] The 30% threshold allows for a single object to be assigned to more than one but less than four different source regions.

[2] Note that in the determination of the albedo distribution, the "Com" and "Low" albedo bins of Morbidelli et al. (2002) were merged to a single bin spanning the range $0 \leq p_V \leq 0.089$.

In their analysis, Morbidelli et al. (2002) have merged the HUN and PHO populations with the MC population, hence, there are no albedo distribution model predictions for these two populations. However, rough independent average albedo model estimates are extracted from other publications. Warner et al. (2009) argue that the large majority of the Hungarias have flat X or E–type spectra (see Section 1.2.4) similar to their prototype, (434) Hungaria, which has a measured V–band albedo of 0.38, which they believe is typical for all Hungarias. I adopt this albedo as the model prediction for all Hungaria asteroids. Bell (1989) found the Phocaeas to consist of about two thirds S–type and one third C–type asteroids. Assuming the average albedos of S and C–type NEOs (0.26 and 0.13, respectively) as derived from *ExploreNEOs* data (Thomas et al. 2011), the average albedo of NEOs coming from the Phocaeas amounts to 0.21.

4.1.1.3 Source Population Albedos

I derive the average albedos and albedo distributions of the source population members from measured albedos from the literature: measured albedos of main belt asteroids are extracted from Masiero et al. (2011), who have published measurements of more than 100000 main belt asteroids, derived from thermal flux densities measured by WISE (see Section 2.3). The albedo information from Masiero et al. (2011) was combined with orbital elements that were extracted from the JPL Small–Body Data Browser. Albedo measurements of JFC nuclei were taken from the compilation of cometary nuclei albedos by Lamy et al. (2004) (see also Table 4.2 on page 112).

Members of the main belt source populations are identified using the following dynamical criteria that are based on Bottke et al. (2002b), if not noted otherwise:

- HUN: $1.77 < a < 2.06$ AU and $i > 15°$.
- ν_6: The location of the ν_6 resonance has to be determined using sophisticated dynamical models, due to the complexity of the dynamical problem. The rate at which objects that are close to the ν_6 resonance become unstable depends on their relative location in the resonance (Morbidelli and Gladman 1998). Figure 5 by Bottke et al. (2002b) shows the course of that part of the ν_6 resonance where the instability leads to the most rapid ejection of objects to near–Earth space. Here, I use a polynomial approximation ($i_{\nu_6}(a) = -142.4a^2 + 698.5a - 839.4$ for $2.1 \leq a \leq 2.5$ AU) to describe this section of the resonance. I select those main belt objects as potentially influenced by the ν_6 resonance that are currently located in a 0.05 AU wide strip on the right–hand side of the aforementioned fit to the ν_6 curve (Morbidelli et al. 2002). Furthermore, I reject those objects with $q < 1.3$ and $i > 16°$.
- PHO: $2.1 < a < 2.5$ AU and $i > i_{\nu_6}$ (with i_{ν_6} as defined above).
- MC: $1.3 < q < 1.78$ AU, $2.1 \leq a \leq 2.8$, and $i \leq i_{\nu_6}$ (with i_{ν_6} as defined above).

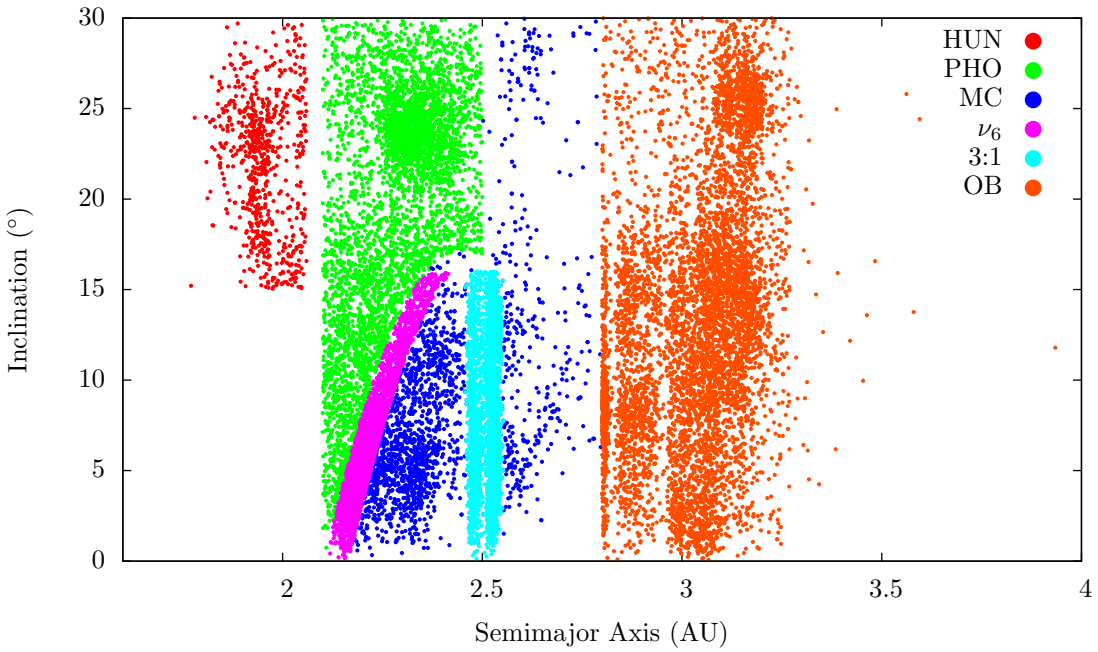

Figure 4.1 The distribution of the NEO source regions in the main belt in a–i–space. The individual populations are: "HUN": Hungarias, "ν_6": ν_6 secular resonance, "PHO": Phocaeas, "MC": Mars crossing population, "3:1": 3:1 mean motion resonance, "OB": outer main belt. The definitions of the individual populations are given in the text. Note that this distribution only shows a part of the asteroid main belt (compare to Figure 1.3 on page 5).

- 3:1: The 3:1 MMR is located at $a = 2.5$ AU. I regard those main belt objects as being currently influenced by the 3:1 MMR that meet the following criteria: $2.48 - 0.075 \cdot e < a < 2.52 + 0.10 \cdot e$ AU, $q > 1.3$ AU, and $i < 16°$(Morbidelli et al. 2002).

- OB: $a \geq 2.8$ AU and $q < 2.4$ AU.

The distribution of the main belt source populations is shown in Figure 4.1. Note that using the aforementioned definitions, some main belt asteroids can be assigned to multiple source populations, which is realistic, since some regions are affected by several mechanisms that can transport asteroids into near–Earth space.

The source population probabilities used in this work were calculated by A. Morbidelli (private communication) based on the method by Bottke et al. (2002b).

4.1.2 Albedo Data

In order to extend the NEO sample size for this analysis, the *ExploreNEOs* albedos, derived by the default *ExploreNEOs* thermal modeling pipeline, were combined with measurements from the NEOWISE program (Mainzer et al. 2011b, see also Section 2.3), amounting to

Table 4.1. NEO and NEO Source Region Albedo Properties.

Method	HUN	ν_6	PHO	MC	3:1	OB	JFC
Offspring Average	0.24±0.16 (38)	0.23±0.16 (632)	0.14±0.16 (36)	0.24±0.17 (291)	0.20±0.15 (69)	0.12±0.10 (51)	0.07±0.08 (20)
Weighted Average	0.25±0.17	0.23±0.16	0.18±0.17	0.23±0.17	0.22±0.16	0.12±0.10	0.08±0.09
Model Prediction	0.38	0.22	0.21	0.19	0.20	0.13	0.04
Source Population	0.34±0.31 (736)	0.21±0.13 (3144)	0.12±0.11 (4470)	0.16±0.12 (2536)	0.16±0.12 (2879)	0.08±0.06 (7033)	0.05±0.02 (7)
Albedo Ratio:							
ϱ_O	0.19±0.08	0.30±0.03	1.1±0.4	0.29±0.04	0.4±0.1	1.1±0.3	3±1.5
ϱ_M	–	0.14	–	0.37	0.16	1.38	∞
ϱ_S	0.58±0.04	0.43±0.02	1.90±0.06	0.96±0.04	0.92±0.03	3.8±0.1	∞

Note. — The offspring sample is that sample of NEOs with a probability $P \geq 0.3$ to originate from the respective source population. The "offspring average" refers to the average albedo of all members of the respective offspring sample; the "weighted average" is the average of all NEOs with measured albedos, weighted by their individual probability P_i to come from source population i. The average albedos and model predictions are illustrated in Figure 4.2. Numbers in brackets refer to the number of objects from which the values in the line above were derived. ϱ_O, ϱ_M, and ϱ_S denote the albedo ratio, which is the ratio between low and high–albedo objects, in the offspring sample, the model prediction, and source population, respectively. For more information cf. the text.

a total number of 851 different NEOs. Furthermore, updated H magnitudes have been used where available: H magnitudes of 87, 29, and 12 NEOs in the *ExploreNEOs* sample were updated using photometry from Hagen et al. (2011), Pravec et al. (2012), and the EARN database, respectively; for 26 of the NEOWISE sample targets updated albedo estimates from Pravec et al. (2012) were used. For objects that were observed more than once by any of the programs, or by both programs, the measured albedos have been averaged to improve the data quality. Note that the NEOWISE target 2009 UV18 was removed from the sample, due to its unrealistically high albedo ($p_V = 0.71$) although being likely of having a JFC origin; Mainzer et al. (2012) suspect this object to show cometary activity, which is likely to affect the thermal flux density measurement. In order to prevent a contamination of the sample, it was removed. The total sample size of 850 NEOs represents ∼9% of the known NEO population as of January 2013, according to the MPC.

4.1.3 Results

The average albedos of the offspring samples and the source populations are illustrated in Figure 4.2, as well as the model predictions. The derived albedo properties and model predictions are also listed in Table 4.1. The comparison of the albedo distributions derived from the source populations and their offspring samples is shown in Figure 4.3.

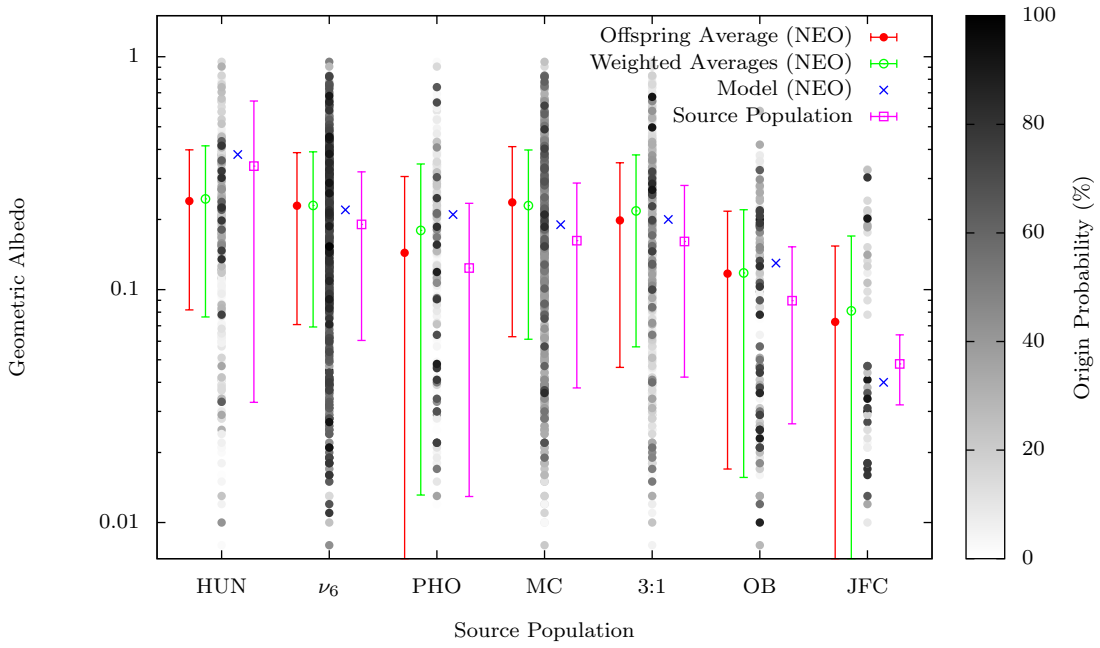

Figure 4.2 The albedo averages of NEOs coming from the different source populations. Each bin represents one NEO source population in the order of increasing average semimajor axis. Population names as in Figure 4.1, "JFC" refers to the Jupiter family comets. Every object is displayed in each of the source population bins according to its measured albedo and its probability of an origin in the respective population; the darker the data point, the higher the object's probability for an origin in the respective population. On the left hand side of the columns, the average NEO albedos with respective standard deviations are depicted, referring to the weighted average (filled red circles) and the average of the offspring samples (open green circles). On the right hand side of the columns are the model predictions for the average NEO albedo (blue crosses) and the average albedos in the respective source population (open purple boxes) shown. The expected trend of decreasing albedo with increasing semimajor axis is obvious. The computed albedo properties are listed in Table 4.1.

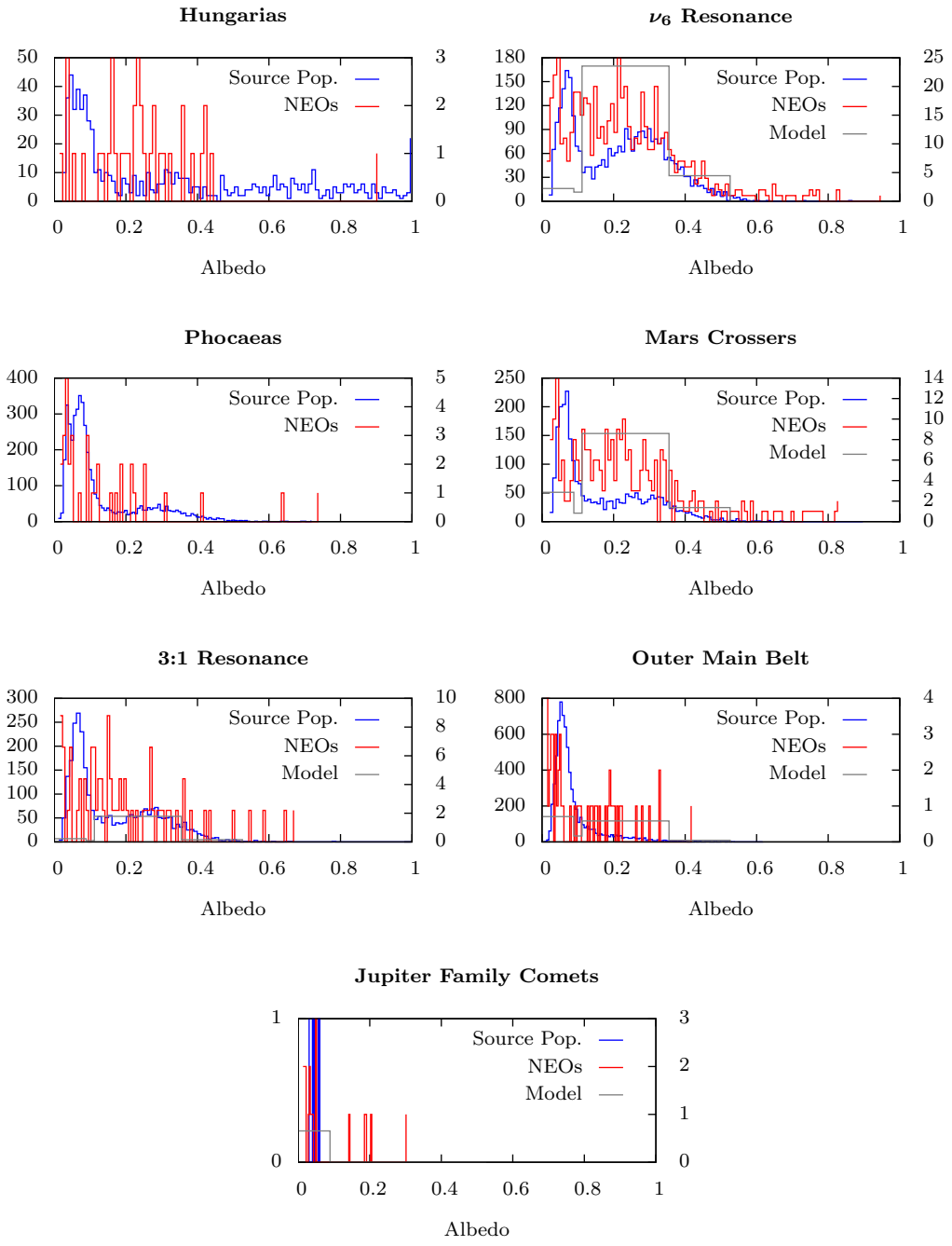

Figure 4.3 Comparison of the albedo histograms of the source populations ("Source Pop.") with the respective offspring samples ("NEOs") and the model prediction ("Model") for the NEO offspring sample. The left–hand scale refers to the number of objects in the source population in each albedo bin (blue histogram), the right–hand scale refers to the offspring samples (red histogram) and model predictions (grey histogram), which are normalized to the same scale. The height of the model prediction albedo bins assumes that all offspring sample objects are evenly distributed in the bin, according to the composition determined by the model. Note that no model predictions exist for the Hungarias and Phocaeas from Morbidelli et al. (2002).

4.1.4 Discussion

4.1.4.1 Comparison of the Average Albedos

The agreement between the two albedo averaging methods is good, which is evident from Figure 4.2 and Table 4.1. The agreement supports the credibility of both methods. In the following discussion, the averages of the "weighted average" method will be adopted, which is based on a larger sample size. Note that the large standard deviations are caused by the albedo scatter inherent to the samples.

The good agreement between the different averaging methods also supports the applied $P_i \geq 0.3$ threshold in the definition of the offspring samples, which are considered representative of all those NEOs that come from the respective source populations in the following. I check the validity of this approach by introducing a $P_i > 0.5$ offspring sample for each source population. Note that this definition implies two things: (1) each NEO can only be assigned to a single source population, and (2) that this single population is automatically that source population with the highest individual origin probability. Calculating the average albedos from this sample returns basically the same results; the largest difference in the average albedos occurs for the offspring of the Mars crossing population, which increases by 0.03, still well within the uncertainties. All other albedo averages change by $\sim$0.01. The $P_i \geq 0.3$ definition of the offspring samples is preferred over the more intuitive $P_i > 0.5$ approach due to the larger sample sizes, which significantly improve the statistics.

Figure 4.2 and the average albedos listed in Table 4.1 clearly reflect the trend of decreasing average albedo with increasing semimajor axis inherent to the main asteroid belt (see Section 1.2.2). In general, the average albedos derived from the NEO population agree with both the predicted model albedos and the average albedos from the source populations; differences are discussed below.

4.1.4.2 Comparison of the Individual Albedo Distributions

A visual inspection of the albedo distribution histograms of the offspring, predicted model, and source population samples (Figure 4.3) shows a coarse agreement between the offspring and model distributions. A comparison between the source populations and respective offspring samples shows a distinct peak of low–albedo ($p_V \leq 0.1$) objects in the former, which is lacking in many of the offspring populations. The lack of low–albedo objects is even more pronounced in the model predictions. I investigate the deficiency in low–albedo objects using the "albedo ratio", $\varrho = N_{\rm lo}/N_{\rm hi}$, which is defined as the ratio of the numbers of objects with $p_V \leq 0.1$, $N_{\rm lo}$, and the number of objects with $p_V > 0.1$, $N_{\rm hi}$, for a specific albedo distribution. The albedo ratio provides a simple means for comparing the ratio of low–albedo and high–albedo objects in a sample, and should be similar in a source population and its offspring sample, if no albedo–dependent mechanisms are involved in the transport mechanisms from the source population to the NEO population. In order

to take into account statistical variations caused by the low number of objects in some of the samples, I adopt a Poissonian description of the uncertainty, which is determined as

$$\sigma_\varrho = \varrho \cdot \sqrt{\left(\frac{\sqrt{N_{\rm lo}}}{N_{\rm lo}}\right)^2 + \left(\frac{\sqrt{N_{\rm hi}}}{N_{\rm hi}}\right)^2} = \varrho \cdot \sqrt{\frac{1}{N_{\rm lo}} + \frac{1}{N_{\rm hi}}}.$$

The values of ϱ determined for the offspring (ϱ_O), predicted model (ϱ_M), and the source populations (ϱ_S) are listed in Table 4.1. Note that ϱ_M uses a different albedo threshold, $p_V = 0.112$, which is unlikely to affect the overall result. Table 4.1 shows that $\varrho_O < \varrho_S$ for all source populations, which hints towards a systematic deficiency of low–albedo objects in the NEO population compared to the source populations. The model prediction, ϱ_M, usually agrees better with ϱ_O, supporting the model simulations by Morbidelli et al. (2002). Note that ϱ_O and ϱ_S are derived for different size ranges: the known main belt asteroids (ϱ_S) are on average significantly larger than the NEOs (ϱ_O) considered here. Hence, the lack of low–albedo objects in the offspring samples might hint to a size–dependent albedo distribution in both populations. The deficiency of low–albedo objects in the NEO population, however, is unlikely to be only the result of discovery bias, since the same bias also applies for objects in the main belt. The impact and possible origin of the deficiency is also discussed in Section 6.1.

In the following, the individual source populations are discussed in detail (cf. Figures 4.2 and 4.3, and Table 4.1):

- Most of the **Hungaria** offspring objects have intermediate albedos, whereas both the predicted model albedo in the NEOs and the average albedo of the current Hungaria population in the main belt are higher by roughly 0.1. The predicted model albedo suffers from the fact that it is solely based on the single albedo[3] measurement of (434) Hungaria. However, a comparison of the albedo distributions of the offspring and source population (Figure 4.3) points into the same direction, which is also suggested by the 3–times lower albedo ratio ϱ for the offspring sample compared to the source population. The Hungaria offspring shows a lack of high–albedo objects ($p_V \geq 0.45$); only one object with $p_V \sim 0.9$ is present, which is likely to be based on a unreliable absolute magnitude measurement, since this extreme albedo is unrealistic. I investigate if the lack of high–albedo objects in the Hungaria offspring is a selection effect: Figure 4.1 shows an accumulation of Hungaria asteroids near the center of the respective area in a–i space that is populated by the core population of the Hungaria group, which is dynamically much more stable than the surrounding areas. Restricting the albedo histogram to the core population

[3](434) Hungaria is an E–type asteroid, which are known to be abundant in the Hungaria population (Warner et al. 2009). The albedo range of E–type asteroids covers values from 0.1 – 0.5, possibly even higher values, which brackets the albedo measurement of (434) Hungaria and is supported by the source population albedo distribution.

($1.8 < a < 1.95$ AU, $17 < i < 29°$) reveals that most high–albedo Hungarias are indeed members of this core population, and hence unlikely to be transported into near–Earth space. Thus, the lack of high–albedo Hungaria offspring in the NEO population is likely to be a selection effect. The nature of the deficiency in low–albedo objects, however, is unclear; observational bias may play a role. Physical selection effects, based on albedo for instance, may be possible in the light of the dependency of the magnitude of the Yarkovsky effect (see Footnote 3 on page 8) on the thermal properties of the asteroid, including its albedo.

- The offspring of the $\boldsymbol{\nu_6}$ **secular resonance** in the NEO population covers the whole range of albedos, similar to their parent population in the asteroid main belt. There is no preference for high or low albedos, which can be interpreted in terms of the large degree of mixing close to the ν_6 resonance. The average albedo of the ν_6 offspring agrees well with the model prediction for the offspring by Morbidelli et al. (2002), and the average albedo of those main belt objects that are currently near the resonance. The albedo histograms of the offspring and main belt ν_6 populations are similar in overall shape, although the albedos of the former are fairly uniformly distributed for $0 \geq p_V \geq 0.3$, whereas the latter is clearly double–peaked in the same range. The bulk of the offspring albedos matches the predicted model distribution. The albedo ratio ϱ_O is slightly lower than ϱ_S; ϱ_M is even lower than ϱ_O, suggesting a strong deficiency in low–albedo objects in the model used by Morbidelli et al. (2002).

- The **Phocaea** offspring, main belt and predicted model albedos agree reasonably well. The range of albedos agrees with the prediction by Bell (1989) that two third of the Phocaeas are S–type asteroids with intermediate albedos and one third are C–type asteroids with low albedos. Note that both the offspring and the source population albedo histograms show a peak at low albedos, which is confirmed by the agreement of ϱ_O and ϱ_S within 2σ. However, the relative number of low–albedo objects is still higher in the source population.

- Similarly to the ν_6 offspring, the **Mars crosser** offspring has well–mixed albedos, given the large range in a that is influenced by Mars (see Figure 4.1). The MC offspring average albedo is slightly higher than both the model prediction (Morbidelli et al. 2002) and the main belt average. The agreement between the model and offspring albedo distributions is reasonable, as reflected by the albedo ratios. The albedo ratio of the source population, however, is higher by a factor of $\sim$3. It is noteworthy that the highest albedos of offspring members are higher by $\sim$0.2 than those of the source population asteroids. Such high albedos are found in the main belt only among the Hungarias. A contamination of the Mars crossing offspring sample with Hungaria descendants is possible; its investigation requires detailed dynamical modeling.

- The **3:1 mean motion resonance** offspring albedos are intermediate, which agrees with the model prediction (Morbidelli et al. 2002) and the average from the main belt source population. A resemblance of the shape of the source population and offspring albedo distributions is obvious from Figure 4.3. The ratio of low albedos in the offspring sample is lower compared to the source population by a factor of 2.5, and higher than the model prediction by a factor of 2.

- The model prediction and average albedo of the **outer main belt** offspring agree well. The average albedo of objects in the source population is slightly lower. The albedo distributions of the offspring, model, and source population agree well, covering the same albedo range. The albedo ratio of the offspring sample agrees well with the model, wheres the ratio is significantly higher for objects from the source population. As expected, outer main belt asteroids are on average the darkest objects in the asteroid main belt, which is also true for most of its offspring in the NEO population.

- The offspring of the **Jupiter family comets** have on average the lowest albedos of all NEOs. The derived average JFC offspring albedo is higher than both the model prediction and the average albedo as derived from JFC nuclei (see Table 4.2 on page 112 and Lamy et al. 2004). The discrepancy is caused by a small number of putative JFC offspring members with intermediate albedos that are likely to be the result of inaccurate H magnitude estimates, cometary activity that is misinterpreted as a high–albedo body, or shortcomings in the calculations of the origin probabilities. The comparison of the albedo distributions shows that neither of the source population nor the predicted model albedos is higher than 0.1, which is the case for several objects in the offspring sample. The albedo ratios of the model and source population are ∞, due to the non–existence of high–albedo objects in both samples. The existence of intermediate to high–albedo objects among putative JFC descendants is also discussed in Section 6.1.

The above analysis shows the general agreement of the NEO albedo distribution with that of its source populations, with a few exceptions. The discovered discrepancies include the lack of low–albedo objects in the NEO population, the deficiency of high–albedo objects in the Hungaria offspring, and the existence of NEOs of cometary origin with atypical albedos. The investigation of the aforementioned discrepancies requires a more detailed analysis, possibly involving sophisticated dynamical modeling based on the work by Bottke et al. (2002b) and Morbidelli et al. (2002), which is beyond the scope of this work. See also Section 6.1 for a discussion of the possible origins of the observed discrepancies.

4.1.5 Conclusions

- The average albedos measured in the NEO population agree well with the average albedos of their respective source regions and predicted model albedos (Morbidelli et al. 2002) in all but two cases: (1) the Hungaria offspring in the NEO population shows a deficiency in high albedo (> 0.42) asteroids, which is likely to be caused by selection effects, and (2) NEOs originating from the JFCs with usually low albedos are contaminated by objects with intermediate albedos that might be incorrectly identified, or show some kind of cometary activity.

- The albedo distributions of the offspring samples mostly agree with the predicted model albedo distributions (Morbidelli et al. 2002). However, I find a significant lack of low–albedo objects in all offspring populations compared to the source populations, which might hint to a size–dependent albedo distribution in both populations. The low–albedo/high–albedo ratios of the two samples agree only coarsely in the case of the ν_6 resonance and the Phocaea offspring.

- The trend of decreasing albedo with increasing heliocentric distance in the main belt asteroids (see, e.g., Masiero et al. 2011) is reflected in the NEO offspring populations.

- The results of this analysis support the predictions made for the origin of NEOs and the NEO albedo distribution (Morbidelli et al. 2002) derived from the Bottke et al. (2002b) model.

4.2 Assessment of the Cometary Contribution to the NEO Population

4.2.1 Introduction

The NEO population comprises fragments from the asteroid main belt and objects of cometary origin (see Section 1.1.3.2 and Öpik 1963; Wetherill 1988; Binzel et al. 1992). Most of the comets are former Jupiter family comets (JFCs, see Section 1.1.5.1) with orbits that take them into near–Earth space.

The dynamical lifetimes of NEOs are typically of the order of 10^7 yrs (Morbidelli and Gladman 1998), which is significantly longer than the activity lifetimes of JFCs ($\sim$12000 yrs, Levison and Duncan 1997). Hence, most comets in near–Earth space are likely to have ceased activity, becoming "dormant" or "extinct" comets, which are indistinguishable from low–albedo asteroids (Wetherill 1991). Levison and Duncan (1997) estimate that 78% of all JFCs are extinct. Observational evidence of such a dormant or extinct comet was found in the NEO (4015) Wilson–Harrington, which displayed cometary activity in 1946, but never since (Bowell et al. 1992; Fernández et al. 1997). As in the case of Wilson–Harrington, it is not clear whether the activity of objects of cometary origin has ceased only temporarily or for good. It is possible that volatile material is still present in deeper surface layers, which might be excavated by collisions. An analog to such objects can be found in the asteroid main belt: some asteroids have recently been observed to show comet–like activity, probably being triggered by various mechanisms, such as recent impacts, ice sublimation, or cracking at extreme temperatures (Jewitt 2012). Since it is not clear whether such objects in the NEO population are dormant or extinct comets, I refer to them using the more general term "cometary object".

The determination of the cometary object fraction in the NEO population is important in order to understand the formation and evolution of the Solar System. Cometary objects have most likely impacted Earth and contributed to the deposits of water and organic materials on its surface (Alexander et al. 2012; Hartogh et al. 2011, and references therein). Comets are directly linked to the outer regions of the Solar System (see Section 1.1.5.2), including the Centaurs and TNOs, which contain the most pristine objects. Furthermore, it is important to know the frequency and physical properties of the different types of objects in the NEO population from the point of view of impact–hazard mitigation. Since NEOs are among the most easily accessible objects in space, the possibility of cometary objects in near–Earth space provides the unique opportunity to study such objects with manned or unmanned space missions.

In this analysis, I study the fraction of objects of cometary origin in the NEO population and give a list of candidate objects that are likely to be of cometary origin. This analysis is based on the results of the *ExploreNEOs* and NEOWISE (see Section 2.3) programs, which represents the largest sample of measured albedos of NEOs available to

date.

Note that part of this analysis has been submitted to a peer–reviewed journal for publication. In the following presentation, I focus on the work performed by myself, and I explicitly mark contributions made by others.

4.2.1.1 Identification of Cometary Objects

I identify cometary object candidates in the NEO population using a statistical approach, based on the dynamical and physical ensemble properties of both NEOs and comets. I first identify objects with comet–like orbits, making use of (1) the Tisserand parameter with respect to Jupiter, T_J (see Section A.1.3.1), and (2) the minimum orbit intersection distance with respect to Jupiter, $MOID_J$, based on statistically determined criteria. In the second step, I select objects with comet–like albedos from those with comet–like orbits.

T_J is a dynamical quantity that describes how much the orbit of an object is linked to the gravitational pull of Jupiter and is approximately conserved during encounters with the planet. Its definition is shown in Equation A.1 on page 233. Hence, T_J can be used as an discriminator of the nature of an object: comets usually have $T_J \leq 3.0$, whereas asteroids have $T_J > 3.0$. This discrimination is not irrevocable, since T_J is only fully conserved under idealized conditions; asteroids can end up having $T_J \leq 3.0$, and vice versa. Nevertheless, T_J can be used as a strong indicator for a comet–like orbit. For a more profound discussion of the Tisserand parameter, I refer to Section A.1.3.1.

$MOID_J$ describes the distance between a body and Jupiter during closest encounter, usually expressed in units of AU. JFCs are scattered into the inner Solar System as a result of close encounters with Jupiter (Levison and Duncan 1997). Their arguments of perihelion (see Section A.1.1) are clustered around 0 and 180° (Fernández 2005), enabling them to have frequent close encounters with Jupiter, indicated by a low $MOID_J$. Sosa et al. (2012) showed that comets in near–Earth space are more likely to have a low $MOID_J$ than asteroids (their Figure 1), which is also apparent from Figure 4.5. However, $MOID_J$ should not be used as a standalone dynamical discriminant, since asteroids can have low values of $MOID_J$ as well, even without having a cometary origin. However, in combination with T_J it can be used as an empirical indicator to identify comet–like orbits.

In order to properly identify objects with comet–like orbits I define two upper limits for both T_J and $MOID_J$, forming a "**tight**" and a "**loose**" sample of objects. The tight sample is designed to make a sharp distinction in dynamical terms between comet–like orbits and those of ordinary asteroids, and therefore aims to contain the highest possible fraction of cometary objects, i.e., to include the largest possible absolute number of cometary objects and the lowest possible absolute number of asteroids at the same time. This approach may lead to the exclusion of some objects that are of cometary origin, but have orbits that differ from the strict definition of "comet–like". The loose sample is designed to include the largest possible number of cometary objects, at the

expense of inevitably including a number of ordinary asteroids. Both sample definitions are legitimate, but based on different strategies. The combination and comparison of the results obtained with both samples improves the overall result and allows for the estimation of its statistical uncertainties. All tight sample objects are automatically loose sample members, as well. The sub–sample of objects of the loose sample that are not members of the tight sample is referred to as the "complementary sample".

I identify "**cometary object candidates**" that are likely to be of cometary origin in the dynamical and physical sense from the two dynamically selected samples by applying an upper limit on the geometric albedo. The choice of the sample criteria including T_J and $MOID_J$, as well as the albedo upper limit of cometary objects, is discussed in Section 4.2.2. The two subsamples of cometary object candidates and their ensemble properties are presented in Section 4.2.3.

In this work, I also utilize orbital simulations based on Bottke et al. (2002b), which give the probabilities that each object originates from a number of possible source regions, most of which lie within the asteroid main belt and the JFCs, to make a better distinction between asteroidal and cometary objects.

4.2.1.2 Albedo Sample

This analysis is based on albedos measured by the *ExploreNEOs* program (see Section 2.2.3), using the default *ExploreNEOs* thermal modeling pipeline (see Section 2.2.3). As part of this work, J. Hora (CfA Harvard) was able to recover for the first time data for three *ExploreNEOs* objects, (3552) Don Quixote, (4015) Wilson–Harrington, and (52762) 1998 MT24, the first of which was saturated in both (3.6 and 4.5 μm) channels of the IRAC instrument (see Section 2.2.2.1). Observations of the latter two objects were saturated in the 4.5 μm band only. In order to derive flux densities from the saturated images, he fit a calibrated PSF model to the unsaturated wings of the measured PSF, ignoring the saturated parts of the image. This method has been well tested on a number of saturated observations of calibration stars and other objects (Marengo et al. 2009). He added an additional 5% uncertainty in quadrature to those fluxes to account for the increased calibration uncertainty. Three other targets, 2004 QF1, (152952) 2000 GC2, and (162825) 2001 BO61 were too faint to be detected in the 3.6 μm band, and the results presented here are based on the 4.5 μm flux measurement only.

In order to determine accurate albedos, precise measurements of the absolute magnitude H and the photometric slope parameter G are crucial (see Section 3.6). Where available, I replace the default JPL Horizons Systems (accessed September 2012) H magnitudes by values taken from peer–reviewed publications (Hagen et al. 2011; Pravec et al. 2012) (87 updates by Hagen, 29 by Pravec) and EARN (12 updates). Where no measured values are available, I have to rely on the default H magnitudes and assume an uncertainty $\Delta H = 0.5$ mag for each object. In Table 4.3, I list H, G, and their respective sources.

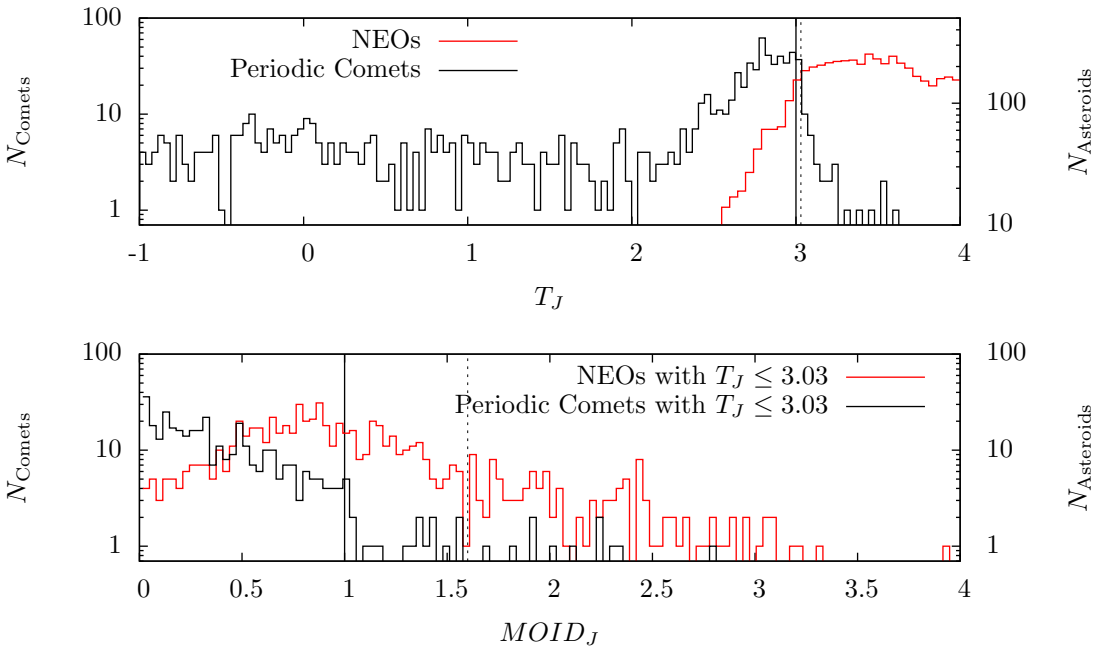

Figure 4.4 Logarithmic histograms of the distributions of T_J (upper panel) and $MOID_J$ (lower panel) among the known periodic comet and NEO populations. The dotted and dashed lines depict the tight ($T_J \leq 3.0$, $MOID_J \leq 1.0$) and loose ($T_J \leq 3.03$, $MOID_J \leq 1.6$) sample criteria (cf. text), respectively, the sample criteria which have been selected based on the shown T_J and $MOID_J$ distributions of the known periodic comets. Note that the $MOID_J$ histograms (lower panel) only include those periodic comets and NEOs with $T_J \leq 3.03$, since $MOID_J$ is only a secondary criterion.

I increase the albedo sample size by adding 471 albedo measurements of 415 different NEOs observed by the NEOWISE program (Mainzer et al. 2011b, and also see Section 2.3). I update the albedos of 26 NEOWISE sample targets based on new measurements of H from Pravec et al. (2012).

The combined *ExploreNEOs* and NEOWISE samples comprise 1060 albedo measurements of 851 different NEOs, covering wide ranges in both T_J and $MOID_J$. This sample represents $\sim 9\%$ of the known NEO population (Minor Planet Center Observations Database, as of February 2013).

4.2.2 Preliminary Considerations

The dynamical considerations are based on compilations of the orbital elements of the known asteroids (ASTORB Orbital Parameter Database) and comets (Cometary Orbit Database). I extract the NEO content of the ASTORB database by restricting the perihelion distance $q \leq 1.3$. Furthermore, I only consider periodic comets. The following analysis is based on a total of 8991 known NEOs and 379 known periodic comets.

Tisserand Parameter. The upper panel of Figure 4.4 shows the distribution of T_J values in the known population of periodic comets, and in the known NEO population, as of June 2012. Tisserand parameters for both asteroids and comets were computed using Equation A.1 on page 233. It is clear that most comets have $T_J \leq 3$, whereas most asteroids have larger values of T_J. Since T_J is only approximately conserved, the limit of $T_J \leq 3.0$ has to be somewhat softened. There are very few Encke-type comets with $T_J > 3$. Based on the histogram, I choose to set the tight and loose limits to $T_J \leq 3.0$ and $T_J \leq 3.03$, which include 95.3% and 97.3% of all known periodic comets, respectively, but only 6.8% and 7.9% of the known NEOs. The loose limit value is somewhat arbitrary but guarantees the inclusion of most comets while still rejecting most of the asteroids.

Minimum Orbit Intersection Distance. $MOID_J$ of both asteroids and comets was calculated by L. Wasserman (Lowell Observatory, private communication), using the method described by Sitarski (1968). $MOID_J$ was calculated for those asteroids that are not members of the Jupiter Trojans, Hildas, or in the 4:3 mean motion resonance with Jupiter. In the case of comets, $MOID_J$ was determined for periodic comets only. Since $MOID_J$ is not a dynamical invariant, it provides only a snapshot image of the dynamical characteristics of the asteroid and comet populations. The deductions made from the distributions, however, are still justified, since a statistical approach to identify extinct comets in the NEO population is utilized. The lower panel of Figure 4.4 shows the distribution of $MOID_J$ for the periodic comet and asteroid populations with $T_J \leq 3.03$. It is obvious that most periodic comets have $MOID_J \leq 1$ AU, whereas most asteroids have larger values. Based on the lower panel of Figure 4.4, i.e., in combination with $T_J \leq 3.0/3.03$, I define the tight limit as $MOID_J \leq 1.0$ AU, and the loose limit as $MOID_J \leq 1.6$ AU, including 86.8% (329 in absolute numbers) and 95.3% (361) of the periodic comet population, respectively, and 3.9% (354) and 6.4% (576) of the known NEO population. Both $MOID_J$ limits are chosen somewhat arbitrarily. The exact definition of the $MOID_J$–limits does barely affect the statistical results of this work. Figure 4.5 shows the distribution of the *ExploreNEOs* and NEOWISE sub–samples, as well as other NEOs and periodic comets, in T_J-$MOID_J$ space.

Albedo. Fernández et al. (2005) find an albedo upper limit of $p_R \leq 0.075$ for cometary objects in the NEO population that is based on albedo determinations of comets in the R band, compiled by Lamy et al. (2004) and an assumed albedo uncertainty of 30%. In the *ExploreNEOs* and NEOWISE programs, geometric albedos of the sample targets are determined in the V band, p_V. I take an approach that is similar to that of Fernández et al. (2005), and define an upper limit for cometary V–band albedos based on previously measured albedos of JFCs. In Table 4.2, I present the V–band albedos for the small number of JFCs for which this information has been measured. From these measured

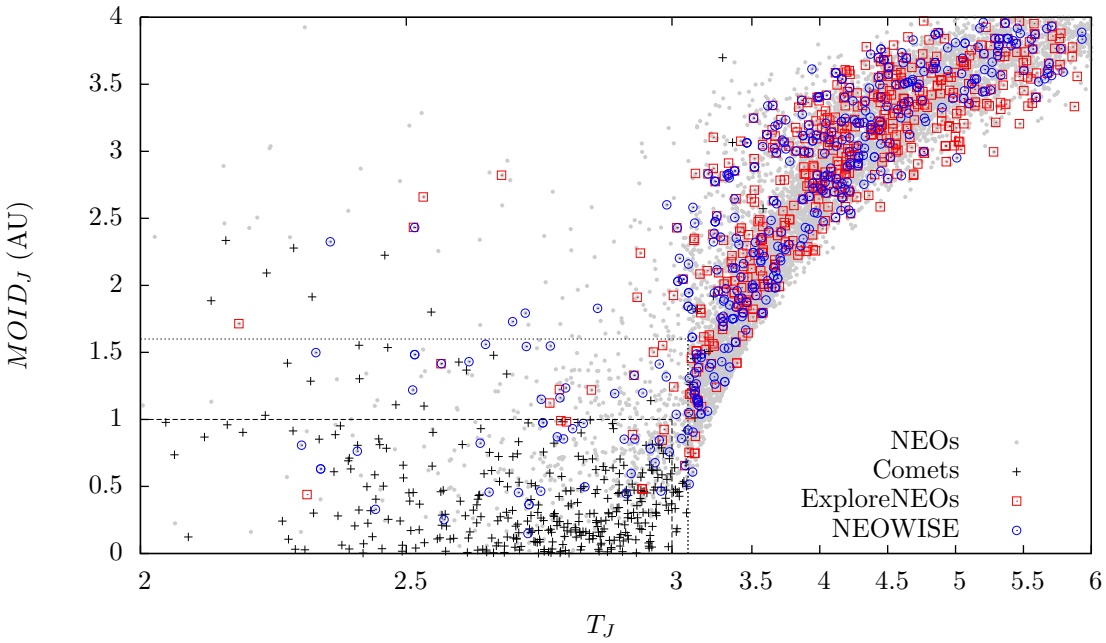

Figure 4.5 $MOID_J$ as a function of T_J. Grey dots represent known asteroids, crosses are known periodic comets, open squares are ExploreNEOs targets, and open circles are NEOWISE targets. The two rectangles represent the boundaries of the tight ($T_J \leq 3.0$, $MOID_J \leq 1.0$, dashed line) and loose ($T_J \leq 3.03$, $MOID_J \leq 1.6$, dotted line) samples, respectively. The loose sample includes the tight sample. Note the different abscissa scales for $T_J > 3.03$ and $T_J < 3.03$. The difference in the distributions of comets and NEOs is obvious. 86.8% and 95.3% of all periodic comets meet the dynamical requirements of the tight and loose samples, respectively; only 3.9% and 6.4% of the known NEOs meet the same criteria. There are 31 and 57 objects with measured albedos, meeting the criteria of the tight and loose sample, respectively.

Table 4.2. V–band albedos of JFC Nuclei.

Name	p_V	Reference
2P/Encke	0.046 ± 0.023	Fernández et al. (2000)
9P/Tempel 1	0.056 ± 0.007	Li et al. (2007)
10P/Tempel 2	0.03 ± 0.01	Campins et al. (1995)
22P/Kopff	0.042 ± 0.006	Lamy et al. (2002)
28P/Neujmin 1	0.06 ± 0.01	Campins et al. (1995)
49P/Arend-Rigaux	0.04 ± 0.01	Campins et al. (1995)
81P/Wild 2	0.059 ± 0.004	Li et al. (2009)

Note. — This compilation of V band albedos yields an average value of $\langle p_V \rangle = 0.048 \pm 0.016$. The albedo uncertainty of 49P has been recalculated based on the diameter uncertainty given by Campins et al. (1995).

albedos I determine the mean albedo $\langle p_V \rangle$ to be 0.048 ± 0.016, where the uncertainty is the quadratic sum of the standard deviation and the root mean square of the uncertainties of the individual objects listed in Table 4.2. This approach to estimating this uncertainty takes into account both internal and external uncertainties, i.e., it includes the uncertainties of the individual albedo measurements as well as the scatter inherent to the ensemble of albedos. It is my intention to determine an upper limit albedo for JFCs, so I define the albedo limit as the mean value and add the uncertainty of 0.016, yielding $p_V \leq 0.064$. All the cometary albedos listed in Table 4.2 agree with this limit. The limit is also comparable to, but slightly lower than, the Fernández value (I obtain $p_R = 0.071$ instead of 0.075), assuming a typical normalized spectral reflectivity gradient for comets of 10%/1000Å (Lamy et al. 2004).

Source Region Probabilities. Source region probabilities were calculated by A. Morbidelli (OCA Nice, private communication), based on Bottke et al. (2002b). Figure 4.6 shows the distribution of NEOs originating from some source regions in T_J–$MOID_J$ space. The plots clearly show the concentration of a dynamical group (the Hungarias, see Section 1.1.2.1), and the widespread distribution of NEOs coming from the 3:1 resonance. An intriguing fact is that NEOs from both the JFCs and the outer main belt end up with low T_J and low $MOID_J$. The outer main belt is defined as having semimajor axes $a \geq 2.82$ AU (Bottke et al. 2002b). Objects from both populations are known to have low albedos, which makes it hard to distinguish between the offspring of either population. The results of the dynamical simulations (Bottke et al. 2002b) are utilized to make this distinction. In the following, I denote the probability of an object having an origin in the JFCs or the outer main belt as $P_{\rm JFC}$ and $P_{\rm OB}$, respectively. The probability of an object having an origin in other parts of the main belt is then $1 - (P_{\rm JFC} + P_{\rm OB})$. The physical properties of NEOs that are likely to have originated from the outer main belt and other subpopulations

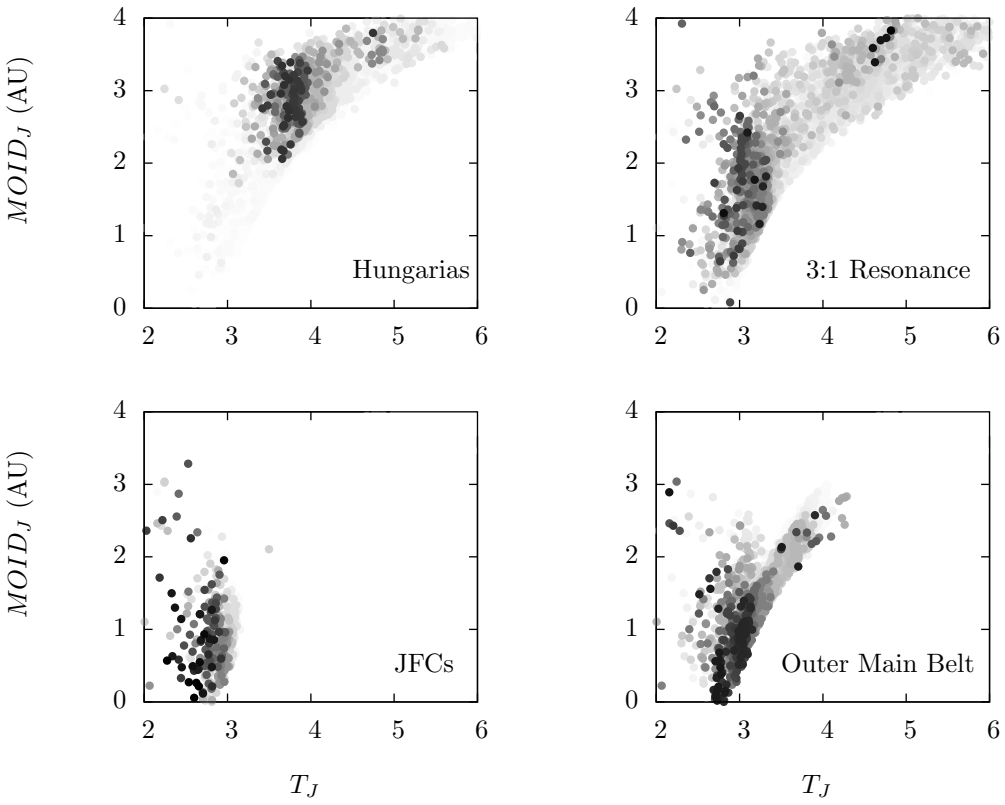

Figure 4.6 Source region probabilities projected on the $MOID_J$ vs. T_J plane (as in Figure 4.5). The plots show the probability distributions of NEOs that originate from the JFCs (bottom left), the outer main belt (bottom right), the Hungarias (top left), and the 3:1 mean motion resonance (top right) in grey–scale: the darker the point, the higher the probability of an origin in the specific source region. The plots clearly show that objects originating from the Hungarias are concentrated in a confined area, whereas objects scattered from the 3:1 resonance cover a large range in both T_J and $MOID_J$. A comparison of the individual plots shows that the JFCs and the outer main belt contribute to the same area in T_J–$MOID_J$ space, and are therefore hard to distinguish in these terms. Sophisticated dynamical models are necessary to disentangle both source populations. The 3:1 resonance descendants populate a space that is similar to that of outer main belt descendants in T_J, but usually have larger values of $MOID_J$.

in the main are the subject of Section 4.1.

4.2.3 Results

Out of the 851 different NEOs (1060 albedo measurements in total) in the combined ExploreNEOs and NEOWISE samples, only 31 and 57 meet the dynamical requirements of the tight and loose sample, respectively. The object list is given in Table 4.3. For each object, I list T_J and $MOID_J$, the geometric albedo, p_V, diameter, d, absolute magnitude, H, slope parameter, G, and references for the latter two. Furthermore, I give P_{JFC} and P_{OB}, whether each object can be considered a cometary object candidate ("Cand."), and

its Δv value. Δv depicts the total specific linear momentum that is necessary to reach that object with a spacecraft, and has been calculated by M. Mueller (SRON, private communications), using the same method as used by Mueller et al. (2011). The upper and lower parts of the table list the tight and loose sample objects, respectively. Objects that have been observed more than once were grouped together and their albedos averaged. Where albedo determinations of a single object from both ExploreNEOs and NEOWISE data have been combined, the H magnitude has been averaged as well. Those objects in the tight sample that have low albedos ($p_V \leq 0.064$) are considered cometary object candidates and are flagged with a "tight" in the cometary candidate column ("Cand."). Loose sample objects that meet the low–albedo criterion are considered possible cometary candidates and are flagged by "loose" in the respective column, i.e., they are "loose sample cometary object candidates". Objects from both samples that fail to meet the low albedo criterion, or objects that fail to meet even the loose sample dynamical criteria, are considered ordinary asteroids and have "no" in the candidate column.

Figure 4.7 shows the albedo distribution of NEOs with $T_J \leq 3.5$. A significantly lower albedo of the $T_J \leq 3.0$ sample compared to that of higher values of T_J is not immediately obvious, since high albedos can be found irrespective of T_J. This is contrary to the trend found by Fernández et al. (2005, depicted as green dots in Figure 4.7), who found only very few objects with $T_J \leq 3.0$ above their $p_R = 0.075$ limit, describing comet–like albedos. I discuss this discrepancy in Section 4.2.4.4 in detail. Based on the sample criteria, 14 out of 31 tight sample objects can be considered "tight sample cometary object candidates" and 26 out of 57 objects from the loose sample cannot be excluded from being "loose sample cometary object candidates".

The average albedos derived from the samples of the 14 tight and 26 loose cometary objects candidates are 0.03 ± 0.04 in both cases, using the weighted mean and the respective standard deviation; the weights are the reciprocal fractional uncertainties. Both averages are lower than the upper limit albedo (0.064) derived in Section 4.2.2.

Table 4.3. Albedo Results of NEOs on Cometary Orbits.

Name	T_J	$MOID_J$ (AU)	p_V	d (km)	H (mag)	G	Ref.	P_{JFC}	P_{OB}	Cand.	Δv (km/s)
tight sample:											
2006 HY51	2.303	0.808	$0.157^{+0.071}_{-0.071}$	$1.22^{+0.23}_{-0.23}$	17.20	0.15	2	0.00	0.14	no	14.8
(3552) Don Quixote	2.313	0.440	$0.027^{+0.019}_{-0.017}$	$20.24^{+1.38}_{-1.57}$	13.0	0.15	5	1.00	0.00	tight	11.0
2010 FJ81[a]	2.339	0.631	$0.041^{+0.016}_{-0.016}$	$0.46^{+0.09}_{-0.09}$	20.80	0.15	2	0.90	0.09	tight	13.1
2010 KY127	2.408	0.763	$0.129^{+0.063}_{-0.063}$	$1.77^{+0.29}_{-0.29}$	16.60	0.15	2	0.00	0.00	no	19.6
(248590) 2006 CS	2.442	0.329	$0.018^{+0.007}_{-0.007}$	$4.73^{+0.84}_{-0.84}$	16.60	0.15	2	0.76	0.04	tight	15.5
2006 KZ112	2.571	0.253	$0.269^{+0.045}_{-0.045}$	$1.18^{+0.03}_{-0.03}$	16.70	0.15	2	0.00	0.12	no	14.4
2010 GQ75	2.639	0.823	$0.106^{+0.029}_{-0.029}$	$0.37^{+0.02}_{-0.02}$	20.20	0.15	2	0.00	0.09	no	15.4
2010 GK23	2.656	0.458	$0.303^{+0.127}_{-0.127}$	$0.28^{+0.04}_{-0.04}$	19.70	0.15	2	0.79	0.04	no	11.4
2010 DK34	2.711	0.455	$0.152^{+0.031}_{-0.031}$	$0.28^{+0.01}_{-0.01}$	20.40	0.15	2	0.15	0.45	no	10.7
2009 KC3	2.729	0.149	$0.023^{+0.018}_{-0.018}$	$2.19^{+0.45}_{-0.45}$	18.00	0.15	2	0.11	0.89	tight	7.4
(5370) Taranis[a]	2.731	0.365	$0.044^{+0.011}_{-0.011}$	$5.82^{+0.63}_{-0.63}$	15.20	0.15	2	0.23	0.76	tight	8.9
2010 FZ80	2.753	0.465	$0.018^{+0.004}_{-0.004}$	$0.87^{+0.01}_{-0.01}$	20.30	0.15	2	0.15	0.45	tight	10.1
2010 GX62[a]	2.757	0.975	$0.027^{+0.015}_{-0.015}$	$0.87^{+0.25}_{-0.25}$	20.20	0.15	2	0.70	0.20	tight	8.9
2009 WO6	2.784	0.871	$0.034^{+0.008}_{-0.008}$	$2.49^{+0.01}_{-0.01}$	17.30	0.15	2	0.91	0.04	tight	10.6
2011 BX18	2.791	0.991	$0.012^{+0.011}_{-0.006}$	$3.02^{+0.74}_{-0.66}$	18.02	0.15	1	0.34	0.58	tight	8.3
2009 XE11	2.796	0.855	$0.038^{+0.006}_{-0.006}$	$2.72^{+0.02}_{-0.02}$	17.00	0.15	2	0.28	0.71	tight	8.4
(217796) 2000 TO64	2.801	0.982	$0.197^{+0.107}_{-0.070}$	$1.11^{+0.28}_{-0.21}$	17.14	0.15	4	0.02	0.08	no	11.6
2010 AG79	2.813	0.931	$0.018^{+0.003}_{-0.003}$	$0.89^{+0.01}_{-0.01}$	20.20	0.15	2	0.68	0.12	tight	11.2
2006 KD1	2.833	0.970	$0.180^{+0.049}_{-0.049}$	$1.14^{+0.12}_{-0.12}$	17.20	0.15	2	0.00	0.05	no	11.7
2009 UV18	2.836	0.498	$0.709^{+0.098}_{-0.098}$	$1.00^{+0.01}_{-0.01}$	16.00	0.15	2	0.57	0.42	no	7.6
2010 JL33	2.910	0.853	$0.047^{+0.009}_{-0.009}$	$1.78^{+0.03}_{-0.03}$	17.70	0.15	2	0.49	0.39	tight	7.9
2010 CN44	2.914	0.446	$0.185^{+0.036}_{-0.036}$	$0.34^{+0.01}_{-0.01}$	19.70	0.15	2	0.33	0.64	no	7.0

Table 4.3 (cont'd)

Name	T_J	$MOID_J$ (AU)	p_V	d (km)	H (mag)	G	Ref.	P_{JFC}	P_{OB}	Cand.	Δv (km/s)
2010 LR68	2.923	0.597	$0.017^{+0.004}_{-0.004}$	$2.25^{+0.15}_{-0.15}$	18.30	0.15	2	0.80	0.19	tight	7.4
(163250) 2002 GH1	2.925	0.886	$0.172^{+0.190}_{-0.093}$	$2.46^{+0.76}_{-0.61}$	15.60	0.15	1	0.00	0.00	no	11.6
(293054) 2006 WP127[a]	2.944	0.483	$0.176^{+0.153}_{-0.092}$	$0.68^{+0.16}_{-0.15}$	18.43	0.15	1	0.02	0.26	no	8.4
2010 GT7	2.959	0.781	$0.326^{+0.064}_{-0.064}$	$0.22^{+0.01}_{-0.01}$	20.20	0.15	2	0.24	0.63	no	7.4
(230979) 2005 AT42	2.968	0.678	$0.207^{+0.047}_{-0.047}$	$1.52^{+0.04}_{-0.04}$	16.50	0.15	2	0.16	0.75	no	7.5
2010 LV108	2.979	0.466	$0.029^{+0.005}_{-0.005}$	$0.23^{+0.01}_{-0.01}$	22.60	0.15	2	0.18	0.74	tight	6.8
(277616) 2006 BN6[a]	2.982	0.845	$0.110^{+0.063}_{-0.039}$	$1.34^{+0.26}_{-0.22}$	17.40	0.15	1, 2	0.01	0.18	no	8.7
2000 JY8	2.985	0.925	$0.328^{+0.246}_{-0.153}$	$1.10^{+0.26}_{-0.21}$	16.64	0.15	1	0.14	0.40	no	7.9
2010 GS7	2.995	0.758	$0.107^{+0.025}_{-0.025}$	$0.20^{+0.01}_{-0.01}$	21.50	0.15	2	0.24	0.63	no	7.2
loose sample: (omitting those objects that are already listed in the tight sample)											
2010 JG87	2.330	1.499	$0.202^{+0.040}_{-0.040}$	$0.41^{+0.02}_{-0.02}$	19.30	0.15	2	0.91	0.04	no	12.1
2010 NW1	2.512	1.220	$0.189^{+0.101}_{-0.101}$	$1.16^{+0.23}_{-0.23}$	17.10	0.15	2	0.32	0.65	no	12.8
2010 DH77[a]	2.516	1.484	$0.010^{+0.003}_{-0.003}$	$0.57^{+0.06}_{-0.06}$	21.80	0.15	2	0.09	0.87	loose	11.1
2000 HD74[a]	2.566	1.416	$0.098^{+0.072}_{-0.069}$	$1.35^{+0.62}_{-0.61}$	18.02	0.15	1, 2	0.13	0.50	no	15.0
2005 YY93	2.618	1.431	$0.084^{+0.016}_{-0.016}$	$1.75^{+0.06}_{-0.06}$	17.10	0.15	2	0.00	0.13	no	11.8
2003 UL12	2.649	1.560	$0.200^{+0.051}_{-0.051}$	$1.08^{+0.02}_{-0.02}$	17.20	0.15	2	0.08	0.90	no	8.4
2004 YR32	2.726	1.544	$0.031^{+0.007}_{-0.007}$	$2.29^{+0.28}_{-0.28}$	17.60	0.15	2	0.74	0.20	loose	8.6
2004 EB	2.754	1.150	$0.036^{+0.011}_{-0.011}$	$2.54^{+0.24}_{-0.24}$	17.20	0.15	2	0.65	0.31	loose	8.7
(20086) 1994 LW	2.770	1.123	$0.013^{+0.014}_{-0.007}$	$4.80^{+1.26}_{-1.12}$	16.90	0.15	1	0.65	0.31	loose	9.3
2001 HA4	2.771	1.548	$0.047^{+0.011}_{-0.011}$	$1.85^{+0.04}_{-0.04}$	17.60	0.15	2	0.34	0.23	loose	9.6
2000 LK	2.788	1.223	$0.126^{+0.113}_{-0.060}$	$0.77^{+0.17}_{-0.16}$	18.43	0.15	1	0.00	0.12	no	13.0
2010 LG64	2.789	1.161	$0.012^{+0.005}_{-0.005}$	$1.12^{+0.49}_{-0.49}$	20.20	0.15	2	0.00	0.00	loose	12.8
2009 WF104	2.800	1.235	$0.047^{+0.009}_{-0.009}$	$2.23^{+0.03}_{-0.03}$	17.20	0.15	2	0.67	0.31	loose	8.0

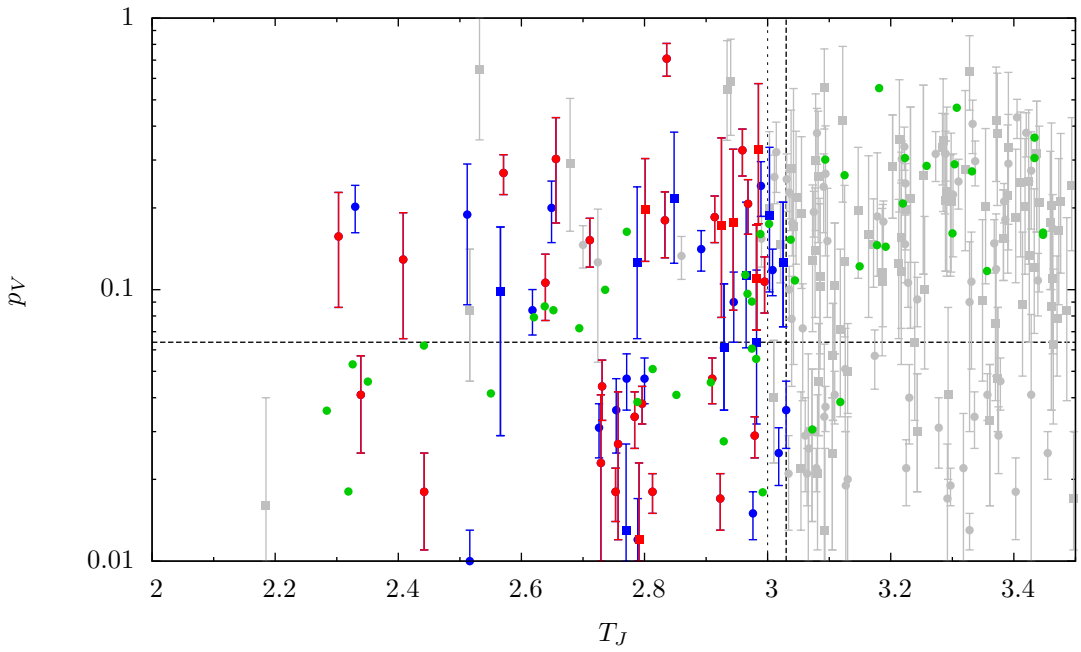

Figure 4.7 Albedos of all NEOs considered in this work with $T_J \leq 3.5$. Circles and boxes represent *ExploreNEOs* and NEOWISE data, respectively; red and blue symbols show tight and loose dynamical sample members, grey symbols depict NEOs that are neither tight, nor loose sample members. Green circles are data from Fernández et al. (2005), shown for comparison, and transformed into V–band albedos using the spectral reflectivity gradient given in Section 4.2.2. The vertical dotted and dashed lines represent the tight and loose T_J limits, respectively. The horizontal dashed line depicts the $p_V \leq 0.064$ upper limit that I apply to identify cometary object candidates. I find a number of high albedo objects at low values of T_J in both the *ExploreNEOs* and NEOWISE samples, which is not present in the Fernández et al. (2005) data. Neither the tight nor the loose sample show the clear correlation of T_J and albedo that is apparent in the Fernández et al. (2005) data (see Section 4.2.4.4).

According to the source region simulations listed in Table 4.3, all cometary object candidates in the tight sample show a clear preference for an origin in the JFCs or the outer main belt, having either $P_{\rm JFC} \geq 0.45$ or $P_{\rm OB} \geq 0.45$. Interestingly, only 7 out of the 12 complementary sample cometary candidates, comprising all members of the loose sample that are not members of the tight sample, show a similar preference. The other sample objects have low to negligible probabilities of having originated from either the JFCs or the outer main belt. Table 4.4 gives the average source region probabilities for the JFCs and the outer main belt of the different subsamples. As to be expected, the average JFC source region probability of a tight sample object (32%) is higher than that of a loose sample object (27.8%). The complementary sample has a lower average JFC source region probability (21.7%). Applying the albedo criterion ($p_V \leq 0.064$) to the samples amplifies this gradient: the average $P_{\rm JFC}$ of the tight, loose and complementary cometary candidate samples are 53.8%, 41.8% and 27.8%, respectively. Surprisingly, the

Table 4.3 (cont'd)

Name	T_J	$MOID_J$ (AU)	p_V	d (km)	H (mag)	G	Ref.	P_{JFC}	P_{OB}	Cand.	Δv (km/s)
(214088) 2004 JN13	2.848	1.220	$0.216^{+0.164}_{-0.091}$	$2.95^{+0.84}_{-0.68}$	14.95	0.15	4	0.16	0.75	no	7.8
2009 ST103	2.892	1.193	$0.141^{+0.024}_{-0.024}$	$0.85^{+0.01}_{-0.01}$	18.10	0.15	2	0.34	0.23	no	8.5
(136874) 1998 FH74[a]	2.929	1.329	$0.061^{+0.044}_{-0.025}$	$3.81^{+1.00}_{-0.87}$	15.80	0.15	1, 2	0.00	0.00	loose	12.1
2010 JE	2.945	1.197	$0.090^{+0.026}_{-0.026}$	$0.41^{+0.05}_{-0.05}$	20.20	0.15	2	0.13	0.65	no	7.5
2005 GL9	2.965	1.503	$0.113^{+0.097}_{-0.052}$	$1.54^{+0.37}_{-0.31}$	17.07	0.15	1	0.00	0.00	no	12.2
2010 MU111	2.976	1.413	$0.015^{+0.003}_{-0.003}$	$1.95^{+0.01}_{-0.01}$	18.60	0.15	2	0.00	0.00	loose	12.6
(265032) 2003 OU	2.982	1.552	$0.064^{+0.054}_{-0.032}$	$2.57^{+0.61}_{-0.57}$	16.62	0.15	1	0.00	0.00	loose	13.0
2010 GH65	2.989	1.317	$0.241^{+0.055}_{-0.055}$	$0.49^{+0.02}_{-0.02}$	18.70	0.15	2	0.15	0.29	no	8.4
2003 WL25	3.003	1.242	$0.187^{+0.147}_{-0.089}$	$1.54^{+0.35}_{-0.31}$	16.53	0.15	1	0.00	0.04	no	10.1
2010 FY80	3.008	1.038	$0.118^{+0.023}_{-0.023}$	$0.45^{+0.01}_{-0.01}$	19.70	0.15	2	0.07	0.22	no	8.0
(16064) Davidharvey	3.018	0.858	$0.025^{+0.006}_{-0.006}$	$4.10^{+0.59}_{-0.59}$	16.56	-0.14	3	0.13	0.83	loose	7.2
(8201) 1994 AH2[a]	3.025	0.656	$0.126^{+0.084}_{-0.053}$	$2.09^{+0.52}_{-0.44}$	16.30	0.15	1, 2	0.02	0.26	no	7.8
(26760) 2001 KP41	3.030	0.920	$0.036^{+0.010}_{-0.010}$	$5.39^{+0.37}_{-0.37}$	15.58	0.05	3	0.06	0.85	loose	7.9

Note. — The column "Cand." describes whether the respective object can be considered a tight sample cometary object candidate ("tight"), cannot be excluded from being a loose sample cometary object candidate ("loose"), or most likely is not of cometary origin, i.e., it does not even meet the loose sample criteria ("no") or fails to meet the albedo criterion. There are 14 out of 31 objects in the tight sample that meet the albedo upper-limit of 0.064. In the loose sample, 26 out of 57 meet the albedo criterion. Δv values have been calculated using the same method as by Mueller et al. (2011).

[a]Object has more than one albedo measurement; p_V, d, and H magnitude given here represent averaged values. Albedo uncertainties are quadratic sums of the standard deviation and the root–mean–square of the individual uncertainties.

References. — (1): Trilling et al. (2013); (2): Mainzer et al. (2011b); (3): Pravec et al. (2012); (4): Hagen et al. (2011); (5): This work.

Table 4.4. Average Source Region Probabilities of NEOs.

Sample	Criteria	P_{JFC} (%)	P_{OB} (%)
tight	$T_J \leq 3.0$, $MOID_J \leq 1.0$	32.0 ± 5.9	32.5 ± 5.1
tight cc.	$T_J \leq 3.0$, $MOID_J \leq 1.0$, $p_V \leq 0.064$	53.8 ± 8.5	37.1 ± 8.4
loose	$T_J \leq 3.03$, $MOID_J \leq 1.6$	27.8 ± 4.1	32.9 ± 3.8
loose cc.	$T_J \leq 3.03$, $MOID_J \leq 1.6$, $p_V \leq 0.064$	41.8 ± 6.6	35.0 ± 6.3
complementary	$3.0 < T_J \leq 3.03$, $1.0 < MOID_J \leq 1.6$	21.7 ± 5.4	33.4 ± 6.1
complementary cc.	$3.0 < T_J \leq 3.03$, $1.0 < MOID_J \leq 1.6$, $p_V \leq 0.064$	27.8 ± 9.0	32.6 ± 9.8

Note. — The abbreviation "cc." refers to the respective cometary candidate sample. Uncertainties are standard deviations, reflecting the scatter in the probabilities of the individual objects. The complementary sample includes those objects that are members of the respective loose sample but not of the tight sample.

outer main belt origin probability is somewhat stable throughout the different sample definitions (32.5%–37.1%).

Among the cometary object candidates of the tight sample I identify 8 objects, (3552) Don Quixote, 2010 FJ81, (248590) 2006 CS, 2010 GX62, 2009 WO6, 2010 AG79, 2010 JL33, and 2010 LR68, with $P_{\rm JFC} \geq 0.49$. I set an arbitrary limit of 0.49 for the source region probability; choosing the more intuitive value of 0.5 would exclude 2010 JL33, which should be included on the basis of its still high JFC origin probability. The objects listed above are immediate candidates for a cometary origin. 6 other targets are also members of the tight sample but have a lower JFC origin probability. Most of the remaining 12 objects of the complementary sample (cf. Table 4.4) have a comparatively low probability of a JFC origin, but cannot be excluded as having a JFC origin. The Δv parameters of the tight sample cometary object candidates range from 7.4 to 15.5 km/s, whereas the complete loose sample covers values from 6.4 to 19.6 km/s.

4.2.4 Discussion

4.2.4.1 Assessment of the Size–Limited Fraction of Cometary Objects in the NEO Population

In the following analysis, I use an approach similar to that used by DeMeo and Binzel (2008).

From Table 4.3, I find 31 objects that meet the tight sample criteria of having a comet–like orbit, 14 (45.2%) of which also meet the albedo criterion and can be considered cometary candidates. 57 objects meet the loose sample criteria of which 26 (45.6%) have cometary albedos. I derive uncertainties on the latter estimates by exploring the numbers of objects for which $(p_V \pm \sigma_{pV}^{\pm}) \leq 0.064$, where $\sigma_{pV}^{\pm}$ is the respective 1σ uncertainty upper/lower uncertainty as listed in Table 4.3: the number of objects in the

tight sample is constant, the loose sample covers the range of 24–29. Hence, 45.2% and $45.6 \pm 5.3\%$ of those NEOs on comet–like orbits according to the tight and loose[4] sample definitions, respectively, also have comet–like albedos and can be considered cometary object candidates. These percentages describe the probability of a randomly picked NEO that meets the tight and loose sample dynamical criteria to have $p_V \leq 0.064$ as well.

I estimate the fraction of the total (known + unknown) NEO population that is on comet–like orbits. In the known NEO population I find 354 (3.9%) and 576 (6.4%) NEOs to meet the tight and loose sample dynamical criteria, respectively. Both estimates suffer from the incompleteness of the known NEO population and are affected by observational bias, underestimating the number of low–albedo and low–T_J[5] objects among the NEOs. In an attempt to de–bias both estimates, I make use of the work of Stuart (2003), who estimated that 30% of the total NEO population in a size–limited sample have $T_J \leq 3.0$. I use this estimate to de–bias the fractions of NEOs on comet–like orbits according to the tight and loose sample dynamical criteria using the following line of thought: 609 known NEOs (6.8%) have $T_J \leq 3.0$; the estimate of the total (known + unknown) NEO population based on Stuart (2003) is 30%, which is larger by a factor of 4.4. Assuming the dynamical distribution in T_J–$MOID_J$ space (see Figure 4.5) of the known and unknown fractions of the NEO population to be similar, I compute the fractions of the total NEO population that meet the tight and loose sample dynamical criteria as 3.9%×4.4 =17.2% and 6.4%×4.4 = 28.2%, respectively. The numbers denote the probabilities of a randomly picked known or unknown NEO to meet the tight or loose sample criteria. Stuart (2003) does not provide an uncertainty on his estimate. Given the fact that his results are based on survey data that are a decade old, I adopt a conservative 50% relative uncertainty on his estimate, propagating into the tight and loose sample estimates as $17.2 \pm 8.6\%$ and $28.2 \pm 14.1\%$, respectively.

As mentioned before, NEOs that originated from the JFC population and the outer main belt populate similar areas in T_J–$MOID_J$ phase–space (cf. Figure 4.6) and are both known to have low albedos, making them barely distinguishable using this method. I apply the computed source region probabilities to make the distinction between the two object types. The averaged probabilities $\langle P_{\mathrm{JFC}} \rangle$ of tight and loose sample cometary object candidates actually being of cometary origin, are, according to Table 4.4, $(53.8 \pm 8.5)\%$ and $(41.8 \pm 6.6)\%$, respectively.

I derive the fraction of NEOs that are of cometary origin as the product of the proba-

[4]I neglect the asymmetry between the upper (5.3%) and lower (3.5%) uncertainties and adopt the larger upper uncertainty for the sake of simplicity.

[5]The discovery of low–T_J objects is hampered by their high eccentricities, making them spend more time near aphelion, where they are more likely to elude discovery.

bilities of having a comet–like orbit and albedo, and to be of JFC origin ($\langle P_{\mathrm{JFC}} \rangle$):

$$(17.2 \pm 8.6)\% \times 45.2\% \times (53.8 \pm 8.5)\% = (4.2 \pm 2.2)\%, \text{ and}$$
$$(28.2 \pm 14.1)\% \times (45.6 \pm 5.3)\% \times (41.8 \pm 6.6)\% = (5.4 \pm 2.9)\%$$

of total NEO population, based on the tight and loose sample definitions, respectively, are of cometary origin.

Both estimates are equally legitimate and agree within their uncertainties. I adopt the rounded average $(5 \pm 3)\%$ as the final estimate of the fraction of cometary objects in the NEO population. Note that this estimate is derived for a size–limited sample of the NEO population.

4.2.4.2 Discussion of the Prerequisites

The previous analysis is based on a number of prerequisites and assumptions that are discussed in the following sections.

Discussion of the Robustness of the Method. The largest uncertainty in this assessment is introduced by the estimate of the fraction of NEOs on comet–like orbits. Here, I utilize the estimate of the fraction of NEOs with $T_J \leq 3.0$ by Stuart (2003). I have to rely on this estimate due to the incompleteness of known NEO population for low–albedo and low–T_J objects. I note that his estimate is nearly a decade old and based on results of the LINEAR survey with a strictly limited number of known NEOs at that time. Nevertheless, it still provides the best available estimate of the fraction of NEOs on comet–like ($T_J \leq 3.0$) orbits. The adopted relative uncertainty of 50% might be overestimated, which implies that the uncertainties on the final result are smaller than expected.

A more robust approach would require the use of model distributions of the total NEO population (e.g., Bottke et al. 2002b) to estimate the completeness of the known NEO population. Such an approach is the subject of future work and will provide better estimates of the fraction of NEOs on comet–like orbits and the respective uncertainties.

Dynamical and Albedo Criteria. I assume the dynamical sample criteria and albedo limit (cf. Section 4.2.2) to describe the subset of cometary objects in the NEO population well. Earlier analyses (Fernández et al. 2005; DeMeo and Binzel 2008) based their sample on $T_J \leq 3.0$ only. Their approach does not account for the segregation of cometary and asteroidal objects in terms of $MOID_J$ that is inherent to the NEO population (Sosa et al. 2012). In the currently known small body populations, $T_J \leq 3.0$ is met by 93.7% (355 in absolute numbers) of the periodic comets and 6.8% (609) of the NEOs. In Section 4.2.2, I have shown that the tight sample criteria are met by 86.8% (329) of the periodic comets and 3.9% (354) of the NEOs. The loose sample criteria are met by 95.3% (361)

of the periodic comets and 6.4% (576) of the NEOs. Comparing the numbers shows that the absolute number of ordinary asteroids is lower in both samples compared to the $T_J \leq 3.0$ selection, and that the absolute number of periodic comets is higher in the loose sample compared to the $T_J \leq 3.0$ selection. Hence, the loose sample criteria include more comets and fewer asteroids than the more simple $T_J \leq 3.0$ selection. Comparing the ratio of cometary to asteroidal objects in the individual samples shows that it is higher in the tight (329/[329+354]=48%) and loose samples (361/[361+576]=39%) compared to the $T_J \leq 3.0$ selection (355/[355+609]=37%). Hence, the sample definitions used in this analysis provide a better description of the distribution of objects on comet–like orbits, and therefore better describe the cometary object population. Figure 4.6 shows that the sample definitions also provide a better separation from objects that are likely to have been brought to the NEO population by the 3:1 mean motion resonance compared to the simple $T_J \leq 3.0$ criterion.

Comparing the averaged albedos of the tight and loose sample cometary object candidates, both of which yield 0.03 ± 0.04 (cf. Section 4.2.3), with the upper limit albedo $p_V \leq 0.064$ based on the measured albedos of comets (Table 4.2), shows that the albedos of cometary objects, as identified in this work, are significantly lower than the adopted upper limit. Hence, the overall results do not depend strongly on the choice of the albedo upper limit.

Source Region Probabilities. The disentanglement of the cometary and outer main belt fraction in the dynamically and physically selected samples is based on the JFC origin probabilities provided by Bottke et al. (2002b). This approach is legitimate, since most periodic comets are JFCs (329 out of 379 have $2.0 \leq T_J \leq 3.0$), and the comet origin sample considered in Bottke et al. (2002b) is not strictly confined to $2.0 \leq T_J \leq 3.0$. Possible contributions from LPCs are not taken into account. A weakness of the work of Bottke et al. (2002b) is that they neglect gravitational perturbations of the terrestrial planets in their comet integrations. The results of Levison et al. (2006) suggest that their inclusion leads to increased numbers of dormant comets with $T_J > 3.0$. In the case of comets, Bottke et al. (2002b) have also neglected the dynamical effects of cometary activity. Furthermore, the NEO sample on which their analysis is based is more than a decade old and has been calibrated using a population of only 138 NEOs that were discovered by the Spacewatch program (e.g., Rabinowitz 1994). However, Mainzer et al. (2011b) showed that the NEO model population used by Bottke et al. (2002b) is reasonably consistent with the observed population.

4.2.4.3 Comparison with Other Works

I compare the estimates of the fraction of cometary objects in the NEO population, based on a size–limited sample, with previous assessments:

- Bottke et al. (2002b) used dynamical simulations of a de–biased synthetic NEO population to estimate the fraction of cometary objects in the NEO population and found a fractional content of (6±4)% in the magnitude–limited NEO population with $13 < H < 22$. The conversion from magnitude to size–limited estimates is nontrivial, increasing their estimate easily by a factor of 2–3 (DeMeo and Binzel 2008). Hence, the result of this analysis is smaller, but still agrees within their uncertainties. I partially base the analysis of this work on results of their work, but since I am using a different approach by having based the analysis on measured albedos, I can rule out to be biased by their result.

- Fernández et al. (2005) based their assessment on albedo measurements of 10, dynamically selected NEOs. Their sample selection was solely based on observability and is therefore not de–biased, and has to be assumed to be magnitude–limited. From their target sample they selected objects on comet–like orbits using $T_J \leq 3.0$ and objects with albedos $p_R \leq 0.075$. They find 4% of all NEOs to be of cometary origin. Applying the factor of 2–3 for the conversion from their magnitude to a size–limited sample, places the result of this analysis again lower than their estimate.

- DeMeo and Binzel (2008) used a method similar to the one used here. They based their analysis on 39 NEOs with $T_J \leq 3.0$. In order to identify cometary object candidates, they either require $p_R \leq 0.075$ or a C, D, T, or P taxonomic classification of the object and derived a fractional content of (8 ± 5)% in a size–limited sample of the total NEO population, which is slightly higher than the result of this analysis. They also base their result on the assumption that 30% of all NEOs in a size–limited sample have $T_J \leq 3.0$ (Stuart 2003), which is, at least partially, responsible for the good agreement.

The estimates of the fraction of cometary objects in the NEO population in this work are lower than earlier estimates. Note that the estimates are purely based on the results of the ExploreNEOs and NEOWISE programs; no other albedo measurements from the literature have been utilized, in order to provide an independent assessment of the fraction of cometary objects in the NEO population.

4.2.4.4 High Albedos Among the Low-T_J NEOs

In Figure 4.7, I show the albedos of the sample targets as a function of T_J, together with albedo measurements used by Fernández et al. (2005). The latter found that of the 13 objects they plotted with $T_J \leq 2.6$ (10 of their own and 3 from the literature), all had albedos $p_R \leq 0.075$, within the uncertainties. However, I find objects meeting the tight and loose sample dynamical criteria with $T_J \leq 2.6$ that have high albedos (e.g., 2006 HY51 with $T_J = 2.3$ and $p_V = 0.157$). I use a two–dimensional two–sample Kolmogorov-Smirnov test (KS test, Press et al. 1992) to explore whether the tight and loose samples

show significant differences compared to the Fernández et al. (2005) sample. The KS test is a non–parametric test that determines the significance level (p–value) at which the "Null Hypothesis" that two data samples are drawn from the same population, can be rejected. Small p–values refer to a high probability that the two samples are drawn from different populations. Large values of p, however, do not coercively mean that the two samples are drawn from the same population; it just means a low probability that they are drawn from entirely different populations. In order to provide the best compatibility, I restrict all samples to the range $2.0 \leq T_J \leq 3.03$. I find p–values of 4.8% and 4.3% for the tight and loose samples, respectively, compared to the Fernández et al. (2005) sample. Both p–values are lower then 5%, i.e., it is likely that both samples are drawn from a different population than the Fernández et al. (2005) at a $\sim 2\sigma$ confidence level. The p–value for all *ExploreNEOs*/NEOWISE targets with $2.0 \leq T_J \leq 3.03$ compared to the Fernández et al. (2005) data is 1.6%, increasing the probability of a different origin. I suspect the deviation between the individual samples to be caused by the higher degree of incompleteness of the NEO population at the time of the Fernández et al. (2005) analysis. I can exclude the vulnerability of the *ExploreNEOs* sample to optical discovery bias as a cause for the existence of high–albedo objects at low T_J, since the effect is observed in the NEOWISE sample as well (cf. Figure 4.7). Furthermore, I find a number of low–albedo objects with $3.2 \leq T_J \leq 3.5$, a range in which no such objects were known at the time of the literature search by Fernández et al. (2005). These findings suggest the albedo distribution of cometary objects to be less strictly correlated to the dynamical distribution as previously expected (Fernández et al. 2005).

I also find objects with high probabilities of having their origin in the JFC region, but with exceptionally high albedos (cf. Table 4.3) in the tight and loose samples. It is possible, that some of these objects show some kind of cometary activity and therefore appear to have albedos much higher than expected. Some candidates for cometary activity are 2010 GK23 ($p_V = 0.303$, $P_{\mathrm{JFC}} = 0.79$), 2009 UV18 ($p_V = 0.709$, $P_{\mathrm{JFC}} = 0.57$, cometary activity has already been suggested by Mainzer et al. 2012) and 2012 JG87 ($p_V = 0.202$, $P_{\mathrm{JFC}} = 0.91$). Cometary activity has been discovered in NEO (3552) Don Quixote (see below and Section 4.3). Detailed observations will be necessary to clarify the question of cometary activity in the other objects.

4.2.4.5 Individual Objects

In the course of this analysis, object (3552) Don Quixote was found to have an unrealistically low albedo ($p_V = 0.001$) according to the default *ExploreNEOs* pipeline results, which is much lower than earlier estimates by Veeder et al. (1989) ($p_V = 0.02$) and Fernández (1999) ($p_V = 0.045$). The observational data were re–analyzed (see above) and the discrepancy was found to be caused by cometary activity of the object (see Section 4.3 for a detailed discussion). Diameter and albedo results given in Table 4.3 refer to the properties

of the nucleus only, and are in good agreement with earlier results.

The lowest Δv parameters of the tight and loose–sample objects are 6.8 and 6.4 km/s, respectively. The most easily accessible and most promising cometary object candidate is 2010 LV108 (Δv=6.8 km/s). For comparison, the Δv parameter of the Moon and Mars are 6.0 and 6.3 km/s, respectively (Benner 2012).

Four loose–sample cometary object candidates have $P_{\rm JFC} = P_{\rm OB} = 0$: 2010 LG64, (136874) 1998 FH74, 2010 MU111, and (265032) 2003 OU. Despite their comet–like orbits and albedos, dynamical simulations (Bottke et al. 2002b) suggest clear preferences for an origin of each of the objects from a region in the inner main belt with a probability larger than 50%. These objects are interesting cases for further examination, given the discrepancies between their dynamical and physical properties, which might help to learn more about the differences between asteroidal and cometary objects.

The implications of the findings for our picture of the Solar System are further discussed in Section 6.1.

4.2.5 Conclusions

- I have determined the fraction of cometary objects in the NEO population based on a size–limited sample. I find (5 ± 3)% of the total NEO population to have a cometary origin, which is lower but comparable to earlier estimates in the literature.

- I have identified 8 objects that are the most promising cometary candidates: (3552) Don Quixote, 2010 FJ81, (248590) 2006 CS, 2010 GX62, 2009 WO6, 2010 AG79, 2010 JL33, and 2010 LR68. Object (3552) Don Quixote was found to show cometary activity (see Section 4.3). The most promising cometary candidate with the lowest Δv parameter is 2010 LV108 (Δv=6.8 km/s).

- In contrast to the results of Fernández et al. (2005), I find a number of NEOs with $T_J \leq 2.6$ to have high, non–comet–like, albedos. This finding suggests that the albedo distribution is less strictly correlated with the dynamical distribution than the results of Fernández et al. (2005) appear to suggest.

- I show that combining the widespread $T_J \leq 3.0$ criterion to identify cometary objects with a $MOID_J$ criterion is a useful means to refine the identification of objects on comet–like orbits.

4.3 The Discovery of Cometary Activity in NEO (3552) Don Quixote

The NEO (3552) Don Quixote was observed in the framework of the ExploreNEOs program. Due to an error in the observation planning, all image data turned out to be saturated. The IRAC data of Don Quixote have been recovered and reanalyzed in the course of my assessment of the cometary content of the NEO population (Section 4.2). The recovered images show extended emission around the object, which I interpret as cometary activity.
In the following section, I present and discuss the reanalyzed IRAC data of Don Quixote. I constrain the bulk of the emission as molecular line emission from CO_2, estimate the gas and dust production rates, and try to constrain the cause and longevity of the activity from additional observations from the literature.
Note that this analysis was done in collaboration with other scientists. In the following presentation I focus on the work performed by myself, and I explicitly mark contributions made by others, most of which were provided by J. Hora (CfA Harvard), one of the leading IRAC instrument specialists.

4.3.1 Introduction

The NEO population is replenished from collisional fragments from main belt asteroids (Wetherill 1979; Bottke et al. 2002b) and short–period comets (see also Wetherill 1979; Weissman et al. 2002, and Section 1.1.3). Short–period comets are also referred to as Jupiter family comets (JFCs, see Section 1.1.5), due to their strong dynamical link to Jupiter. The dynamical lifetimes of JFCs are expected to far exceed their active lifetimes (Levison and Duncan 1997). Hence, it is likely that the NEO population includes a significant number of extinct or dormant comets, which have finally or at least temporarily, ceased being active (Weissman et al. 2002).

As of January 2013, 93 comets in near–Earth space, i.e., comets with perihelion distance $q \leq 1.3$ AU and periods lower than 200 yrs, are known, according to the JPL Near Earth Object Program Website. One example of a comet that appears to have ceased activity and has become a dormant or extinct comet is 107P/Wilson–Harrington. Wilson–Harrington was discovered in 1949 as an active comet, was subsequently lost and re–discovered in 1979 as NEO (4015) 1979 VA and confirmed as Wilson–Harrington in 1992, lacking any trace of cometary activity (Bowell et al. 1992; Fernández et al. 1997). Occasionally, objects that were originally designated as asteroids have to be reclassified after activity was detected in optical follow–up observations performed after their initial discovery (e.g., DeMeo and Binzel 2008, and references therein). Usually, activity is discovered in such cases a few weeks or months after the discovery of the object itself. Similar to other short–period comets, these objects usually have diameters smaller than 20 km

(Lamy et al. 2004).

NEO (3552) Don Quixote was discovered in 1983 as an asteroid. Combined data from Binzel (1987) and Weidenschilling et al. (1990) estimate Don Quixote's rotational period to be ∼7 hrs and its V–band lightcurve amplitude to be 0.57 mag (peak–to–peak). Its photometric $B-V$ index is 0.83 (Weidenschilling et al. 1990), and its H magnitude is estimated as $H = 13.0$ mag as provided by the Minor Planet Center Observations Database (accessed November 2012). Don Quixote's orbit, having a period of 8.68 yrs and a Tisserand parameter (see Section A.1.3.1) with respect to Jupiter of $T_J = 2.313$, resembles very much the orbit of typical JFCs, which is supported by dynamical simulations (Hahn and Rickman 1985). Veeder et al. (1989) obtained thermal–infrared observations of Don Quixote and used a thermal model to derive a diameter of 18.7 km and a geometric V–band albedo of 0.02, which makes Don Quixote the 3rd–largest known NEO after (1036) Ganymed and (433) Eros. The low albedo, which agrees well with the classification of Don Quixote as a D–type asteroid (Hartmann et al. 1987; Binzel et al. 2004), is typical for cometary nuclei (Lamy et al. 2004). Bottke et al. (2002b) have used their dynamical model of the NEO population to determine Don Quixote's probability to be of JFC origin, which turns out to be 100%. Of all NEOs, Don Quixote is the prime candidate for having a cometary origin. Since it has never been reported to show any sign of activity, it was believed to be an extinct, or at least dormant comet (Weissman et al. 1989, 2002).

4.3.2 Observations and Data Reduction

4.3.2.1 Spitzer IRAC Observations

Don Quixote was observed by the Spitzer Infrared Array Camera (IRAC, Fazio et al. 2004, see also Section 2.2.2.1) within the *ExploreNEOs* program on August 22, 2009, at 19:48 UT. The observations at 3.6 and 4.5 μm were taken 18 days prior to Don Quixote's perihelion passage, when the target had a heliocentric distance of 1.23 AU, a solar phase angle of 55°, and a distance from Spitzer of 0.55 AU.

The observations (AOR 32690176) consist of 9 single frames with individual frame times of 12 s in each band, using the "moving cluster" mode (see Section 2.2.2.1). Between the individual frames the telescope pointing was changed in such a way that the 3.6 and 4.5 μm detectors are integrated alternately to provide nearly simultaneous imaging in both bands. Additionally, the pointing was offset for each frame differently (Trilling et al. 2010) in order to provide dithering, a procedure that makes use of more detector area to smooth background effects (see Section A.2.1.1). The final 3.6 and 4.5 μm mosaics were constructed by aligning the individual frames in each band in the rest frame of Don Quixote, based on its projected motion, using the standard *ExploreNEOs* data reduction pipeline. In the following, these maps will be referred to as "unprocessed maps" for the purposes of the further analysis; the maps are shown in Figure 4.8, top row. The image

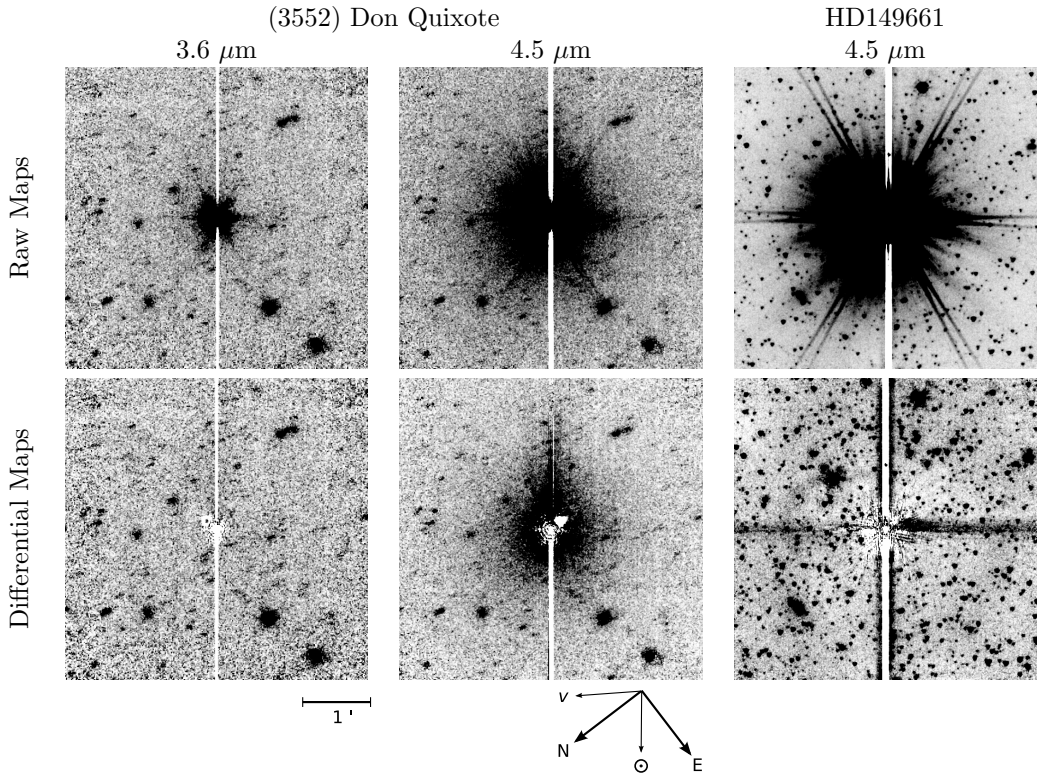

Figure 4.8 Inverted raw (top row) and PSF–subtracted differential (bottom row) Spitzer IRAC maps of (3552) Don Quixote at 3.6 μm (left) and 4.5 μm (center), and a 4.5 μm map of HD149661 (right) for comparison. The white bars through the object's center are image artifacts, caused by the well–known "column pull–down" effect (see Section 2.2.2.1 and the IRAC Instrument Handbook 2012; Spitzer Observer's Manual 2007), observed in IRAC channel 1 and 2 mosaics. The white fringes and triangular areas in the differential mosaics are the result of a misalignment of the model and mosaic PSFs during the subtraction, and well–understood ghost images of the overexposed target (see Section 2.2.2.1), respectively. The differential 4.5 μm map of Don Quixote clearly shows a diffuse, elongated feature centered on the saturated object that is not visible in the 3.6 μm map. The feature is extended in the anti–solar direction, as indicated below the maps (v indicates the velocity vector of the object). The differential mosaic of HD149661 does not show any extended emission. The horizontal bars emerging from the star in the differential mosaics are caused by the "muxbleed" effect (see Section 2.2.2.1 and the IRAC Instrument Handbook 2012), due to overexposure of the star. There is no known effect that would lead to a radial brightening around a saturated point source. HD149661 is 3.8 mag brighter than Don Quixote at the time of observation; hence, any saturation effect producing the radially symmetric extended emission around Don Quixote would lead to the same effect in HD149661.

reduction was performed by J. Hora (CfA Harvard).

Due to an error in the proper retrieval of the object geometry[6] during the observation planning (see Section 2.2.3), the frame times were overestimated, and the object was found to be saturated in all frames. In the course of my work on the assessment of the cometary fraction in the NEO population (see Section 4.2), the flux densities of 3 saturated objects could be recovered by J. Hora, using a PSF fitting technique: the IRAC PSF (see Figure 2.7 on page 54) was subtracted from the unprocessed maps after aligning with the object's image and scaling in such a way as to minimize the residual, which is derived from the non–saturated wings of the PSF and its spikes (see Figure 2.7 on page 54). The object's flux density was then derived from the scaling factor of the PSF, within an accuracy of 1% (Marengo et al. 2009).

Application of the subtraction technique to Don Quixote revealed the existence of extended emission around Don Quixote in the 4.5 μm band, but not at 3.6 μm (see Figure 4.8, bottom row). The subsequent image processing is described below.

4.3.2.2 Additional Observation Data

I have searched the literature for previous observations of Don Quixote to compare with the *ExploreNEOs* IRAC observations. I was unable to find reliable optical photometry data on Don Quixote. For instance, the "4th Release of the Sloan Digital Sky Survey Moving Object Catalog" (Ivezic et al. 2002) contains no observations of Don Quixote. The only available source of large quantities of optical photometry data is the MPC, which collects astrometric observations that are occasionally accompanied by very rough photometric information, and are therefore useless for a detailed analysis.

Thermal–infrared observations are listed in Table 4.5, illustrated in Figure 4.9, and discussed below.

WISE Observations. The Minor Planet Center reports four observations of the "Wide–Field Infrared Survey Explorer" (WISE, Wright et al. 2010, see also Section 2.3) of Don Quixote in September 2010 during the "3–band cryogenic" phase of the mission. The observations took place with Don Quixote at $r = 3.9$ AU and 410 days after the same perihelion passage relevant to the *ExploreNEOs* IRAC observations. I accessed the measured flux densities via the "WISE 3–Band Cryo Known Solar System Object Possible Association List" provided by the NASA/IPAC Infrared Science Archive/WISE Observations Database. Note that especially the sensitivity of the 11.6 μm band measurement is degraded compared to the fully cryogenic part of the mission. The "association list" provides magnitudes derived using point source profile–fitting and multi–aperture photometry. I converted the reported magnitudes into flux density units using the zero-point magnitudes

[6] A check of the *ExploreNEOs* observation planning protocols revealed that Don Quixote is the only case suffering from this planning error.

Table 4.5. Don Quixote Observations.

Observatory	Date & Time (UT)	λ (μm)	r (AU)	Δ (AU)	α (°)	F (mJy)	σ_F (mJy)	Ref
Spitzer/IRAC*	09-08-22 19:48	3.6	1.229	0.550	55.4	210	10	1
Spitzer/IRAC*	09-08-22 19:48	4.5	1.229	0.550	55.4	970	50	1
IRTF/SpeX	09-10-18	S	1.314	0.303	15.5	–	–	3
IRTF	83-10-13 09:21	10.1	1.574	0.664	23.1	9000†	100	2
IRTF	83-10-13 10:04	10.1	1.575	0.665	23.1	7200†	100	2
WISE	10-09-28 10:22	3.4	3.922	3.812	14.8	0	0.1	4
WISE	10-09-28 10:22	4.6	3.922	3.812	14.8	0	0.1	4
WISE	10-09-28 10:22	11.6	3.922	3.812	14.8	39	8	4
WISE	10-09-27 13:44	3.4	3.924	3.818	14.8	0	0.1	4
WISE	10-09-27 13:44	4.6	3.924	3.818	14.8	0	0.2	4
WISE	10-09-27 13:44	11.6	3.924	3.818	14.8	28	6	4
WISE	10-09-27 16:54	3.4	3.925	3.817	14.8	0	0.1	4
WISE	10-09-27 16:54	4.6	3.925	3.817	14.8	0	0.2	4
WISE	10-09-27 16:54	11.6	3.925	3.817	14.8	36	7	4
WISE	10-09-28 07:11	3.4	3.928	3.813	14.8	0	0.1	4
WISE	10-09-28 07:11	4.6	3.928	3.813	14.8	0.1	0.1	4
WISE	10-09-28 07:11	11.6	3.928	3.813	14.8	47	5	4

Note. — The observations are ordered by Don Quixote's heliocentric distance. $F = 0$ refers to a non–detection of the object; the respective flux density uncertainty then gives the 95% confidence upper limit flux density (see text). The meanings of the columns are: Date & Time: date and time of the observation mid–times (YY-MM-DD HH:MM), λ: monochromatic wavelength ("S" in case of spectroscopic observations), r: heliocentric distance, Δ: distance from the observer, α: solar phase angle, F: measured flux density (not color–corrected, if not mentioned otherwise), σ_F: 1σ uncertainty on the measured flux, or the 95% (2σ) confidence upper limit flux density;

*Spitzer/IRAC flux densities of Don Quixote refer to the thermal–infrared emission of the nucleus only;

†flux densities from Veeder et al. (1989) are color–corrected;

References. — (1) this work; (2) Veeder et al. (1989); (3) Thomas (2013); (4) WISE data as extracted from the WISE 3–Band Cryo Known Solar System Object Possible Association List (see text)

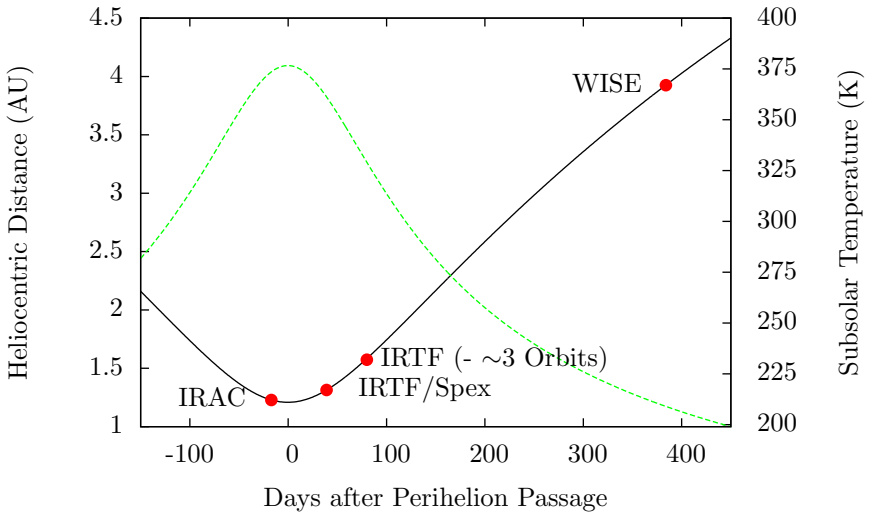

Figure 4.9 Don Quixote's heliocentric distance as a function of time. The black continuous line represents the heliocentric distance as a function of the number of days after its perihelion passage. The red dots indicate the relative position in its orbits at the time of the individual observations listed in Table 4.5. Observations that were performed in a different orbit cycle are marked. The green dashed line indicates the subsolar temperature on the surface of Don Quixote according to the model fit discussed in Section 4.3.3.3.

reported in Wright et al. (2010) and list them in Table 4.5. As it turned out, Don Quixote was too faint to be clearly detected in most of the 3.5 and 4.6 μm measurements. In this case, the data represent 2σ upper limit flux densities, covering a 95% confidence interval.

IRTF Photometry. Don Quixote was observed by Veeder et al. (1989) using the NASA Infrared Telescope Facility (IRTF). They report two N–band (10.1 μm) magnitudes measured on October 13, 1983, which were converted into flux density units using a calibration spectrum of Vega (Rieke et al. 2008) and are listed in Table 4.5. The observations of Veeder et al. (1989) took place with Don Quixote at $r = 1.57$ AU, 80 days after perihelion, nearly three orbits earlier than the IRAC observations.

IRTF SpeX Spectroscopy. C. A. Thomas (NASA Goddard Spaceflight Center, at that time Northern Arizona University) has obtained spectroscopic observations of Don Quixote in the wavelength range 0.6–2.6 μm using the SpeX instrument (Thomas 2013). SpeX (Rayner et al. 2003) is a medium resolution spectrograph and imager unit at the IRTF. The SpeX spectrum was obtained on October 18, 2009, 40 days after its perihelion passage in the same orbit of Don Quixote as the IRAC observations. Don Quixote and the solar standard star Landolt 113-276 were observed simultaneously. The data were reduced using SpeXtool (Cushing et al. 2004) and the telluric atmosphere correction was done using the ATRAN model atmosphere (Lord 1992; Rivkin et al. 2004, e.g.,). The spectrum

shown in Figure 4.13 on page 140 was produced by division of the measured spectrum of Don Quixote by that of the solar analog star, resulting in a measure of the reflectance of the object's surface. The reduction of the spectral data was performed by C. Thomas, and is explained in detail in Thomas (2013).

4.3.3 Spitzer/IRAC Data Analysis

4.3.3.1 Emission from the Nucleus

The flux density of the unresolved core was estimated using the aforementioned PSF–fitting routine by J. Hora. The results of the PSF subtraction are shown in the bottom row of Figure 4.8. The derived flux densities listed in Table 4.5 are those of the point–like nucleus of the object.

4.3.3.2 Emission from the Coma and the Tail

A detailed inspection of the IRAC maps after PSF subtraction revealed extended emission in the form of a coma–like structure in the 4.5 μm map (Figure 4.8, bottom row). In contrast, the 3.6 μm map shows no sign of a diffuse source component. The extended emission at 4.5 μm also shows a tail–like elongation towards the top of the map, pointing away from the direction of the Sun.

In order to derive a quantitative estimate of the extended emission, I applied a radial averaging routine to the PSF–subtracted images, deriving the median of all pixel values in annuli centered on the object's center with a width of 1 pixel; the results in both bands are plotted in Figure 4.10. The median was used to minimize the effect of outliers and noise. Areas that are contaminated by image artifacts were excluded from the averaging. The extended emission in the 4.5 μm mosaic clearly follows a $1/\varrho$ profile, where ϱ is the angular distance from the object's center. This is the radial profile predicted for free expansion of material from a nucleus, e.g., from sublimating ices, and is characteristic of cometary comae (Jewitt and Meech 1987). Subtracting the $1/\varrho$ profile from the differential map reveals a clear elongated structure that resembles a cometary tail (see Figure 4.11). The radial profile of the 3.6 μm map is dominated by noise, but a weak linear trend is shown in Figure 4.10.

I measure the total flux densities of the extended emission by integrating over the fitted profiles and subtracting the background, yielding 6.7 ± 5.5 and 64 ± 7 mJy at 3.6 and 4.5 μm respectively. The uncertainty of the 3.6 μm flux density measurement is significant, yielding a signal–to–noise ratio of only 1.2, and raising doubts whether extended emission has been detected or not at this wavelength. The background level and its uncertainty were measured as the median and standard deviation, respectively, in four different areas of both maps that are unaffected by background sources and subsequently averaged. The measured flux densities are aperture corrected using the IRAC surface brightness correction factors

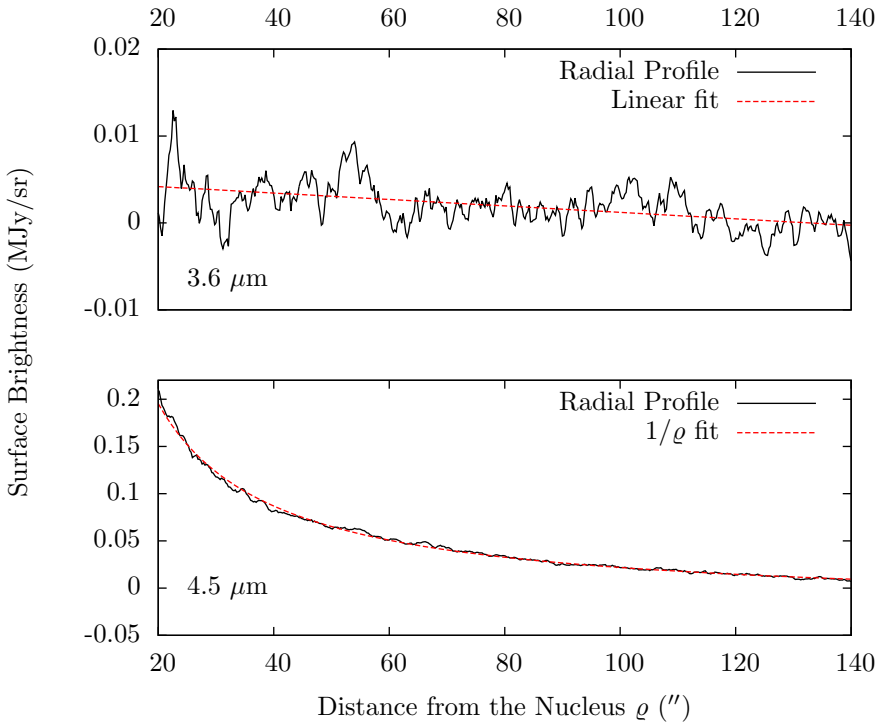

Figure 4.10 Radial median plots of the differential 3.6 μm (top) and 4.5 μm (bottom) mosaics. The radial profiles were produced by taking the median of the pixel values in annuli with a width of 1 pixel, centered on the object's center. Each point on the profile equals the median value derived from the annulus with the given distance from the center. Both radial profiles were fitted over the whole range plotted here. The 3.6 μm radial profile (top panel) shows a slight negative trend (dashed line) in surface brightness versus radial distance. The 4.5 μm radial profile (bottom panel) clearly shows a reciprocal trend with radial distance, which is perfectly described by a $1/\varrho$ profile, where ϱ is the distance from the object's center. Note the different scales on the vertical axes of the panels.

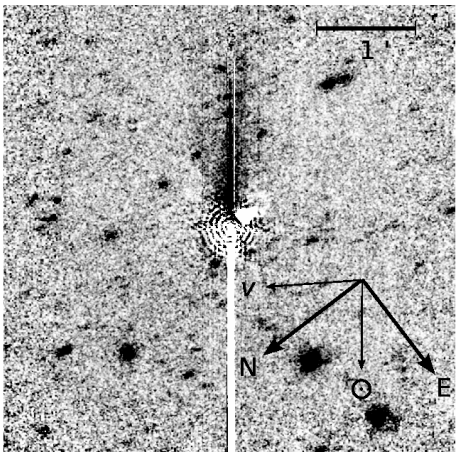

Figure 4.11 Don Quixote's tail. This map shows the differential 4.5 μm map of Don Quixote from which the fitted $1/\varrho$ radial profile shown in Figure 4.10 has been subtracted. The resulting map clearly shows the tail of Don Quixote with a length of $\sim 2'$. The white concentric rings around the object center are image artifacts from the PSF subtraction.

(IRAC Instrument Handbook 2012). The flux densities were derived by integration over an aperture with radius $196''$. This is the distance from the center of the object at which the measured signal equals the background median.

I estimate the intensity of the emission in the tail by summing up pixel values in the respective area of the 3.6 and 4.5 μm maps, excluding areas that are affected by background sources, and subtracting the median background value as determined from two adjacent areas. I derive flux densities of about 0.6 and 1.6 mJy at 3.6 and 4.5 μm respectively, both of which have large uncertainties and are therefore adopted as upper limits to the emission of the tail.

4.3.3.3 Thermal Modeling of the Nucleus

I apply the NEATM (see Section 3.2.4) to all measured thermal–infrared flux densities listed in Table 4.5, combined with $H = 13.0$ mag (Minor Planet Center Observations Database, accessed September 2012), to derive the diameter and albedo of Don Quixote's nucleus. The WISE flux densities are color corrected using a polynomial fit to the color correction coefficients listed in Wright et al. (2010). The upper flux density limits are included in the modeling in such a way as to have a nominal flux density of zero and an uncertainty equal to the measured upper limit (see Table 4.5). In order to subtract contributions from reflected solar light to the short–wavelength bands, a reflectance ratio between the optical and infrared wavelengths of 1.4 (see Section 3.7.1.1 and Trilling et al. 2010; Harris et al. 2011) is assumed; based on the results of the measured IRTF SpeX spectrum (see Figure 4.13 and the discussion below), the model fit has been repeated using a reflectance ratio of 0.4, leading to nearly identical diameter and albedo results.

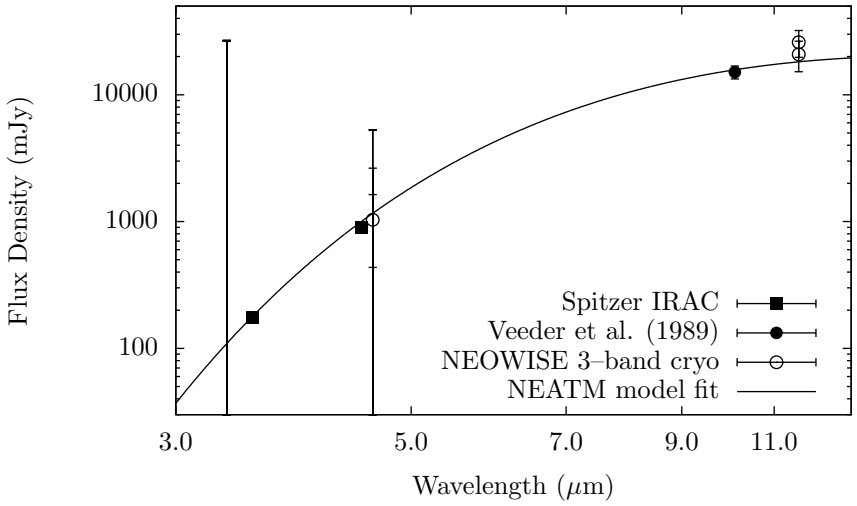

Figure 4.12 Thermal model fit of Don Quixote's nucleus. The fluxes used in the modeling and shown in the plot are given in Table 4.5. Note that all flux densities shown here are color–corrected, corrected for contributions from reflected solar light, and normalized to the geometry of the Spitzer observations by scaling the flux densities to the Spitzer–centric distance at the time of the IRAC observations. Flux uncertainties are shown for each data point and represent 1σ uncertainties; uncertainties of the IRAC and IRTF measurements are covered by their symbols. The line depicts the best–fit thermal model to the data points using the NEATM.

The resulting best–fit diameter and albedo are 18.5 ± 0.4 km and $0.03^{+0.02}_{-0.01}$, using a best–fit $\eta = 0.84 \pm 0.03$. The results agree well with earlier estimates of the physical properties of Don Quixote (18.7 km, Veeder et al. 1989). This measurement confirms Don Quixote to be the 3–rd largest known NEO.

The best fit of the model SED to the measured thermal–infrared fluxes is shown in Figure 4.12. The good agreement of the model fit with most of the data points is obvious. Note that only the *ExploreNEOs* IRAC measurements have been corrected for emission from the coma; all other flux density measurements can in principle include contributions from the coma. I discuss the possibility of such inclusions in Section 4.3.4.4.

4.3.4 Discussion

4.3.4.1 Discussion of the Spitzer IRAC Data

In the following, I discuss the robustness of the IRAC observations and rule out the possibility of the extended emission being due to image artifacts.

- *The observed emission is not a background object.* Inspection of the field of the sky in which Spitzer observed Don Quixote in the Digitized Sky Surveys (Digitized Sky Survey) and the Two Micron All Sky Survey (Skrutskie et al. 2006) show no extended object bright enough to be the source of the observed diffuse emission. The

closest bright star, HD 22634 with $V = 6.7$ mag, is separated from Don Quixote at the time of the observation by some $6.3'$, outside the field of view.

- *Stray–light or scattered light as the source of the emission can be ruled out.* The stray–light and scattered–light behavior of Spitzer's IRAC instrument is well understood (see the IRAC Instrument Handbook 2012; Spitzer Observer's Manual 2007). At the time of the IRAC observations no sufficiently bright background sources were present in the stray–light avoidance zones of either IRAC channel (see Section 2.2.2.1).

- *The extended emission is not caused by latency effects.* The PSF subtraction from the 4.5 μm band image shows the extended emission to be centered on the object. This would not be the case if the emission was an image artifact caused by latency, i.e., left–over charge in the pixel wells from previous integrations, given the dithering between the individual frames. Latencies would occur at that position in the field where the object was located in the previous integration, leading to the occurrence of multiple apparitions in the image.

- *The extended emission is not an image artifact caused by the saturation of the object.* The possibility that the coma is the result of saturation of the mosaics can be ruled out, since the detector behavior and PSFs for these bands are well characterized (IRAC Instrument Handbook 2012; Spitzer Observer's Manual 2007). For comparison reasons, J. Hora has examined observations of stars with a wide range of brightnesses, many of which were saturated, but none of which show extended emission. As an example, I show a saturated image of calibration star HD 149961 in Figure 4.8, rightmost column. HD 149961 is significantly brighter ($\Delta m = 3.8$ mag) than Don Quixote at the time of its observation, however, the image does not show any signs of extended emission.

- *The extended emission is not an image artifact introduced by the subtraction of the PSF.* J. Hora has applied the PSF subtraction technique (Marengo et al. 2009) to images of calibration stars and found no equivalent of the extended emission observed in the case of Don Quixote. Improper scaling of the PSF can lead to residuals in the differential image. In that case, however, residuals of the spikes would be visible, being the brightest parts of the PSF (see Figure 2.7 on page 54). Furthermore, improper alignment of the PSF with respect to the object leads to artifacts that do not have a radial symmetric nature like the extended emission observed in Don Quixote.

4.3.4.2 Constraining the Nature of the Emission

The nature of the extended coma–like emission can be constrained using the ratio of the infrared flux densities, $F_{4.5}/F_{3.6}$, which has a value of $\geq$8.5, with a 1σ confidence interval covering the range from 4.7 to 59, based on the measured fluxes and uncertainties. A model for cometary dust (Kelley and Wooden 2009; Reach et al. 2012), applied by W. Reach (SOFIA–USRA, private communication), determines the expected ratio of $F_{4.5}/F_{3.6}$ from thermal emission from dust and reflected sunlight, yielding a value of less than 5 for a comet at 1.23 AU from the Sun. Hence, it is very likely that the measured 4.5 μm flux density has a third contribution, which is most probably molecular line emission from CO (at 4.7 μm) and/or CO_2 (at 4.3 μm) (see e.g., Bockelée-Morvan et al. 2004), stimulated by photo–dissociation. Both emission lines fall well within the IRAC 4.5 μm bandpass and have been observed in many comets, with CO_2 typically dominating for comets in the inner Solar System (Ootsubo et al. 2012; Reach et al. 2012). The emission line nature explains the lack of a clear detection of the emission in the 3.6 μm band, where only aromatic hydrocarbons and CH_3OH are known to emit, but their features are weak in comets. I focus in the following analysis on a possible CO_2 origin of the emission, which is more likely than emission from CO; however, I note that a CO component cannot be entirely ruled out.

If the extended emission detected at 3.6 μm is real, it is most likely emitted from dust particles that are launched from the surface by the CO_2 gas drag, since reflected solar light dominates over thermal emission at 3.6 μm and $r = 1.22$ AU in the cometary dust model (Reach et al. 2012).

The upper limit nature of both flux density measurements of the tail precludes the use of the $F_{4.5}/F_{3.6}$ ratio as an indicator for the nature of the emission. Instead, I take a different approach here. I measure the length of the tail as $\sim 2'$ from Figure 4.11, which equals $\sim$48000 km. Assuming an expansion velocity of the gas of 0.72 km s^{-1} (0.8 km s^{-1} $\times$ $r^{-0.5}$ with $r = 1.22$ AU, Ootsubo et al. 2012), the lifetime of the particles is required to be $\geq$0.77 days, which is well within the lifetime for dissociation by sunlight of CO and CO_2, 22.9 and 8.6 days (data from A'Hearn et al. 1995, normalized to $r = 1.22$ AU assuming an inverse–square relationship), respectively. Hence, I cannot exclude the possibility that the tail emission is also due to molecular line emission.

4.3.4.3 Gas and Dust Production Rates

I estimate the gas and dust production rates from the measured 4.5 and 3.6 μm flux densities, respectively, assuming (1) the 3.6 μm flux density to be purely reflected solar light from dust grains, and (2) the 4.5 μm flux density to be dominated by line emission, with a contribution from thermal emission from dust. Taking into account the uncertain nature of the measured 3.6 μm flux density, I adopt for this discussion an upper limit of $\leq$12.2 mJy (6.7+5.5 mJy), which equals a conservative 1σ upper limit (see Table 4.5).

I adopt the widely used $Af\rho$–formalism, introduced by A'Hearn et al. (1984), to determine the properties of the dust coma, based on the assumption that the upper limit flux density at 3.6 μm is from reflected solar light. $Af\rho$, measured in units of cm, is the product of the dust grain bond albedo (A), the filling factor of the grains (f), and the linear radius[7] of the field of view at the distance of the comet (ρ), and is hence independent of the characteristics of the observation.

$$Af\rho = \frac{(2\Delta r)^2}{\rho}\frac{F_c}{F_s},$$

where r is the heliocentric distance of the comet in AU, Δ the distance to the observer in AU, F_c and F_s are the measured flux density of the coma and the solar light flux density at 1 AU, respectively, in the same band. I determine F_s as the integral of the measured solar spectrum by Rieke et al. (2008) convolved with the spectral response function of the IRAC 3.6 μm band (see Figure 2.6 on page 53) over its bandwidth. Using the aperture size of 196″, I obtain $Af\rho \leq 11$ cm, which is comparable to values measured in JFCs (A'Hearn et al. 1995).

$Af\rho$ can be converted into a dust production rate

$$Q_{\mathrm{dust}} = (Af\rho)\ \frac{2}{3}\frac{\varrho_d a v_d}{A_p},$$

where ϱ_d is the dust density, a the dust grain radius, v_d the escape velocity, and A_p the geometric albedo of the dust particles (Jorda 1995; Fornasier 2013), assuming a fixed grain size. I adopt values that are typical for short–period comets: $v_d = 0.72$ km s^{-1} (using the expansion velocity of gas[8]: 0.8 km s^{-1} $\times$ $r^{-0.5}$ with $r = 1.22$ AU, Ootsubo et al. (2012)), $a \sim 15$ μm (average of the range of particle sizes found for short–period comet 67P/Churyumov-Gerasimenko by Bauer et al. 2012), $\varrho_d = 1$ g cm^{-3} (Bauer et al. 2012), and $A_p = 0.15$ (Kelley and Wooden 2009). I obtain an upper limit on the production rate of $\leq$5.3 kg s^{-1}. This estimate is again comparable to other short–period comets (e.g., Bauer et al. 2011).

In the next step, I determine the CO_2 gas production rate from the 4.5 μm flux density measurement. Firstly, I correct the measured flux density for the contribution from thermal flux emitted from dust, based on the results derived above. I determine the contribution of thermal emission from dust as the integral of the product of the thermal emission from dust convolved with the 4.5 μm spectral response function (see Figure 2.6) using a model provided by Kelley and Wooden (2009):

$$F_{\mathrm{therm}} = \frac{(1-\bar{A})}{A(\alpha)}\pi B_\lambda(T)\frac{(Af\rho)}{\Delta^2}\rho, \tag{4.1}$$

[7] $\rho(\mathrm{km}) = 725.27 \times \Delta(\mathrm{AU}) \times \Theta('')$, where Θ is the angular size of the aperture in which the flux density of the coma was measured in units of arcseconds and Δ is the comet–observer distance in AU.

[8] Since the dust component is probably driven by the sublimation of gas, its use here is justified.

where $\bar{A} \sim 0.32$ is the mean bolometric Bond albedo of the dust (Gehrz and Ney 1992), $A(\alpha)$ is the phase angle dependent Bond albedo (which is assumed to be 0.15 for $\alpha \leq 60°$, Kelley and Wooden 2009), and $B_\lambda(T)$ is the Planck function (see Equation 3.5 on page 70) with temperature $T \sim 306$ K$\times 1.22^{-0.5} = 277$ K (Kelley and Wooden 2009). Given the upper limit nature of the 3.6 μm flux density measurement, I constrain that part of the emission at 4.5 μm resulting from molecular line emission to the range $24 < F < 64$ mJy.

I determine the CO_2 production rate based on the single–species Haser (1957) model, which describes the number density of molecules, n, in a distance ρ from the nucleus. The Haser model assumes the coma to be the result of a uniform, spherically symmetric outflow of molecules from a point–like nucleus at a constant speed. The emission is caused by the photo–dissociation of the CO_2 molecules. The number density (km^{-3}) is defined as

$$n(\rho) = \frac{Q}{4\pi\rho^2 v} \exp(-\rho/\gamma),$$

where Q is the production rate (s^{-1}), v the radial outflow velocity (km s^{-1}), and $\gamma = \tau v$, the scale length (km), which is the product of the photo–dissociation lifetime of CO_2, τ (in s^{-1}), and the outflow velocity. I adopt the expansion velocity of gas at the heliocentric distance of Don Quixote, $v = 0.8 \times 1.22^{-0.5} = 0.72$ km s^{-1} (Ootsubo et al. 2012) and the lifetime of CO_2 (Crovisier 2002), also scaled to the heliocentric distance, $\tau = 5.0 \cdot 10^5$s $\times$ $1.22^2 = 7.4 \cdot 10^5$ s. In order to derive the production rate Q, the column density $N(\rho)$ in units of km^{-2} has to be derived from the number density by integration along the line of sight (see, e.g., Helbert 2003), assuming the coma to be optically thin. The column density is related to the measured flux density F in units of W m^{-2} μm^{-1} via

$$N(\rho) = \frac{4\pi F \cdot 10^{-9}}{Q(hc/\lambda)g\pi\rho^2}\Delta^2,$$

where h is Planck's constant, c the velocity of light in the vacuum, $\lambda = 4.26$ μm the CO_2 emission line wavelength, and g the fluorescence efficiency of this line ($g = 2.6 \cdot 10^{-3}$s^{-1} $\times$ $1.22^{-2} = 1.75 \cdot 10^{-3}$ s^{-1}, corrected for the heliocentric distance (Crovisier 2002). The factor 10^{-9} stems from the conversion from km to μm. Solving this equation yields a range of the CO_2 production rate of $Q = (0.7 - 1.8) \cdot 10^{26}$ molecules s^{-1}, which is well within the range of other short–period comets that exhibit CO_2 emission (Reach et al. 2012).

4.3.4.4 Constraints from Additional Data

I explore the literature data for additional evidence of the observed activity: the measured flux densities are compared to the sum of the predicted thermal emission from the nucleus (see Section 4.3.3.3) and the predicted upper limit of the thermal emission from the dust (see Equation 4.1). I scale ($Af\rho$) according to the heliocentric distance of the respective

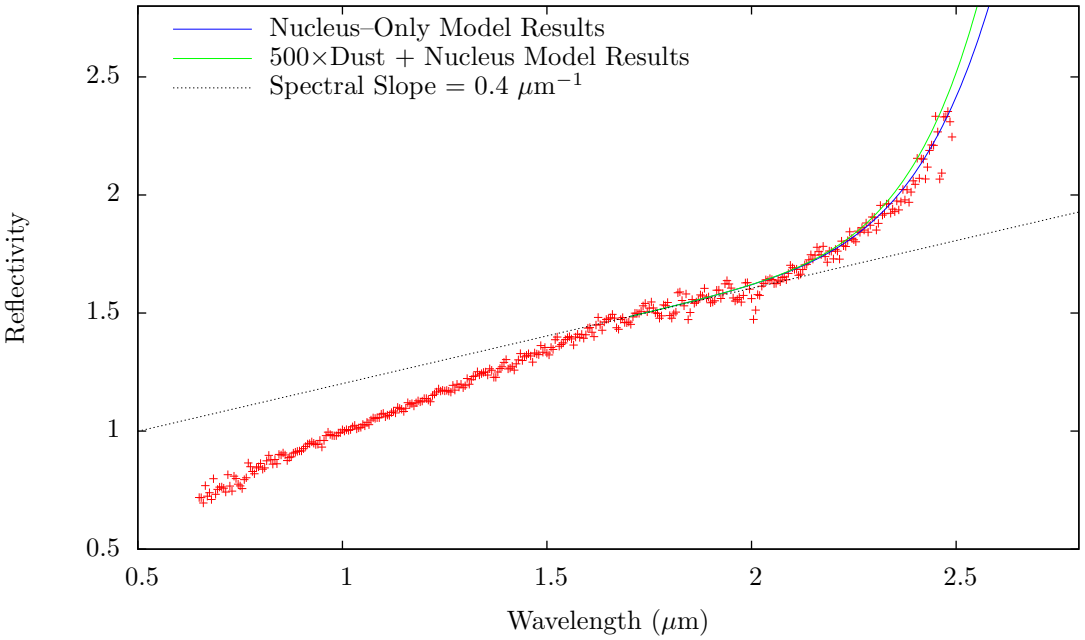

Figure 4.13 IRTF SpeX spectrum of Don Quixote (red crosses), taken 26 days after the *Explore-NEOs* Spitzer IRAC observations. The blue line depicts the predicted thermal emission from the nucleus, solely based on the best–fit thermal model. A possible contribution from thermal emission from dust, based on the properties of the dust coma as derived from the 3.6 μm flux density, is 5 orders of magnitude smaller than the emission from the nucleus. I apply an amplification factor of 500 to the predicted dust emission, which provides an upper limit on the presence of dust (green lines) from the spectrum. See the text for details. Spectral data from Thomas (2013).

observation using the relation $(Af\rho)_{r/\mathrm{AU}} = (Af\rho)_{1\mathrm{AU}} \times r^{-2.3}$ (A'Hearn et al. 1995).

Flux Density Measurements. Unfortunately, none of the flux density measurements from the literature has the required accuracy (see Table 4.5) to unambiguously confirm or rule out the presence of activity. The accuracy of the IRTF observations (Veeder et al. 1989) is reduced by the discrepancy between the two individual measurements (see Table 4.5), and the WISE observations suffer from their low signal–to-noise ratio and the upper limit nature of the measurements.

IRTF spectroscopic data. Figure 4.13 shows Don Quixote's reflectivity as a function of wavelength; the reflectivity is defined as the ratio of the measured flux density per wavelength and the spectrum of a solar analog star. The featureless spectrum has a spectral slope of $\sim$0.7 for λ<1.7 μm and $\sim$0.4 for λ>1.7 μm, which agrees with the previous classification of a D–type asteroid (Hartmann et al. 1987; Binzel et al. 2004) and other D–type asteroids (DeMeo et al. 2009; Bus and Binzel 2002b, see also Figure 1.10). At the long–wavelength end of the spectrum the reflectivity increases dramatically, which

is caused by contaminations from thermal emission from the nucleus. In the following, I use the derived properties of the nucleus and the dust coma to investigate the question whether the activity can be constrained from this so–called "thermal tail".

The dotted line in Figure 4.13 presents the linear slope that was fit to the spectrum in the wavelength range 1.7–2.1 μm and is unaffected by the tail. I computed the thermal emission from the nucleus and the dust coma for this wavelength range using the thermal model of the nucleus (see Section 4.3.3.3) and the model for thermal emission from dust (Equation 4.1), using the respective best–fit parameters derived above. The aperture size was chosen as $60''$, which equals the length of the slit used in the observations. It turns out that the thermal emission from dust is 5 orders of magnitude fainter than the emission from the nucleus, not affecting the shape of the model spectrum. The model of the emission from the nucleus shown in Figure 4.13 (blue line) presents the thermal emission from the nucleus divided by a 5780 K black body spectrum, representing the solar analog spectrum, and added to the fixed slope of 0.4. Note that no fitting parameters are used here; the fit to the measured thermal tail is good. Multiplying the contribution from the dust coma thermal emission with a factor of 500 results in the green line in Figure 4.13, which provides an upper limit to the contribution from thermal emission from dust to the spectral data. This factor translates into an upper limit of the dust production rate of 2500 kg s^{-1}, which is significantly larger than the value derived from IRAC observations, but does not prove the presence of activity.

The lack of precision in the additional observations precludes a further constraining of the activity. None of the observations can unambiguously rule out the presence or absence of activity.

4.3.4.5 Cause and Longevity of the Activity

The observational results discussed above allow only for speculations on the cause and longevity of the observed activity. The observation of CO_2 line emission implies the existence of CO_2 ice; the ice is presumably buried under a thick layer of insulating material (Rickman et al. 1990) to explain its existence in near–Earth space.

Two scenarios are possible to explain the observed activity: (1) subsurface CO_2 sublimates due to heating caused by the proximity to the Sun, leading to continuous activity, or (2) the observed activity is part of an outburst event and hence spontaneous. The lack of evidence in the additional observation data for the presence or absence of activity precludes further discussion on the cause and longevity of the activity. Further observations are necessary to constrain the cause and longevity of the activity. Additional observations in a wavelength range similar to IRAC's 4.5 μm band during the next perihelion passage in May 2018 may help to resolve the nature of Don Quixote's activity as spontaneous or continuous. Furthermore, observations in the optical will provide constraints on the dust

content of the activity.

4.3.4.6 Implications

Don Quixote has long since been believed to be of cometary origin (e.g., Hahn and Rickman 1985; Weissman et al. 1989; Bottke et al. 2002b), so the discovery of activity in this object is no surprise. A literature search among IAU Circulars[9] (No. 8578–8778) shows that a significant fraction of asteroids are identified to show cometary activity in follow–up observations. However, most of the discoveries of activity follow few weeks or months after the discovery of the object. It is unlikely that Don Quixote, the primary candidate for a cometary origin among the NEOs, was only insufficiently observed over the last three decades after its discovery to reveal possible activity. I suppose that the activity, if continuous, evaded discovery due to the fact that it is most likely triggered by the sublimation of CO_2 ice, the line emission of which is not observable in the optical.

The existence of CO_2 ice puts constraints on Don Quixote's origin: its interior must have formed at very low temperatures ($\leq$60 K) to condensate CO_2 and must have remained cold since (Yamamoto 1985). Hence, in order to retain CO_2 ice over a long time, the subsurface layers of Don Quixote must have temperatures of 60 K and below on average. This upper limit temperature provides constraints on the thermal properties of Don Quixote's surface layers. A thermophysical model can be used to explore the depth of the heat wave penetrating into the top surface layers of Don Quixote.

Don Quixote is the third–largest near–Earth asteroid (see above); the discovery of cometary activity makes this objects also one of the largest short–period comets with a measured diameter (Lamy et al. 2004).

The implications of this discovery for our picture of the Solar System are discussed in Section 6.1.

4.3.5 Conclusions

- I find evidence for cometary activity in NEO (3552) Don Quixote, the third–largest object in near–Earth space, in *ExploreNEOs* data. Based on dynamical simulations, Don Quixote has long since been suspected to be of cometary origin (Hahn and Rickman 1985; Weissman et al. 1989; Bottke et al. 2002b), but activity has never been reported. Don Quixote provides physical evidence for the hypothesis that short–period comets contribute to the NEO population.

- Extended emission is obvious in the 4.5 μm band observations, but marginal at 3.6 μm. I interpret the lack of a clear coma at 3.6 μm such that activity is caused by line emission from CO_2 molecules. CO_2 line emission is visible in the 4.5 but not in

[9] `http://www.cbat.eps.harvard.edu/`

the 3.6 μm band, and has been observed in a number of short–period comets (Reach et al. 2012).

- The *ExploreNEOs* Spitzer observations show a faint anti–sunward directed tail that is possibly made up from CO_2 gas or dust.
- From the 3.6 μm band flux density measurement I determine an upper limit on the dust production rate of $\leq$5.3 kg s^{-1}. Using this estimate and the 4.5 μm flux density measurement, I constrain the CO_2 production rate at the time of the Spitzer observations to the range $(0.7 - 1.8) \cdot 10^{26}$ molecules s^{-1}.
- I investigate other observational data of Don Quixote, including IRTF and WISE imaging data and IRTF SpeX spectroscopic data, none of which are of sufficient quality to unambiguously confirm or rule out the presence of activity.
- The *ExploreNEOs* Spitzer observations combined with the additional observations from the literature allow for a robust thermal model fit of Don Quixote's nucleus, yielding a diameter and albedo of 18.5 ± 0.4 km and $0.03^{+0.02}_{-0.01}$, respectively. Its diameter makes Don Quixote the third–largest known NEO and one of the largest known short–period comets.
- The presence of frozen CO_2 on Don Quixote provides constraints on its origin and thermal properties.

Chapter 5

"TNOs are Cool!" Results

In the following, I present my results on the physical characterization of trans–Neptunian objects (TNOs) and the investigation of their connection to the short–period comets (see Section 1.1.4.2). The diameter and albedo estimates presented here were mostly derived from observations within the TNOs are Cool! program (see Section 2.4.3) and the MIPSKBOs project (see Section B.3); thermal modeling was performed by myself if not noted otherwise. Additional estimates were extracted from the literature.
The following topics are covered in this chapter:

- *The physical characterization of 18 Plutinos based on TNOs are Cool! Herschel PACS data. The presentation in Section 5.1 provides a brief outline of the methods and results of the analysis, which has been published in a peer–reviewed journal (Mommert et al. 2012). See Section C.2 for a reproduction of the full publication.*

- *The investigation of the size and albedo distributions of known TNO subpopulations and the Centaurs (see Section 5.2). The method used here is different to previous approaches to investigate size distributions of small bodies.*

- *I investigate possible correlations between measured albedos and the TNO taxonomy introduced by Barucci et al. (2005) (see also Section 1.2.4), as well as the presence of surface ices (see Section 5.3).*

The integration of the results presented here into our picture of the Solar System is discussed in Section 6.1.

5.1 Physical Characterization of 18 Plutinos

As part of the TNOs are Cool! program I performed a physical characterization of a representative sample of 18 Plutinos that has been published in Mommert et al. (2012). Since this work is not directly relevant in the scope of this work, but nevertheless represents a significant contribution to the TNOs are Cool! program, I give here a brief outline of the data analysis and modeling aspects, and present the results of the analysis. For a full discussion of all the details, see the reproduction of the published manuscript in Section C.2.
Note that the work presented here was performed by myself; contributions made by co–authors are explicitly marked.

5.1.1 Introduction

Plutinos are members of the trans–Neptunian population that orbit the Sun in 3:2 mean motion resonance with Neptune (cf. Section 1.1.4.1). They are named after their prototype, former planet Pluto, and form the largest resonant subpopulation among the TNOs. The physical characterization of the Plutino sample provides insight into their size and albedo distribution, which allows for deductions on the origin of this resonant subpopulation. Plutinos are believed to have an origin similar to that of Pluto (see Section 1.1.4.1).

As part of the *TNOs are Cool!* program, 25 Plutinos were observed, 18 of which were processed and modeled for this work. The sample of 18 Plutinos represents ∼7.5% of the known Plutino population (Minor Planet Center Observations Database, accessed October 2011) and has been selected solely on the basis of Herschel observability in the sense of observation geometry and detector sensitivity. The target sample includes 3 known multiple systems, none of which was resolved in the PACS observations.

5.1.2 Observations and Data Reduction

Herschel PACS observations, data reduction and photometry were performed by the observation planning and data reduction teams of the *TNOs are Cool!* program (see Section 2.4.3). For more detailed information see also Section C.2 and Vilenius et al. (2012); Santos-Sanz et al. (2012); Pál et al. (2012). Observational circumstances and PACS flux densities of the sample targets are summarized in Table 2 of Section C.2.

Due to the questionable reliability of MPC H magnitudes (e.g., Romanishin and Tegler 2005) and the lack of uncertainty estimates, I compute more precise H magnitude estimates with respective uncertainties using published photometry data from the literature and observational data provided by the MPC. All photometric data, as well as lightcurve data and color information, if available, are compiled in Table 3 of Section C.2.

In order to improve the quality of the modeling results, Herschel flux densities have been combined with existing Spitzer MIPS (Section B.3.2) flux density measurements,

Table 5.1. Plutino Adopted Modeling Results.

Object	Data	d (km)	p_V	η
1996 TP66	HS	$154.0^{+28.8}_{-33.7}$	$0.074^{+0.063}_{-0.031}$	$1.20^{+0.35}_{-0.35}$
1999 TC36	HS	$393.1^{+25.2}_{-26.8}$	$0.079^{+0.013}_{-0.011}$	$\mathbf{1.10^{+0.07}_{-0.08}}$
2000 GN171	HS	$147.1^{+20.7}_{-17.8}$	$0.215^{+0.093}_{-0.070}$	$\mathbf{1.11^{+0.24}_{-0.21}}$
2001 KD77	H	$232.3^{+40.5}_{-39.4}$	$0.089^{+0.044}_{-0.027}$	$1.20^{+0.35}_{-0.35}$
2001 QF298	H	$408.2^{+40.2}_{-44.9}$	$0.071^{+0.020}_{-0.014}$	$1.20^{+0.35}_{-0.35}$
2002 VE95	HS	$249.8^{+13.5}_{-13.1}$	$0.149^{+0.019}_{-0.016}$	$\mathbf{1.40^{+0.12}_{-0.11}}$
2002 VR128	H	$448.5^{+42.1}_{-43.2}$	$0.052^{+0.027}_{-0.018}$	$1.20^{+0.35}_{-0.35}$
2002 VU130	H	$252.9^{+33.6}_{-31.3}$	$0.179^{+0.202}_{-0.103}$	$1.20^{+0.35}_{-0.35}$
2002 XV93	HS	$549.2^{+21.7}_{-23.0}$	$0.040^{+0.020}_{-0.015}$	$\mathbf{1.24^{+0.06}_{-0.06}}$
2003 AZ84[a]	HS	$727.0^{+61.9}_{-66.5}$	$0.107^{+0.023}_{-0.016}$	$\mathbf{1.05^{+0.19}_{-0.15}}$
2003 UT292	H	$185.6^{+17.9}_{-18.0}$	$0.067^{+0.068}_{-0.034}$	$1.20^{+0.35}_{-0.35}$
2003 VS2[a]	HS	$523.0^{+35.1}_{-34.4}$	$0.147^{+0.063}_{-0.043}$	$\mathbf{1.57^{+0.30}_{-0.23}}$
2004 EW95	H	$291.1^{+20.3}_{-25.9}$	$0.044^{+0.021}_{-0.015}$	$1.20^{+0.35}_{-0.35}$
2004 PF115	H	$468.2^{+38.6}_{-49.1}$	$0.123^{+0.043}_{-0.033}$	$1.20^{+0.35}_{-0.35}$
2004 UX10	H	$398.1^{+32.6}_{-39.3}$	$0.141^{+0.044}_{-0.031}$	$1.20^{+0.35}_{-0.35}$
2006 HJ123	H	$216.4^{+29.7}_{-34.2}$	$0.281^{+0.259}_{-0.152}$	$1.20^{+0.35}_{-0.35}$
Huya	HS	$438.7^{+26.5}_{-25.2}$	$0.081^{+0.011}_{-0.011}$	$\mathbf{0.89^{+0.06}_{-0.06}}$

Note. — The column "Data" refers to the data set on which the model is based: "H" refers to Herschel–only date, "HS" to Herschel and Spitzer data. η values of floating–η modeling results are highlighted in bold. No adopted values are given for Pluto/Charon, since the NEATM is not applicable to these objects (see text). Table adapted from Mommert et al. (2012).

[a]Based on averaged lightcurve observations.

mostly extracted from Stansberry et al. (2008). The Spitzer measurements are listed in Table 4 of Section C.2.

5.1.3 Thermal Modeling

I derive diameter and albedo estimates from optical and thermal infrared observations, using the NEATM (cf. Section 3.2.4). According to the *TNOs are Cool!* policy, I adopt floating–η results only if the flux density data set includes both Herschel and Spitzer data; especially the Spitzer MIPS 24 μm measurement constrains the object's spectral energy distribution (SED) combined with the Herschel PACS 70, 100, and 160 μm measurements, and allows for a robust determination of the beaming parameter η (see Section 3.5). Herschel data alone are usually not sufficient to constrain η; in this case, the fixed–η model is adopted using $\eta = 1.2 \pm 0.35$ (Stansberry et al. 2008). Non–detections are taken into account in the modeling as 0 $\pm\sigma$ flux density measurements, where σ is the upper limit.

Uncertainties on the measured diameters and albedos are derived using an enhanced Monte–Carlo method that is based on the method introduced in Section 3.3. The method uses a rescaling of the individual flux density uncertainties to force the best possible fit to the randomized data, artificially increasing the uncertainties compared to the simple Monte–Carlo method (see Section 3.1 of the full manuscript in Section C.2 of this work for a more detailed explanation of the method).

5.1.4 Results

The adopted results of each individual object are listed in Table 5.1. For a list of all fixed–η and floating–η modeling results see Table 5 of Section C.2; the best–fit model spectral energy distributions using both modeling approaches are shown in Figure 3 of Section C.2.

Floating–η fits were possible for 12 targets, 7 of which are based on combined Herschel and Spitzer data. The weighted mean η determined from the 7 adopted floating-η model fits yields $\langle\eta\rangle = 1.11^{+0.18}_{-0.19}$, which is consistent with the adopted value of $\eta = 1.20 \pm 0.35$ (Stansberry et al. 2008) applied in the fixed–η approach.

5.1.5 Discussion

Discussion of Selected Targets. All targets are discussed in full detail in Section 4.2 of Section C.2. Here, I discuss only a few scientifically interesting targets:

1999 TC36 : This object is actually a triple system (Trujillo and Brown 2002a; Jacobson and Margot 2007; Benecchi et al. 2010). The adopted diameter and albedo estimates, $393.1^{+25.2}_{-26.8}$ km and $0.079^{+0.013}_{-0.011}$, respectively, agree with earlier estimates by Stansberry et al. (2008): $d = 414.6^{+38.8}_{-38.2}$ km and $p_V = 0.072^{+0.015}_{-0.012}$. The system consists of two similarly sized central components A_1 and A_2 and a more distant

secondary component, B. The nature of this system makes it possible to determine the mean density of the system and, using optical flux differences between the single components, the sizes of the components. Revisiting the calculations performed by Stansberry et al. (2006) and Benecchi et al. (2010) yields new size estimates: $d_{A1} = 272^{+17}_{-19}$ km, $d_{A2} = 251^{+16}_{-17}$ km and $d_B = 132^{+8}_{-9}$ km. The updated mean system density $\varrho = 0.64^{+0.15}_{-0.11}\,\mathrm{g\ cm^{-3}}$ is somewhat higher than the earlier estimate $\varrho = 0.54^{+0.32}_{-0.21}\,\mathrm{g\ cm^{-3}}$ (Benecchi et al. 2010). Assuming material densities of $1.0 \leq \varrho_0 \leq 2.0\,\mathrm{g\ cm^{-3}}$, porosity or fractional void space turns out to make up 36–68% of the volume. All these calculations are based on the assumptions of spherical shape of each component and the same albedo of each component.

2000 GN171 : This object is the smallest Plutino in this sample. Its lightcurve amplitude of 0.61 mag (Sheppard and Jewitt 2002) suggests it either to be highly elongated or to be a binary (Lacerda and Jewitt 2007). Hence, the real diameter of 2000 GN171 might be even smaller.

Pluto : Paradoxically, Pluto is the clear outlier of the Plutino population, being by far the largest and having the brightest surface. Besides that, Pluto was the first TNO discovered to have an atmosphere (Hubbard et al. 1988; Brosch 1995), has a pronounced optical lightcurve caused by albedo variations, and has a moon half its own size. N_2 ice was detected on Pluto's surface, whose sublimation and deposition is accompanied by latent heat transport that results in much lower (higher) dayside (nightside) temperatures than would be expected on an airless body (e.g., Spencer et al. 1997). Despite these facts, I attempt to treat Pluto like any other Plutino and apply the thermal model on Herschel–only Pluto data. For comparison reasons, I calculate the equivalent diameter and albedo range of the Pluto–Charon system from published data (Buie et al. 1997; Gulbis et al. 2006; Sicardy et al. 2006; Young et al. 2007), yielding d=2617 km and $0.44 \leq p_V \leq 0.73$ (see Section 4.2 of Appendix C.2 for more details).

The best–fit fixed–η model yields $d = 2119.9^{+164.5}_{-182.2}$ km, which is more than 3σ from the effective system diameter, and $p_V = 0.730^{+0.162}_{-0.153}$, which is barely consistent with the albedo range given above. The attempt to apply a simple thermal model to Pluto shows the susceptibility of such models to violations of the model assumptions. The failing of the fit has several reasons:

- The replacement of the Pluto/Charon system with a single equivalent body, assuming a single average albedo for both objects, neglects the different contributions to the SED of areas of different temperatures (and albedos).
- Disregarding Pluto's thermal lightcurve (Lellouch et al. 2000, 2011) might have introduced a perceptible distortion of the SED.

Table 5.2. Average Albedos of Plutinos, other TNO subpopulations and the JFCs.

Population	Average Albedo	N	Reference
Centaurs	0.06	21	1
Plutinos	0.08 ± 0.03	17	2
Cold Classicals[a]	0.16 ± 0.05	6	3
Hot Classicals[a]	0.09 ± 0.05	12	3
Scattered Disk Objects[b]	0.07/0.05	8	4
Detached Objects[b]	0.17/0.12[c]	6[c]	4
TNOs and Centaurs	$0.07 - 0.08$	47	1
JFCs	0.048 ± 0.016	7	5

Note. — N denotes the number of data points. Table adapted from Mommert et al. (2012). The average albedo of the JFCs has been updated based on 4.2.

[a]unweighted mean

[b]unweighted/weighted mean, based on relative uncertainties

[c]excluding Eris

References. — (1): Stansberry et al. (2008); (2): this work; (3): Vilenius et al. (2012); (4): Santos-Sanz et al. (2012); (5): Section 4.2

- Thermal models do not take atmospheric effects into account.

Due to the failed model fit and Pluto's uniqueness among the Plutinos, I exclude it from the following discussion of the properties of the Plutino sample.

Sample Statistics. Excluding Pluto, the weighted mean of the albedo, weighted with reciprocal absolute uncertainties, yields 0.08 ± 0.03, which agrees well with the range of typical geometric albedos of the TNO and Centaur sample of Stansberry et al. (2008). Table 5.2 presents a comparison of the mean albedos of the Plutino sample with different TNO subpopulations and the JFCs. It turns out that the average albedo of the Plutinos agrees well with that of the scattered disk, Centaur and hot classical population. Most of the Plutinos appear to have darker surfaces than the cold classical TNOs and detached objects. In the light of the newly determined average albedo of JFC nuclei (see Section 4.2), Plutinos have on average slightly brighter surfaces than JFCs. However, taking into account the uncertainties the residual is not large enough to exclude Plutinos from the list of possible JFC source regions.

As part of this work, I have produced a cumulative size distribution of the Plutinos,

based on the measured albedo distribution and the absolute magnitudes provided by the MPC. This analysis has been superseded by that one discussed in Section 5.2.

The weighted average albedo of the Plutino sample derived here, $\langle p_V \rangle = 0.08 \pm 0.03$, can be used in combination with Equation 1.4 on page 23 to provide the first absolute calibration of the Plutino size scale. Based on the H magnitudes provided by the MPC (as of Sept. 14, 2012), the smallest known Plutinos have diameters of down to 16 km (1999 DA8 with H=12.4 mag). Note that this estimate suffers from the unreliability of the MPC H magnitudes and the uncertainty in the average albedo, given the scatter of the albedos that is obvious from Table 5.1. However, it still provides an idea of the size of the smallest currently known Plutinos.

5.1.6 Correlations

A check for correlations of the physical parameters, orbital properties and intrinsic optical colors of the Plutino sample has been performed by Nuno Peixinho (University of Coimbra, private communications), using a modified Spearman rank correlation analysis technique that takes into account the uncertainties inherent to the data sample (see Santos-Sanz et al. 2012; Mommert et al. 2012, for a detailed introduction of the method). The results of the method are estimates of the most probable correlation coefficient $\langle \rho \rangle$ accompanied by the probability P (p–value) of that $\langle \rho \rangle$ value to occur given no relationship in the sample, i.e., to occur by pure chance. The lower the value of P the higher the significance level of the correlation. I present the 68% confidence interval for the correlation value $\langle \rho \rangle$, i.e., the interval which includes 68% of the bootstrapped values. This confidence interval equals the canonical 1σ interval of a Gaussian distribution. As an additional aid in reading the P values, I list its Gaussian–σ equivalent significance P_σ.

It turns out that most parameters are uncorrelated. Only very few parameter pairs show reasonably strong evidence of correlation. Those and a few other interesting results are listed in Table 5.3, plotted in Figure 5.1, and briefly discussed in the following (I refer to Section C.2 for a full discussion):

- There is no strong and significant trend between diameter d and albedo p_V (cf. Figure 5.1 and Table 5.3) as observed in the combined scattered disk and detached objects population (Santos-Sanz et al. 2012) and the classical population (Vilenius et al. 2012).

- Both diameter and albedo seem to be clearly uncorrelated with the η value.

- The absolute magnitude H is not correlated with diameter, albedo, or η, which implies that the sample is not biased towards large and high (or low) albedo objects. This finding, however, does not exclude a discovery bias on diameters smaller than those examined here or a discovery bias based on geometrical aspects.

Table 5.3. Modified Spearman Rank Correlation Analysis Plutino Results.

Parameters	N	$\langle\rho\rangle$	P	P_σ
physical parameters:				
d / p_V	17	$-0.32^{+0.29}_{-0.24}$	0.217	(1.24)
d / η	7	$-0.12^{+0.61}_{-0.54}$	0.806	(0.25)
p_V / η	7	$0.08^{+0.61}_{-0.67}$	0.870	(0.16)
H / d	17	$-0.30^{+0.37}_{-0.30}$	0.234	(1.19)
H / p_V	17	$-0.19^{+0.30}_{-0.27}$	0.468	(0.73)
H / η	7	$0.08^{+0.72}_{-0.81}$	0.868	(0.17)
orbital and physical parameters:				
e / d	17	$-0.62^{+0.18}_{-0.13}$	0.008	(2.67)
d / q	17	$0.62^{+0.13}_{-0.17}$	0.008	(2.67)
d / $r^\star$	17	$0.58^{+0.16}_{-0.22}$	0.015	(2.43)
p_V / $r^\star$	17	$0.10^{+0.30}_{-0.32}$	0.711	(0.37)
color information, orbital, and physical parameters:				
s / $r^\star$	13	$-0.58^{+0.46}_{-0.26}$	0.038	(2.07)
s / d	13	$-0.62^{+0.32}_{-0.20}$	0.025	(2.24)
s / H	13	$0.20^{+0.36}_{-0.42}$	0.523	(0.64)
$(B-R)$ / d	13	$-0.50^{+0.29}_{-0.21}$	0.082	(1.74)

Note. — N is the number of sample data points; $\langle\rho\rangle$ and P are the most probable correlation coefficient and the probability of the most probable correlation coefficient to occur given no relationship in the sample (cf. text), respectively. The uncertainty of $\langle\rho\rangle$ denotes its 68 % confidence level. P_σ is the significance expressed in terms of σ. This table lists only the results of parameter pairs that meet the following criteria: $|\langle\rho\rangle| \geq 0.3$ and $P \leq 0.1$, or which are of special interest. Parameter pairs are sorted by parameter type. All correlation coefficients were calculated excluding Pluto. Correlation analyses taking η into account are based solely on the 7 floating-η fit solutions. In order to assess the effects of discovery bias, the heliocentric distance at the time of discovery $r^\star$ is included. To improve the readability, I refrain from listing all correlation values of the color indices with $r^\star$ and d. Instead I only show the correlation values of the spectral slope, s, with $r^\star$ and d, which gives similar results. Table adapted from Mommert et al. (2012).

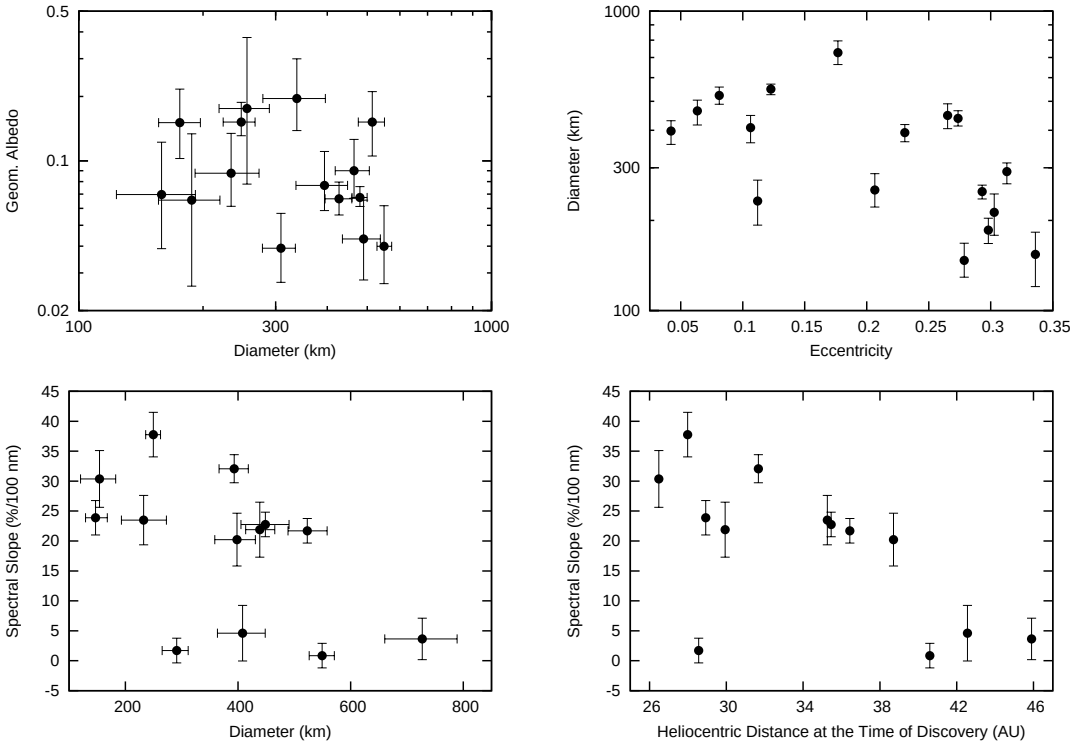

Figure 5.1 Plots of some correlations. **Upper left**: there is no correlation between diameter and albedo; **upper right**: a clear anti–correlation between eccentricity and diameter is the result of a detection bias; **lower left**: smaller Plutinos appear to be redder than larger ones, which contradicts what was previously suggested by Peixinho et al. (2004) based on the intrinsic brightness H of a different Plutino sample; **lower right**: the color of Plutinos is correlated to the heliocentric distance at the time of their discovery, which hints towards a color bias. Figures adapted from Mommert et al. (2012).

- There is a significant anti–correlation between eccentricity e and diameter d (cf. Figure 5.1), suggesting objects on highly eccentric orbits to be smaller. This trend is considered to be caused by discovery bias, since objects on more eccentric orbits come closer to the Sun, which significantly improves their detectability.

- The correlation between diameter d and the heliocentric distance of each object at the time of its discovery, $r^\star$, compared to the lack of correlation between albedo p_V and $r^\star$, shows that the likelihood of detection solely depends on size, and is rather independent of the object's albedo. A bias towards high (and low) albedos as a result of the nature of discovery can be ruled out. This supports the representativeness of the measured albedo distribution for the Plutino population and shows that the nature of the discovery bias is size–dependent.

- Most color indices and the spectral slope, s, are anti–correlated with heliocentric distance at the time of an object's discovery, $r^\star$ (Figure 5.1). The farther an object

is, the less red it seems to be. This points to a probable color bias in the sample, maybe induced by the common use of R band filters and the improved sensitivity in red bands of state–of–the–art detectors, which are used in TNO surveys. However, there is a lack of bluer objects at shorter heliocentric distances, which should be detectable, despite their color. This might suggest that such objects do not exist, at least not within this sample.

- I cannot confirm a trend found by Hainaut and Delsanti (2002) and Peixinho et al. (2004) of bluer Plutinos being intrinsically fainter using the spectral slope s as a measure of color. The correlation analysis of $B-R$ and H leads to similar results: $\langle\rho\rangle = 0.25^{+0.35}_{-0.43}$ and $P = 0.420$. The sample suggests precisely the opposite, with a trend between the spectral slope s and the diameter d showing smaller Plutinos to be redder (Figure 5.1). However, Peixinho et al. (2004) find their trend due to a "cluster" of blue Plutinos with $H_R > 7.5$, which is equal to $H \geq 8$, i.e., objects at magnitude/size ranges which are not represented in the Plutino sample of this work. Hence, both effects might be the result of selection effects.

I also check for a correlation between the presence of surface ices (see Table 3 in Section C.2) and albedo or diameter; information on the presence of ices have been extracted from the compilation in Barucci et al. (2011), based on spectroscopic analyses. A qualitative analysis shows that 5 of the objects with ice have high albedos (>0.11), with 1999 TC36 being the only icy object with a typical (0.07) Plutino albedo. Thus there is qualitative evidence that icy Plutinos have higher albedos than is typical. 1996 TP66 and 2000 GN171 are the only objects with good spectra indicating the lack of water ice. Their albedos (0.07 and 0.22, respectively) span most of the range of the measured albedos. This seems to indicate that Plutinos lacking water ice can have almost any albedo (although the lack of a detection of 70 μm emission from 1996 TP66 by either Spitzer or Herschel casts considerable doubt on the accuracy of its albedo determination). It seems remarkable that these two objects, which are free of ices, are also the two smallest objects (∼150 km) of the sample. However, the small number of spectroscopically examined objects does not allow for a conclusion, whether the presence of ices is correlated to the object diameter. See also Section 5.3 for a more detailed discussion of a possible correlation of albedo and diameter with the presence of ices.

5.1.7 Conclusions

- The diameter and albedo range of this Plutino sample yields $150-730$ km and $0.04-0.28$, respectively. Excluding Pluto, the weighted mean of the Plutino albedo distribution is 0.08 ± 0.03 and agrees with the average albedos observed for the scattered disk, Centaur and the hot classical population. The average albedo of the JFC population is slightly lower than that of the Plutinos.

- The floating-η fits yield a weighted mean η for the Plutino sample of $1.11^{+0.18}_{-0.19}$, which agrees with the canonical $\eta = 1.20 \pm 0.35$ (Stansberry et al. 2008) utilized in the fixed–η fits.

- The refinement of the size estimates of the components of 1999 TC36 yields: $d_{A1} = 272^{+17}_{-19}$ km, $d_{A2} = 251^{+16}_{-17}$ km and $d_B = 132^{+8}_{-9}$ km; the new bulk density of the multiple system is $\varrho = 0.64^{+0.15}_{-0.11}$ g cm^{-3}.

- Pluto is the clear outlier of the Plutino population, being by far the largest object with the brightest surface. It was shown, that a simple canonical thermal model of Pluto leads to inadequate results, probably mainly due to the multi–component nature of its surface, thermal lightcurve and atmosphere.

- Using measured albedos I calibrated the Plutino size scale for the first time, revealing that the smallest known Plutino may have diameters as small as 16 km.

- There is no correlation between albedo and diameter, as well as H, and diameter, albedo and η, respectively. This shows that the sample is not biased towards large and high (or low) albedo objects. Furthermore, a correlation between diameter and the heliocentric distance at the time of discovery has been found, but not between the albedo and the heliocentric distance at the time of discovery. This finding leads to the conclusion that the nature of the discovery bias is mainly size–dependent.

- A significant correlation between diameter and eccentricity (and perihelion distance) is very likely to be caused by a detection bias based on geometrical aspects.

- There are hints to a color bias in the sample: Plutinos, which have been farther from the Sun at the time of their discovery seem to be bluer and smaller Plutinos tend to be redder, which contradicts previous finding by Peixinho et al. (2004).

- There is qualitative evidence that icy Plutinos have higher albedos than the average of the sample.

5.2 The Size and Albedo Distributions of the Known TNO Subpopulations

The size distributions (see Section 1.2.2.3) of individual TNO subpopulations are important for constraining their origin and collisional evolution; the individual albedo distributions are indicative for compositional differences between the subpopulations. Currently available size distributions are derived from measurements of the cumulative luminosity distribution, describing the number of objects (N) with absolute magnitudes brighter than a threshold H, $N(<H)$, which are then extrapolated to cumulative size distributions, $N(>d)$, assuming a fixed albedo for all objects (Petit et al. 2008). This approach, neglects the albedo variety that is inherent to the individual subpopulations. A proper transformation from the luminosity distribution to the size distribution requires knowledge of the albedo distribution. The large number of albedos measured in the course of the TNOs are Cool! program (see Section 2.4.3) enables the investigation of the subpopulation albedo distribution, which in turn provides the basis for the proper analysis of the size distribution.

The approach I take here is different from that used in previous works (see Petit et al. 2008, for a review): I use albedo measurements from the TNOs are Cool! program and the literature to create albedo distributions of the individual subpopulations, which I then combine with absolute magnitude estimates to determine their size distributions. This method provides an absolute measurement of the size distribution that is independent from the measurement of the luminosity distribution and takes into account the individual albedo distribution, instead of assuming a common albedo for all objects. I compare the albedo and size distributions of Jupiter family comets (JFCs) with those of the individual TNO subpopulations to explore the possible origin of the JFCs in the TNO population. This work is based on the discussion of the Plutino size distribution in (Mommert et al. 2012, see also Section C.2) and supersedes the results presented there.

5.2.1 Method

Using Equation 1.4 on page 23 ($d = 1329/\sqrt{p_V} \cdot 10^{-H/5}$), the diameter of an object can be determined from its absolute magnitude (H) and its albedo (p_V). Measured albedos are available for only a small fraction of all TNOs; rough estimates of H, however, are available for all known objects, provided by the Minor Planet Center Observations Database (accessed January 2013). I derive the size distributions of individual TNO subpopulations[1] using a statistical approach, based on the available albedo measurements and the H magnitude estimates as provided by the Minor Planet Center Observations Database

[1] In the following analysis, I count the Centaur population as a TNO subpopulations, which is technically not the case .

(accessed January 2013) for the individual subpopulations. The following outline describes the method for one subpopulation.

The method is based on a Monte–Carlo approach, in which randomized albedos are combined with H magnitudes to obtain size estimates using Equation 1.4. The albedos are drawn from an albedo probability density function (see below) that is based on the measured albedos of this subpopulation, ensuring that the randomized albedos follow the same distribution as the measured ones. For each H magnitude of the subpopulation, one randomized albedo is drawn. The H magnitudes are also randomly varied within their uncertainties. After all H have been assigned an albedo, both parameter sets are transformed into a set of diameters using Equation 1.4. The diameters are turned into an evenly binned cumulative size distribution for this subpopulation. The shape of this size distribution is based on the set of ranomized albedos and might be significantly different for a second random draw. In order to find the most likely of all possible size distributions for this subpopulation, the method is repeated 1000 times, and the average and standard deviation of each individual diameter bin are derived from the 1000 repetitions, resulting in the most–likely size distribution of this subpopulation and its uncertainty, respectively.

I compare the size distribution produced from this Monte–Carlo approach with a simplified one, assuming a "monochromatic" albedo distribution in which all objects have the same fixed albedo. In that case, the individually randomized H magnitudes are all combined with a fixed albedo value, resulting in a size distribution that does not take into account the albedo distribution of the subpopulation, only the variation in H. The best choice for this fixed albedo value is the median of the albedo distribution, which guarantees that the number of albedos higher than the median equals the number of albedos lower than the median; this approach minimizes the bias toward high or low albedos. In the following, the result of this method will be referred to as the "monochromatic size distribution", whereas the aforementioned method, using the full albedo distribution, will be referred to as the "Monte–Carlo size distribution".

5.2.1.1 Albedo Probability Density Function (PDF)

Measured albedo distributions consist of sets of discrete values. Random draws from this set only allow for a strictly limited combinatorial variation. A more realistic approach takes into account the uncertainties of the individual albedo measurements in the form of the albedo probability density function (PDF), $f(p_V)$. The PDF of an individual albedo measurement i, $f_i(p_V)$, describes the probability to pick the albedo value p_V in a random draw by integration over the infinitesimal width dp_V: $\int f_i(p_V)\ dp_V$. The most prominent PDF is the normal distribution, which is distributed around its mean value with a spread described by its standard deviation. The normally distributed probability density peaks at the mean value of the distribution and decreases more or less rapidly with the distance from the peak, depending on its standard deviation. Each individual albedo PDF is

normalized in such a way that $\int_0^1 f_i(p_V)dp_V = 1$, where the integration limits are the physically reasonable albedo limits[2]. The albedo PDF of the entire subpopulation is given by the sum of the individual PDFs of its constituents i

$$f(p_V) = \sum_i f_i(p_V).$$

In the analysis of the Plutino size distribution (Mommert et al. 2012, see also Appendix C.2), I used a two–sided normal distribution for the description of the individual albedo PDFs: its left and right wings were defined as normal distributions with a standard deviation equal to the lower and upper albedo uncertainties, σ_{pV}^- and σ_{pV}^+, respectively. This approach suffers from a discontinuity in the PDF at the location of the mean value of both distributions, caused by the different normalization factors of the two wings in the case $\sigma_{pV}^- \neq \sigma_{pV}^+$ (see Figure B.3 on page 252 for an example), which is common in the case of albedo uncertainties (see Section B.2 for a discussion). The discontinuity leads to artifacts in the PDF that are unphysical. For this work, I revise this approach and replace the description of the individual PDFs by a log–normal distribution. As shown in Section B.2, the log–normal distribution (Equation B.3 on page 251),

$$f(p_V, \bar{\mu}, \bar{\sigma}) = \frac{1}{p_V \cdot \bar{\sigma}\sqrt{2\pi}} \exp\left(-\frac{1}{2}\frac{(\log(p_V) - \bar{\mu})^2}{\bar{\sigma}^2}\right),$$

with the median albedo $\exp(\bar{\mu})$, and scale parameter $\bar{\sigma}$ provides a more realistic description of the albedo uncertainty distribution. I determine the scale parameter $\bar{\sigma}$ for each albedo measurement from its upper uncertainty[3], σ_{pV}^+, as derived from the Monte–Carlo method or given in the literature (see Section B.2):

$$\bar{\sigma} = \log\left(\frac{p_V + \sigma_{pV}^+}{p_V}\right).$$

The median of the albedo PDF, p_V^m, which is utilized in the derivation of the monochromatic size distribution, is then defined as

$$\int_0^{p_V^m} f(p_V)\ dp_V = \int_{p_V^m}^1 f(p_V)\ dp_V.$$

[2]Geometric albedos larger than unity are possible (e.g., on icy moons of the giant planets, see Section 1.2.2), but have not yet been found among the TNO or Centaur populations. Here, the range 0 to 1 is used.

[3]The upper albedo uncertainty has been found to provide better precision in the derivation of $\bar{\sigma}$ (see Section B.2).

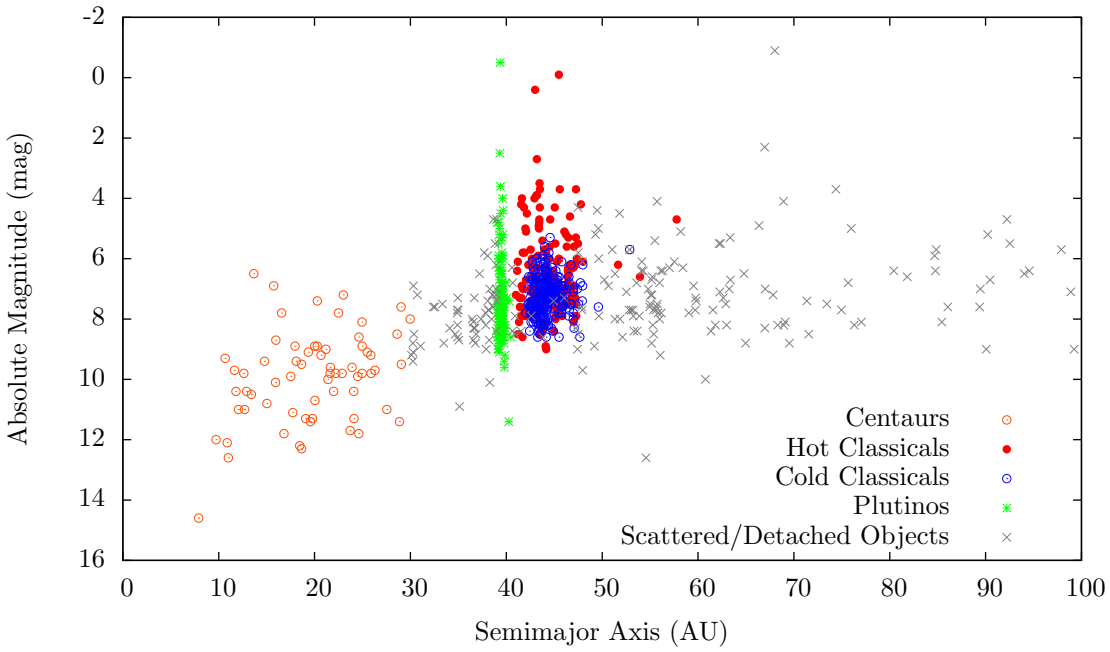

Figure 5.2 Absolute magnitudes of all known TNOs and Centaurs, as of January 2013 (Minor Planet Center Observations Database), as a function of their semimajor axis (compare to Figure 1.5 on page 12). The systematic offset of 0.3 mag (see text and Benecchi et al. 2011) has been added to H magnitudes shown here. The statistical variation added on top follows a normal distribution with $\sigma = 0.3$ mag, and is not included in this plot. Note that 26 scattered/detached objects are off the plot with a>100 AU. The four objects with H<0.05 are (from low to high a): (134340) Pluto, (136108) Haumea, (136472) Makemake, and (136199) Eris, the four known dwarf planets in the trans–Neptunian region.

5.2.2 Prerequisites

In the following, I describe the data samples utilized in this analysis.

5.2.2.1 Absolute Magnitudes and Dynamical Classification

This analysis requires estimates of the absolute magnitude H of all known TNOs and Centaurs. H magnitudes and orbital elements for the sample objects of the individual subpopulations are extracted from the Minor Planet Center Observations Database as of January 24, 2013. The classification scheme used by the MPC mostly agrees with the classification scheme used in the *TNOs are Cool!* program (Gladman et al. 2008, see also Section 1.1.4.1). Note that the MPC merges the three subpopulations of the Centaurs, scattered disk, and detached objects into their definition of the Centaurs. Since the scattered disk and detached objects can only be disentangled using sophisticated dynamical modeling, they are considered equal in the following analysis and are referred to as "scattered/detached" objects. The scattered/detached contribution to the MPC Centaur definition is identified using $a \geq a_N$, with the semimajor axis of Neptune, $a_N = 30.1$ AU; all objects with $a < a_N$ are considered "real Centaurs" (see Section 1.1.4.1 and Gladman et al. 2008). Due to the significant differences in the physical properties of hot ($i \geq 5°$) and cold classicals ($i < 5°$) (see Section 1.1.4.1), I make use of this distinction and examine both samples separately. Note that an analysis of resonant subpopulations other than the Plutinos is precluded due to the lack of a significant number of measured albedos of such objects. The investigation of the size distributions of "other resonants" will be postponed to future work. Hence, I restrict my investigation of the size distributions to the following TNO subpopulations: Centaurs, hot and cold classicals, Plutinos, and scattered/detached objects.

The MPC classification scheme is applied to all known objects. In order to restrict this analysis to only those objects with orbits that are sufficiently reliable, I exclude objects that were observed over less than 3 oppositions (this criterion has been adopted from Gladman et al. 2008, see also Section 1.1.4.1). Furthermore, the reliability of the MPC H magnitudes is highly questionable (see, e.g., Romanishin and Tegler 2005; Benecchi et al. 2011), since most of them are based on astrometric observations with poor photometric quality. However, the lack of properly measured magnitudes for most TNOs makes the MPC H magnitudes indespensable for this analysis. Benecchi et al. (2011) found the H magnitudes provided by the MPC to be systematically brighter by 0.3 mag than H magnitudes derived from Hubble Space Telescope observations, which also agrees with earlier assessments of the MPC H magnitude accuracy (Romanishin and Tegler 2005). Thus, I add an offset to each MPC H magnitude that is drawn from a normal distribution with a mean of 0.3 mag and a 1σ standard deviation of 0.3 mag, taking into account systematic and statistical variations, respectively. The estimate of the statistical uncertainty (0.3 mag) agrees with the findings of Romanishin and Tegler (2005).

The H magnitudes used in this work are plotted as a function of semimajor axis in Figure 5.2. The sample sizes are listed in Table 5.5. The samples of measured H magnitudes, which represent the known sample of each subpopulation, will be referred to in the following as the "**H magnitude sample**" of the respective subpopulations.

5.2.2.2 Albedo Data

Albedo measurements utilized in this analysis are derived from the literature[4], most of which were derived in the framework of the *TNOs are Cool!* program. The albedos from the literature are selected based on the measurement technique: for the reliability of the albedo PDFs it is necessary to have albedos with realistic uncertainty estimates. Hence, only albedo measurements using asymmetric uncertainties that are derived using the method described in (Mueller et al. 2011, see also Section 3.3), or a similar method, are adopted. Only 2 resonant objects other than Plutinos were found to have measured albedos; I postpone the analysis of the size distribution of the "other resonants" to the future, when a larger set of measured albedos from the *TNOs are Cool!* program is available.

The albedos, their uncertainties and log–normal scale parameters $\bar{\sigma}$, as derived from the upper albedo uncertainty, are listed in Table 5.4 by subpopulation. The samples of objects with measured albedos of the individual subpopulations, from which the albedo PDFs are generated, will be referred to as the "**albedo samples**" in the following.

I explore the representativeness of the albedo samples for the individual subpopulations. Figure 5.3 shows the distribution of H magnitudes for each subpopulation as a function of the albedo. The plots show variations in the albedo distributions as a function of H in all subpopulations. Note that the albedo distribution for intrinsically faint objects (high values of H) is heavily impacted by observation bias, since those objects are most difficult to discover; hence, it is impossible to comment on the reliability of this part of the albedo distribution. However, it is obvious that intrinsically bright objects ($H > 0.05$ mag), the majority of which can be assumed to be discovered, all have extraordinarily high albedos ($p_V > 0.5$), a phenomenon that has been observed before (e.g., Brown 2008, and references therein, see also Figure 5.2) and is discussed in Section 5.3. In order to minimize the impact of the significant change in the albedo distribution for intrinsically bright objects, I split the hot classical and scattered/detached albedo PDFs, where objects with $H < 0.05$ are present, into two independent PDFs:

[4] A significant number of albedos were derived in the framework of the *MIPSKBOs* project, which is outlined in Section B.3.

Table 5.4. TNO Subpopulation Albedo Samples.

Object	p_V	σ_{pV}^{-}	σ_{pV}^{+}	$\bar{\sigma}$	d (km)	H	Ref
			Centaurs				
2060	0.080	0.029	0.056	0.53	234	6.5	Section B.3
5145	0.174	0.093	0.303	1.008	127	7.0	Section B.3
7066	0.079	0.039	0.092	0.772	57	9.6	Section B.3
8405	0.060	0.023	0.040	0.51	86	9.0	Section B.3
10199	0.071	0.028	0.044	0.482	263	6.4	Section B.3
10370	0.144	0.069	0.378	1.287	88	8.0	Section B.3
31824	0.079	0.043	0.127	0.958	45	10.1	Section B.3
32532	0.103	0.042	0.081	0.58	66	9.0	Section B.3
52872	0.032	0.012	0.022	0.523	52	10.8	Section B.3
52975	0.107	0.071	0.148	0.868	55	9.3	Section B.3
54598	0.041	0.017	0.029	0.534	201	7.6	Section B.3
55576	0.123	0.057	0.110	0.638	122	7.5	Section B.3
60558	0.042	0.021	0.049	0.773	87	9.4	Section B.3
63252	0.037	0.018	0.032	0.623	35	11.5	Section B.3
83982	0.276	0.135	0.478	1.004	51	8.5	Section B.3
95626	0.059	0.022	0.036	0.476	220	7.0	Section B.3
119315	0.032	0.016	0.034	0.723	89	9.6	Section B.3
119976	0.126	0.056	0.103	0.597	25	10.9	Section B.3
120061	0.079	0.032	0.056	0.535	79	8.9	Section B.3
136204	0.057	0.020	0.036	0.489	101	8.7	Section B.3
145486	0.094	0.039	0.071	0.562	30	10.8	Section B.3
248835	0.048	0.018	0.030	0.485	77	9.5	Section B.3
2000 GM137	0.046	0.018	0.039	0.614	9	14.3	Section B.3
2004 QQ26	0.045	0.021	0.049	0.736	79	9.5	Section B.3
2005 RO43	0.044	0.026	0.060	0.86	220	7.3	Section B.3
Median	0.071						
			Hot Classicals				
19308	0.168	0.082	0.221	0.839	409	4.5	Section B.3
19521	0.05	0.016	0.03	0.47	600	5.0	Vilenius et al. (2012)
20000	0.088	0.049	0.089	0.698	816	3.7	Section B.3
35671	0.043	0.021	0.035	0.595	446	5.8	Section B.3
50000	0.219	0.089	0.216	0.686	910	2.5	Section B.3
55565	0.186	0.085	0.163	0.629	686	3.3	Section B.3
55637	0.129	0.059	0.119	0.653	705	3.6	Section B.3
120347	0.040	0.016	0.024	0.47	953	4.2	Section B.3
126154	0.091	0.048	0.110	0.792	350	5.5	Section B.3
136108	0.959	0.347	0.218	0.204	1345	0.02	Section B.3
136472	0.573	0.188	0.531	0.655	2148	-0.4	Section B.3
148780	0.071	0.021	0.049	0.524	257	6.4	Vilenius et al. (2012)
1996 TS66	0.180	0.088	0.238	0.842	163	6.4	Section B.3
2000 OK67	0.20	0.08	0.21	0.717	151	6.5	Vilenius et al. (2012)
2001 KA77	0.155	0.046	0.091	0.461	252	5.6	Vilenius et al. (2012)
2001 QC298	0.070	0.025	0.049	0.53	299	6.1	Section B.3
2001 QD298	0.164	0.086	0.150	0.649	246	5.6	Section B.3
2002 KW14	0.24	0.07	0.14	0.459	181	5.9	Vilenius et al. (2012)
2002 MS4	0.051	0.022	0.036	0.534	934	4.0	Vilenius et al. (2012)

Table 5.4 (cont'd)

Object	p_V	σ^-_{pV}	σ^+_{pV}	$\bar{\sigma}$	d (km)	H	Ref
2002 XW93	0.038	0.015	0.027	0.536	560	5.4	Vilenius et al. (2012)
2004 GV9	0.077	0.0077	0.0084	0.103	680	4.2	Vilenius et al. (2012)
2005 RN43	0.107	0.018	0.029	0.239	679	3.9	Vilenius et al. (2012)
Median	0.118						
			Cold Classicals				
48639	0.369	0.142	0.237	0.049	194	5.3	Section B.3
66652	0.343	0.175	0.358	0.071	153	5.9	Section B.3
79360	0.090	0.017	0.027	0.026	333	5.6	Vilenius et al. (2012)
88611	0.22	0.08	0.141	0.049	177	6.0	Vilenius et al. (2012)
135182	0.294	0.137	0.206	0.053	165	5.9	Section B.3
2001 QB298	0.167	0.082	0.162	0.067	196	6.1	Section B.3
2001 QY297	0.104	0.050	0.094	0.064	278	5.9	Vilenius et al. (2012)
2001 RZ143	0.191	0.045	0.066	0.029	140	6.7	Vilenius et al. (2012)
2001 XR254	0.17	0.05	0.19	0.075	200	6.1	Vilenius et al. (2012)
2002 KX14	0.097	0.013	0.014	0.013	455	4.9	Vilenius et al. (2012)
2002 VT130	0.097	0.049	0.098	0.069	323	5.6	Section B.3
2003 QA91	0.134	0.059	0.104	0.057	289	5.5	Section B.3
2003 QR91	0.058	0.024	0.039	0.051	277	6.5	Section B.3
2003 UR292	0.16	0.08	0.019	0.011	104	7.4	Vilenius et al. (2012)
2005 EF298	0.16	0.07	0.13	0.059	174	6.4	Vilenius et al. (2012)
Median	0.16						
			Plutinos				
15820	0.310	0.160	0.243	0.578	91	7.1	Section B.3
28978	0.308	0.141	0.337	0.739	549	3.2	Section B.3
32929	0.400	0.231	0.853	1.141	66	7.5	Section B.3
33340	0.028	0.013	0.024	0.619	398	6.5	Section B.3
38628	0.081	0.011	0.011	0.127	439	5.1	Section 5.1
90482	0.243	0.110	0.283	0.772	936	2.3	Section B.3
120348	0.264	0.111	0.338	0.824	365	4.3	Section B.3
1996 TP66	0.074	0.031	0.063	0.615	154	7.5	Section 5.1
1999 TC36	0.079	0.011	0.013	0.152	393	5.4	Section 5.1
2000 GN171	0.215	0.070	0.093	0.359	147	6.5	Section 5.1
2001 KD77	0.089	0.027	0.044	0.401	232	6.4	Section 5.1
2001 QF298	0.071	0.014	0.020	0.248	408	5.4	Section 5.1
2002 VE95	0.149	0.016	0.019	0.12	249	5.7	Section 5.1
2002 VR128	0.052	0.018	0.027	0.418	448	5.6	Section 5.1
2002 VU130	0.179	0.103	0.202	0.755	252	5.5	Section 5.1
2002 XV93	0.04	0.015	0.020	0.405	549	5.4	Section 5.1
2003 AZ84	0.107	0.016	0.023	0.194	727	3.7	Section 5.1
2003 QX111	0.051	0.022	0.048	0.663	283	6.6	Section B.3
2003 UT292	0.067	0.034	0.068	0.7	186	6.9	Section 5.1
2003 VS2	0.147	0.043	0.063	0.356	523	4.1	Section 5.1
2004 EW95	0.044	0.015	0.021	0.39	291	6.7	Section 5.1
2004 PF115	0.123	0.033	0.043	0.299	468	4.5	Section 5.1
2004 UX10	0.141	0.031	0.044	0.271	398	4.8	Section 5.1
2006 HJ123	0.281	0.152	0.259	0.653	216	5.3	Section 5.1
Median	0.115						

Table 5.4 (cont'd)

Object	p_V	σ_{pV}^-	σ_{pV}^+	$\bar{\sigma}$	d (km)	H	Ref
Scattered/Detached Objects							
26181	0.214	0.102	0.291	0.858	262	5.2	Section B.3
26375	0.118	0.048	0.096	0.595	444	4.7	Section B.3
29981	0.051	0.023	0.044	0.622	103	8.8	Section B.3
33128	0.052	0.028	0.065	0.81	213	7.2	Section B.3
42355	0.044	0.003	0.003	0.065	185	7.7	Santos-Sanz et al. (2012)
44594	0.111	0.062	0.119	0.728	151	7.1	Section B.3
60608	0.054	0.024	0.054	0.693	117	8.5	Section B.3
65489	0.056	0.006	0.006	0.101	281	6.5	Santos-Sanz et al. (2012)
82075	0.408	0.213	0.329	0.591	229	4.8	Section B.3
84522	0.037	0.015	0.028	0.563	1164	3.9	Section B.3
87555	0.104	0.051	0.114	0.74	92	8.3	Section B.3
90377	0.336	0.072	0.072	0.194	990	1.8	Pál et al. (2012)
136199	0.845	0.088	0.088	0.099	2454	-1.1	Santos-Sanz et al. (2012)
1996 TL66	0.11	0.015	0.021	0.174	339	5.4	Santos-Sanz et al. (2012)
2001 FP185	0.046	0.007	0.007	0.141	332	6.4	Santos-Sanz et al. (2012)
2001 QR322	0.047	0.022	0.040	0.615	180	7.7	Section B.3
2002 PN34	0.049	0.006	0.006	0.115	112	8.7	Santos-Sanz et al. (2012)
2002 XU93	0.038	0.004	0.004	0.1	164	8.1	Santos-Sanz et al. (2012)
2003 FY128	0.079	0.015	0.01	0.119	460	5.1	Santos-Sanz et al. (2012)
2005 EB299	0.083	0.045	0.089	0.728	101	8.3	Section B.3
2005 QU182	0.328	0.109	0.16	0.397	416	3.8	Santos-Sanz et al. (2012)
2005 TB190	0.148	0.036	0.051	0.296	464	4.4	Santos-Sanz et al. (2012)
2007 OC10	0.127	0.028	0.04	0.273	309	5.4	Santos-Sanz et al. (2012)
2007 UK126	0.167	0.038	0.058	0.298	599	3.7	Santos-Sanz et al. (2012)
2010 EK139	0.261	0.047	0.047	0.165	450	3.8	Pál et al. (2012)
Median	0.104						

Note. — σ_{pV}^- and σ_{pV}^+ denote the lower and upper limit albedo uncertainty, as derived in the referenced publication (Ref). The scale parameter, $\bar{\sigma}$, of the log–normal distribution is derived from the upper albedo uncertainty (see text). d is the diameter as determined by the thermal model. H magnitudes are those used in the reference. The median as derived from the albedos listed here (not using the albedo PDF) is given for each subpopulation. Results from Section B.3 are derived within the *MIPSKBOs* project.

I introduce the "**faint albedo PDF**" that is derived from intrinsically faint objects with H magnitudes $H > 0.05$, and the "**bright albedo PDF**" that is derived from intrinsically bright objects with $H \leq 0.05$ objects. H is here the randomized magnitude, including the systematic and statistical variations discussed above. Hence, for each H magnitude it has to be checked, whether the albedo is drawn from the bright or faint albedo PDF. This measure provides a more realistic description of the measured albedo distributions.

5.2.3 Results

Figure 5.4 shows the albedo PDFs of the individual subpopulations; the size distributions of the known TNO subpopulations are shown in Figure 5.5 and discussed below. In Figure 5.5, I show the "cumulative distribution of the measured diameters" as grey circles, referring to the number of objects with measured diameters larger than that given in the

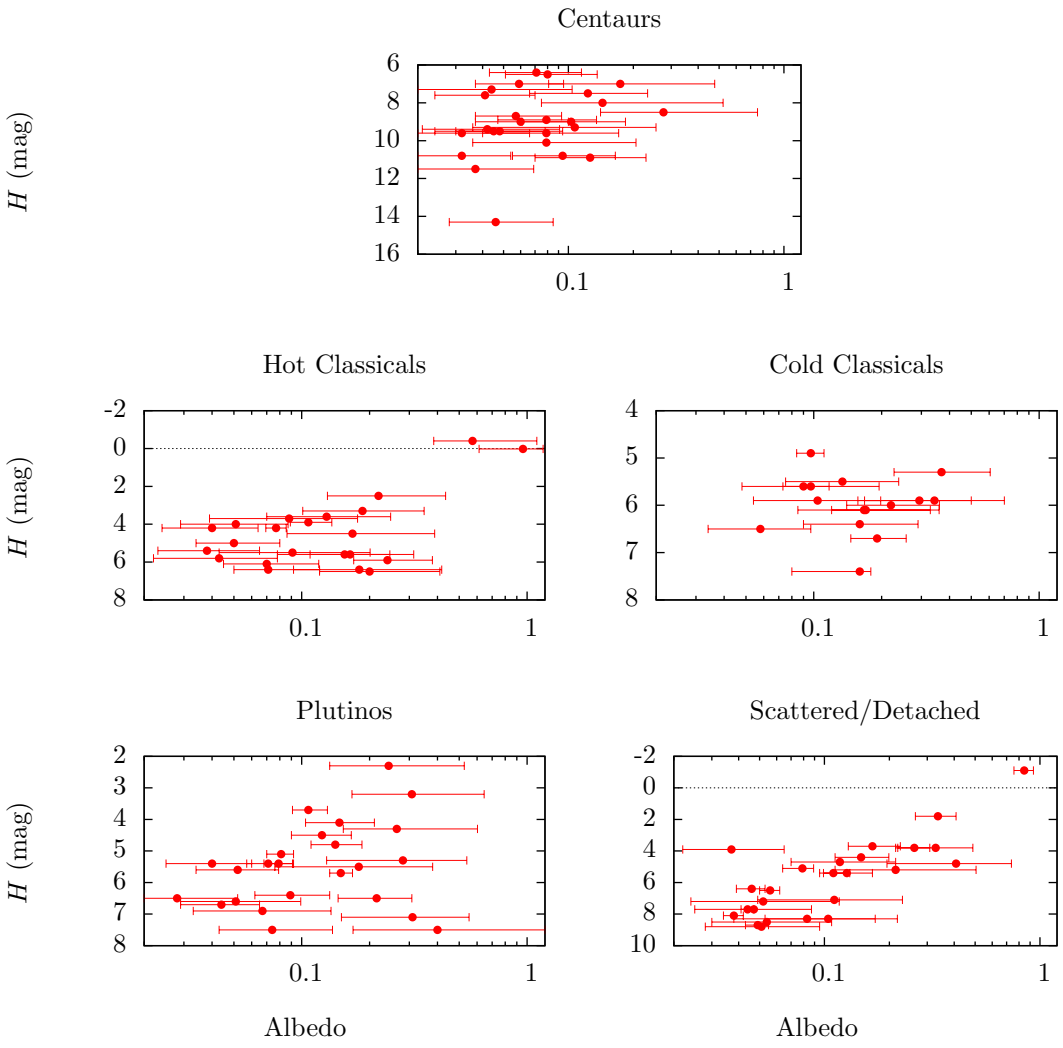

Figure 5.3 H magnitude as a function of the albedo for the individual subpopulation samples used in this work. The plots show that only the hot classicals and the scattered/detached subpopulations are subject to significant trends between the two parameters. In both cases, the trend is induced by the existence of high–albedo objects with high intrinsic brightnesses (low H). In order to take the different albedo distributions for intrinsically bright and faint objects into account, I split both albedo distributions at $H = 0.05$ mag (dotted line) into a "bright" ($H \leq 0.05$), and a "faint" ($H > 0.05$) albedo PDF (see text).

plot. The diameter of each albedo sample object is listed in Table 5.4. This distribution, in the following referred to as the "**measured diameter distribution**", shows a significant break that is caused by the incompleteness of the sample at smaller diameters. The median albedos as derived from the individual albedo PDFs are depicted in Figure 5.4 and listed in Table 5.5.

I derive the size distribution slopes[5] q of the individual cumulative size distributions, assuming a simple power–law relation, which is common use (see Section 1.2.2.3, $N(>d) \propto d^{-(q-1)}$). The slopes are derived using a by–eye fit to the size distributions shown in Figure 5.5. Formal fitting algorithms were tested, but it turned out that the derived slopes were highly sensitive to the fitting range. For the fit I disregard the regime of the largest diameters, where uncertainties are large, and the turn–over at smaller diameters, which is caused by the incompleteness of the H magnitude sample at intrinsically faint targets (large H). Note that the incompleteness of the H distribution for faint objects precludes any comments on the size distribution of objects smaller than a critical threshold diameter, d_c. I define the threshold diameter as that diameter where the simple power law leaves the 1σ standard deviation interval of the Monte–Carlo size distribution, depicted by the dashed lines. The derived slopes are plotted in Figure 5.5 and the slope parameters are listed in Table 5.5, together with the respective threshold diameters.

5.2.4 Discussion

5.2.4.1 Individual Size Distributions

In the following, I discuss the properties of the individual cumulative size distributions as shown in Figure 5.5, and the properties albedo PDFs shown in Figure 5.4. The comparison with results from the literature is performed below.

- **Centaurs** are smaller than most TNOs; the largest Centaur has $d \sim 300$ km. Their cumulative size distribution follows the simple power law only over a small range in diameter before the incompleteness of the H sample forces the distribution to gradually change its slope. The monochromatic size distribution agrees with that of the Monte–Carlo method within the uncertainties. However, the monochromatic size distribution suggests a somewhat steeper power–law slope. The measured diameter distribution, too, suggests a steeper slope of the size distribution for the largest objects. The albedo PDF of the Centaurs is single–peaked at low albedos.
  The comparison of the size distribution slopes shows similar slopes for the Centaurs, hot classicals, Plutinos and scattered/detached objects. This similarity agrees with dynamical simulations that show that the Centaur population is a transition population, fed by these subpopulations (see Section 1.1.4.1).

[5]Note that the power–law coefficient that is fit to the plots is $(q+1)$. The values listed in Table 5.5, however, are q.

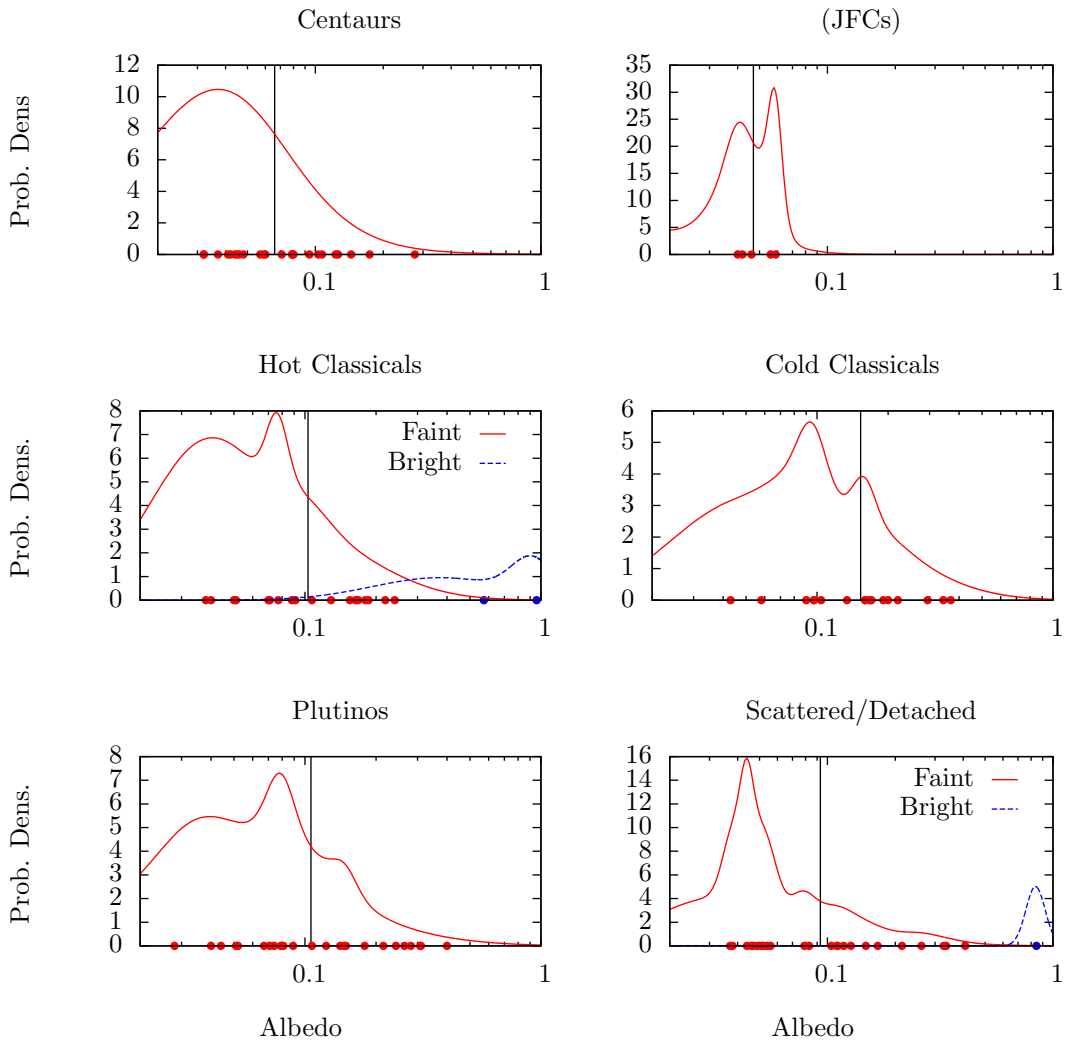

Figure 5.4 Albedo PDFs of the individual subpopulation albedo samples. PDFs are shown as lines; dots at the bottom indicate individual albedo measurements. Red lines and dots refer to object with $H > 0.05$ ("faint" albedo sample), whereas blue lines and dots refer to objects with $H \leq 0.05$ ("bright" albedo sample) (see text for details). The black vertical bars represent the median of the albedo PDF (in the case of hot classicals and scattered/detached objects of the combined faint+bright albedo PDF) as derived from the albedo PDF and listed in Table 5.5. The JFC albedo PDF, as derived from Table 4.2, is shown for comparison. Note the log–normal scale in albedo.

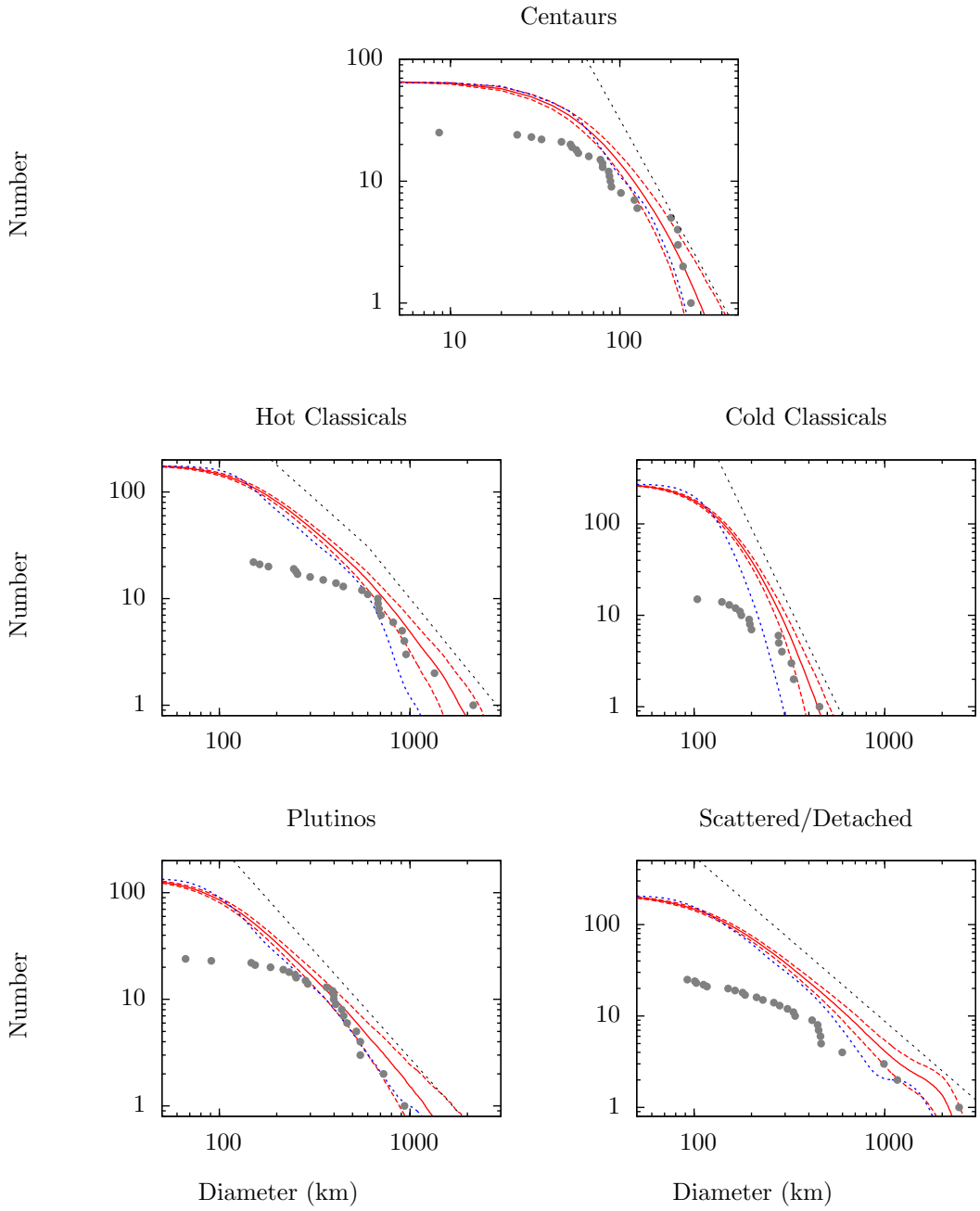

Figure 5.5 Cumulative size distributions of the known TNO subpopulations as derived from the H magnitude and albedo samples. The red continuous line depicts the results of the Monte–Carlo method, based on the albedo PDF, as shown in Figure 5.4; uncertainties are shown as red dashed lines. The blue dashed line depicts the monochromatic size distribution, using the fixed albedo for all objects; the median albedo of the PDF is used here for the fixed albedo (see Table 5.5). The grey dots indicate the measured diameter distribution, which is the cumulative distribution of the actually measured sizes of the objects listed in Table 5.4. The dotted line represents the best–fit power–law slopes of the cumulative size distribution as listed in Table 5.5; the line is offset in the vertical axis from the measured size distribution to improve readability.

Table 5.5. TNO Subpopulation Size and Albedo Distribution Summaries.

Subpopulation	N_{pV}	N_{MPC}	p_V^m	q (d_c km)	q_{lit}
Centaurs	25	65	0.066	3.5 (100)	3.7–4.0 (a)
Hot Classicals	25	161	0.103	3.2 (600)	2.8–5.0 (b,c)
				2.6 (200)	2.8–5.0 (b,c)
Cold Classicals	15	286	0.153	5.3 (200)	5.1–7.0 (b,c)
Plutinos	24	137	0.106	3.0 (200)	5.5 (d)
Scattered/Detached	25	215	0.093	2.8 (250)	5.0 (e)
Jupiter Family Comets	6				2.9 (a)
Trans–Neptunian Region					4.15–4.45 (a)

Note. — N_{pV} denotes the number of objects in the respective albedo sample; N_{MPC} is the number of objects in the respective H magnitude sample. The median albedo, p_V^m, is defined in Equation 5.2.1.1. The power–law slope parameter q is derived from Figure 5.5. Note that in this table q is listed, whereas $(q-1)$ is fitted to the cumulative size distributions in Figure 5.5 (see also Section 1.2.2.3). d_c denotes the critical lower limit diameter where the simple power law leaves the 1σ confidence interval of the Monte–Carlo size distribution, indicated by the red dashed lines in Figure 5.5. q_{lit} gives the size distribution power–law slopes for the respective subpopulations from the literature, where available. The slope parameter of the JFCs is given for comparison.

References. — (a): Lamy et al. (2004) and references therein; (b): Fraser et al. (2010); (c): converted using $q = 5\alpha+1$ (see Section 1.2.2.3) from Petit et al. (2011); (d): Gladman et al. (2012) (determined for a range $8 < H < 9$); (e): Shankman et al. (2013) found the scattered disk population to be best approximated by a divoted luminosity distribution, using $\alpha = 0.8$ for $H < 9$ mag and $\alpha = 0.5$ for fainter objects. The differential size distribution performs a step at $H = 9$ mag (see their Figure 2). Since only few objects with $H > 9$ mag are in the H sample used here (see Figure 5.2), I adopt $\alpha = 0.8$, which should dominate the size distribution investigated here; the size distribution slope was derived using $q = 5\alpha + 1$.

- The **hot classicals** are clearly larger than the **cold classicals**, and have a cumulative size distribution that is significantly shallower, which is also reported from the investigation of the luminosity function of the classical TNOs (Fraser et al. 2010). The hot classicals are the only subpopulation that appears to have a kink in their size distribution at diameters of ∼600 km, the significance of which is questionable: the kink might be caused by the incompleteness of the H sample at small diameters. The monochromatic size distributions of both subpopulations show significantly steeper slopes than the respective Monte–Carlo distributions, and disagree for the largest objects. This deviation is likely to be caused by the wide range of albedos measured in both samples that is only insufficiently described by a fixed albedo for all objects. A comparison of the albedo PDFs of both subpopulations shows a preference for higher albedos in the cold compared to the hot classicals. Also note that the "bright" albedo sample PDF of the hot classicals is smeared over a wide range in albedo, caused by the large albedo uncertainty of object (136108) Haumea. The cumulative distribution of measured diameters shows a good agreement with the Monte–Carlo size distributions for the largest objects for both classical subpopulations.

  The differences in the slope, the overall sizes, and the albedo PDFs of the hot and cold classicals confirm findings of previous works (e.g., Brucker et al. 2009; Fraser et al. 2010, and see Section 1.1.4.1) and suggest different accretional and collisional environments of both subpopulations. The shallower size distribution slope of the dynamically excited hot classicals point towards an evolution that was subject to destructive collisions, whereas the steep slope of the cold classicals prefers a past that was less dominated by impacts. The exact interpretation of the different evolutions requires detailed modeling, which is beyond the scope of this work.

- The results presented here on the **Plutino** size distribution supersede those presented by Mommert et al. (2012) (see also Section C.2). Using the larger number of measured albedos and the more sophisticated albedo PDF based on a log–normal description of the albedo uncertainties, the Plutino cumulative size distribution is best described by a single power law, instead of a broken power–law (Mommert et al. 2012). The Monte–Carlo distribution agrees with both the monochromatic and the measured diameter size distributions over a wide range. The median albedo of the Plutinos derived here (0.106) is somewhat higher than the weighted average derived by Mommert et al. (2012) (0.08 ± 0.03).

  The lack of albedo measurements of other resonant objects precludes a comparison of the Plutino size distribution with that of other resonant groups. This will be the subject of future work.

- The **scattered/detached** subpopulations have the shallowest of all size distributions determined here. The "hook"–like feature at the large–size end is presumably an artifact introduced by the overrepresentation of intrinsically bright objects in the H magnitude distribution (see discussion below). I can rule out the "hook" to be caused by the separate bright albedo PDF, since it is also present in the monochromatic size distribution, which does not use a separate bright object albedo. The cumulative measured diameter distribution suggests an even shallower slope, which is likely to be the result of an observational bias, causing a lack of small objects. The albedo PDF is single–peaked for the bright (red line) and faint (blue line) albedo samples, individually.
  A disentanglement of the contributions from the scattered and detached object subpopulations requires dynamical modeling for a proper classification of all objects for which H magnitude estimates exist and is the subject of future work.

5.2.4.2 Robustness of the Subpopulation Classification

In the classification of the H sample objects, I rely on the classification scheme utilized by the MPC, which might be slightly different than the scheme by Gladman et al. (2008). The latter is used in the classification of the albedo samples. A comparison of Figures 5.2 and 1.5 on page 12, the latter being based on the Gladman et al. (2008) classification scheme used in the *TNOs are Cool!* program, shows good agreement. Furthermore, the statistical nature of the analysis method is able to compensate for a small number of misclassifications. Additional dynamical modeling is necessary to improve on the classification, and to be able to disentangle the scattered and detached subpopulations. This will be the subject of future work.

5.2.4.3 Robustness of the Method

In order to properly describe the measured albedo distribution for each subpopulation, I make use of the albedo PDF (see above), which describes each individual albedo measurement using a log–normal distribution, taking into account the uncertainties of the measurement.

I investigate the robustness of the albedo PDF by comparing the median of the albedo PDF, p_V^m (given in Table 5.5), with the median derived from the discrete albedo values listed in Table 5.4 for each subpopulation. The comparison shows that most median albedos agree better than within 0.01, in the case of the hot classicals the agreement is within 0.02, amounting to less than 20% fractional deviation. The discrepancies are caused by the fact that the median based on the PDF takes into account the uncertainties, which is not the case for the median derived from discrete values. Nevertheless, the overall agreement supports the robustness of the albedo PDF.

Furthermore, the cumulative size distributions shown in Figure 5.5 show that the large–size ends of the distributions agree within their uncertainties with the diameters of the largest known objects (rightmost grey circles) for each subpopulation. This agreement supports the robustness of the method and shows that the size distributions are properly calibrated with respect to the absolute number of objects.

5.2.4.4 Robustness of the Albedo Distribution

The comparison of Figures 5.2 and 5.4 shows that a significant number of objects in the H sample is fainter than the faintest object in the respective albedo sample. Strictly speaking, the measured albedo distribution is representative for only that portion of the subpopulation with similar H magnitudes. The albedo distribution of fainter members of the subpopulation is yet unexplored, and might differ from the one that is shown in Figure 5.4. In order to explore the impact of such a possible discrepancy on the results of this analysis, I introduce the critical magnitude H_c, which is roughly defined as the lowest H magnitude of the bulk of all available albedo measurements per subpopulation. From Figure 5.4, I read H_c=[11.5, 7.0, 6.5, 7.5, 9.0] mag for the [Centaur, hot classical, cold classical, Plutino, scattered/detached] subpopulation. I determine the lower size limit, d_l, to which the critical magnitude translates using Equation 1.4 on page 23, assuming an albedo that is equal to the respective subpopulation median albedo, p_V^m (see Table 5.5). I estimate d_l ∼[25, 160, 170, 130, 70] km for the [Centaur, hot classical, cold classical, Plutino, scattered/detached] subpopulation. Comparing d_l to the critical diameters (d_c) listed in Table 5.5, for which the determined power–law slopes are valid, shows that $d_l < d_C$ for all subpopulations, and hence that the power–law slope of each of them is derived for a size range that is well–described by the measured albedo distribution.

Nevertheless, I cannot rule out the measured albedo distributions to be subject to bias, for instance causing a lack of low–albedo objects. Providing proper de–biasing of the albedo distribution will be the subject of future work. In the following, I discuss possible consequences of bias on the results of this analysis.

5.2.4.5 Impact of Bias

- Low albedos significantly hamper discovery by optical means, leading to a lack of known low–albedo objects and a simultaneous overrepresentation of high–albedo objects compared to the real albedo distribution. Albedo bias directly impacts the albedo PDF (Figure 5.4), possibly leading to an overestimation in the frequency of high albedos, which in turn overestimates the number of large objects, decreasing the slope q of the cumulative size distribution. Indeed, the measured diameter distribution of the Centaur population, which is closest to us, shows a steeper slope compared to the results of the Monte–Carlo method (see Figure 5.5). This steeper slope for the large objects, most of which are likely to have been discovered, might

suggest that the real size distribution is actually steeper than found by the method. Accounting for the albedo bias requires sophisticated de–biasing using existing models of the TNO region (e.g., Petit et al. 2011), and will be the subject of future work.

- The strong dependence of the apparent magnitude from the distance of an object (see Equation 1.2 on page 20, $V \propto 2\log(r)$) favors the discovery of objects that are close and hampers the detection of more distant objects. Consequentially, TNOs at large distances are more likely to be discovered if they have a high intrinsic brightness (low H) compared to their fainter siblings. This causes an overrepresentation of intrinsically bright objects in the H magnitude sample and distorts the shape of the size distribution, as might be visible for the scattered/detached subpopulation in Figure 5.5. The compensation of this effect requires sophisticated de–biasing of the H magnitude sample, and will be the subject of future work.

5.2.4.6 Comparison with Size Distributions from the Literature

The derived power–law slopes from the Monte–Carlo size distributions and previous results from the literature, which are based on luminosity functions and assume a fixed albedo, are listed in Table 5.5. The slopes of the Monte–Carlo method roughly agree with those found in the literature, but tend to be lower than the slopes found in the literature, which is presumably caused by the incompleteness of the H samples and shows the need for proper de–biasing. In the case of the Plutinos and the scattered/detached subpopulation, the slope derived by the Monte–Carlo method is significantly smaller compared to the result from the literature.

In the case of the Plutinos, Gladman et al. (2012) estimated the slope based on objects with $8 < H < 9$ mag, which refers to sizes[6] of 65–100 km, which is significantly smaller than the smallest diameters for which the size distribution's slope was determined (see value d_c in Table 5.5). A different slope of the Plutino size distribution for larger objects is possible; however, I was unable to find other results in the literature.

The literature slope of the scattered/detached subpopulation is based on a luminosity distribution derived by Shankman et al. (2013), and is solely based on scattered disk objects with $H < 9$. Comparing the H magnitudes of the H magnitude sample (Figure 5.2) and the albedo sample (Figure 5.4) shows that both samples cover roughly the same range in H. Hence, an albedo bias seems to be unlikely as the cause of the discrepancy; more likely seems to be the incompleteness of the H sample to cause the different size distribution slope. The lack of a measured size or luminosity distribution of the detached objects precludes a statement on whether the mixing of the two subpopulations might contribute to the discrepancy.

[6] Assuming a fixed albedo equal to the measured median albedo of the Plutino subpopulation of $p_V^m = 0.106$ (see Table 5.5).

5.2.4.7 The Origin of the Jupiter Family Comets (JFCs)

Dynamical models show that JFCs are likely to originate from TNO subpopulations, specifically the Centaur, scattered disk and Plutino subpopulations (see Section 1.1.5.2). The results of this work allow for a comparison of the physical properties of these populations, providing an additional test for this hypothesis:

- The albedo PDFs (see Figure 5.4) of most of the TNO subpopulations, but especially of the Centaur, hot classical, and scattered/detached subpopulations, favor low, comet–like, albedos. The albedo PDF of the JFCs, based on the compilation used in Section 4.2 (see Table 4.2 on page 112), is shown for comparison in Figure 5.4. I investigate the overlap of the JFC albedo PDF with the individual TNO subpopulation albedo PDFs by convoluting both distributions, i.e., I calculate the integral of the product of the JFC and the other albedo PDF over the whole albedo range, resulting in a qualitative estimate of the similarity of the distributions. The larger the overlap of the two distributions, the higher the resulting number. The results of this methods agree with those of the visual inspection performed above: the values derived for the [Centaur, hot classical, cold classical, Plutino, scattered/detached] populations are [8.6, 5.5, 2.5, 4.9, 7.8] and show the strongest overlap between the JFCs albedo PDF and that of the Centaurs, hot classicals, and scattered/detached objects.

- JFCs that are ejected from TNO subpopulations necessarily have a similar size distribution to their source populations, assuming the ejection mechanism is size–independent. The comparison of the power–law slopes of the TNO subpopulations with that of the JFCs (see Table 5.5) shows that all but the cold classicals have similar slopes. Hence, only the cold classical subpopulation can be excluded to be a source of JFCs, based on the size distribution, due its steep size distribution. However, this result has to be taken with care: the size distribution slopes derived in this work are only valid for diameters d >100–250 km, depending on the subpopulation, which is significantly larger than the largest the JFCs: Lamy et al. (2004) have based their measurement of the JFC size distribution slope on objects with $d < 20$ km, which is significantly smaller than most of the known TNOs. However, Bernstein et al. (2004) found evidence for a break in the TNO size distributions at sizes $d \leq 100$ km towards a shallower size distribution, which would improve the agreement between some of the measured TNO subpopulations size distributions with that of the JFCs.

The results of this analysis provide additional physical evidence for a link between the JFCs and the TNOs; especially albedo and size distributions of the Centaur, hot classical and scattered/detached subpopulations seem to agree with the characteristics of the Jupiter Family Comets.

5.2.5 Conclusions

- I present cumulative size distributions of the TNO subpopulations based on the H magnitudes of the known members and the measured albedo distribution of a small sample. This method is independent from the measurement of the luminosity function, on which most available size distribution estimates are based. The results of this independent method agree with previous results.

- The power–law slopes of the size distributions as derived with this method are [3.5, 3.2, 5.3, 3.0, 2.8] for the [Centaur, hot classicals, cold classicals, Plutinos, scattered/detached objects]. The size distributions follow the simple power law relation for diameters larger than 100–250 km, depending on the subpopulation; the method gives no hints on the size distribution of objects smaller than this range, due to the incompleteness of the known TNO subpopulations at small diameters.

- The size and albedo distributions of the hot and cold classical population differ significantly, which was already observed (Brucker et al. 2009; Fraser et al. 2010) before, and suggests a different origin and evolution of the two populations.

- The size distribution slopes of all TNO subpopulations but the cold classicals agree with that of the JFCs (Lamy et al. 2004). The JFC albedo distribution agrees best with that of the Centaur, hot classical, and scattered/detached subpopulations.

5.3 Correlations of Measured Albedos with the TNO Taxonomy and the Presence of Ices

A TNO taxonomy based on measured color indices (Tegler and Romanishin 1998) has been suggested by Barucci et al. (2005) and Fulchignoni et al. (2008) (see Section 1.2.4). The taxonomy distinguishes between four different types, BB, BR, IR, and RR, which range from neutral–greyish to extremely red in color, in this order. The individual types are associated with spectral slopes, absorption band depths, and the presence of ices: according to Barucci et al. (2011), ices can be present on all types; all of the BB–type TNOs seem to have surface ices, whereas they have not yet been unambiguously identified on IR–type TNOs.
The lack of a sufficient number of measured albedos of TNOs has so far precluded an investigation of a possible correlation of the color–based taxonomic classification as suggested by Barucci et al. (2005) with albedo (Fulchignoni et al. 2008). Such a correlation is present in the main belt asteroid and NEO taxonomy (see Section 1.2.4), where the albedo can used to coarsely constrain the taxonomic complex (see Section 1.2.4). Based on the results of the TNOs are Cool! program and data from the literature, I explore the albedo ranges of the TNO taxonomy. Furthermore, I investigate a possible correlation of albedo with the presence of surface ices.

5.3.1 Data

Precise multiband–photometry (i.e., color indices) or spectroscopic analyses are necessary for a reliable taxonomic classification, both of which are available only for a very limited sample of TNOs, given their faintness. Hence, only a small part of the known TNO population has taxonomic classifications using the scheme provided by Barucci et al. (2005). The overlap between those TNOs with measured albedos and those with taxonomic classifications (to my knowledge as of February 2013) amounts to a total of 71 objects, all of which are listed in Table 5.6. The taxonomic classifications were taken from Fulchignoni et al. (2008), Perna et al., and Barucci et al. (2011). Note that some objects have been assigned multiple taxonomic types, which is the result of ambiguities in the definition of the different types and a lack of precision in the derivation of the color indices. Objects with multiple classifications are assigned to each type to properly take into account such ambiguities.

Information on the presence of ices used in this analysis are extracted from Barucci et al. (2011), who compiled a list of objects with adequate spectroscopic measurements. They base their assessment of the presence of surface ices on (1) the depth of water ice absorption bands, and (2) the spectral slope between 2.05 and 2.3 μm, which is indicative for the presence of water and methanol ices. The depth of the water ice absorption bands allows for a qualitative estimation of the amount of water ice on the surface. They assign

each object with adequate spectroscopic measurements to one of the following groups: confirmed to harbor ices (Y), likely to harbor ices (T, for "tentative"), most likely not to harbor ices (N); I adopt this classification scheme in Table 5.6. Objects with significant amounts of water ice, i.e., a water ice band depth $D \geq 20\%$ (see Barucci et al. 2011), are highlighted in the table. Barucci et al. (2011) find that objects with significant amounts of ices are intrinsically brighter ($H \leq 6$ mag), and they also find that all objects with BB–type classifications seem to have ices on their surfaces.

The albedo data used in this analysis stem from the *TNOs are Cool!* program and the *MIPSKBOs* project (see Section B.3 and Mueller et al. 2013). The albedos used in this analysis are listed in Table 5.6.

5.3.2 Method

In order to explore possible correlations of the TNO color taxonomy and the presence of ices with albedo, I calculate different statistical quantities of the individual samples: the arithmetic average, the weighted average, and the median. The weight of the weighted average is defined as the reciprocal mean of the upper and lower fractional uncertainties, $2/(\sigma^{+}_{pV}/p_V + \sigma^{-}_{pV}/p_V)$, leading to a better representation of the bulk properties than using the absolute uncertainties as weights[7]. For the uncertainties of the arithmetic and weighted average I adopt their respective unweighted and weighted 1σ standard deviations, respectively. For the median I use a different approach, and give the range of albedos that bracket 68.3% of all albedos centered around the median.

I also compare the albedo distributions of the individual samples using the non–parametric and distribution–free Kolmogorov–Smirnov test (KS test, see, e.g., Press et al. 1992). The KS test compares the cumulative distributions of two one–dimensional samples and returns the probability at which the "Null Hypothesis", i.e., that both samples are drawn from the same population, can be rejected. The test results in a p–value; $(1 - p)$ is the probability at which both samples can be rejected to be drawn from the same population. The lower p, the higher the probability that both sample distributions are different.

5.3.3 Results

Figure 5.6 shows a comparison of the albedo distributions of the individual taxonomic classes. The averages and median values with respective confidence intervals of each taxonomic type, as well as the results of the KS test are listed in Table 5.7.

[7]The log–normal nature of the albedo uncertainties (see Section B.2) gives rise to the effect that the absolute uncertainties of high–albedo objects are higher compared to those of low–albedo objects. The fractional uncertainties, σ_{pV}/p_V, however, are similar over the whole range of albedos. The weighted average of a sample of albedos using the absolute uncertainties as weights, is biased towards low albedos, which have lower absolute uncertainties. However, the weighted average using the fractional uncertainties is less biased towards low albedos and leads to a more realistic average.

Table 5.6. TNO Taxonomy and Ice Sample.

Object	p_V	σ_{pV}^{-}	σ_{pV}^{+}	d (km)	H (mag)	Tax. Class.	Ices?	Ref.
2060	0.080	0.029	0.056	235	6.5	BB	Y	1, 2
5145	0.174	0.093	0.303	126	7.0	RR	Y	1, 2
7066	0.079	0.039	0.092	56	9.6	RR	–	1, 3
8405	0.060	0.023	0.040	86	9.0	BR	N	1, 2
10199	0.071	0.028	0.044	262	6.4	BR	Y	1, 2
15820	0.310	0.160	0.243	90	7.1	RR	–	1, 3
15874	0.11	0.015	0.021	339	5.4	BB	T	4, 2
19308	0.168	0.082	0.221	408	4.5	BB	Y	1, 2
19521	0.05	0.016	0.03	600	5.0	IR	N	5, 2
20000	0.088	0.049	0.089	816	3.7	IR	N	1, 2
26181	0.214	0.102	0.291	262	5.2	RR	Y	1, 2
26375	0.118	0.048	0.096	444	4.7	IR	T	1, 2
28978	0.308	0.141	0.337	549	3.2	IR	T	1, 2
29981	0.051	0.023	0.044	102	8.8	BR	N	1, 2
31824	0.079	0.043	0.127	45	10.1	RR	Y	1, 2
32532	0.103	0.042	0.081	65	9.0	BR	Y	1, 2
32929	0.400	0.231	0.853	66	7.5	BR	–	1, 3
33128	0.052	0.028	0.065	212	7.2	RR	–	1, 3
33340	0.028	0.013	0.024	398	6.5	IR	N	1, 2
35671	0.043	0.021	0.035	446	5.8	BB	–	1, 3
38628	0.081	0.011	0.011	438	5.1	IR	T	6, 2
42355	0.044	0.003	0.003	185	7.7	BR	Y	4, 2
44594	0.111	0.062	0.119	150	7.1	RR	T	1, 2
48639	0.369	0.142	0.237	194	5.3	RR	–	1, 3
50000	0.219	0.089	0.216	909	2.5	RR	Y	1, 2
52872	0.032	0.012	0.022	52	10.8	BR	T	1, 2
52975	0.107	0.071	0.148	55	9.3	RR	–	1, 3
54598	0.041	0.017	0.029	200	7.6	BR	Y	1, 2
55565	0.186	0.085	0.163	686	3.3	IR	N	1, 2
55576	0.123	0.057	0.110	121	7.5	RR	T	1, 2
55637	0.129	0.059	0.119	704	3.6	IR	N	1, 2
60558	0.042	0.021	0.049	86	9.4	BR	N	1, 2
60608	0.054	0.024	0.054	116	8.5	BR	–	1, 3
63252	0.037	0.018	0.032	34	11.5	BR	N	1, 2
65489	0.056	0.006	0.006	281	6.5	–	Y	4, 2
66652	0.343	0.175	0.358	152	5.9	RR	N	1, 2
79360	0.090	0.017	0.027	333	5.6	RR	N	5, 2
82075	0.408	0.213	0.329	229	4.8	BR	–	1, 3
83982	0.276	0.135	0.478	51	8.5	RR	Y	1, 2
84522	0.037	0.015	0.028	1163	3.9	–	T	1, 2
90377	0.336	0.072	0.072	990	1.8	RR	**Y**	7, 2
90482	0.243	0.110	0.283	935	2.3	BB	**Y**	1, 2
95626	0.059	0.022	0.036	219	7.0	BR	–	1, 3
120061	0.079	0.032	0.056	79	8.9	BR	T	1, 2
120348	0.264	0.111	0.338	365	4.3	IR/RR/BR	T	1, 8, 2
136108	0.959	0.347	0.218	1344	0.02	BB	**Y**	1, 2
136199	0.845	0.088	0.088	2454	-1.1	BB	Y	4, 2

Table 5.6 (cont'd)

Object	p_V	σ_{pV}^-	σ_{pV}^+	d (km)	H (mag)	Tax. Class.	Ices?	Ref.
136472	0.573	0.188	0.531	2147	-0.4	BR	Y	1, 2
148780	0.071	0.021	0.049	257	6.4	RR	–	5, 3
1996 TP66	0.074	0.031	0.063	154	7.5	RR	N	6, 2
1996 TS66	0.180	0.088	0.238	162	6.4	RR	–	1, 3
1999 TC36	0.079	0.011	0.013	393	5.4	RR	Y	6, 2
2000 GN171	0.215	0.070	0.093	147	6.5	IR	N	6, 2
2000 OK67	0.20	0.08	0.21	151	6.5	RR	–	5, 3
2001 FP185	0.046	0.007	0.007	332	6.4	IR	–	4, 3
2001 KA77	0.155	0.046	0.091	252	5.6	RR	–	5, 3
2001 KD77	0.089	0.027	0.044	232	6.4	RR	–	6, 3
2001 QF298	0.071	0.014	0.020	408	5.4	BB	–	6, 3
2001 QY297	0.104	0.050	0.094	278	5.9	BR	–	5, 3
2002 KX14	0.097	0.013	0.014	455	4.9	RR/IR	N	5, 2
2002 PN34	0.049	0.006	0.006	112	8.7	BR	T	4, 2
2002 VE95	0.149	0.016	0.019	249	5.7	RR	Y	6, 2
2002 XU93	0.038	0.004	0.004	164	8.1	–	N	4, 2
2003 AZ84	0.107	0.016	0.023	727	3.7	BB	Y	6, 2
2003 FY128	0.079	0.015	0.01	460	5.1	BR	N	4, 2
2003 VS2	0.147	0.043	0.063	523	4.1	–	Y	6, 2
2004 GV9	0.077	0.0077	0.0084	680	4.2	BR	N	5, 2
2004 UX10	0.141	0.031	0.044	398	4.8	BR	T	6, 2
2005 QU182	0.328	0.109	0.16	416	3.8	–	N	4, 2
2005 RN43	0.107	0.018	0.029	679	3.9	RR/IR	N	5, 2
2007 UK126	0.167	0.038	0.058	599	3.7	–	T	4, 2

Note. — σ_{pV}^- and σ_{pV}^+ denote the lower and upper albedo uncertainty, such that the 1σ uncertainty range is $p_V - \sigma_{pV}^-$ to $p_V + \sigma_{pV}^+$; d is the diameter; H denotes the absolute magnitude. The column "Ices?" denotes if the respective object is known to harbor ices (Y), most likely not to harbor ices (N), or tentatively classified to harbor ices (T). Objects with "**Y**" show significant water ice absorption band depths and are hence likely to have significant amounts of ices on their surfaces."Tax. Class." gives the taxonomic classification of the individual objects based on the scheme used by Barucci et al. (2005) and Fulchignoni et al. (2008). The column "Ref." lists the references for the albedo, diameter, H, and the taxonomic classification; all information on the presence of ices are extracted from Barucci et al. (2011).

References. — (1): Section B.3 and Mueller et al. (2013), (2): Barucci et al. (2011), (3): Fulchignoni et al. (2008), (4): Santos-Sanz et al. (2012), (5): Vilenius et al. (2012), (6): Section 5.1 and Mommert et al. (2012), (7): Pál et al. (2012), (8): Perna et al.

Figure 5.7 and Table 5.8 show the respective results for the correlation of the albedos with the presence of ices.

5.3.4 Discussion

5.3.4.1 Albedo Correlations with the TNO Taxonomy

Figure 5.6 shows that all four taxonomic types cover wide ranges in albedo that mostly overlap. Nevertheless, some differences between the samples can be found: the neutral BB and BR types show albedos higher than 0.4, which is not the case for the redder types, IR and RR. Furthermore, most of the objects with BB and BR type classification are clustered at albedos $p_V \leq 0.2$ with some outliers with higher albedos, whereas IR and RR

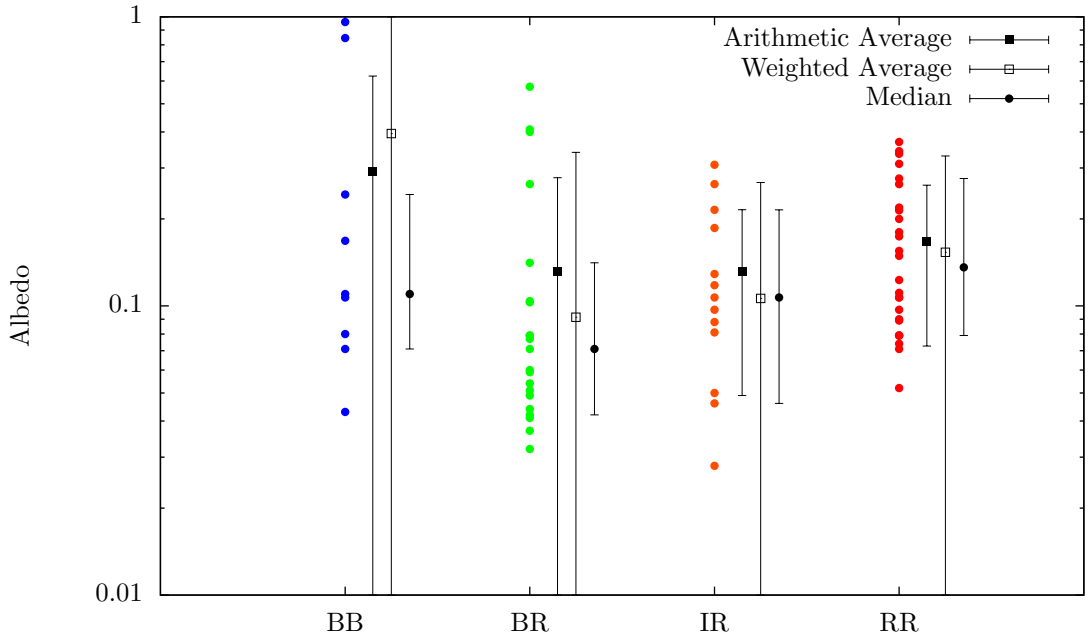

Figure 5.6 Measured albedo versus taxonomic type, according to Table 5.6. Colored circles represent individual albedos; filled and empty boxes symbolize the arithmetic and weighted averages, respectively, and the median is symbolized by filled circles. The results of the statistical quantities and the distribution of the albedos per taxonomic type are discussed in the text. The two BB–type objects with the highest albedos are (136108) Haumea (top) and (136199) Eris.

Table 5.7. Correlations of Albedo with TNO Taxonomy.

Property	BB	BR	IR	RR
Sample Size	9	21	13	26
Arithm. Average	0.29 (±0.33)	0.13 (±0.15)	0.13 (±0.08)	0.17 (±0.09)
Weighted Average	0.39 (±1.12)	0.09 (±0.25)	0.11 (±0.16)	0.15 (±0.18)
Median	0.11	0.07	0.11	0.14
(1σ)	(0.07–0.24)	(0.04–0.14)	(0.05–0.22)	(0.08–0.28)
(min–max)	(0.04–0.96)	(0.03–0.57)	(0.03–0.31)	(0.05–0.37)
p–value (BB, ...)	–	11.9%	92.3%	85.0%
p–value (BR, ...)	11.9%	–	6.7%	1.0%
p–value (IR, ...)	92.3%	6.7%	–	68.5%
p–value (RR, ...)	85.0%	1.0%	68.5%	–

Note. — Uncertainties of the averages are 1σ standard deviations; the numbers in brackets below the median give the 1σ confidence interval equivalent, which includes 68.3% of all albedos around the median, and the overall range of albedos in the respective sample ("min–max"). The results of the KS test are listed as p–values, denoting the significance level at which the possibility that samples from different taxonomic types are drawn from the same population can be rejected. The lower p, the higher is the probability that both samples are different (e.g., $p \leq 0.05$ complies with a 2σ significance).

Table 5.8. Correlation of Albedo with the Presence of Ices.

Property	Non–Icy	Possibly Icy	Icy
Sample Size	19	13	21
Arithm. Average	0.11 (±0.09)	0.12 (±08)	0.24 (±0.25)
Weighted Average	0.10 (±0.19)	0.10 (±0.15)	0.11 (±0.21)
Median	0.08	0.11	0.15
(1σ)	(0.04–0.19)	(0.04–0.17)	(0.07–0.28)
(min–max)	(0.03–0.34)	(0.03–0.31)	(0.04–0.96)
p–value (Non–Icy, ...)	–	23.5%	11.5%
p–value (Poss. Icy, ...)	23.5%	–	25.0%
p–value (Icy, ...)	11.5%	25.0%	–

Note. — Explanations see Table 5.7.

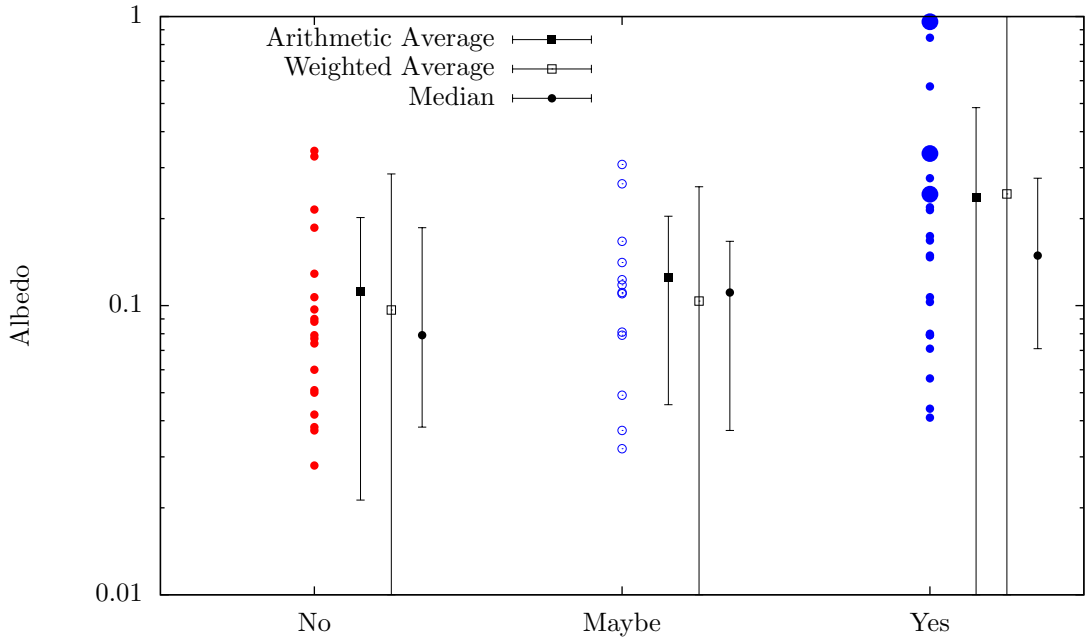

Figure 5.7 Albedos of objects on which the presence of ices has been most likely ruled out ("No"), is likely but not unambiguous ("Maybe"), and confirmed ("Yes"). Colored circles depict individual albedo measurements; large blue circles depict objects with significant amounts of ices on their surface (see Table 5.7 and Barucci et al. (2011)); filled and empty boxes represent the arithmetic and weighted averages, respectively, and filled circles denote the median of the respective albedo distribution. Uncertainties of the means and median are the 1σ standard deviations and the 1σ confidence interval, bracketing 68.3% of all albedos centered around the median, respectively. The three objects on which the presence of ices is confirmed with the highest albedos are (136108) Haumea (top), (136199) Eris, and (136472) Makemake (bottom).

objects are evenly distributed in a more limited range of albedo.

A comparison between the three statistical quantities used to describe the albedo properties for each taxonomic type shows good agreement for the BR, IR and RR–types. In the case of the BB–type TNOs, both averages are strongly impacted by the two high–albedo objects in the sample. Since the focus of this study is on the bulk properties of the individual type samples, I adopt the values and confidence intervals of the median, which is less affected by outliers. A visual check shows that the adopted 68.3% confidence interval around the median describes the sample bulk of each type reasonably well. The BR, IR, and RR–type samples show a slight trend of increasing albedo with redness, although the trend is of questionable significance, given the large degree of scatter in the measured albedo (see also Figure 5.6). The results of the KS test (see Table 5.7) show that we cannot exclude the possibility that the samples used in this analysis are drawn from a common parent population, except for the BR and RR–type samples with $p = 1\%$, implying the samples are different at a 2.6σ significance level.

The fact that neutral–colored BB–type TNO surfaces are among the most reflective surfaces of the TNOs investigated here agrees with the findings of Barucci et al. (2011) that the presence of ices cannot be excluded in these objects. Interestingly, extremely red RR–type TNOs seem to show a lack of objects with $p_V \leq 0.05$. Usually, reddish objects are also among those with the lowest albedo, for instance in the case of cometary nuclei (Lamy et al. 2004) and Jupiter Trojans (Barucci et al. 2002). However this effect might also be due to discovery bias inherent to the sample (see below).

The robustness of this analysis depends critically on the reliability of the albedo measurements, which in turn depends on the accuracy of the H magnitudes. Especially in the case of the *MIPSKBOs* results, less reliable H magnitude estimates had to be used, due to the lack of accurate photometric data (see Section B.3). This analysis will be redone including the final *MIPSKBOs* thermal modeling results, which will be based on more accurate H magnitudes, and the complete *TNOs are Cool!* sample.

A more conservative approach to the KS test would be to take into account the individual albedo uncertainties, similar to the Monte–Carlo Spearman rank analysis in Santos-Sanz et al. (2012). Furthermore, the analysis, especially of the BB–type sample, suffers from the small sample size. A larger number of objects with measured albedos and taxonomic classifications will help to better constrain the bulk properties of the individual albedo distribution. The sample sizes will grow with the release of the yet unpublished *TNOs are Cool!* results (Vilenius et al. 2013; Pál et al. 2013) and future large–scale photometric surveys of the TNOs will increase the number of objects with taxonomic classifications.

It is important to bear in mind that the object samples of each taxonomic type used here are subject to bias, including the optical discovery bias and selection effects introduced by the observational constraints and sensitivity of the instruments with which the thermal–

infrared measurement for the derivation of the albedo were performed. Hence, it is likely that especially the low–albedo contribution to the individual types is higher than suggested by this analysis. Properly accounting for the bias is a very complex task, which I postpone to a future analysis that will include all of the *TNOs are Cool!* data. Nevertheless, this first investigation provides indications that differences in the albedo distributions between the individual taxonomic types are present.

5.3.4.2 Albedo Correlations with the Presence of Ices

The albedo distributions of the three samples (icy, maybe icy, non–icy) shown in Figure 5.7 are similar, but it is noteworthy that the three highest–albedo objects ($p_V \geq 0.4$) are all confirmed to be icy. The arithmetic and weighted average of the albedo mostly agree with the median; only in the case of the icy sample, which suffers from high–albedo outliers, both averages are clearly higher than the median. Again, I adopt the median that better describes the bulk properties of the samples. Interestingly, the median albedo (as well as both averages) of the individual samples increases with the likelihood of ices on their surfaces. However, the trend is barely significant, given the large degree of albedo scatter in the samples. The results of the KS test (see Table 5.8) show that all samples cannot be precluded to be similar at a 1σ significance level.

I explore the nature of the three highest–albedo objects with confirmed ices. Interestingly, all three objects, namely (136108) Haumea, (136199) Eris, and (136472) Makemake, are considered dwarf planets (see Section 1.1.1), due to their considerably larger sizes compared to other small bodies. Excluding those three objects from the "icy" sample, lowers the sample averages and the median (0.13, 68.3% confidence interval: 0.06–0.24), reducing the significance of the albedo trend. Furthermore, without the dwarf planets, the albedo ranges in all three samples are similar. The presence of ices on TNOs and Centaurs that are not considered dwarf planets does not appear to affect their albedos.

I further investigate a possible relationship between the albedo, diameter, and the presence of ices. Barucci et al. (2011) show that all objects with significant amounts of ices on their surface are intrinsically bright. The reverse is not always the case: not all intrinsically bright objects harbor ices, although the three brightest objects with $H < 3.0$ mag are indeed icy. H depends on diameter and albedo: using the albedo and diameter measurements listed in Table 5.6, I am able to consider the relative contribution of these two parameters. Figure 5.8 shows the diameter distribution as a function of albedo for those TNOs that have been confirmed to have surface ices (blue circles), those that have been shown to be ice–free (red boxes), and those that are likely to harbor ices (green open circles). Interestingly, all objects with $d > 900$ km (above the dotted line) are associated with surface ices, three of which even have significant amounts of ices. The only object that has not been proven to have surface ices with $d > 900$ km is (84522) 2002 TC302, although its presence is likely (Barkume et al. 2008; Barucci et al. 2011). Intriguingly,

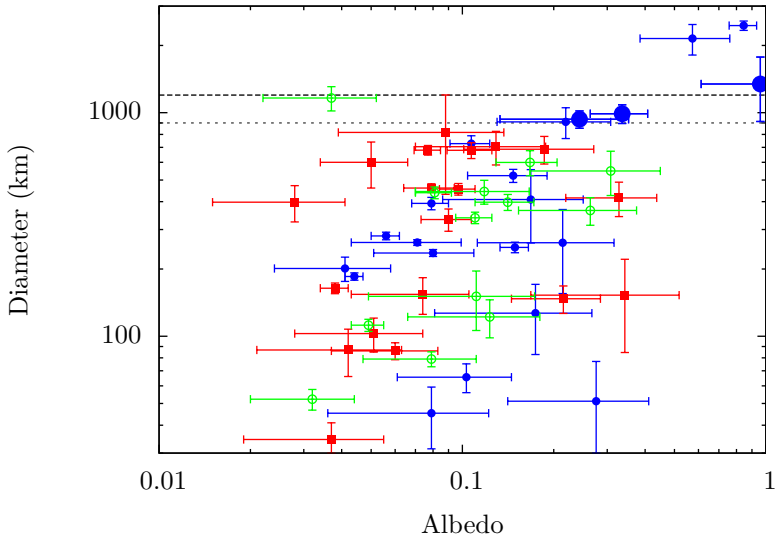

Figure 5.8 Diameter as a function of albedo for the TNO and Centaur samples with (blue circles) and without (red circles) surface ices, and those for which the presence of ices cannot be ruled out (green circles). The large blue circles indicate objects with significant amounts of surface ices. The plot suggests that objects with $d > 900$ km (dotted line) are very likely to have ices on their surface. Objects with $d > 1200$ km (dashed line) all have icy surfaces and extraordinarily high albedos.

2002 TC302 is also the only object with a low albedo ($p_V = 0.037$) and $d > 900$ km. All objects with $d > 1200$ km have been shown to harbor ices and have extraordinarily high albedos. The distribution of icy objects shows a clear trend of albedo increasing with diameter, which is also apparent in those objects that are likely to be icy, but not in the non–icy objects. I conclude that large ($d > 900$ km) objects are more likely to have high albedos, presumably due to the presence of surface ices.

The finding that all objects with $d > 1200$ km have high albedos agrees with the results of Schaller and Brown (2007), who show that only the largest and coolest TNOs are able to retain surface volatiles. The escape of volatile molecules is caused by their thermal excitement and occurs when their velocity exceeds the escape velocity given by the gravitational attraction of the body. The larger and more massive an object, the more easily it can retain its surface volatiles – possibly in the form of a thin atmosphere. At sufficient distance from the Sun, the volatile atmospheres can collapse and create rime–like high–albedo layers on the surface (Brown 2008). Hence, many, if not all, large TNOs may harbor ices, and consequentially have high albedos.

The verification of this hypothesis does not necessarily require spectroscopic investigation of all large TNOs: the persistence of an albedo trend with increasing diameter in future data will provide strong evidence. Note that the finding of a trend of increasing albedo with increasing diameter is contrary to that expected in the presence of detection

bias: it is more intuitive to expect a larger number of low–albedo objects with large diameters, the large size compensating for the low albedo. The opposite is the case, which suggests the lack of large low–albedo TNOs to be real.

5.3.5 Conclusions

5.3.5.1 TNO Taxonomy

- I have determined the median albedos of the [BB, BR, IR, RR] taxonomic types as [0.11, 0.07, 0.11, 0.14] with 1σ confidence intervals of [0.07–0.24, 0.04–0.14, 0.05–0.22, 0.08–0.28], respectively. A slight trend of increasing median albedo is observed in the order BR–IR–RR. However, this trend is below the 1σ confidence interval, and hence not significant.

- Only the albedos of BB and BR–type TNOs extend into the high–albedo regime ($p_V \geq 0.4$), whereas those of the IR and RR–types are constrained to a smaller range. The highest albedos are found in the BB–type TNOs, probably most (perhaps all) of which have icy surfaces (Barucci et al. 2011).

- Only the albedo distributions of the IR and BR–type TNOs have a high probability to originate from different populations (99%); all other types cannot be ruled out to originate from the same population.

5.3.5.2 Presence of Ices

- The median albedo of all known TNOs with icy surfaces (0.15, 1σ confidence interval 0.07–0.28) is slightly higher than the median of TNOs that are known not to have icy surfaces (0.08, 0.04–0.19). The trend is clearly affected by the presence of large TNOs with extraordinarily high albedos.

- Objects known to harbor significant amounts of surface ices have high albedos.

- The KS test shows that the icy/non–icy sample distributions are similar and cannot be excluded to originate from the same population.

- From the albedo/diameter distribution of all TNOs for which information on the presence of ices is available, I hypothesize that all TNOs with diameters larger than 900 km are very likely to harbor ices and that objects larger than 1200 km have high albedos caused by the presence of ices.

Chapter 6

Discussion

In the following sections, I discuss the implications of the results presented in Chapters 4 and 5 in the context of our current picture of the Solar System. Furthermore, I give an outlook on future work that is related to this work, and present a new approach in the thermal modeling of NEOs.

6.1 Implications for our Picture of the Solar System

6.1.1 Near–Earth Objects and their Source Populations

6.1.1.1 Comparing the Physical Properties of NEOs and their Source Populations (Section 4.1)

- *The comparison of NEO albedos, taken as a rough guide to mineralogy, with those of their individual source populations supports the transport mechanisms derived from dynamical modeling.* Using the source region probabilities provided by Bottke et al. (2002b), I have compared the average albedos of NEOs and their individual source populations (see Section 4.1 and Figure 4.2 on page 99). The agreement of the average albedos in the source and offspring populations supports the current picture of the transport mechanisms towards the NEO population. Discrepancies are discussed in the following.

- *The lack of low–albedo objects in the NEO population compared to its source populations suggests a size–dependent albedo distribution, or an albedo–dependent transport mechanism.* The comparison of the albedo distributions of NEOs and their respective source populations shows a significant lack of low–albedo objects in the NEO population compared to their main belt source populations. This effect is yet unexplained by NEO model distributions (Morbidelli et al. 2002). There are various possible reasons for this deficiency.
  Firstly, it may be a consequence of a size–dependence in the albedo distributions of NEOs and main belt asteroids: most main belt asteroids are significantly larger than their NEO descendants, the latter of which are the collisional debris of the former. It is possible that smaller NEOs, having fresher surfaces than their parent bodies due to recent collisions, have higher albedos. This effect has been observed in S and Q–type asteroids (Delbo' et al. 2003), however, not in low–albedo C–type asteroids, or similar. Still, Thomas et al. (2011) found that NEOs of the individual taxonomic types have in general higher albedos than their equivalents in the main belt, including the low–albedo types.
  Secondly, the deficiency might by a consequence of the albedo dependence of the Yarkovsky force (see Footnote 3 on page 8), which is most efficient in the case of small, low–albedo objects and less efficient for large and high–albedo objects. The exact impact of such an albedo–dependent effect on the albedo distribution of the NEOs would have to be explored using sophisticated dynamical modeling. However, the Yarkovsky force is known to be an albedo–dependent effect, and might therefore be involved.
  Thirdly, the definition of the individual source populations in the main belt might be inaccurate. As in the case of the Hungarias, where a lack of high–albedo objects in

the NEO population turned out to be the result of a selection effect (see Section 4.1), the deficiency might be the result of an inaccurate definition of the source region boundaries.

6.1.1.2 Assessment of the Cometary Contribution to the NEO Population (Section 4.2)

- *The fraction of NEOs with a cometary origin is slightly smaller than estimated from previous analyses.* The fraction of NEOs of cometary origin derived in Section 4.2 is smaller compared to previous estimates. The size–limited estimate by DeMeo and Binzel (2008) is slightly higher whereas the discrepancies between magnitude and size–limited estimates preclude a direct comparison to the results of Fernández et al. (2005) and Bottke et al. (2002b), although these estimates must be higher in a size–limited formulation. A smaller contribution from comets to the NEO population implies that less volatile–rich and organic material from the trans–Neptunian region is currently transported to the inner Solar System. Note that due to the relatively short dynamical lifetimes of NEOs (∼10 Myrs, Morbidelli and Gladman 1998) the assessment in Section 4.2 only allows for deductions on the current NEO population, but not on the past population. A lower fraction of cometary objects in the NEO population also bears implications with respect to the impact hazard mitigation: comet–like, i.e., carbonaceous, material is believed to be more porous than silicaceous asteroid material (Weissman et al. 2004), requiring a different approach for a possible mitigation mission of a cometary body.

- *The albedo distribution of NEOs on cometary orbits is more complex than previously assumed.* A previous investigation of the contribution from comets to the NEO population (Fernández et al. 2005) revealed that all objects on distinct comet–like orbits ($T_J \leq 2.6$) also have comet–like albedos. The analysis in Section 4.2 does not support this picture: Figure 4.7 on page 117 shows a significant number of objects with $T_J \leq 2.6$ and intermediate to high albedos. This might either imply that (1) there are NEOs of cometary origin with non–comet–like albedos, or (2) that the number of asteroidal objects on comet–like orbits is higher than previously expected. (1) seems unlikely to be the case, since cometary nuclei measured so far have albedos lower than 0.06 (Lamy et al. 2004). The investigation of (2) requires detailed dynamical modeling of asteroids with non–comet–like albedos to reveal their real origin. Nevertheless, the results of this analysis demonstrate that not all NEOs on comet–like orbits have low albedos.

  Further observations will be necessary to investigate the possibility that the high, not comet–like albedos found in some objects on comet–like orbits may be caused by some kind of activity, mimicking a colder surface temperature and thus a higher

albedo. If such an effect is significant for some of the high–albedo objects on comet–like orbits, cometary activity among NEOs might be much more frequent than expected (see the discussion of Don Quixote below).

6.1.1.3 The Discovery of Cometary Activity in (3552) Don Quixote (Section 4.3)

- *Activity might be more common than previously assumed in NEOs.* Some asteroids after their discovery have to be reclassified as comets as they show a coma or a tail in follow–up observations. The discovery of cometary activity in NEO (3552) Don Quixote, nearly two decades after its discovery as an asteroid, shows that activity, and thus the existence of volatiles, can remain undiscovered over a long time. In the case of Don Quixote, the discovery was probably hampered by the fact that the activity is most likely to be triggered by CO_2 gas, which emits line emission at 4.3 μm, but is not revealed in the optical. Reach et al. (2012) and Ootsubo et al. (2012) show that CO_2 is found in a significant number of short–period comets. This again implies that the number of NEOs with undiscovered activity might be larger than previously assumed.

- *Don Quixote's activity shows that volatiles are able to exist over long periods in near–Earth space.* Based on the analysis in Section 4.3, I am unable to constrain the cause or longevity of the observed activity. Nevertheless, the discovery shows that volatiles like CO_2 can be present on NEOs, probably buried in subsurface reservoirs at low temperatures (Yamamoto 1985, estimates an upper limit temperature of 60 K to preserve CO_2). Given the significant fraction of NEOs with a cometary background (see Section 4.2), this might imply that significant amounts of volatiles can be retained in the NEO population.

- *CO_2 has been detected in short–period comets, but not in TNOs.* The discovery of CO_2 line emission in Don Quixote and other short–period comets (Reach et al. 2012; Ootsubo et al. 2012) implies the existence of frozen CO_2 in the source regions of these comets, namely the trans–Neptunian region and the Centaurs. Spectroscopic analyses of these objects have so far failed to unambiguously identify significant amounts of highly volatile ices like CO or CO_2 on their surfaces (DeMeo et al. 2010; Barucci et al. 2011), although their existence is anticipated (Levi and Podolak 2009). The finding of CO_2 in comets and in near–Earth objects suggests that ices are buried in deep surfaces layers of some NEOs, shielded from discovery and the heating of the Sun.

- *The undetected activity of NEOs contributes to Earth's impact hazard.* Out–gassing from cometary activity leads to an additional momentum transfer to the object

that is able to change the orbit of comets from their purely Keplerian orbits (see, e.g., Yeomans et al. 2004). The combination of localized out–gassing in the form of jets with the rotation of the body can cause the perturbations to be quasi–chaotic, leading to unpredictable changes in the orbit of the object. Non–gravitational forces acting on potentially hazardous objects can significantly increase the uncertainties in their orbits and impact predictions.

6.1.2 Trans–Neptunian Objects and Short–Period Comets

6.1.2.1 The Physical Characterization of 18 Plutinos (Section 5.1)

- *The measured albedo distribution of the Plutinos agrees with current formation models.* The Plutino albedo distribution ranges from 0.04 to 0.28 with a weighted average of 0.08. The albedo of Pluto is exceptionally high (0.49–0.66, Buie et al. 1997). The measured albedo distribution agrees with formation models of the Plutinos based on the resonance capture scenario (Malhotra 1993; Hahn and Malhotra 2005, also see Section 1.1.4.1): Plutinos are captured in the 2:3 mean motion resonance during Neptune's outward–migration. According to this hypothesis, the Plutinos are likely to have formed at different heliocentric distances in the planetesimal disk, giving rise to different compositions and thus different albedos. A monochromatic Plutino albedo distribution would not be consistent with this formation model.

- *Pluto is not a typical Plutino.* Pluto is significantly larger than all other known Plutinos, has a moon half of its own size, and is the only Plutino known to have an atmosphere. These properties make Pluto, the prototype of all Plutinos in the dynamical sense, a rather special object among the Plutinos, and even among other TNOs[1]. The lack of objects of the size of Pluto places important constraints on the ejection rate of objects from the Plutino subpopulation towards the JFCs: the larger the number of Pluto–sized objects, the higher the ejection rates (de Elía et al. 2008; di Sisto et al. 2010). Assuming that the intrinsically brightest Plutinos have been found by now and based on the physical characterization performed in Section 5.1, the existence of a second object of the size of Pluto among the Plutinos can be most certainly ruled out.

- *The ensemble thermal properties of the Plutinos (and most other TNOs) are dominated by thermal inertia and rotational effects, not by surface roughness.* From the sample Plutinos that were modeled using the floating–η method I derive a weighted mean of $\langle\eta\rangle = 1.11^{+0.18}_{-0.19}$. The fact that $\langle\eta\rangle > 1.0$ shows that the surface temperature of the sample objects is in general lower than in the idealized STM case (see Section 3.2.2). According to the discussion in Section 3.5, $\eta > 1.0$ rules out the possibility

[1]Only the scattered disk object (136199) Eris is known to be of similar size to Pluto; the presence of an atmosphere has not been directly detected but cannot be ruled out (Sicardy et al. 2011).

that most Plutinos have high surface roughness, since beaming effects that lead to an increase in observed peak surface temperature are evidently dominated by effects that lower the temperature (e.g., thermal inertia and fast rotation). However, Table 5 in Section C.2 also shows cases with $\eta < 1.0$ in the Plutino sample, which can only be explained with a significant degree of surface roughness. The value of $\langle\eta\rangle$ for the Plutino sample agrees with that found by Stansberry et al. (2008) for a larger sample of Centaurs and TNOs ($\eta = 1.2 \pm 0.35$), leading to the same conclusions in this case. The determination of the thermal inertia from the *TNOs are Cool!* requires assumptions on the spin–axis orientation of the objects, as well as on the degree of surface roughness (Lellouch et al. 2013).

6.1.2.2 The Size and Albedo Distributions of the Known TNO Subpopulations (Section 5.2)

- *JFCs most likely originate from the Centaur, hot classical, and scattered/detached subpopulations.* The comparison of the albedo and size distributions of the JFCs and the TNO subpopulations shows the best match for the three aforementioned populations. The slopes of the size distributions agree for most subpopulations, except for the cold classicals, which is significantly steeper. However, in the comparison of the size distribution slopes one has to keep in mind that the slopes are derived from different size regimes: the largest JFCs are smaller than most of the known TNOs and Centaurs. Bernstein et al. (2004) show that the size distribution of TNOs is likely to break at $d \leq 100$ km towards a shallower size distribution, improving the agreement between the subpopulations mentioned above and the JFCs. Sophisticated observation programs will be necessary to explore the size distributions of the TNOs in the same size range as the JFCs.

- *Hot and cold classicals are likely to have different origins.* Differences in the hot/cold classical size distributions have been found by Fraser et al. (2010), and are confirmed here, using a different method. The cold classical size distribution is significantly steeper, steeper than any of the other TNO subpopulations. This implies that cold classicals are collisionally less evolved than other subpopulations, supporting the hypothesis that cold classicals formed where they are found today. Hot classicals were possibly pushed to their current orbits by the migration of the giant planets, in the course of which their inclinations and eccentricities were excited, increasing the rate of destructive mutual collisions (Morbidelli et al. 2008, and references therein).

- *The albedo variety in the TNO and Centaur albedo distributions is not reflected in the albedos of cometary nuclei.* The results of Section 5.2 show that the albedos of members of the main source populations of the Jupiter family comets, the Centaurs, hot classical, and scattered disk objects (see Figure 5.4 on page 167), are not re-

stricted to low albedos. This variety in the albedo distribution is not reflected by JFCs nuclei (see Table 4.2 and Lamy et al. 2004), either implying a selection effect, favoring low–albedo objects in the transition to comets, or a process that changes their surface characteristics. Selection effects can be ruled out, since the ejection of objects from the source regions can be described by dynamical means only (e.g., Levison and Duncan 1997), and non–gravitational forces such as the Yarkovsky force are negligible at the heliocentric distances dealt with here. Doressoundiram et al. (2008) suggest a number of resurfacing processes that affect the color indices of TNOs, and more than likely also their albedos. The most obvious resurfacing effect in the case of cometary transition objects is ice re–condensation and/or dust deposition from coma activity. An explanation for the low–albedos of JFCs might be found in such processes.

6.1.2.3 Correlations of Measured Albedos with the TNO Taxonomy and the Presence of Ices (Section 5.3)

- *The TNO taxonomy introduced by Barucci et al. (2005) is barely correlated to albedo.* The albedo trend between the different taxonomic classes is not significant and the albedo ranges mostly overlap. This behavior is in contrast to the asteroid taxonomy (see Section 1.2.4, or e.g., DeMeo et al. 2009), where albedo can be used to coarsely constrain the taxonomic complex and to rule out some taxonomic types. In the case of TNOs, the lack of correlation between the albedo and the color indices hints towards a large compositional variety in the surfaces of TNOs. Efforts to design a new TNO taxonomy that takes into account the albedo have been started (Dalle Ore et al. 2011).

- *Objects larger than d=900 km are likely to have surface ices and objects with* $d >$ 1200 *km may all have ices and high albedos.* Barucci et al. (2011) show that intrinsically bright objects are likely to harbor surface ices. I utilize measured diameters and albedos to refine this assertion by converting it into a size–limit. I find that objects larger than 900 km are likely to retain surface ices. Moreover, I find all objects larger than $d > 1200$ km to have extraordinarily high albedos. Schaller and Brown (2007) show that large TNOs are able to retain volatiles on their surfaces. Brown (2008) hypothesizes that volatile atmospheres of large TNOs might collapse and form high–albedo surfaces. This analysis sets the lower limit for the size of such objects to 1200 km. While objects smaller than 900 km may have surfaces ices, these objects do not show a significant trend between the presence of surface ices and their albedos.

6.2 Future Work

In the following, I present an outlook on future projects that are based on this work. In Section 6.2.3, I present a new approach to thermal modeling that is especially relevant to NEOs.

6.2.1 Near–Earth Objects

- In my *assessment of the cometary contribution to the NEO population* (Section 4.2), I make use of the estimate that 30% of all NEOs have orbits with $T_J \leq 3.0$ by Stuart (2003). As discussed in Section 4.2.4.1, this estimate is based on the rather small sample of NEOs known at that time and should therefore now be re–visited. A more robust approach to determine the fraction of NEOs on comet–like orbits uses a sophisticated and de–biased NEO distribution model (e.g., Bottke et al. 2002b; Morbidelli et al. 2002). The use of NEOWISE data requires a separate de–biasing (Mainzer et al. 2011b), since WISE was not subject to optical discovery bias during its survey mission. The proper implementation of both de–biasing models might lead to slightly different results, but it should improve the accuracy of the final estimate of the fraction of cometary objects in the NEO population.

- The *discovery of cometary activity in NEO (3552) Don Quixote* (Section 4.3) is solely based on *ExploreNEOs* Spitzer IRAC observations; other observations from the literature have been shown to lack sufficient accuracy to further constrain the observed activity. Future observations of Don Quixote are necessary to constrain the cause and longevity of its activity. Don Quixote's next perihelion passage will occur in May 2018. Deep optical and infrared[2] observations will be necessary to search for activity. In the meantime, I plan to lead observing proposals to observe other cometary candidate NEOs (see Section 4.2) that come as close to the Sun as Don Quixote and might also exhibit activity.

- In Section B.1, I perform a *comparison of the ExploreNEOs and NEOWISE (see Section 2.3) diameter and albedo results*, revealing large discrepancies in some objects. A further analysis of the discrepancies is precluded by the lack of detailed information on the circumstances of the WISE observations. Efforts to obtain these data have been started: the full "All-Sky Data Release" (NASA/IPAC Infrared Science Archive/WISE Observations Database) data set has been downloaded. The extraction of the measured NEO flux densities are the subject of future work. The WISE fluxes will be used to perform a detailed comparison of the modeling results using the *ExploreNEOs* thermal modeling pipeline and other thermal models. The

[2]Spitzer is unlikely to be operational for another 5 years, but the James Webb Space Telescope with imaging and spectroscopy capabilities in the wavelength range 0.6 to 5 μm (NIRCAM) is currently planned to be launched by 2018.

modeling results of both programs will benefit from a thorough investigation of the discrepancies. The combined data set will also be used as a test sample for the thermal model proposed in Section 6.2.3.

6.2.2 Trans–Neptunian Objects

- The *imminent completion of the TNOs are Cool! data reduction* will add measured flux densities for another ∼70 TNOs and Centaurs to the *TNOs are Cool!* sample, from which diameters and albedos will be derived. Furthermore, the final thermal modeling of the *MIPSKBOs* project sample (see Section B.3), using measured H magnitudes instead of rough estimates, will also increase the sample size of TNOs and Centaurs with reliably measured physical properties. Both data sets will be used to re–assess the results of this work, and increase the confidence level of the results.

- The *investigation of the TNO subpopulation size and albedo distributions* will also benefit from the proper de–biasing of the albedo and H magnitude samples, e.g., using the results of the "Canadian France Ecliptic Plane Survey" (CFEPS, Petit et al. 2011). The survey provides a synthetic model of the Kuiper belt, which can be used to investigate the observation bias of the known population and to revise the number estimates. The de–biasing will especially improve the representativeness of the size distribution at smaller diameters.

6.2.3 New Approaches in Thermal Modeling

I introduce a concept for a new thermal model that is designed to better fit the spectral energy distribution (SED) of atmosphereless bodies that are observed at high phase angles. Note that this model approach has not yet been implemented and tested.

6.2.3.1 The Tilted Thermal Asteroid Model – TITAM

Motivation. The NEATM (Harris 1998, also see Section 3.2.4) provides the most robust and precise diameters and albedos of all types of thermal models in cases in which full thermophysical modeling is not possible due to lack of knowledge of necessary parameters. The variable beaming parameter η in the NEATM allows for a reasonable fit to the observed SED in most cases for all kinds of atmosphereless Solar System bodies. However, in the case of observations performed at large solar phase angles, when the observer sees a large portion of the night side of the object, the diameters derived by the NEATM are systematically overestimated, and the albedos underestimated (see Section 3.2.4 for a discussion). Wright (2007) showed the NEATM diameters to be accurate to within 10% for observations performed at solar phase angles less than 60°, and to be significantly less accurate for larger phase angles.

The discrepancy is caused by the fact that the NEATM assumes the thermal–infrared emission of the object's night side to be zero, which is not the case for real objects with thermal inertias $\Gamma > 0$ (see Section 1.2.7). Proper accounting for the night–side emission would significantly improve the quality of the model results, but in turn requires detailed knowledge of the thermal and rotational properties of the object (see Section 3.5 for a brief discussion of thermophysical models). Wolters and Green (2009) came up with an empirical model accounting for night–side emission: the "night emission stimulated thermal model" (NESTM) computes the predicted contribution from the night–side as a function of the phase angle, assuming a fixed value of the thermal inertia. They find that the NESTM, assuming a thermal inertia of 200 SI units, provides better results for a variety of NEOs compared to the NEATM for $\alpha > 45°$, and sometimes results that are inferior to the NEATM for smaller phase angles. The disadvantage of the NESTM is its fixed thermal inertia, providing only reasonable results for objects that have Γ similar to the assumed value.

A better approach to a new thermal model would not assume a fixed thermal inertia. As shown in Section 3.2, the extreme cases of $\Gamma = 0$ and $\Gamma = \infty$ (STM and FRM, respectively, Sections 3.2.2 and 3.2.3) are covered by available thermal models. In the following, I describe the combination of the STM and FRM in such a way as to cover the whole range of $0 < \Gamma < \infty$, which can provide a better description of the surface temperature distribution of NEOs.

The Model. I propose the "Tilted Thermal Asteroid Model" (TITAM) that was developed together with A. W. Harris (DLR), which deviates from the definition of previous thermal models (see Section 3.2) in taking into account the "subsolar latitude", β, of the model body. The subsolar latitude is defined in such a way that $\beta = 0$ if the Sun is in the equatorial plane of the model body and $\beta = 90°$ if the Sun is located parallel to the spin axis.

The TITAM model assumptions are the same as for the FRM:

- The model body is assumed to be spherical,
- to spin rapidly, and to have a large thermal inertia ($\Gamma \to \infty$).

Thus, the temperature distribution of the TITAM is similar to that of the FRM (in case of $\beta = 0$, see Section 3.2.3), leading to an isolatitudinal temperature distribution. The TITAM temperature distribution differs from that of the FRM in the fact that the Sun is not fixed in the equatorial plane but is variable according to the subsolar latitude β, in a range $0 \leq \beta \leq 90°$. This impacts the surface temperature distribution in two ways: (1) the highest temperatures are found at latitude β, and (2) the illuminated hemisphere is tilted by the angle β against the direction to the Sun. Consequentially, (2) complicates the calculation of the temperature distribution: in a body–fixed coordinate system (with

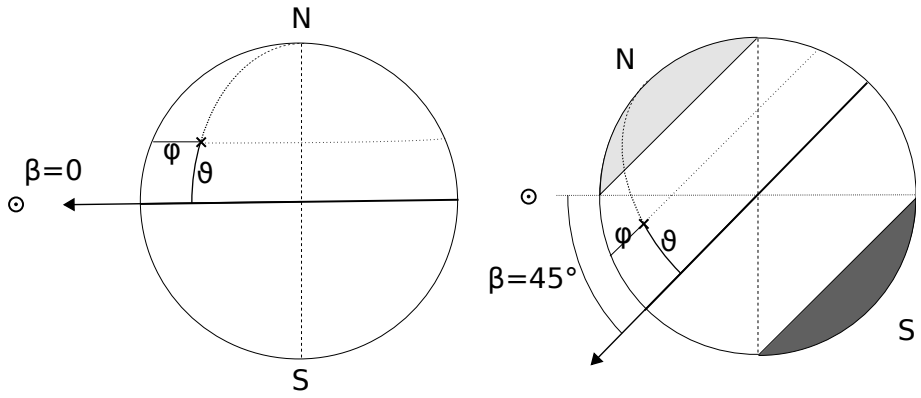

Figure 6.1 Illustration of the body–centered coordinate system of the TITAM. For $\beta = 0$ (left sketch), the Sun ($\odot$) lies in the equatorial plane, indicated by the thick horizontal line. The dashed line connecting the northern ("N") and the southern pole ("S") indicates the terminator, the division between the day and night sides of the body. Any point on the model body (indicated by a cross) is described by its longitude φ and its latitude ϑ; $\vartheta = 0$ at the equator, $\vartheta = 90°$at the northern and $\vartheta = -90°$at the southern pole. The longitude is defined as $\varphi = 0$ with respect to the direction to the Sun. $\beta > 0$ (right sketch) tilts the spin axis of the model body towards the direction to the sun; due to the rapid rotation of the model body, the temperature distribution is isolatitudinal. For $\beta > 0$, the area surrounding the northern pole is always illuminated ("eternal day", light grey area) and the area around the southern pole is never illuminated ("eternal night", dark grey). The extent of the respective areas is a function of β (see Equation 6.1).

longitude φ and latitude ϑ as defined in Figure 6.1) geometrical considerations show that the longitude of the terminator, $\varphi_{\text{terminator}}(\beta, \vartheta)$ can be described as

$$\varphi_{\text{terminator}}(\beta,\vartheta) = \begin{cases} 0, & \text{if } \vartheta < (\beta - \pi/2) \text{ (eternal night)} \\ \pi, & \text{if } \vartheta > \beta \text{ (eternal day)} \\ \arccos\left(\frac{\tan(\vartheta)}{\tan(\pi/2-\beta)}\right), & \text{else.} \end{cases} \tag{6.1}$$

Note that $\varphi_{\text{terminator}}$ is undefined for $\beta = 90°$; in this case, the terminator lies in the equatorial plane for all φ (see Footnote 3 on page 198). The derivation of the surface temperature distribution follows the same reasoning as in the case of the FRM (Equation 3.11 on page 77) except that the insolation on an isolatitudinal band with width $d\vartheta$ is limited to longitudes $-\varphi_{\text{terminator}} < \varphi < \varphi_{\text{terminator}}$, with $\varphi_{\text{terminator}}$ as defined in Equation 6.1, which introduces a factor $\int \cos(\varphi)\ d\varphi = \sin(\varphi_{\text{terminator}})$:

$$\frac{(1-A)S_\odot}{r^2} \cdot \cos(\vartheta - \beta) \cdot \frac{d^2}{2}\cos(\vartheta)\ \ d\vartheta \sin(\varphi_{\text{terminator}}) = \epsilon\sigma T^4 \cdot \pi \frac{d^2}{2}\cos(\vartheta)\ d\vartheta.$$

The factor $\cos(\vartheta - \beta)$ is the modified cosine–law of the insolation, taking into account the tilt of the model body against the direction to the Sun. Finally, the TITAM surface

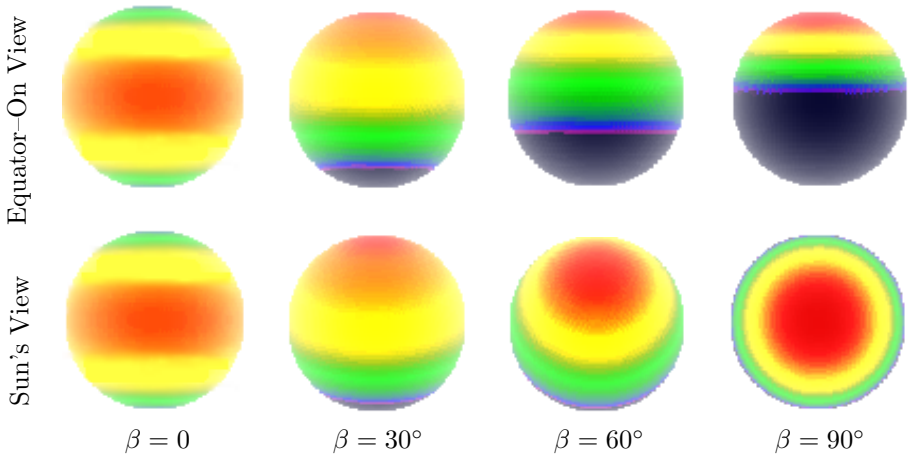

Figure 6.2 TITAM surface temperature distributions for different values of β as seen from a equator–on perspective (top row) and from the Sun (bottom row). The similarities to the STM and FRM are obvious in the case of $\beta = 90°$ and $\beta = 0$, respectively. The intermediate cases of $\beta = 30°$ and $\beta = 60°$ provide temperature distributions that are "smeared out" compared to the extreme cases. The temperature distributions were simulated using a thermophysical model with a high thermal inertia and a rapid spin rate.

temperature distribution can be expressed as:

$$\begin{aligned} T(\vartheta) &= T_{SS} \cdot \sin(\varphi_{\text{terminator}})^{1/4} \cos(\vartheta - \beta)^{1/4}, \text{ with} \\ T_{SS} &= \left[\frac{S_{\odot}(1-A)}{r^2 \pi \bar{\eta} \sigma \epsilon} \right]^{1/4}. \end{aligned} \tag{6.2}$$

The TITAM beaming factor $\bar{\eta}$ modulates the color temperature of the temperature distribution in the same way as the NEATM beaming factor η (see Sections 3.2.4 and 3.5); however, note that both factors are different and not related.

The extremes of the TITAM temperature distribution are given by $\beta = 0$ (Sun equator–on) and $\beta = 90°$ (Sun pole–on). Combining Equations 6.1 and 6.2 yields that $\beta = 90°$ results in the STM temperature distribution[3] (see Equation 3.8 on page 76) and $\beta = 0$ results in the FRM temperature distribution (see Equation 3.11 on page 77), making the TITAM a hybrid model between the STM and the FRM. Figure 6.2 shows examples of the TITAM surface temperature distribution using different values of β. The TITAM beaming parameter $\bar{\eta}$ adds an additional degree of freedom in fitting to SEDs that are subject to surface roughness and other effects that impact the thermal properties of a body.

Flux densities are derived from the temperature distribution using Equation 3.14 on page 80, which accounts for the solar phase angle.

[3]Strictly speaking, the temperature distribution is not defined for $\beta = 90°$; in this case the derivation of Equation 6.2 results in $\sin(\varphi_{\text{terminator}}) = \pi$, since $\int \cos(\varphi)\, d\varphi = 2\pi$.

Discussion. The formulation of the TITAM surface temperature distribution facilitates a combination of the extreme cases of the STM and the FRM temperature distributions. Thus, TITAM provides more flexibility in fitting observed SEDs than existing thermal models. Variation of β improves the reproduction of surface temperature distributions of real small bodies with finite thermal inertias.

The greater flexibility can be used to overcome the problem of the missing night–side emission of the NEATM in the following way: in the case of high–phase angle observations, a low–β temperature distribution covers a surface area larger than one hemisphere with non–zero surface temperatures, mimicking the night–side emission. Note that it is not necessary for the model to exactly reproduce the real object's surface temperature distribution; a temperature distribution with similar temperatures, covering similar fractions of the surface provides a sufficient approximation of the object's SED.

Different modeling approaches are conceivable: (1) a floating–β fit provides by definition the best fit to the observed data, but requires at least 3 thermal infrared measurements for fitting its three free model fit parameters: d or p_V, β, and $\bar{\eta}$; (2) a fixed–β fit can be used where only 2 thermal–infrared measurements are necessary. Each of the forementioned approaches can be combined with a fixed or a floating $\bar{\eta}$, depending on the number of available data points.

The TITAM is a potentially powerful thermal model that may overcome the limitations of the NEATM and improve on the results of thermal modeling. Its implementation and testing will be the subject of future work.

Chapter 7

Conclusions

Primary Aims

- **I find that the average albedos of NEOs and their proposed source populations agree within their uncertainties (Section 4.1), supporting the current dynamical models for the replenishment of the NEO population (Bottke et al. 2002b; Morbidelli et al. 2002)**. I find a lack of low–albedo objects in the NEOs compared to their main belt source populations and the model predictions. The deficiency may be caused by a size–dependency of asteroid albedos, selection effects, or observational bias (see Section 6.1).

- **Based on albedo measurements of the ExploreNEOs and NEOWISE programs, I have determined the fraction of NEOs that are of cometary origin in a size–limited sample to be $(5 \pm 3)\%$ (Section 4.2)**. This estimate is lower than most previous estimates of this fraction. I find 8 objects that are most likely of cometary origin – one of which actually shows cometary activity (see below). In contrast to the results of Fernández et al. (2005) I find a number of NEOs on comet–like orbits with intermediate to high albedos. This finding suggests that the albedo distribution of NEOs is less strictly correlated with their dynamical distribution than previously expected.

- **I find evidence for cometary activity in ExploreNEOs data of NEO (3552) Don Quixote, which is the primary candidate for a NEO of cometary origin based on its orbit (Section 4.3)**. The observed activity is most likely triggered by the sublimation and photo–dissociation of CO_2 ice. A literature search reveals additional observations of Don Quixote, in none of which I can unambiguously confirm or exclude the presence of activity. The combination of the literature data with the *ExploreNEOs* flux densities of the nucleus confirm previous diameter and albedo measurements ($d = 18.5$ km, $p_V = 0.03$, Veeder et al. 1989); Don Quixote is the third–largest known NEO and one of the largest known short–period comets (Lamy et al. 2004); its case provides physical evidence for the hypothesis that short–period comets contribute to the NEO population. Furthermore, the discovery of CO_2 ice on a NEO shows that volatiles, and hence cometary activity, might be more common in NEOs than expected.

- **I find the size and albedo distributions of most known TNO subpopulations to be mostly comparable to that of the short–period comets (Section 5.2).** The size distributions are derived based on measured albedo and absolute magnitude distributions instead of being based on the luminosity distribution. The comparison with the albedo and size distributions of the short–period comets shows that the Centaur, hot classical, and scattered disk/detached subpopulations are most likely the sources of these comets, which is in agreement with dynamical models (see

Section 1.1.5.2). Furthermore, I find significant differences in the size distributions of the hot and cold classical Kuiper belt objects, which suggest different origins and evolutions of these subpopulations.

Secondary Aims

- **The physical characterization of a representative sample of the Plutino subpopulation (Section 5.1) yields diameter and albedo ranges of 150–730 km and 0.04–0.28, respectively.** The variety in the albedos suggests a diverse subpopulation in terms of composition. The analysis shows that Pluto is the clear outlier of the Plutino population, being by far the largest object with the brightest surface. I find a significant correlation between diameter and eccentricity that is likely to be caused by discovery bias. A possible color–trend of distant Plutinos being bluer and smaller Plutinos being redder contradicts previous findings by Peixinho et al. (2004). Furthermore, I find qualitative evidence that icy Plutinos have higher than average albedos.

- **I find that TNOs larger than 900 km are likely to harbor ices and that objects larger than 1200 km have high albedos, presumably caused by the presence of large amounts of surface ices.** I have investigated a possible correlation between the color–based TNO taxonomy (Barucci et al. 2005), as well as the presence of surface ices, with albedo (Section 5.3). The median albedos of the individual taxonomic types, ranging from neutral in color to the reddest objects, [BB, BR, IR, RR], are [0.11, 0.07, 0.11, 0.14]. My analysis shows marginal variations in the albedo distributions between the individual types. The highest albedos are found for the BB–type TNOs, most of which are icy (Barucci et al. 2011).
  For all taxonomic types, icy objects are found to have on average slightly higher albedos. However, the low significance of the trend precludes inferences from albedo on the presence of ices. I find objects that are known to harbor significant amounts of surface ices to have significantly higher albedos.

Conclusions from Related Work (Chapter B)

- I have performed an assessment of the accuracy of the *ExploreNEOs* results, based on a Monte–Carlo approach (Section B.1). I find the root–mean–square uncertainties of the default *ExploreNEOs* thermal modeling pipeline to be 20% in diameter and 50% in albedo, which agrees well with the results of an alternative approach (Harris et al. 2011).
  Furthermore, I have compared the *ExploreNEOs* results with those of the NEOWISE program. I find small median discrepancies in the diameters and albedos of both

programs. Therefore, the results of the two programs can be combined to study ensemble properties of the NEO population. However, the results for individual objects can be considerably different.

- I have performed Monte–Carlo analyses to investigate the uncertainties of thermal modeling results (see Section B.2). I find that diameter uncertainties are best described by a normal distribution, whereas albedo uncertainties follow a log–normal distribution, which has implications for the interpretation of albedo uncertainties. Furthermore, I have designed an analytical uncertainty model that enables the estimation of lower limits for diameter and albedo uncertainties as a function of the model input parameter uncertainties.

- In the course of the *MIPSKBOs* project (Section B.3) I contributed to a re–analysis of all TNO and Centaur observations performed with the Spitzer MIPS instrument. I derived preliminary diameter and albedo estimates from the data. Final diameters and albedos will be published by Mueller et al. (2013).

Bibliography

A'Hearn, M. F. and the DEEP IMPACT Team, 2011. In *American Astronomical Society Meeting Abstracts #217*, *Bulletin of the American Astronomical Society*, volume 43, 306.08.

A'Hearn, M. F., Schleicher, D. G., Millis, R. L., Feldman, P. D., and Thompson, D. T., 1984. *AJ*, **89**, 579–591.

A'Hearn, M. F., Millis, R. L., Schleicher, D. G., Osip, D. J., and Birch, P. V., 1995. *Icarus*, **118**, 223–270.

Alexander, C. M. O. ., Bowden, R., Fogel, M. L. et al., 2012. *Science*, **337**, 721–.

Allen, D. A., 1971. *NASA Special Publication*, **267**, 41.

ASTORB Orbital Parameter Database. `ftp://ftp.lowell.edu/pub/elgb/astorb.html`. Provided by Lowell Observatory, accessed June 2012.

Bailey, M. E., Chambers, J. E., and Hahn, G., 1992. *A&A*, **257**, 315–322.

Barkume, K. M., Brown, M. E., and Schaller, E. L., 2008. *AJ*, **135**, 55–67.

Barucci, M. A., Boehnhardt, H., Dotto, E. et al., 2002. *A&A*, **392**, 335–339.

Barucci, M. A., Belskaya, I. N., Fulchignoni, M., and Birlan, M., 2005. *AJ*, **130**, 1291–1298.

Barucci, M. A., Brown, M. E., Emery, J. P., and Merlin, F., 2008. In Barucci, M. A., Boehnhardt, H., Cruikshank, D. P., Morbidelli, A., and Dotson, R., eds., *The Solar System Beyond Neptune*, 143–160.

Barucci, M. A., Alvarez-Candal, A., Merlin, F. et al., 2011. *Icarus*, **214**, 297–307.

Bauer, J. M., Walker, R. G., Mainzer, A. K. et al., 2011. *ApJ*, **738**, 171.

Bauer, J. M., Kramer, E., Mainzer, A. K. et al., 2012. *ApJ*, **758**, 18.

Bell, J. F., 1989. *Icarus*, **78**, 426–440.

Belskaya, I. N., Levasseur-Regourd, A., Shkuratov, Y. G., and Muinonen, K., 2008. *Surface Properties of Kuiper Belt Objects and Centaurs from Photometry and Polarimetry*, 115–127.

Benecchi, S. D., Noll, K. S., Grundy, W. M., and Levison, H. F., 2010. *Icarus*, **207**, 978–991.

Benecchi, S. D., Noll, K. S., Stephens, D. C., Grundy, W. M., and Rawlins, J., 2011. *Icarus*, **213**, 693–709.

Benner, L. M., 2012. URL `http://echo.jpl.nasa.gov/~lance/delta_v/delta_v.rendezvous.html`. Accessed September 2012.

Bernstein, G. M., Trilling, D. E., Allen, R. L. et al., 2004. *AJ*, **128**, 1364–1390.

Binzel, R. P., 1987. *Icarus*, **72**, 135–208.

Binzel, R. P., Xu, S., Bus, S. J., and Bowell, E., 1992. *Science*, **257**, 779–782.

Binzel, R. P., Lupishko, D., di Martino, M., Whiteley, R. J., and Hahn, G. J., 2002. *Asteroids III*, 255–271.

Binzel, R. P., Rivkin, A. S., Stuart, J. S. et al., 2004. *Icarus*, **170**, 259–294.

Binzel, R. P., Morbidelli, A., Merouane, S. et al., 2010. *Nature*, **463**, 331–334.

Bockelée-Morvan, D., Crovisier, J., Mumma, M. J., and Weaver, H. A., 2004. *The composition of cometary volatiles*, 391–423.

Bottke, W. F., Jr. and Melosh, H. J., 1996a. *Icarus*, **124**, 372–391.

Bottke, W. F., Jr. and Melosh, H. J., 1996b. *Nature*, **381**, 51–53.

Bottke, W. F., Jr., Cellino, A., Paolicchi, P., and Binzel, R. P., 2002a. *Asteroids III*, 3–15.

Bottke, W. F., Jr., Morbidelli, A., Jedicke, R. et al., 2002b. *Icarus*, **156**, 399–433.

Bottke, W. F., Jr., Vokrouhlický, D., Rubincam, D. P., and Broz, M., 2002c. *Asteroids III*, 395–408.

Bowell, E., Hapke, B., Domingue, D. et al., 1989. In Binzel, R. P., Gehrels, T., and Matthews, M. S., eds., *Asteroids II*, 524–556.

Bowell, E., Buie, M. W., and Picken, H., 1992. *IAU Circ.*, **5586**, 1.

Britt, D. T., Yeomans, D., Housen, K., and Consolmagno, G., 2002. *Asteroids III*, 485–500.

Brosch, N., 1995. *MNRAS*, **276**, 571–578.

Brož, M. and Vokrouhlický, D., 2008. *MNRAS*, **390**, 715–732.

Brown, M. E., 2008. *The Largest Kuiper Belt Objects*, 335–344.

Brucker, M. J., Grundy, W. M., Stansberry, J. A. et al., 2009. *Icarus*, **201**, 284–294.

Buie, M. W., Tholen, D. J., and Wasserman, L. H., 1997. *Icarus*, **125**, 233–244.

Burbine, T. H., McCoy, T. J., Meibom, A., Gladman, B., and Keil, K., 2002. *Asteroids III*, 653–667.

Bus, S. J. and Binzel, R. P., 2002a. *Icarus*, **158**, 146–177.

Bus, S. J. and Binzel, R. P., 2002b. *Icarus*, **158**, 106–145.

Bus, S. J., Vilas, F., and Barucci, M. A., 2002. *Asteroids III*, 169–182.

Campins, H., Osip, D. J., Rieke, G. H., and Rieke, M. J., 1995. *Planet. Space Sci.*, **43**, 733–736.

Carey, S. J., Surace, J. A., Glaccum, W. J. et al., 2010. In *Society of Photo-Optical Instrumentation Engineers (SPIE) Conference Series*, *Society of Photo-Optical Instrumentation Engineers (SPIE) Conference Series*, volume 7731.

Catalina Sky Survey Website. `http://www.lpl.arizona.edu/css/`. Accessed in November 2012.

Cheng, A. F., 2002. *Asteroids III*, 351–366.

Cheng, A. F., Santo, A. G., Heeres, K. J. et al., 1997. *J. Geophys. Res.*, **102**, 23695–23708.

Clark, B. E., Bus, S. J., Rivkin, A. S., Shepard, M. K., and Shah, S., 2004. *AJ*, **128**, 3070–3081.

Cometary Orbit Database. `ftp://cdsarc.u-strasbg.fr/pub/cats/B/comets/comets.dat`. Data provided by P. Rocher, IMCCE, accessed June 2012.

Crovisier, J., 2002. `http://lesia.obspm.fr/perso/jacques-crovisier/basemole`, accessed September 2012.

Cushing, M. C., Vacca, W. D., and Rayner, J. T., 2004. *PASP*, **116**, 362–376.

Dalle Ore, C. M., Cruikshank, D. P., Roush, T. L., and Emery, J. P., 2011. In *EPSC-DPS Joint Meeting 2011*, 44.

Davies, J. K., McFarland, J., Bailey, M. E., Marsden, B. G., and Ip, W.-H., 2008. In Barucci, M. A., Boehnhardt, H., Cruikshank, D. P., Morbidelli, A., & Dotson, R., ed., *The Solar System Beyond Neptune*, 11–23. The University of Arizona Press.

de Elía, G. C., Brunini, A., and di Sisto, R. P., 2008. *A&A*, **490**, 835–842.

de Graauw, T., Helmich, F. P., Phillips, T. G. et al., 2010. *A&A*, **518**, L6.

Defending Planet Earth, 2010. Near-earth object surveys and hazard mitigation strategies. `http://www.nap.edu/`. Accessed in November 2012.

Delbo', M., 2004. The nature of near-earth asteroids from the study of their thermal infrared emission. Ph.D. thesis, Freie Universität Berlin, Germany.

Delbo', M., Harris, A. W., Binzel, R. P., Pravec, P., and Davies, J. K., 2003. *Icarus*, **166**, 116–130.

Delbo', M., Dell'Oro, A., Harris, A. W., Mottola, S., and Mueller, M., 2007. *Icarus*, **190**, 236–249.

DeMeo, F. E. and Binzel, R. P., 2008. *Icarus*, **194**, 436–449.

DeMeo, F. E., Binzel, R. P., Slivan, S. M., and Bus, S. J., 2009. *Icarus*, **202**, 160–180.

DeMeo, F. E., Barucci, M. A., Merlin, F. et al., 2010. *A&A*, **521**, A35.

di Sisto, R. P., Brunini, A., and de Elía, G. C., 2010. *A&A*, **519**, A112.

Digitized Sky Survey. `http://archive.stsci.edu/cgi-bin/dss_form`. Accessed in September 2012.

Dohnanyi, J. S., 1969. *J. Geophys. Res.*, **74**, 2531.

Doressoundiram, A., Boehnhardt, H., Tegler, S. C., and Trujillo, C., 2008. *Color Properties and Trends of the Transneptunian Objects*, 91–104.

Duncan, M. J. and Levison, H. F., 1997. *Science*, **276**, 1670–1672.

Duncan, M. J., Levison, H. F., and Budd, S. M., 1995. *AJ*, **110**, 3073–+.

EARN. European asteroid research node. `http://earn.dlr.de/`. Accessed in January–February 2013.

Edgeworth, K. E., 1949. *MNRAS*, **109**, 600–609.

Elliot, J. L., Kern, S. D., Clancy, K. B. et al., 2005. *AJ*, **129**, 1117–1162.

Fazio, G. G., Hora, J. L., Allen, L. E. et al., 2004. *ApJS*, **154**, 10–17.

Fernández, J. A., ed., 2005. *Comets - Nature, Dynamics, Origin and their Cosmological Relevance*, *Astrophysics and Space Science Library*, volume 328.

Fernández, Y. R., 1999. Physical properties of cometary nuclei. Ph.D. thesis, University of Maryland College Park.

Fernández, Y. R., McFadden, L. A., Lisse, C. M., Helin, E. F., and Chamberlin, A. B., 1997. *Icarus*, **128**, 114–126.

Fernández, Y. R., Lisse, C. M., Käufl, H. U. et al., 2000. *Icarus*, **147**, 145–160.

Fernández, Y. R., Jewitt, D. C., and Sheppard, S. S., 2005. *AJ*, **130**, 308–318.

Fornasier, S., 2013. TNOs are Cool: A survey of the trans–Neptunian region. VIII. Combined Herschel PACS and SPIRE observations of 9 bright targets at 70–500 μm. Submitted.

Fraser, W. C., Kavelaars, J. J., Holman, M. J. et al., 2008. *Icarus*, **195**, 827–843.

Fraser, W. C., Brown, M. E., and Schwamb, M. E., 2010. *Icarus*, **210**, 944–955.

Froeschle, C. and Scholl, H., 1989. *Celestial Mechanics and Dynamical Astronomy*, **46**, 231–251.

Fujiwara, A., Kawaguchi, J., Yeomans, D. K. et al., 2006. *Science*, **312**, 1330–1334.

Fulchignoni, M., Belskaya, I., Barucci, M. A., de Sanctis, M. C., and Doressoundiram, A., 2008. In Barucci, M. A., Boehnhardt, H., Cruikshank, D. P., Morbidelli, A., and Dotson, R., eds., *The Solar System Beyond Neptune*, 181–192.

Gehrz, R. D. and Ney, E. P., 1992. *Icarus*, **100**, 162–186.

Gehrz, R. D., Roellig, T. L., Werner, M. W. et al., 2007. *Review of Scientific Instruments*, **78**(1), 011302.

Gladman, B., Marsden, B. G., and Vanlaerhoven, C., 2008. In Barucci, M. A., Boehnhardt, H., Cruikshank, D. P., Morbidelli, A., & Dotson, R., ed., *The Solar System Beyond Neptune*, 43–57. The University of Arizona Press.

Gladman, B., Lawler, S. M., Petit, J.-M. et al., 2012. *AJ*, **144**, 23.

Gomes, R., Levison, H. F., Tsiganis, K., and Morbidelli, A., 2005. *Nature*, **435**, 466–469.

Gordon, K. D., Rieke, G. H., Engelbracht, C. W. et al., 2005. *PASP*, **117**, 503–525.

Gordon, K. D., Engelbracht, C. W., Fadda, D. et al., 2007. *PASP*, **119**, 1019–1037.

Grav, T., 2013. MIPS Observations of Icy Moons of Jupiter and Saturn. In preparation.

Grieve, R. A. F. and Shoemaker, E. M., 1994. In Gehrels, T., Matthews, M. S., and Schumann, A. M., eds., *Hazards Due to Comets and Asteroids*, 417.

Griffin, M. J., Abergel, A., Abreu, A. et al., 2010. *A&A*, **518**, L3.

Gulbis, A. A. S., Elliot, J. L., Person, M. J. et al., 2006. *Nature*, **439**, 48–51.

Hagen, A. R., Trilling, D. E., Penprase, B. E. et al., 2011. Accurate H-magnitudes for 87 Near Earth Objects and New Albedos & Diameters for 72 Near Earth Objects . Submitted.

Hahn, G. and Bailey, M. E., 1990. *Nature*, **348**, 132–136.

Hahn, G. and Rickman, H., 1985. *Icarus*, **61**, 417–442.

Hahn, J. M. and Malhotra, R., 2005. *AJ*, **130**, 2392–2414.

Hainaut, O. R. and Delsanti, A. C., 2002. *A&A*, **389**, 641–664.

Harris, A. W., 1998. *Icarus*, **131**, 291–301.

Harris, A. W. and Harris, A. W., 1997. *Icarus*, **126**, 450–454.

Harris, A. W., Mueller, M., Lisse, C. M., and Cheng, A. F., 2009. *Icarus*, **199**, 86–96.

Harris, A. W., Mommert, M., Hora, J. L. et al., 2011. *AJ*, **141**, 75.

Hartmann, W. K., Tholen, D. J., and Cruikshank, D. P., 1987. *Icarus*, **69**, 33–50.

Hartogh, P., Lis, D. C., Bockelée-Morvan, D. et al., 2011. *Nature*, **478**, 218–220.

Haser, L., 1957. *Bulletin de la Societe Royale des Sciences de Liege*, **43**, 740–750.

Helbert, J., 2003. Studying the longterm evolution of gas activity in the coma of comet c/1995 o1 (hale-bopp), with a special focus on the chemistry of carbon bearing molecules. Ph.D. thesis, Freie Universität Berlin, Germany.

Herschel, W., 1800. *Royal Society of London Philosophical Transactions Series I*, **90**, 255–283.

Herschel Observer's Manual, 2012. `http://herschel.esac.esa.int/Docs/Herschel/html/observatory.html`. Herschel Consortium, Version 4.1.3, accessed January–February 2013.

Herschel Science Archive. `http://herschel.esac.esa.int/Science_Archive.shtml`. Accessed January–February 2013.

Herschel Science Centre. `http://herschel.esac.esa.int`. Accessed January–February 2013.

Hicks, M. D., Buratti, B. J., and Rabinowitz, D. L., 2000. In *AAS/Division for Planetary Sciences Meeting Abstracts #32*, *Bulletin of the American Astronomical Society*, volume 32, 1000.

Hirayama, K., 1918. *AJ*, **31**, 185–188.

Holsapple, K., Giblin, I., Housen, K., Nakamura, A., and Ryan, E., 2002. *Asteroids III*, 443–462.

Horner, J., Evans, N. W., Bailey, M. E., and Asher, D. J., 2003. *MNRAS*, **343**, 1057–1066.

Horner, J., Evans, N. W., and Bailey, M. E., 2004. *MNRAS*, **354**, 798–810.

Houck, J. R., Roellig, T. L., van Cleve, J. et al., 2004. *ApJS*, **154**, 18–24.

Hovis, W. A. J. and Callahan, W. R., 1966. *J. Opt. Soc. Am.*, **56**, 639–643.

Howell, S. B., 2000. *Handbook of CCD Astronomy*. Cambridge University Press.

Hsieh, H. H. and Jewitt, D., 2006. *Science*, **312**, 561–563.

Hubbard, W. B., Hunten, D. M., Dieters, S. W., Hill, K. M., and Watson, R. D., 1988. *Nature*, **336**, 452–454.

Integrated Data Language (IDL). `http://www.exelisvis.com/ProductsServices/IDL.aspx`. Accessed February 2013.

IRAC Instrument Handbook, 2012. `http://irsa.ipac.caltech.edu/data/SPITZER/docs/irac/iracinstrumenthandbook/`. Spitzer Science Center, Version 2.0.2, accessed September–December 2012.

Irvine, W. M., 1998. *Orig Life Evol Biosph.*, **28**, 365–83.

Ivezic, Z., Juric, M., Lupton, R. H., Tabachnik, S., and Quinn, T., 2002. In Tyson, J. A. and Wolff, S., eds., *Society of Photo-Optical Instrumentation Engineers (SPIE) Conference Series*, *Society of Photo-Optical Instrumentation Engineers (SPIE) Conference Series*, volume 4836, 98–103.

Jacobson, S. and Margot, J. L., 2007. In *AAS/Division for Planetary Sciences Meeting Abstracts #39*, *Bulletin of the American Astronomical Society*, volume 38, 519–+.

Jakosky, B. M., 1986. *Icarus*, **66**, 117–124.

Jewitt, D., 2012. *AJ*, **143**, 66.

Jewitt, D., Luu, J., and Marsden, B. G., 1992. *IAU Circ.*, **5611**, 1.

Jewitt, D. C. and Meech, K. J., 1987. *ApJ*, **317**, 992–1001.

Johnson, H. L. and Morgan, W. W., 1953. *ApJ*, **117**, 313.

Jorda, L., 1995. Ph.D. thesis, University of Paris 7.

JPL Horizons Systems. `http://ssd.jpl.nasa.gov/horizons.cgi`. See text for individual access dates.

JPL Near Earth Object Program Website. `http://neo.jpl.nasa.gov`. Accessed November 2012.

JPL Small–Body Data Browser. `http://ssd.jpl.nasa.gov/sbdb.cgi#top`. See text for access dates.

Jurić, M., Ivezić, Ž., Lupton, R. H. et al., 2002. *AJ*, **124**, 1776–1787.

Kaasalainen, M., Mottola, S., and Fulchignoni, M., 2002. *Asteroids III*, 139–150.

Keller, H. U., 1989. In Hunt, J. J. and Guyenne, T. D., eds., *Physics and Mechanics of Cometary Materials*, *ESA Special Publication*, volume 302, 39–45.

Kelley, M. S. and Wooden, D. H., 2009. *Planet. Space Sci.*, **57**, 1133–1145.

Kenyon, S. J., Bromley, B. C., O'Brien, D. P., and Davis, D. R., 2008. *Formation and Collisional Evolution of Kuiper Belt Objects*, 293–313.

Kirkwood, D., 1866. *Proc. Am. Assoc. Adv. Sci.*, 8–14.

Kirkwood, D., 1869. *MNRAS*, 96–102.

Kopp, G. and Lean, J. L., 2011. *Geophysical Research Letters*, **38**(1), n/a–n/a. ISSN 1944-8007. URL `http://dx.doi.org/10.1029/2010GL045777`.

Kuiper, G. P., 1951. *Proceedings of the National Academy of Science*, **37**, 1–14.

Lacerda, P. and Jewitt, D. C., 2007. *The Astronomical Journal*, **133**(4), 1393. URL `http://stacks.iop.org/1538-3881/133/i=4/a=1393`.

Lagerros, J. S. V., 1996. *A&A*, **310**, 1011–1020.

Lamy, P. L., Toth, I., Jorda, L. et al., 2002. *Icarus*, **156**, 442–455.

Lamy, P. L., Toth, I., Fernandez, Y. R., and Weaver, H. A., 2004. In Festou, M. C., Keller, H. U., and Weaver, H. A., eds., *Comets II*, 223–264.

Laskar, J., 1990. *Icarus*, **88**, 266–291.

Lebofsky, L. A. and Spencer, J. R., 1989. In Binzel, R. P., Gehrels, T., and Matthews, M. S., eds., *Asteroids II*, 128–147.

Lebofsky, L. A., Sykes, M. V., Tedesco, E. F. et al., 1986. *Icarus*, **68**, 239–251.

Lellouch, E., Laureijs, R., Schmitt, B. et al., 2000. *Icarus*, **147**, 220–250.

Lellouch, E., Stansberry, J., Emery, J., Grundy, W., and Cruikshank, D. P., 2011. *Icarus*, **214**, 701–716.

Lellouch, E., Santos-Sanz, P., Mommert, M., Lacerda, P., and Duffard, R., 2013. TNOs are Cool: A survey of the trans–Neptunian region. Thermal properties of Kuiper Belt objects and Centaurs from combined Herschel and Spitzer observations. In preparation.

Levi, A. and Podolak, M., 2009. *Icarus*, **202**, 681–693.

Levison, H. F. and Duncan, M. J., 1997. *Icarus*, **127**, 13–32.

Levison, H. F., Shoemaker, E. M., and Shoemaker, C. S., 1997. *Nature*, **385**, 42–44.

Levison, H. F., Dones, L., and Duncan, M. J., 2001. *AJ*, **121**, 2253–2267.

Levison, H. F., Terrell, D., Wiegert, P. A., Dones, L., and Duncan, M. J., 2006. *Icarus*, **182**, 161–168.

Li, J.-Y., A'Hearn, M. F., Belton, M. J. S. et al., 2007. *Icarus*, **187**, 41–55.

Li, J.-Y., A'Hearn, M. F., Farnham, T. L., and McFadden, L. A., 2009. *Icarus*, **204**, 209–226.

Li, J.-Y., Kuchner, M. J., Allen, R. J., and Sheppard, S. S., 2011. *Icarus*, **211**, 1007–1021.

Limpert, E., Stahel, W. A., and Abbt, M., 2001. *BioScience*, **151**, 341–352.

Lord, S. D., 1992. NASA Technical Memorandum 103957. Technical report, NASA.

Luu, J. X. and Jewitt, D. C., 1990. *AJ*, **100**, 913–932.

Mainzer, A., Bauer, J., Grav, T. et al., 2011a. *ApJ*, **731**, 53.

Mainzer, A., Grav, T., Bauer, J. et al., 2011b. *ApJ*, **743**, 156.

Mainzer, A., Grav, T., Masiero, J. et al., 2011c. *ApJ*, **741**, 90.

Mainzer, A., Grav, T., Masiero, J. et al., 2011d. *ApJ*, **736**, 100.

Mainzer, A., Grav, T., Masiero, J. et al., 2012. *ApJ*, **752**, 110.

Malhotra, R., 1993. *Nature*, **365**, 819–821.

Marengo, M., Stapelfeldt, K., Werner, M. W. et al., 2009. *ApJ*, **700**, 1647–1657.

Masiero, J. R., Mainzer, A. K., Grav, T. et al., 2011. *ApJ*, **741**, 68.

Matson, D. L., 1971a. I. astronomical photometry at wavelengths of 8.5, 10.5, and 11.6μm. ii. infrared emission from asteroids at wavelengths of 8.5, 10.5, and 11.6μm. Ph.D. thesis, California Institute of Technology.

Matson, D. L., 1971b. *NASA Special Publication*, **267**, 45.

Matson, D. L., Veeder, G. J., Tedesco, E. F., and Lebofsky, L. A., 1989. In Binzel, R. P., Gehrels, T., and Matthews, M. S., eds., *Asteroids II*, 269–281.

Melita, M. D. and Brunini, A., 2000. *Icarus*, **147**, 205–219.

Mellon, M. T., Jakosky, B. M., Kieffer, H. H., and Christensen, P. R., 2000. *Icarus*, **148**, 437–455.

Merline, W. J., Weidenschilling, S. J., Durda, D. D. et al., 2002. *Asteroids III*, 289–312.

Michel, P., Benz, W., Tanga, P., and Richardson, D. C., 2001. *Science*, **294**, 1696–1700.

Minor Planet Center List of Trojan Minor Planets. `http://www.minorplanetcenter.net/iau/lists/Trojans.html`. Accessed in November 2012.

Minor Planet Center Observations Database. `http://minorplanetcenter.net/db_search`. See text for individual access dates.

MIPS Instrument Handbook, 2011. `http://irsa.ipac.caltech.edu/data/SPITZER/docs/mips/mipsinstrumenthandbook/`. Spitzer Science Center, Version 3, accessed December 2012.

Miyamoto, H., Yano, H., Scheeres, D. et al., 2006. In Mackwell, S. and Stansbery, E., eds., *37th Annual Lunar and Planetary Science Conference*, *Lunar and Planetary Inst. Technical Report*, volume 37, 1686.

Mommert, M., Harris, A. W., Kiss, C. et al., 2012. *A&A*, **541**, A93.

Morbidelli, A., 1997. *Icarus*, **127**, 1–12.

Morbidelli, A., 2002. *Modern celestial mechanics : aspects of solar system dynamics*.

Morbidelli, A., 2005. *ArXiv Astrophysics e-prints*. ArXiv:astro-ph/0512256.

Morbidelli, A. and Gladman, B., 1998. *Meteoritics and Planetary Science*, **33**, 999–1016.

Morbidelli, A. and Henrard, J., 1991. *Celestial Mechanics and Dynamical Astronomy*, **51**, 169–197.

Morbidelli, A., Jedicke, R., Bottke, W. F., Michel, P., and Tedesco, E. F., 2002. *Icarus*, **158**, 329–342.

Morbidelli, A., Levison, H. F., Tsiganis, K., and Gomes, R., 2005. *Nature*, **435**, 462–465.

Morbidelli, A., Levison, H. F., and Gomes, R., 2008. In Barucci, M. A., Boehnhardt, H., Cruikshank, D. P., Morbidelli, A., and Dotson, R., eds., *The Solar System Beyond Neptune*, 275–292.

Morrison, D., 1973. *Icarus*, **19**, 1.

Morrison, D. and Lebofsky, L., 1979. In Gehrels, T., ed., *Asteroids*, 184–205.

Morrison, D., Harris, A. W., Sommer, G., Chapman, C. R., and Carusi, A., 2002. *Asteroids III*, 739–754.

Mueller, M., 2007. Surface properties of asteroids from mid-infrared observations and thermophysical modeling. Ph.D. thesis, Freie Universität Berlin, Germany.

Mueller, M., Delbo', M., Hora, J. L. et al., 2011. *AJ*, **141**, 109.

Mueller, M., Stansberry, J. A., Mommert, M., and Grundy, W., 2013. The MIPSKBOs Project. In preparation.

Müller, T. G., Lellouch, E., Böhnhardt, H. et al., 2009. *Earth Moon and Planets*, **105**, 209–219.

Müller, T. G., Lellouch, E., Stansberry, J. et al., 2010. *A&A*, **518**, L146+.

Müller, T. G., Nielbock, M., Balog, Z., Klaas, U., and Vilenius, E., 2011. PACS Photometer Point–Source Calibration, PICC-ME-TN-037. Technical report, Herschel PACS consortium, `http://herschel.esac.esa.int/twiki/pub/Public/PacsCalibrationWeb/pacs_bolo_fluxcal_report_v1.pdf`.

Nakamura, T., Noguchi, T., Tanaka, M. et al., 2011. *Science*, **333**, 1113–.

NASA/IPAC Infrared Science Archive/WISE Observations Database. `http://irsa.ipac.caltech.edu/Missions/wise.html`. Accessed January–February 2013.

NASA's IDL astronomy user's library. `http://idlastro.gsfc.nasa.gov/`. Accessed February 2013.

Nesvorný, D., Morbidelli, A., Vokrouhlický, D., Bottke, W. F., and Brož, M., 2002. *Icarus*, **157**, 155–172.

Nesvorný, D., Jenniskens, P., Levison, H. F. et al., 2010. *ApJ*, **713**, 816–836.

New Horizons Mission Website. `http://pluto.jhuapl.edu`. Accessed in December 2012.

Noll, K. S., Grundy, W. M., Stephens, D. C., Levison, H. F., and Kern, S. D., 2008. *Icarus*, **194**, 758–768.

Oort, J. H., 1950. *Bull. Astron. Inst. Netherlands*, **11**, 91–110.

Ootsubo, T., Kawakita, H., Hamada, S. et al., 2012. *ApJ*, **752**, 15.

Öpik, E. J., 1951. *Proc. R. Irish Acad. Sect. A, vol. 54, p. 165-199 (1951).*, **54**, 165–199.

Öpik, E. J., 1963. *Adv. Astron. Astrophys.*, **2**, 219.

Ott, S., 2010. In Mizumoto, Y., Morita, K.-I., and Ohishi, M., eds., *Astronomical Data Analysis Software and Systems XIX*, *Astronomical Society of the Pacific Conference Series*, volume 434, 139.

PACS Observer's Manual, 2011. `http://herschel.esac.esa.int/Docs/PACS/html/pacs_om.html`. PACS Consortium, Version 2.4, accessed September–December 2012.

Pál, A., Kiss, C., Müller, T. G. et al., 2012. *A&A*, **541**, L6.

Pál, A., Mommert, M., Müller, T. G. et al., 2013. TNOs are Cool: A survey of the trans-Neptunian region. Analysis of Resonant Objects from Herschel and Spitzer observations. In preparation.

PanSTARRS Website. `http://pan-starrs.ifa.hawaii.edu/public/home.html`. Accessed November 2012.

Peixinho, N., Boehnhardt, H., Belskaya, I. et al., 2004. *Icarus*, **170**, 153–166.

Perna, D., Barucci, M. A., Fornasier, S. et al.

Petit, J.-M., Morbidelli, A., and Chambers, J., 2001. *Icarus*, **153**, 338–347.

Petit, J.-M., Kavelaars, J. J., Gladman, B., and Loredo, T., 2008. In Barucci, M. A., Boehnhardt, H., Cruikshank, D. P., Morbidelli, A., and Dotson, R., eds., *The Solar System Beyond Neptune*, 71–87.

Petit, J.-M., Kavelaars, J. J., Gladman, B. J. et al., 2011. *AJ*, **142**, 131.

Pilbratt, G. L., Riedinger, J. R., Passvogel, T. et al., 2010. *A&A*, **518**, L1.

Poglitsch, A., Waelkens, C., Geis, N. et al., 2010. *A&A*, **518**, L2.

Pravec, P., Harris, A. W., Kušnirák, P., Galád, A., and Hornoch, K., 2012. *Icarus*, **221**, 365–387.

Press, W. H., Teukolsky, S. A., Vetterling, W. T., and Flannery, B. P., 1992. *Numerical recipes in C. The art of scientific computing.*

Putzig, N. E., Mellon, M. T., Kretke, K. A., and Arvidson, R. E., 2005. *Icarus*, **173**, 325–341.

Rabinowitz, D. L., 1994. *Icarus*, **111**, 364–377.

Rayner, J. T., Toomey, D. W., Onaka, P. M. et al., 2003. *PASP*, **115**, 362–382.

Reach, W. T., Kelley, M., and Vaubaillon, J., 2012. Survey of cometary CO_2, CO, and particulate emissions using the Spitzer Space Telescope. Submitted.

Resolution 5A of the IAU General Assembly 2006 in Prague. `http://www.iau.org/public_press/news/detail/iau0603/`. Accessed in November 2012.

Rickman, H., Fernandez, J. A., and Gustafson, B. A. S., 1990. *A&A*, **237**, 524–535.

Rieke, G. H., Young, E. T., Engelbracht, C. W. et al., 2004. *ApJS*, **154**, 25–29.

Rieke, G. H., Blaylock, M., Decin, L. et al., 2008. *AJ*, **135**, 2245–2263.

Rivkin, A. S., Howell, E. S., Clark, B. E., Lebofsky, L. A., and Britt, D. T., 1997. In *Lunar and Planetary Institute Science Conference Abstracts*, *Lunar and Planetary Inst. Technical Report*, volume 28, 1183.

Rivkin, A. S., Binzel, R. P., Sunshine, J. et al., 2004. *Icarus*, **172**, 408–414.

Romanishin, W. and Tegler, S. C., 2005. *Icarus*, **179**, 523–526.

Rubincam, D. P., 2000. *Icarus*, **148**, 2–11.

Santos-Sanz, P., Lellouch, E., Fornasier, S. et al., 2012. *A&A*, **541**, A92.

Schaller, E. L. and Brown, M. E., 2007. *ApJ*, **659**, L61–L64.

Scheeres, D. J., Durda, D. D., and Geissler, P. E., 2002. *Asteroids III*, 527–544.

Schorghofer, N., 2008. *ApJ*, **682**, 697–705.

Schuster, M. T., Marengo, M., and Patten, B. M., 2006. In *Society of Photo-Optical Instrumentation Engineers (SPIE) Conference Series*, *Society of Photo-Optical Instrumentation Engineers (SPIE) Conference Series*, volume 6270.

Shankman, C., Gladman, B. J., Kaib, N., Kavelaars, J. J., and Petit, J. M., 2013. *ApJ*, **764**, L2.

Sheppard, S. S. and Jewitt, D. C., 2002. *AJ*, **124**, 1757–1775.

Shoemaker, E. M., Williams, J. G., Helin, E. F., and Wolfe, R. F., 1979. *Earth-crossing asteroids - Orbital classes, collision rates with earth, and origin*, 253–282.

Sicardy, B., Bellucci, A., Gendron, E. et al., 2006. *Nature*, **439**, 52–54.

Sicardy, B., Ortiz, J. L., Assafin, M. et al., 2011. *Nature*, **478**, 493–496.

Sitarski, G., 1968. *Acta Astron.*, **18**, 171.

Skrutskie, M. F., Cutri, R. M., Stiening, R. et al., 2006. *AJ*, **131**, 1163–1183.

Sosa, A., Fernández, J. A., and Pais, P., 2012. *A&A*, **548**, A64.

Spaceguard Survey Report, 1992. `http://impact.arc.nasa.gov/downloads/spacesurvey.pdf`. Accessed November 2012.

Spencer, J. R., Lebofsky, L. A., and Sykes, M. V., 1989. *Icarus*, **78**, 337–354.

Spencer, J. R., Stansberry, J. A., Trafton, L. M. et al., 1997. *Volatile Transport, Seasonal Cycles, and Atmospheric Dynamics on Pluto*, 435.

Spitzer Heritage Archive. `http://sha.ipac.caltech.edu/applications/Spitzer/SHA/`. Accessed January–February 2013.

Spitzer Observer's Manual, 2007. `http://irsa.ipac.caltech.edu/data/SPITZER/docs/files/spitzer/som8.0.pdf`. Spitzer Science Team, Version 8.0, accessed January–February 2013.

Spitzer Space Telescope Handbook, 2011. `http://irsa.ipac.caltech.edu/data/SPITZER/docs/spitzermission/missionoverview/spitzertelescopehandbook/`. Spitzer Science Center, Version 2.0, accessed January–February 2013.

Stansberry, J. A., Grundy, W. M., Margot, J. L. et al., 2006. *ApJ*, **643**, 556–566.

Stansberry, J. A., Grundy, W., Brown, M. et al., 2008. In Barucci, M. A., Boehnhardt, H., Cruikshank, D. P., Morbidelli, A., and Dotson, R., eds., *The Solar System Beyond Neptune*, 161–179.

Stern, S. A. and Trafton, L. M., 2008. In Barucci, M. A., Boehnhardt, H., Cruikshank, D. P., Morbidelli, A., and Dotson, R., eds., *The Solar System Beyond Neptune*, 365–380.

Stuart, J. S., 2003. Observational constraints on the number, albedos, sizes, and impact hazards of the near-earth asteroids. Ph.D. thesis, Massachusetts Institute of Technology, Cambridge, MA.

Stuart, J. S. and Binzel, R. P., 2004. *Icarus*, **170**, 295–311.

Tanga, P., Comito, C., Paolicchi, P. et al., 2009. *ApJ*, **706**, L197–L202.

Tedesco, E. F., 1990. *Minor Planet Circulars*, **17256-17273**.

Tedesco, E. F., Veeder, G. J., Fowler, J. W., and Chillemi, J. R., 1992. The IRAS Minor Planet Survey. Technical report, Phillips Laboratory, Hanscom Air Force Base, MA.

Tedesco, E. F., Noah, P. V., Noah, M., and Price, S. D., 2002. *AJ*, **123**, 1056–1085.

Tegler, S. C. and Romanishin, W., 1998. *Nature*, **392**, 49.

Tholen, D. J., 1984. *Asteroid taxonomy from cluster analysis of photometry.* Tucson: University of Arizona, 1984.

Thomas, C. A., 2013. In preparation.

Thomas, C. A., Trilling, D. E., Emery, J. P. et al., 2011. *AJ*, **142**, 85.

Thomas, P. C., Parker, J. W., McFadden, L. A. et al., 2005. *Nature*, **437**, 224–226.

Tiscareno, M. S. and Malhotra, R., 2003. *AJ*, **126**, 3122–3131.

Tiscareno, M. S. and Malhotra, R., 2009. *AJ*, **138**, 827–837.

Trilling, D. E., Mueller, M., Hora, J. L. et al., 2008. *ApJ*, **683**, L199–L202.

Trilling, D. E., Mueller, M., Hora, J. L. et al., 2010. *AJ*, **140**, 770–784.

Trilling, D. E., Mommert, M., Mueller, M. et al., 2013. ExploreNEOs. VI. Second data release and preliminary size distribution of near Earth objects. Submitted.

Trujillo, C. A. and Brown, M. E., 2002a. *IAU Circ.*, **7787**, 1–+.

Trujillo, C. A. and Brown, M. E., 2002b. *ApJ*, **566**, L125–L128.

Tsiganis, K., Gomes, R., Morbidelli, A., and Levison, H. F., 2005. *Nature*, **435**, 459–461.

Veeder, G. J., Hanner, M. S., Matson, D. L. et al., 1989. *AJ*, **97**, 1211–1219.

Verbiscer, A. J., French, R. G., and McGhee, C. A., 2005. *Icarus*, **173**, 66–83.

Viggh, H. E. M., Stokes, G. H., Shelly, F. C., Blythe, M. S., and Stuart, J. S., 1998. In Galloway, R. G. and Lokaj, S., eds., *Space 98*, 373.

Vilenius, E., Kiss, C., Mommert, M. et al., 2012. *A&A*, **541**, A94.

Vilenius, E., Kiss, C., Müller, T. G. et al., 2013. TNOs are Cool: A survey of the trans-Neptunian region IX. Analysis of classical Kuiper belt objects from Herschel and Spitzer observations. In preparation.

Walsh, K. J., Richardson, D. C., and Michel, P., 2008. *Nature*, **454**, 188–191.

Warm Spitzer Observer's Manual, 2012. `http://ssc.spitzer.caltech.edu/warmmission/propkit/som/som11.1.pdf`. Spitzer Science Team, Version 11.1, accessed January–February 2013.

Warner, B. D., Harris, A. W., Vokrouhlický, D., Nesvorný, D., and Bottke, W. F., 2009. *Icarus*, **204**, 172–182.

Weidenschilling, S. J., Paolicchi, P., and Zappala, V., 1989. In Binzel, R. P., Gehrels, T., and Matthews, M. S., eds., *Asteroids II*, 643–658.

Weidenschilling, S. J., Chapman, C. R., Davis, D. R., Greenberg, R., and Levy, D. H., 1990. *Icarus*, **86**, 402–447.

Weissman, P. R., 1996. In Rettig, T. and Hahn, J. M., eds., *Completing the Inventory of the Solar System*, *Astronomical Society of the Pacific Conference Series*, volume 107, 265–288.

Weissman, P. R., A'Hearn, M. F., Rickman, H., and McFadden, L. A., 1989. In Binzel, R. P., Gehrels, T., and Matthews, M. S., eds., *Asteroids II*, 880–920.

Weissman, P. R., Bottke, W. F., Jr., and Levison, H. F., 2002. *Asteroids III*, 669–686.

Weissman, P. R., Asphaug, E., and Lowry, S. C., 2004. *Structure and density of cometary nuclei*, 337–357.

Werner, M. W., Roellig, T. L., Low, F. J. et al., 2004. *ApJS*, **154**, 1–9.

Wetherill, G. W., 1979. *Icarus*, **37**, 96–112.

Wetherill, G. W., 1988. *Icarus*, **76**, 1–18.

Wetherill, G. W., 1991. In Newburn, R. L., Jr., Neugebauer, M., and Rahe, J., eds., *IAU Colloq. 116: Comets in the post-Halley era*, *Astrophysics and Space Science Library*, volume 167, 537–556.

Whipple, F. L., 1950. *ApJ*, **111**, 375–394.

Wide–Field Infrared Survey Explorer All–Sky Data Release. `http://wise2.ipac.caltech.edu/docs/release/allsky/`. Accessed January–February 2013.

Winter, D. F. and Krupp, J. A., 1971. *Moon*, **2**, 279–292.

Wolters, S. D. and Green, S. F., 2009. *MNRAS*, **400**, 204–218.

Wolters, S. D., Green, S. F., McBride, N., and Davies, J. K., 2008. *Icarus*, **193**, 535–552.

Wright, E. L., 2007. *ArXiv Astrophysics e-prints*.

Wright, E. L., Eisenhardt, P. R. M., Mainzer, A. K. et al., 2010. *AJ*, **140**, 1868.

Yamamoto, T., 1985. *A&A*, **142**, 31–36.

Yeomans, D. K., Chodas, P. W., Sitarski, G., Szutowicz, S., and Królikowska, M., 2004. *Cometary orbit determination and nongravitational forces*, 137–151.

Young, E. F., Young, L. A., and Buie, M., 2007. In *AAS/Division for Planetary Sciences Meeting Abstracts #39*, *Bulletin of the American Astronomical Society*, volume 39, 541.

Index

Acknowledgments

I express my deepest gratitude to Prof. Alan W. Harris who supervised this work and introduced me into the fields of Solar System small–body research and thermal modeling. I thank you for 3.5 yrs of excellent scientific supervision, motivation, compassion, and useful advice in many respects. I explicitly acknowledge all your efforts and patience in teaching me the proper use of the English language; it was certainly not in vain.

I thank Prof. Tilman Spohn, Prof. Ralf Jaumann, Dr. Ekkehard Kührt, and Prof. Alan W. Harris for making it possible for me to conduct this work at the Institute of Planetary Research of the German Aerospace Center (DLR). Furthermore, my gratitude goes to the Deutsche Forschungsgemeinschaft (DFG) and its Special Priority Program "SPP1385: The first 10 Million Years of the Solar System" for the support of this work.

I would like to thank Dr. John A. Stansberry for inviting me on a four–month stay to the University of Arizona, Tucson, to work with him on the *MIPSKBOs* project. My research there significantly exceeded the fields of Solar System sciences, including joint geological field–trips, impact experiments on the driving range, and the exploration of the American Way–of–Life, or was it the Mexican–American? Thank you for still being a most–excellent friend.

Bedankt, Merci, and Danke to Michael "Migo" Mueller for his help with the thermophysical model and so many other things!

I also wish to thank the PIs of the *ExploreNEOs* and *TNOs are Cool!* programs, Prof. David Trilling and Dr. Thomas Müller, for providing me the opportunity to help them pushing the envelope in Solar System research. Thank you, Danke, Merci, Gracias, Grazie, Obrigado and Kiitos to all members of the *ExploreNEOs* and *TNOs are Cool!* programs for your support!

Many thanks and regrets go to the proof readers[1] of this work: Alan, Migo, Uri, Gerhard, Stefano, John, Thomas, Ivanka, Lisa, Stefan, and Philipp.

I would also like to thank all my colleagues at DLR for their support and help in many aspects. *A hungry man is an angry man...* Thanks to all members of the Kantinen–lunch group for the nice company!

Last but not least, danke ich dir, Katja, für deine Unterstützung in den vergangenen

[1] I skip their last names to protect their identities. They are not to blame for any mistakes.

drei Jahren und insbesondere, dass du in den letzten Monaten immer für mich da warst. Versprochen, ich werde mich jetzt wieder um den Abwasch kümmern... Ich danke meiner Familie und meinen Freunden, dass sie mich auf diesem Weg begleitet und unterstützt haben!

This work was financially supported by the DFG SPP1385: "The first 10 Million Years of the Solar System" and the German Aerospace Center (Deutsches Zentrum für Luft– und Raumfahrt, e.V.).

This work is based in part on observations made with the Spitzer Space Telescope, which is operated by the Jet Propulsion Laboratory, California Institute of Technology under a contract with NASA.

Parts of this work are based on observations of the PACS instrument onboard the the Herschel Space Observatory. Herschel is an ESA space observatory with science instruments provided by European-led Principal Investigator consortia and with important participation from NASA. PACS has been developed by a consortium of institutes led by MPE (Germany) and including UVIE (Austria); KU Leuven, CSL, IMEC (Belgium); CEA, LAM (France); MPIA (Germany); INAF-IFSI/OAA/OAP/OAT, LENS, SISSA (Italy); IAC (Spain). This development has been supported by the funding agencies BMVIT (Austria), ESA-PRODEX (Belgium), CEA/CNES (France), DLR (Germany), ASI/INAF (Italy), and CICYT/MCYT (Spain).

This research has made use of the NASA/IPAC Infrared Science Archive, which is operated by the Jet Propulsion Laboratory, California Institute of Technology, under contract with the National Aeronautics and Space Administration.

Appendix A

Supplementary Material

A.1 Important Concepts of Celestial Mechanics

This section provides an introduction to the basic concepts of celestial mechanics that are important for the understanding of this work. I introduce the general geometric parameters, the orbital elements and some dynamical effects that are of importance in the scope of this work. Note that this compilation is far from being complete and my intention is to provide some general basics for readers that are less familiar with the topic. For more details, I refer to standard works of celestial mechanics, like Morbidelli (2002).

A.1.1 Geometric Parameters

The position of a body relative to the observer and the Sun is sufficiently described in space by three parameters (see Figure A.1):

- The "heliocentric distance", r, which describes the distance between the body and the Sun. The heliocentric distance is usually expressed in terms of "astronomical units", which equals the average distance of the Earth from the Sun, roughly $149.6 \cdot 10^6$ km.
- The distance between the observer and the body, Δ, in AU; in case of observations from the Earth, Δ is often referred to as the "geocentric distance".
- The "solar phase angle", α, describing the angle between the observer and the Sun as seen from the body; using the Moon as an example, $\alpha = 0$ describes the full moon (the object is in "opposition"), $\alpha = \pm 90°$ the first/last quarter, and $\alpha = 180°$ the new moon.

The "solar elongation" describes the angle between the body and the Sun as seen from the observer. The pointing of space–based observatories is usually constrained by the solar elongation to provide sufficient shielding from insolation.

A.1.2 Orbital Elements

The orbit of any Solar System body is described by 6 orbital elements that describe the shape of the orbit, its orientation in space, and the position of the body at a given time.

A.1.2.1 Shape of the Orbit

According to Kepler's laws, the orbit of a celestial body can be described as an ellipse with the Sun in one of the two focal points of the ellipse[1]. An ellipse is fully described by two parameters:

[1] In a more general description, Kepler talks about conic sections, which includes parabolic and hyperbolic orbits as observed in comets. Here, however, I will focus on elliptic orbits.

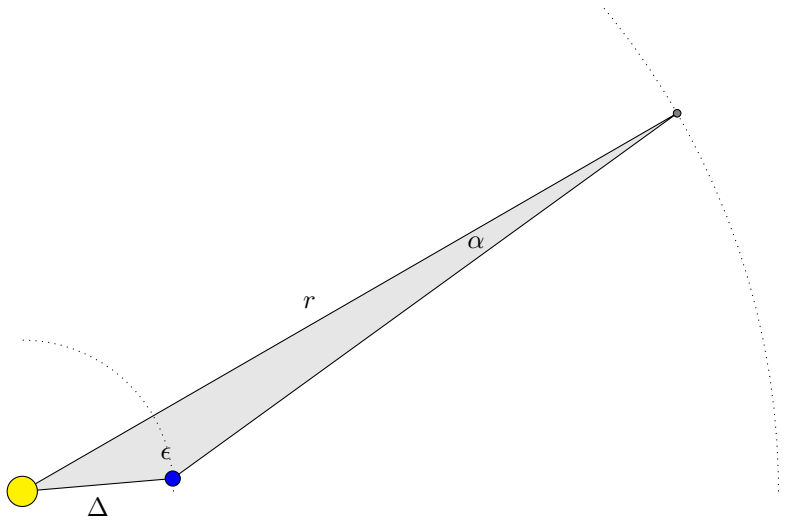

Figure A.1 Definition of the heliocentric and geocentric distances, r and Δ, respectively, the solar phase angle, α, and the solar elongation, ϵ. The Sun (yellow circle), the observer (blue circle), and the target object (grey circle), and the orbits of the latter two are indicated.

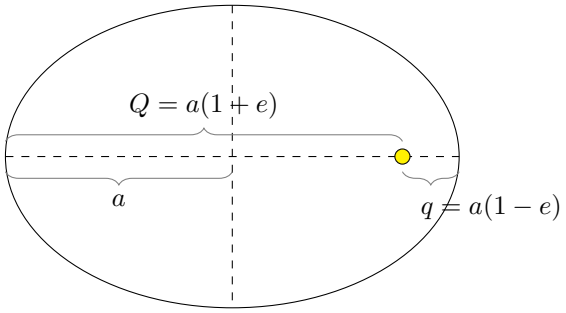

Figure A.2 Example of an elliptic orbit with $e = 0.75$. The semimajor axis, a, the perihelion and aphelion distances, q and Q, respectively, are highlighted. The position of the Sun, in one of the ellipse's focal points, is shown as a yellow circle.

- The "semimajor axis", a, is defined as half the length of the long axis of the ellipse and is usually expressed in terms of AU.

- The "eccentricity", e, is a numerical value between 0 and 1, which describes the ellipticity of the ellipse. $e = 0$ describes a circular orbit, $0 < e < 1$ an elliptic orbit, $e = 1$ a parabolic orbit, and $e > 1$ a hyperbolic orbit. Most small bodies have elliptic orbits; parabolic and hyperbolic orbits occur in comets and other objects that are scattered out of the Solar System.

The "perihelion distance", q, of a body describes its heliocentric distance at the time of its closest encounter to the Sun and is defined as $q = a(1 - e)$. Similarly, the aphelion distance is defined as $Q = a(1 + e)$.

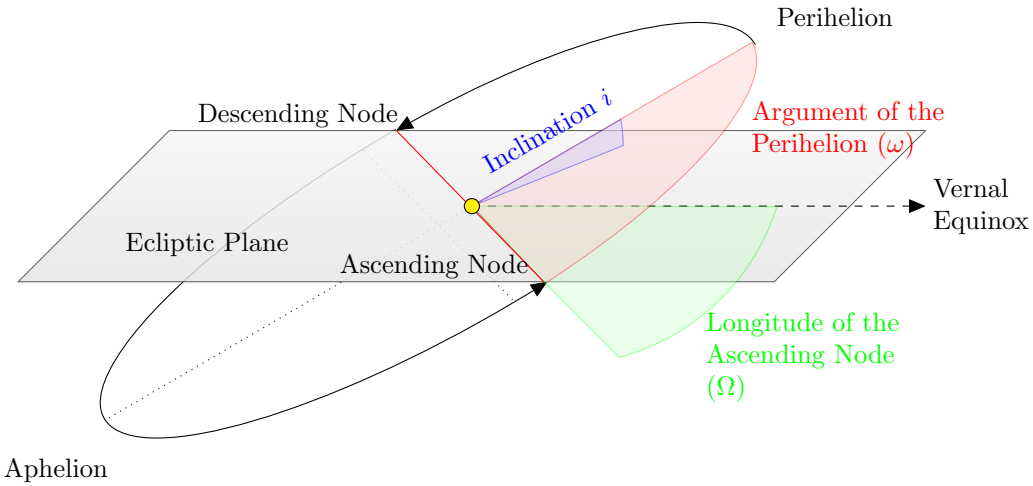

Figure A.3 Illustration of the orientation of an orbit relative to the ecliptic (grey plane) and the vernal equinox. The orbit of the object is depicted by the black ellipse with the Sun (yellow circle) in one of its focal points. The nodal line (red) connects the ascending and descending nodes and intersects the Sun. The plane of the orbits is tilted against the ecliptic by the inclination, i. The orientation of the nodal line relative to the vernal equinox is given by the longitude of the ascending node. The position of the perihelion relative to the nodal line is described by the argument of the perihelion.

A.1.2.2 Orientation in Space

In order to describe the absolute orientation of the orbit in space, 3 elements are necessary:

- The "inclination", i, describes the tilt of the orbit relative to the reference plane, which is the "ecliptic", Earth's orbital plane. Objects with $i = 0$ rotate in the ecliptic plane; $0 < i < 90°$ describes a pro–grade rotation around the Sun, tilted with respect to the ecliptic and with two intersections with the ecliptic. $i > 90°$ describes a retrograde rotation.

- The "Longitude of the ascending node", Ω, describes the angle between the vernal equinox and the ascending node, which is that intersection between the orbital plane and the ecliptic where the object passes from the south of the ecliptic to its northern hemisphere (north and south are defined relative to the reference frame of the Earth). The longitude of the ascending node orients the orbit in the ecliptic plane.

- The "argument of the perihelion", ω, is the angle between the ascending node and the perihelion of the orbit in the orbital plane.

A.1.2.3 Position in the Orbit as a Function of Time

The "mean anomaly" describes the angle between the position of the object and its perihelion at a given time, called "epoch". The definition of the mean anomaly is motivated

by Kepler's second law of celestial mechanics, saying that equal areas are swept in equal intervals of time by a line connecting the Sun and the orbiting body.

The 6 orbital elements introduced above fully describe the problem of celestial motion, which has 6 unknowns, one position and one velocity vector, each in three–dimensional space. The computation of orbits is beyond the scope of this work and described in standard works of celestial mechanics (e.g., Morbidelli 2002).

A.1.2.4 Osculating vs. Proper Elements

The orbits of all celestial bodies are subject to change due to perturbations exerted by other bodies. Hence, one has to distinguish two sets of orbital elements:

Osculating Elements. The Keplerian orbit of a body at a given epoch is described by the "osculating elements", which disregard perturbations and are therefore valid on a short time–scale only. In the absence of perturbations, including the gravitational pull of objects other than the Sun, resonances, and solar wind drag, the osculating elements would be stable. In reality, osculating elements change with time.

Proper Elements. The variations in the osculating elements are quasi–periodic, allowing for the determination of the "proper elements" that are not subject to change. The proper elements can be determined by sophisticated dynamical modeling. The proper elements are important in the identification of asteroid families, which have common sets of proper elements (see Section 1.1.2.1).

A.1.3 More Advanced Dynamical Concepts

A.1.3.1 The Tisserand Parameter

The "Tisserand parameter" is a dynamical quantity that is approximately conserved during encounters of small bodies with a planet in the restricted three–body problem. The restricted three–body problem is a simplification of celestial mechanics using three assumptions: (1) the mass of the target body is assumed to be negligible compared to the mass of the planet; (2) the latter is assumed to have a circular orbit; (3) the orbit of the target body is only influenced by the gravitational forces of the planet and the Sun, i.e., non–gravitational forces and attractions by other bodies are ignored. The Tisserand parameter is diagnostic of an earlier gravitational interaction with a planet and defined as

$$T_P = \frac{a_P}{a} + 2\sqrt{\frac{a}{a_P}\left(1 - e^2\right)}\cos i, \tag{A.1}$$

where a, e, and i are the semimajor axis, eccentricity, and inclination of the small body, respectively, and a_P is the semimajor axis of the planet. The Tisserand parameter with

respect to Jupiter, T_J, is of special interest in orbital dynamics since it can be used as a means to distinguish between asteroidal ($T_J > 3.0$) and cometary ($T_J \leq 3.0$) orbits. It can also be used to distinguish between the different types of comets (cf. Section 1.1.5): long–period and Halley type comets have $T_J < 2.0$, whereas short–period comets have $2.0 \leq T_J \leq 3.0$. The actual T_J boundary between asteroids and comets cannot be precisely determined, since T_J is only conserved in the idealized case of the restricted three–body problem. Comets with $T_J > 3.0$ exist and are called "Encke–type" comets.

The Tisserand parameter can also be interpreted as a measure of the relative velocity, v_{rel}, between a small body and the planet during close encounters. In the case of Jupiter,

$$v_{\mathrm{rel}} = v_J \sqrt{3 - T_J},$$

where v_J is Jupiter's circular orbit velocity about the Sun. Objects with $T_J > 3.0$ are not Jupiter–crossing, whereas objects with $T_J < 3.0$ increase in relative velocity with decreasing T_J.

A.1.3.2 Dynamical Resonances

The orbits of objects around the Sun can be in commensurable resonance, leading to additional stability or chaotic dynamical behavior, depending on the nature of the resonance. The two most important types of resonances are introduced in the following (see also Morbidelli 2002).

Mean Motion Resonances (MMR). Two bodies are in "mean motion resonance" (MMR) if the ratio of the orbital periods of the inner and outer object, p and q, respectively, form a simple integer ratio $p : q$. In such a case, both bodies exert a periodic gravitational influence on each other. Small bodies can be in resonance with planets, leading to exceptionally stable or unstable orbits, depending on whether the nature of the resonance allows for close encounters of the two bodies: if the MMR prevents close encounters, the orbit is extremely stable, whereas it is extremely unstable, if the MMR brings the small body close to the planet, leading to strong perturbations. The dynamical structure of the asteroid main belt is strongly influenced by MMRs with Jupiter, appearing as Kirkwood gaps (see Section 1.1.2.1). Objects occupying an unstable MMR, have their eccentricities pumped up as a result of periodic encounters with the planet, eventually leading to an ejection from the resonance. Other resonances, like the 3:2 MMR with Jupiter that is populated by the Hilda asteroids, lead to extremely stable orbits. MMRs in the trans–Neptunian region are dominated by the gravitational influence of Neptune. The most important example here are the Plutinos, which are in 2:3 resonance with Neptune, having exceptionally stable orbits.

Secular Resonances A "secular resonance" occurs when the precession rates of the longitude of the perihelion or the longitude of the ascending node of two bodies are synchronized. Small bodies in secular resonance with a planet are forced to alter their eccentricity and inclination in the long term. The most prominent example is the ν_6 perihelion secular resonance between main belt asteroids and Saturn (see Section 1.1.2.2 and Froeschle and Scholl 1989). Asteroids approaching this resonance have their eccentricities increased, ending up as Mars crossers and entering the NEO region (Bottke et al. 2002b).

A.2 Basic Observational and Image Analysis Concepts

The following sections provide a coarse introduction into astronomical observation techniques, as well as image analysis concepts that are important for the understanding of this work. For a more complete overview I refer to Howell (2000) and the instrument handbooks.

A.2.1 Observation Techniques

A.2.1.1 Direct Imaging

The most intuitive observation method is direct imaging, producing a picture of the target as seen by the image detector. Since most small bodies are too small and/or too far away to resolve their shapes and surfaces (cf. Section 1.2.2), they appear as point sources, similar to stars. However, even the images of point sources are extended, as a result of diffraction effects occurring at the telescope aperture and other optical parts. The "point–spread function" (PSF) describes the brightness distribution of a perfect point source on the detector array, taking into account diffraction effects in the optical system. The image of an object as seen through any optical system is mathematically represented by the convolution of the real image with the system's PSF. The PSF can be calculated, or derived empirically from observations in the form of a "point response function" (PRF). In this work I use the terms PSF and PRF synonymously.

In a first–order approach, the PSF is described well–enough by its "full width half maximum" (FWHM), which is a measure of the extent of the PSF. The FWHM describes the width of the PSF where its brightness equals half its maximum brightness. The FWHM is independent of the brightness of the point source and therefore the same for all point sources in one image. In order to achieve adequate sampling of the PSF, the detector pixel size has to be smaller than half the FWHM of the PSF, which is a result of the Nyquist theorem.

"Dithering" describes the variation of the target's position on the detector between individual integrations either by changing the telescope pointing or using a chop mirror. The pointing is changed in such a way, as to have the target in the field of view all the time, but occupying different segments of the detector. Dithering helps to minimize the impact of detector–specific artifacts. Furthermore, the combination of dithered images allows for the production of maps with "super–resolution".

The proper motion of Solar System bodies can be taken advantage of by obtaining "follow–up observations". The idea is to observe that field of the sky, where a target was observed before, a second time or more often with the object having moved out of its previous position. The additional images are aligned on the sky background and then subtracted from each other ("sky–subtracted"), cleaning the background of the image, even "behind" the object, if the individual observations are well timed. The time span

between the individual observations is determined by the proper motion of the target and has to be chosen in such a way as to preclude an overlap of the individual object positions.

A.2.1.2 Spectroscopic Observations

Spectroscopic observations allow for a disentanglement of the spectral information of an object, i.e., to display its brightness as a function of wavelength. Usually, dispersive elements like prisms or gratings are inserted in the optical path of the telescope to break down the object's spectrum. The broken down spectrum is measured by an imaging device. As a result of the splitting of the total brightness of an object into a wavelength dependent brightness, the signal per wavelength is much weaker. Hence, spectroscopic observations require long integration times and are usually restricted to bright targets. The comparison of spectral features of Solar System bodies with laboratory measurements of minerals, ices, and other materials allow for constraining their surface composition (see Section 1.2.4). Spectroscopic observations were not conducted as part of this work, however, results from spectroscopic observations have been used in the interpretation of the results (see, e.g., Section 4.3).

A.2.2 Image Analysis

The process of measuring the brightness of an astronomical object, in the following referred to as the target's "signal", is called photometry. The concept of brightness and its "magnitude"–scale have been introduced in Section 1.2.1. In the following, the photometric measurement and subsequent correction steps are briefly discussed.

A.2.2.1 Aperture Photometry

To measure the target' signal, the values of the pixels that are covered by the target's PSF, are summed up. This method is called "aperture photometry", since the fluxes are usually summed up in a circular aperture. However, the measured signal contains contributions from the sky background, which is brightened by effects like air–glow (optical) or zodiacal light (infrared) and subject to noise. The sky background contributions have to be subtracted, in order to isolate the target's signal. The brightness of the sky background is measured in apertures in the vicinity of the object, or in an annulus around the object. It is crucial that the field in which the sky background brightness is measured is not contaminated by a nearby background object. A thorough description and discussion of aperture photometry, as well as other photometric methods, is given in Howell (2000).

The size of the aperture has to be chosen wisely: the larger the aperture, the more important is the proper determination of the sky background brightness, and the more noise is added to the signal. Usually, the aperture is chosen in such a way as to include

most of the target's signal, but not all of it. Hence, the measured signal has to be corrected for this deficiency, which is called "aperture correction".

The signal derived from the corrected image is given in units of digital counts, an artificial unit that is inherent to the sensitivity of the combined system of the telescope and the detector. In order to obtain a physically useful measure of the target's brightness, e.g., magnitude or flux density units, the detector response has to be calibrated, which is done by observing stars or galaxies that do not show or have well–understood brightness variations.

A.2.2.2 Color Correction

Broadband photometric filters allow for photons with a wide range of wavelengths to pass; the measured signal is integrated over the bandwidth of the filter. It is possible to determine the monochromatic signal for an "effective wavelength", λ_0, provided the target's spectral energy distribution, $f(\lambda)$, and the spectral filter and detector response function, $R(\lambda)$, are known. The detector response per integration time, S, is given by

$$S = \int_0^\infty f(\lambda) \frac{R(\lambda)}{hc/\lambda}\, d\lambda, \quad \text{or} \quad S = f(\lambda_0) \int_0^\infty \frac{f(\lambda)}{f(\lambda_0)} \frac{R(\lambda)}{hc/\lambda}\, d\lambda,$$

with $R(\lambda)$ in units of electrons per photon, which requires division by the photon energy hc/λ. The detector response to a target with a spectral energy distribution $f_{\rm tar}(\lambda)$, $S_{\rm tar}$, and that to a calibration source with spectrum $f_{\rm cal}(\lambda)$, $S_{\rm cal}$, is then related to the monochromatic flux densities at the effective wavelength as

$$f_{\rm tar}(\lambda_0) = f_{\rm cal}(\lambda_0) \frac{S_{\rm tar}}{S_{\rm cal}} \frac{1}{K} \tag{A.2}$$

$$K = \frac{f_{\rm cal}(\lambda_0)}{f_{\rm tar}(\lambda_0)} \frac{\int_0^\infty f_{\rm tar}(\lambda) R(\lambda)/(hc/\lambda)\, d\lambda}{\int_0^\infty f_{\rm cal}(\lambda) R(\lambda)/(hc/\lambda)\, d\lambda} \tag{A.3}$$

with the "color correction coefficient", K. Note that K is invariant under rescaling of $f_{\rm tar}(\lambda)$ and $f_{\rm cal}(\lambda)$. Flux densities used in this work are calibrated by the respective observatory data reduction pipelines, assuming a nominal spectral energy distribution of the source, $f_{\rm nom}(\lambda)$.

In order to obtain the color correction coefficient for a small body, the standard method is to approximate its spectral energy distribution, $f_{\rm tar}$, by that of a black body of temperature T, where T is the subsolar temperature or mean temperature of the surface (see Section 3.1). $f_{\rm cal}$ equals the nominal spectrum, $f_{\rm nom}(\lambda)$, which is specified by the respective instrument handbook. Since the surface temperature of small bodies is a function of the measured flux densities, K has to be calculated for each iteration step of the thermal model to account for the current set of free model parameters.

The effective wavelength of a system is usually defined as

$$\lambda_0 = \frac{\int \lambda \; R(\lambda) \; d\lambda}{\int R(\lambda) \; d\lambda}.$$

A.2.2.3 Photometric Uncertainties and the Signal–to–Noise Ratio

Every observation is subject to noise, which is introduced by the detector itself (e.g., the read–out noise), the sky background, or photon statistics. The latter is also referred to as "photon noise", meaning statistical variations in the number of photons that are measured in a given time as a result of the random nature of the photon emission process, best described by Poisson statistics. The quality of an observation can be estimated using the "signal–to–noise ratio" (SNR), which is given by the ratio of the target's signal and the root–mean–square of all individual noise terms. In the case of a bright target, the photon noise dominates the other noise terms, simplifying the determination of the SNR: assuming a Poisson–like behavior of the photon noise, the standard deviation of N photons measured in a specific time is $\sqrt{N}$, and SNR=$N/\sqrt{N} = \sqrt{N}$. This relation provides a useful estimate of the SNR of a bright source.

Appendix B

Related Work

In this Section, I present work done by myself that is related to, but not necessary for the understanding of this work. The following topics are covered:

- *I perform an assessment of the accuracy of the ExploreNEOs thermal modeling results based on a Monte–Carlo approach and compare the results of the ExploreNEOs and NEOWISE programs in Section B.1.*
- *In Section B.2, I investigate the diameter and albedo uncertainties resulting from thermal models. I find that albedo uncertainties follow a log–normal distribution and suggest a new way of citing albedo uncertainties that takes into account their log–normal nature. Furthermore, I design an analytical uncertainty model.*
- *Section B.3 introduces the MIPSKBOs project, in which all TNO and Centaur observations performed with the Spitzer MIPS instrument are reprocessed in a consistent manner. I discuss the specifications of the MIPS instrument and briefly outline the MIPSKBOs pipeline and my contribution to the project. Eventually, I discuss the preliminary thermal modeling of the MIPSKBOs flux density data, which is used in Sections 5.2 and 5.3.*

B.1 Assessment of the Accuracy of the ExploreNEOs Results

Harris et al. (2011) provides an assessment of the accuracy of the default ExploreNEOs thermal modeling pipeline results, to which I have contributed. In the following, I describe my contribution to Harris et al. (2011): an assessment of the uncertainties using a Monte–Carlo approach. In this work, I also compare the diameters and albedos of the full ExploreNEOs sample with the published NEOWISE results (Mainzer et al. 2011b, see also Section 2.3).

B.1.1 Monte–Carlo Uncertainty Assessment

Harris et al. (2011) investigates the accuracy of the *ExploreNEOs* thermal modeling results, to which I have contributed. The accuracy is estimated using two different approaches. The first approach, performed by A. W. Harris, DLR, uses the fact that 13[1] out of the 170 at that time observed *ExploreNEOs* sample objects already had reliably measured diameters and albedos from the published literature. A comparison of the *ExploreNEOs* diameters and albedos with the literature values and consideration of the error contributions result in fractional RMS uncertainties of the *ExploreNEOs* diameters and albedos of ±21% and ±40%, respectively (see Section 5.1 in Harris et al. 2011). In the following, I describe my contribution to Harris et al. (2011).

B.1.1.1 Method

In the second approach, I use the Monte–Carlo method (see Section 3.3) to derive the diameter and albedo uncertainties of the *ExploreNEOs* results (see Section 5.2 in Harris et al. 2011) based on the uncertainties of the model input parameters. This approach provides an assessment of the "internal" uncertainties of the results, whereas the first method provides information on the "external" uncertainties in comparison with "ground–truth" data. Internal and external uncertainties are compared in the course of the analysis.

In order to ensure compatibility, I have restricted this analysis to the same 13 objects that were used in the first analysis performed by Harris. The Monte–Carlo uncertainty analysis is performed for each of the objects using 500 randomized synthetic bodies[2] and adopting the following 1σ uncertainties: flux densities: as measured by the *ExploreNEOs* pipeline; absolute magnitude H: ±0.3 mag; slope parameter G: 0.15 ± 0.05 (values of G outside the range 0.05–0.5 are considered atypical and therefore excluded); η: from Wolters et al. (2008) (see also Section 2.2.3); IR/V reflectance ratio $RR_{\mathrm{IR/V}}$: 1.4±0.2 (see

[1] One NEO, (433) Eros, was excluded in the analysis, since the results of the default *ExploreNEOs* thermal modeling pipeline deviate significantly from the ground–truth data for reasons that are perfectly well understood (Trilling et al. 2010; Harris et al. 2011).

[2] The number of randomized objects was increased to 1000 at a later stage of the *ExploreNEOs* program to minimize statistical variations in the results of the method.

Section 3.7.1.1). The aforementioned uncertainties are mostly similar to those adopted in the default *ExploreNEOs* uncertainty analysis (see Section 2.2.3); for this analysis, realistic uncertainties in G and $RR_{\mathrm{IR/V}}$ have been added.

B.1.1.2 Results and Discussion

The RMS of the individual uncertainties of the sample objects yield 19% and 48% in diameter and albedo, respectively. The diameter uncertainties derived from both methods agree well, whereas the albedo uncertainty using the Monte–Carlo method is higher than using the ground–truth comparison (40%). The smaller albedo uncertainty of the latter method is likely to be the result of the fact that the investigators of the ground–truth results have used the same erroneous H magnitude estimates, provided by the MPC. More accurate H magnitudes are necessary to improve the *ExploreNEOs* albedo uncertainties.

I explore the relative contributions of the individual model input parameter uncertainties. This is achieved by setting the uncertainties of all but one error source at a time to zero. The resulting average uncertainties in diameter and albedo caused by the individual error sources are given in Figure B.1. The quadratic sum of the individual error terms of all objects yields 19.2% and 50.8% in diameter and albedo, respectively, which agrees well with the results of the analysis taking all error terms into account. In the course of Harris et al. (2011), we decided to adopt the conservative uncertainty estimates of 20% and 50% for the *ExploreNEOs* diameters and albedos, respectively.

As can be expected from the discussion in Section 3.6, the absolute magnitude H contributes significantly to the uncertainty in albedo, but not much to the diameter uncertainty. This analysis also shows that the uncertainties in both the diameter and the albedo are mainly driven by the beaming parameter η, which means that minor changes in η significantly impact the measured diameter and albedo. Since the default *ExploreNEOs* thermal modeling pipeline makes use of fixed–η fits (see Section 3.5), a reliable choice of the $\eta(\alpha)$ relation used in the modeling process is essential. The results of this analysis, i.e., the good agreement between the external uncertainties as derived from the comparison with ground–truth data and the internal uncertainties of the method, show that the applied $\eta(\alpha)$ relation is reasonably reliable, as is the thermal modeling pipeline itself.

B.1.1.3 Conclusions

- *ExploreNEOs* diameter and albedo results are reliable to within 20% and 50%, respectively.
- Uncertainties determined with the Monte–Carlo uncertainty analysis are comparable to uncertainties derived from a direct comparison with ground–truth data, supporting the validity of the uncertainties derived with the Monte–Carlo method (see Section 3.3) and the default *ExploreNEOs* thermal modeling pipeline.

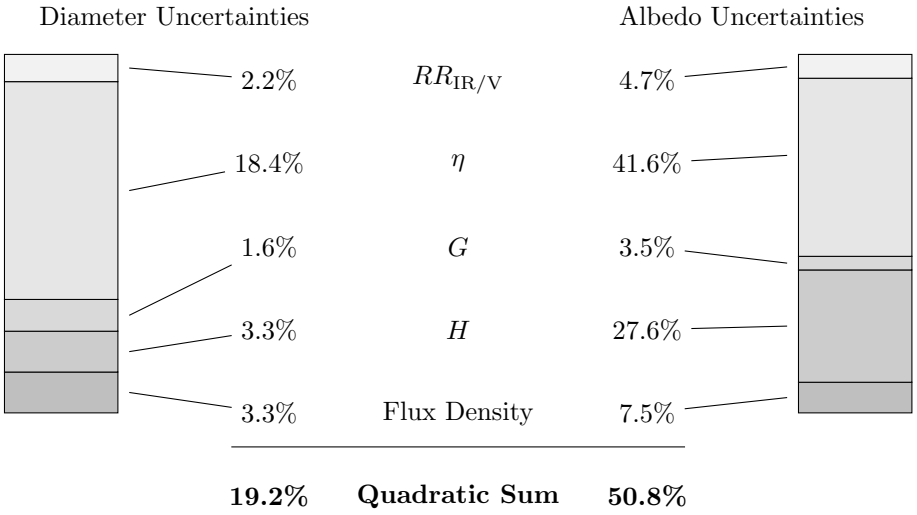

Figure B.1 The absolute uncertainty contributions to the total error budget in diameter (left) and albedo (right), based on the results of the Monte–Carlo method. The two columns represent the relative contributions of the individual uncertainties; the listed percentages are absolute uncertainties.

B.1.2 Comparison with NEOWISE Results

The overlap between the NEOWISE and *ExploreNEOs* samples provides a unique benchmark for the assessment of the accuracy of the *ExploreNEOs* diameters and albedos. In general, it is assumed that NEOWISE results are more accurate, since they are based on observations in up to four MIR bands, allowing for a better measurement of the object's spectral energy distribution. A comparison of the WISE results with data from the literature has been performed in Mainzer et al. (2011d): systematic differences in the flux density measurements were found and translate into minimum systematic errors in diameter and albedo of ∼5–10% and ∼10–20%. The systematic errors should be regarded as minimum errors in cases of good signal–to–noise detections when the beaming parameter and the infrared albedo can be fitted (Mainzer et al. 2011d). The NEOWISE results (Mainzer et al. 2011b) come with individual uncertainties in diameter, albedo, and η for each object. The method that was used to derive these uncertainties is not explicitly described.

B.1.2.1 Method

Diameters and albedos derived from the default *ExploreNEOs* thermal modeling pipeline are compared to the respective NEOWISE measurements, extracted from Table 1 in Mainzer et al. (2011b). The overlap sample includes diameters and albedos from 149 observations of 125 different objects. Some NEOWISE objects have been observed multiple times over a wide range of solar phase angle. Such observations are grouped together in

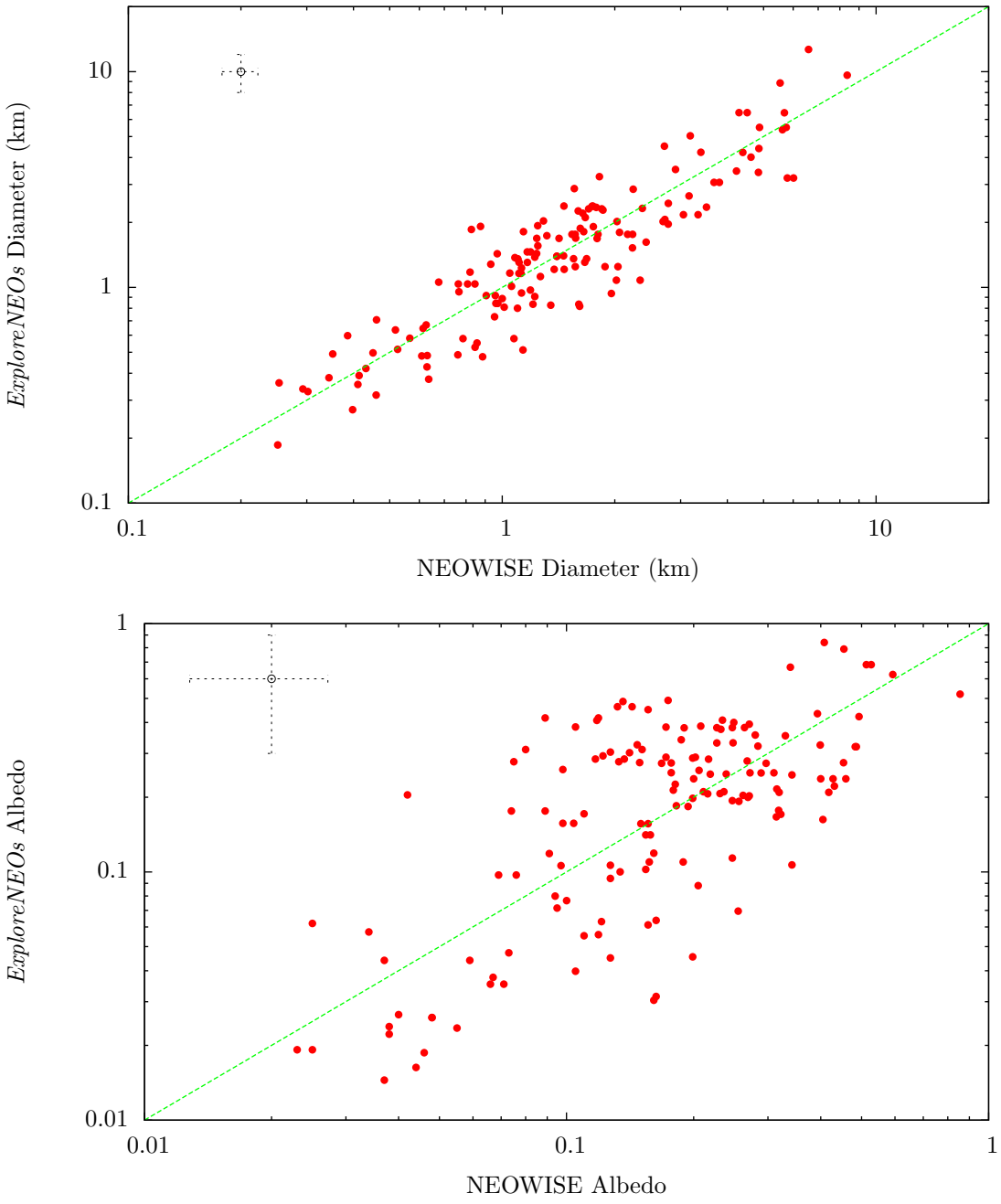

Figure B.2 Comparison of the *ExploreNEOs* and NEOWISE diameter (top) and albedo (bottom) results (Mainzer et al. 2011b). Each observation is depicted by a red point, the green dashed line represents equality, and the empty circle with dotted error bars indicates the RMS uncertainties of both samples: RMS uncertainties of NEOWISE diameters and albedos have been derived from the data in Mainzer et al. (2011b) as 11% and 36%, respectively; *ExploreNEOs* uncertainties as in Harris et al. (2011).

such a way as to have observations with similar phase angles in one group (Mainzer et al. 2011c). The individual *ExploreNEOs* multi–visit targets (see Section 2.2.3) are represented by that single observation per object that was performed at the lowest solar phase angle, minimizing model uncertainties due to large phase angles (see Section 3.7.1.2). Since the solar phase angle of the NEOWISE observations is not given in Mainzer et al. (2011b), the same method cannot be applied in the case of the NEOWISE observations. Objects with multiple NEOWISE diameter and albedo results are kept in the sample, which means that all NEOWISE observations of one object are compared to the respective *ExploreNEOs* observation.

B.1.2.2 Results

Figure B.2 shows the diameters and albedos measured by the two programs plotted against each other. The agreement in diameter seems to be good, whereas a high degree of scatter in the albedo distribution is evident. For this analysis, I define the fractional residuals in diameter and albedo of an object i as

$$\begin{aligned} \Delta_d^i &= (d_i^{\mathrm{NEOWISE}} - d_i^{\mathrm{ExploreNEOs}})/d_i^{\mathrm{ExploreNEOs}}, \text{ and} \\ \Delta_{p_V}^i &= (p_{V,i}^{\mathrm{NEOWISE}} - p_{V,i}^{\mathrm{ExploreNEOs}})/p_{V,i}^{\mathrm{ExploreNEOs}}, \end{aligned}$$

respectively. I determine the average fractional residuals in diameter and albedo over the full overlap sample with $N = 149$ as $1/N \sum_i \Delta_d^i$ and $1/N \sum_i \Delta_{p_V}^i$, respectively, yielding +7% and +22%. Both averages suggest systematic differences between the *ExploreNEOs* and NEOWISE results. However, the medians of the fractional residuals, are both below 1%, suggesting that the major fraction of diameters and albedos are not subject to systematic effects. The deviation of the average fractional residuals from zero is likely to be caused by individual objects with large values of Δ_d and/or Δ_{p_V}.

I now turn to the root–mean–square (RMS) of the fractional residuals. The *ExploreNEOs* and NEOWISE results are obtained from independent sets of flux densities, observational geometries, and H magnitudes. Hence, the mean–square fractional residuals in diameter and albedo should be consistent with the quadratic sum of the individual uncertainties, $\sigma_{\mathrm{ExploreNEOs}}$ and $\sigma_{\mathrm{NEOWISE}}$, i.e., we would expect to find

$$\sum_i \frac{\Delta_i^2}{149} = \sigma_{\mathrm{ExploreNEOs}}^2 + \sigma_{\mathrm{NEOWISE}}^2.$$

The RMS fractional residuals as derived from the overlap sample in diameter and albedo are 38% and 89%, respectively. However, from the individual uncertainties of the *ExploreNEOs* ($\sigma_d = 20\%$, $\sigma_{p_V} = 50\%$) and NEOWISE ($\sigma_d = 11\%$, $\sigma_{p_V} = 36\%$, as derived from the data in Mainzer et al. (2011b)) results, the expected statistical discrepancies of the measured diameters and albedos are 23% and 62%, respectively, which is significantly less

than the RMS fractional residuals.

B.1.2.3 Discussion

The RMS fractional residuals between the results of the two programs exceed those expected on the basis of the diameter and albedo uncertainties of the individual programs. Harris et al. (2011) (see also Section B.1.1) show that *ExploreNEOs* results are comparable to results from the literature with discrepancies that are smaller compared to the differences to the NEOWISE results. The origin of the large discrepancies is not yet clear and might be inherent to either the *ExploreNEOs* or the NEOWISE results. The most likely contributors to the discrepancy are discussed in the following:

Flux density measurements. *ExploreNEOs* and NEOWISE results are based on measurements of the thermal emission of asteroids, using different instruments and at different times. Assuming a proper calibration of both instruments, the different timing of the observations can give rise to lightcurve effects[3] that effect the flux density measurement and hence the measured diameter. Mainzer et al. (2011b) do not list their measured flux densities, precluding a detailed comparison of the measured thermal flux densities of both programs. Efforts to extract the flux densities of NEOs observed with WISE from the "WISE All–Sky Data Release" (NASA/IPAC Infrared Science Archive/WISE Observations Database) have been started and their comparison will be the subject of future work.

H magnitudes. The modeling results of the *ExploreNEOs* and NEOWISE programs are based on H magnitude estimates taken from the JPL Horizons System and the MPC, respectively, the H magnitudes of both of which are known to be of questionable reliability (e.g., Jurić et al. 2002; Pravec et al. 2012). The fractions of objects with deviations of $\Delta_H = |H_{\mathrm{ExploreNEOs}} - H_{\mathrm{NEOWISE}}| \geq [0.05, 0.1, 0.2]$ in the overlap sample are [46%, 32%, 9%]; 54% of the overlap sample targets use the same H magnitude. As discussed in Section 3.6, a difference in H of 0.1 mag can lead to changes in albedo of 10%, presumably making the different H magnitudes one of the main sources of the albedo discrepancy. In order to check this assertion, I repeat the above calculation of the average RMS fractional residuals in diameter and albedo, taking only those objects into account for which both programs use the same H magnitudes, yielding 42% and 77% (instead of 38% and 89%), respectively. As to be expected, the overall discrepancy in albedo decreases by 12%. The increase in the diameter discrepancy is marginal.

[3]The setup of the *ExploreNEOs* observations and the cadence of the NEOWISE observations are designed to minimize the impact of lightcurve effects on the measured flux densities. Nevertheless, a possible impact of such effects cannot be ruled out.

Differences in the thermal modeling approaches. Both the *ExploreNEOs* and the NEOWISE programs utilize a NEATM–based thermal model. The details of the implementation differ between the two programs. As briefly outlined in Section 2.3, the NEOWISE thermal model uses a different approach to subtract the reflected solar light contribution to the two shortest wavelength bands, taking advantage of the two longer wavelength bands that are not affected by reflected solar light. Furthermore, as part of the *ExploreNEOs* modeling, color correction is applied to the measured flux densities based on the black body spectrum with a temperature equal to the subsolar temperature of the object. NEOWISE applies its color correction to the model flux densities based on the temperature of each surface element, possibly leading to slightly different best–fit modeling results.

Most of the NEOWISE results are based on floating–η fits, whereas the default *ExploreNEOs* thermal modeling pipeline uses a fixed-η approach with a linear relation $\eta(\alpha) = (0.013 \pm 0.004)\alpha + (0.91 \pm 0.17)$ (Wolters et al. 2008). The use of the fixed–η approach is necessary due to the contamination of the 3.6 μm band measurements with reflected solar light, which compromises the quality of floating–η fits. Harris et al. (2011) show that this approach nevertheless leads to diameter and albedo results of sufficient quality, compared to data from the literature. As shown in Section B.1.1, η significantly impacts the uncertainty in both the diameter and the albedo. Hence, discrepancies between the η values derived from the linear relation and the best–fit floating η can cause large discrepancies in both the diameter and the albedo. Again, the lack of the measured flux densities in Mainzer et al. (2011b) precludes a detailed analysis of the impact of η on the discrepancies.

Based on this analysis, a revision of the default uncertainties of both the *ExploreNEOs* and the NEOWISE results might be appropriate. Assuming the NEOWISE results better describe reality, the *ExploreNEOs* uncertainties would have to be recalculated as follows: assuming the NEOWISE uncertainties ($\sigma_d = 11\%$, $\sigma_{p_V} = 36\%$) to be still valid, the determined RMS fractional residuals between the *ExploreNEOs* and NEOWISE results, 38% and 89% in diameter and albedo, respectively, lead to *ExploreNEOs* uncertainties of 36% and 81% in diameter and albedo, respectively.

For a complete investigation of the discrepancies, the NEOWISE thermal modeling results have to be scrutinized and compared to the *ExploreNEOs* results using the same thermal modeling pipeline. For such an analysis the flux densities and observational geometries of the WISE observations have to be available, which is not the case so far. Efforts to extract the flux densities of NEOWISE observations from the "WISE All–Sky Data Release" have been started and their analysis will be the subject of future work. The possible causes for the discrepancy between the *ExploreNEOs* and NEOWISE results listed above will be the focus of future analysis.

I regard the *ExploreNEOs* and NEOWISE results as equally accurate, bearing in mind the large uncertainties in both data sets, especially in the case of the albedo estimates.

B.1.2.4 Conclusions

- Small median discrepancies in the diameters and albedos measured by the *ExploreNEOs* and NEOWISE programs show that the results of the two programs can be combined to study ensemble properties of the NEO population.
- The results for individual objects differ considerably. The RMS fractional residuals between the *ExploreNEOs* and NEOWISE data sets are significant (38% for diameter, 89% for albedo). Effects contributing to the discrepancies have been discussed but further analysis requires the availability of the full NEOWISE dataset.

B.2 Exploration of the Thermal Model Uncertainties

Diameter and albedo uncertainties are derived in this work implicitly as part of the thermal modeling process: the adopted Monte–Carlo method (Mueller et al. 2011) varies the model input parameters and derives the uncertainties from the variations in the resulting diameter and albedo distributions (see Section 3.3 for more details).
In the following, I investigate the resulting diameter and albedo distributions and provide a convenient means to estimate the uncertainties in diameter and albedo. Furthermore, I show that the albedo uncertainties follow a log–normal distribution, which has consequences for the interpretation of albedo uncertainties.

B.2.1 Diameter Uncertainties

As discussed in Section 3.6, the diameter of an observed small body is mainly constrained by the measured thermal–infrared flux densities. The albedo and the absolute magnitude H have only minor influence on the diameter. Thus, a coarse estimate of the diameter uncertainty can be obtained by using $\sigma_d/d = 0.5\ \sigma_F/F$, where σ_d and σ_F are the diameter and flux density uncertainties, respectively, (see Section 3.6). This relation holds for single flux density measurements, but is more complex if multiple measurements (i) with irregular uncertainties $\sigma_{d,i}$ are involved.

Thermal models utilize a χ^2 minimization technique to find the best–fit set of free model parameters (Equation 3.6 on page 73), in which the individual flux density measurements are weighted by their individual uncertainties. Hence, that single flux density measurement with the lowest fractional uncertainty ($\min(\sigma_{F,i}/F_i)$) provides the strongest constraints on the model fit. This fact can be taken advantage of to obtain an absolute lower limit on the diameter uncertainties: assuming that all N flux density measurements have the lowest fractional uncertainty, the flux density uncertainty of the average of the N measurements is given by

$$\frac{\min(\sigma_{F,i}/F_i)}{\sqrt{N}}.$$

The reasoning leading to this result is very similar to the derivation of the standard deviation of the mean from the individual standard deviations. Out of a set of flux density measurements that individual measurement with the smallest fractional uncertainty provides the strongest constraints on the model SED. Then, the lower limit of the diameter uncertainty turns out as

$$\frac{\sigma_d}{d} \geq \frac{1}{2}\frac{\min(\sigma_{F,i}/F_i)}{\sqrt{N}}. \tag{B.1}$$

Note that this estimate does not take into account additional uncertainties caused by the beaming factor η or other model parameters. Hence, Equation B.1 can be regarded as the model–intrinsic absolute lower limit diameter uncertainty estimate.

Assuming the flux density uncertainties to be distributed normally, the diameter uncertainties mainly follow a normal distribution, as well. Experience shows that deviations of the diameter uncertainties from the normal distribution are only marginal. The situation with regard to the albedo uncertainties is more complex (see, e.g., Figure 3.6 on page 82) and discussed in the following.

B.2.2 Albedo Uncertainties

In order to investigate the properties of the albedo uncertainty distribution, I make use of the Monte–Carlo method introduced in Section 3.3, in the following referred to as the "MC method". Diameter and albedo distributions are generated from large samples of randomized synthetic model objects. From the resulting diameter and albedo distributions, the uncertainties in the parameters are derived (Section 3.3). The albedo uncertainty distribution is constrained by Equation 1.4 on page 23 ($d = 1329/\sqrt{p_V} \cdot 10^{-H/5}$), which can be rewritten as

$$p_V = \frac{1329^2}{d^2} \cdot 10^{-0.4H}. \tag{B.2}$$

Both the diameter and the H magnitude uncertainty distributions are assumed to follow a normal distribution.

I explore the shape of the albedo uncertainty distribution using a "simplified MC" method, in the course of which large sets of two independent and normally distributed random numbers are generated. The random numbers represent the diameter d and the absolute magnitude H; the distributions of the two parameters are chosen to be within realistic ranges of d and H, respectively. Applying Equation B.2 on the two sets of random numbers results in an albedo uncertainty distribution. The results derived by the simplified MC method are comparable to that of the full MC method. Figure B.3 shows the resulting albedo uncertainty distribution, which has a typical high–albedo tail and different slopes for the low and high albedo regions as observed in albedo uncertainty distributions generated by the MC method (compare to Figure 3.6 on page 82).

A comparison with different statistical distributions shows that the albedo uncertainty distribution can be well approximated by a log–normal distribution (see, e.g., Limpert et al. 2001). The log–normal albedo distribution is defined as

$$f(p_V, \bar{\mu}, \bar{\sigma}) = \frac{1}{p_V \cdot \bar{\sigma}\sqrt{2\pi}} \exp\left(-\frac{1}{2}\frac{(\log(p_V) - \bar{\mu})^2}{\bar{\sigma}^2}\right), \tag{B.3}$$

with its two log–scale parameters, the location parameter $\bar{\mu}$ and the scale parameter $\bar{\sigma}$. The median value of the log–normal distribution in linear space is $\exp(\bar{\mu})$; $\bar{\sigma}$ is a measure of the dispersion and shape of the distribution and can also be regarded as the multiplicative standard deviation (Limpert et al. 2001). The location and scale parameters can be derived as the exponentials of the geometric mean and geometric standard deviations of

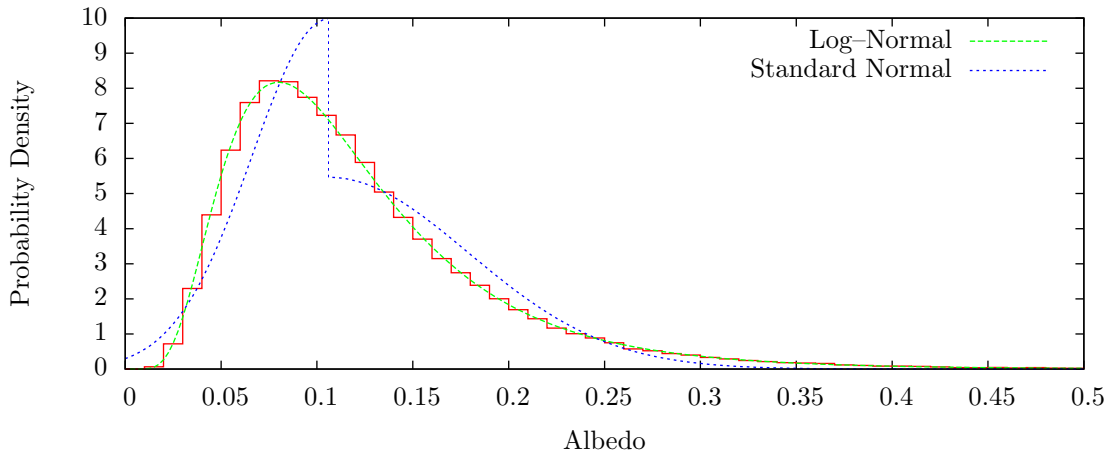

Figure B.3 Results of the simplified MC method (red steps) for the derivation of an albedo distribution, and fits of a log–normal distribution (green dashed line) and a two–sided standard normal distribution (blue dotted line). The albedo distribution is derived from Equation B.2, based on large sets ($N = 10^5$) of normally distributed diameters (4.05±1.16 km) and H magnitudes (15.0±0.5 mag). All three figures are individually normalized to have unity total area. Note that both distributions have the same median value, which is also the mean value of the standard normal distribution. The log–normal distribution clearly provides the best fit to the derived albedo distribution and hence better describes its uncertainties. The two–sided standard normal distribution shows a discontinuity that is caused by the different standard deviations of its wings.

the underlying distributions, respectively. The log–normal distribution is connected to the standard normal (Gaussian) distribution in such a way that if $f(x)$ is normally distributed, $f(\log(x))$ follows a log–normal distribution. Note that the medians of both distributions are equal; hence, the median of the log–normal distribution also equals the mean of the symmetric standard normal distribution. In contrast to the standard normal distribution[4], the $n\sigma$ confidence interval around the median albedo (p_V) of the log–normal distribution is represented in a multiplicative sense: $[p_V / \exp(n\bar{\sigma}), p_V \times \exp(n\bar{\sigma})]$. For instance, the 1σ confidence interval, covering 68.3% of the area under the log–normal distribution, ranges from $p_V / \exp(\bar{\sigma})$ to $p_V \times \exp(\bar{\sigma})$.

Figure B.3 clearly shows the log–normal distribution to fit the albedo uncertainty distribution derived from the simplified MC method much better than the asymmetric standard normal distribution. This can also be seen from Equation B.2: for a fixed diameter, the albedo uncertainty distribution follows $\sim 10^{-H}$, which follows per definition a log–normal distribution, since $10^{-\log(H)} = H^{-1}$ follows a normal distribution.

In the MC method described by Mueller et al. (2011) (also see Section 3.3), the upper and lower albedo uncertainties, σ_{pV}^{+} and σ_{pV}^{-}, respectively, are derived from the resulting

[4]In case of the standard normal distribution the $n\sigma$ confidence intervals are formulated in an additive sense: $[p_V - n\sigma, p_V + n\sigma]$, where σ is the standard deviation of the standard normal distribution. For instance, the 1σ confidence interval, covering a probability of 68.3%, ranges from $p_V - \sigma$ to $p_V + \sigma$.

albedo distribution in such a way that 68.3% of all albedos are bracketed by the range $[p_V + \sigma^+_{pV}, p_V - \sigma^-_{pV}]$ that is centered around the median of the distribution, p_V. This definition is equal to the definition of the 1σ standard deviation of the standard normal distribution. The equivalent albedo range including the same fraction of albedos in the case of the log–normal distribution is $[p_V / \exp(\bar{\sigma}), p_V \times \exp(\bar{\sigma})]$. Hence, the multiplicative standard deviation of the log–normal distribution, $\bar{\sigma}$, can be conveniently derived from the upper and lower uncertainties as obtained by the MC method as implemented by Mueller et al. (2011): $p_V + \sigma^+_{pV} = p_V \times \exp(\bar{\sigma})$, and therefore

$$\bar{\sigma} = \log\left(\frac{p_V + \sigma^+_{pV}}{p_V}\right),$$

and equivalently $\bar{\sigma} = \log(p_V/(p_V - \sigma^-_{pV}))$. The practical use of the above relation is that the log–normal shape parameter $\bar{\sigma}$ can be derived from the upper and lower albedo uncertainties as defined by Mueller et al. (2011). This method allows for the determination of the log–normal albedo uncertainty distribution for albedo measurements from the literature, as long as the uncertainties are derived using a method similar to that of Mueller et al. (2011).

So far, the method relies on the assumption that the simplified MC method based on Equation B.2 produces an albedo uncertainty distribution similar to that of the MC method used on the real measurements. I check this assumption by comparing the agreement of the MC albedo distribution derived from real data with a two–sided standard normal and a log–normal distribution, respectively. Figure B.4 shows the results of this comparison for four different objects, observed with different instruments and modeled with different techniques. $\bar{\sigma}$ was in all cases derived only from the upper albedo uncertainty, which usually provides a better means to constrain the shape of the log–normal distribution than the lower albedo uncertainty, based on the fact that in most cases $\sigma^+_{pV} - p_V > p_V - \sigma^-_{pV}$ (due to the high–albedo tail of the distribution), implying that the relative location of $p_V + \sigma^+_{pV}$ is usually known with a better precision.

The comparison in Figure B.4 shows a good agreement of the log–normal distribution with the MC albedo distribution, supporting its applicability on real data. The agreement with the slopes on each of the wings and the location of the peak are generally better for the log–normal distribution. The two–sided standard normal distributions show the typical "saw–tooth" feature, a discontinuity in the uncertainty distribution caused by the different normalization factors of each of the sides, being a result of significantly different values of σ^+_{pV} and σ^-_{pV}, which is often the case in asymmetric albedo uncertainty distributions. The discontinuity can lead to artifacts in the case of extremely small uncertainties: the resulting peak often exceeds the height of the original albedo uncertainty distribution (see Figure B.4) and is therefore considered unphysical.

Note that the results of this analysis do not undermine the legitimacy of the MC

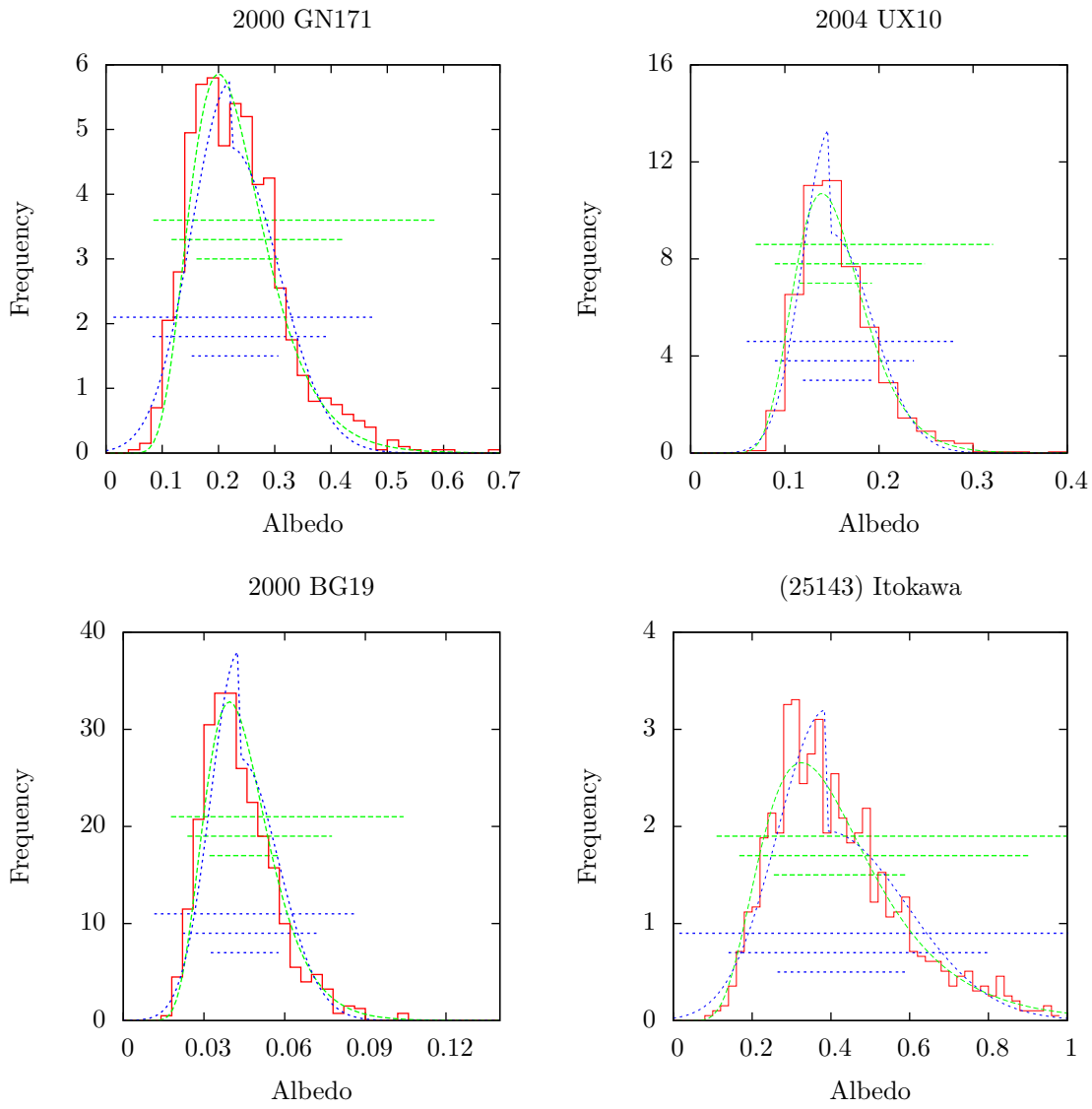

Figure B.4 Albedo uncertainty distributions obtained with the MC method for four different targets: 2000 GN171 (TNO, floating–η fit, Herschel *TNOs are Cool!* data, Mommert et al. (2012)), 2004 UX10 (TNO, fixed–η fit, Herschel *TNOs are Cool!* data, Mommert et al. (2012)), 2000 BG19 (NEO, floating–η fit, Keck data, Delbo' et al. (2003)), and Itokawa (NEO, fixed–η fit, Spitzer *ExploreNEOs* data, Mueller et al. (2011)). The red steps represent the histogram of the albedo distribution as generated from the MC method. Green and blue dashed curves represent the log–normal and standard normal distributions, respectively, based on the albedo median and the upper and lower albedo uncertainties as derived by the MC method. The green and blue dashed horizontal lines indicate the 1, 2, and 3σ confidence intervals (from bottom to top) using the log–normal and standard normal formalisms, respectively. The 1σ intervals are equal by definition; for higher orders of σ, the intervals differ.

method introduced by Mueller et al. (2011), since the 1σ confidence intervals are equal for the log–normal and standard normal distributions. However, the results of this analysis have implications for how albedo uncertainties are interpreted. The usual notation, $p_V \pm \sigma_{pV}^{\pm}$, suggests a standard normal distribution of the uncertainties, i.e., the 68.3% (1σ) confidence level covers the interval $[p_V - \sigma_{pV}^{-}, p_V + \sigma_{pV}^{+}]$, the 95.5% ($2\sigma$) confidence level covers the interval $[p_V - 2 \times \sigma_{pV}^{-}, p_V + 2 \times \sigma_{pV}^{+}]$, etc. However, since the albedo distribution rather follows a log–normal distribution, such an interpretation may be misleading. Figure B.4 shows the individual $n\sigma$ confidence intervals for the individual models using the standard normal and log–normal definitions. In the case of 1σ confidence, the intervals of the standard normal and log–normal distributions are equal by definition. However, for 2σ or larger confidences, both intervals differ significantly, and the log–normal distribution provides a better description of the real albedo uncertainty distribution. Hence, I suggest that in future work the reader is provided with the value of the log–normal scale parameter, $\bar{\sigma}$ in addition to the usual description of the 1σ confidence interval alone, $p_V \pm \sigma_{pV}^{\pm}$. The boundaries of the $n\sigma$ confidence intervals of the albedo distribution are then easily computable as

$$p_V \times \exp(\pm n \times \bar{\sigma}). \tag{B.4}$$

B.2.3 An Analytical Uncertainty Model

Using the results derived above, I construct a simplified analytical model that provides lower limit uncertainty estimates on the diameter and the albedo, given the uncertainties of the model input parameters are known. The uncertainties of the model input parameters, the flux density measurements, F_i, and the absolute magnitude, H, are $\sigma_{F,i}$ and σ_H, respectively. All model input parameter uncertainties are assumed to be distributed normally. The number of thermal–infrared flux density measurements is N.

Using the results of Section B.2.1, an absolute lower limit of the diameter uncertainty, σ_d, is given by Equation B.1. By propagating the uncertainties in the diameter and H through Equation B.2, absolute lower limits on the albedo uncertainties can be determined:

$$\begin{aligned}
\sigma_d(F_i, \sigma_{F,i}, N) &\geq \frac{1}{2} \frac{min(\sigma_{F,i}/F_i)}{\sqrt{N}} \\
\sigma_{pV}^{-}(d_i, \sigma_d, H, \sigma_H) &\geq \frac{1329^2}{(d+\sigma_d)^2} 10^{-0.4 \times (H+\sigma_H)} \\
\sigma_{pV}^{+}(d_i, \sigma_d, H, \sigma_H) &\geq \frac{1329^2}{(d-\sigma_d)^2} 10^{-0.4 \times (H-\sigma_H)}
\end{aligned} \tag{B.5}$$

For verification purposes, I have applied the uncertainty model described in Equation B.5 to the four objects for which the albedo uncertainty distributions are shown in Figure B.4. The diameter and albedo uncertainties derived with this method and the results

Table B.1. Comparison of Uncertainty Model Results.

Object	Method	Analytical Unc. Model			MC Method Results		
		σ_d/d	σ_{pV}^-/p_V	σ_{pV}^+/p_V	σ_d/d	σ_{pV}^-/p_V	σ_{pV}^+/p_V
2004 UX10	fixed–η	≥ 0.037	0.11	0.101	0.098	0.20	0.295
(25143) Itokawa	fixed–η	≥ 0.004	0.229	0.339	0.153	0.321	0.524
2000 BG19	floating–η	$\geq$0.0058	0.256	0.349	0.043	0.244	0.342
2000 GN171	floating–η	≥ 0.027	0.32	0.41	0.11	0.314	0.381

Note. — Comparison of the fractional diameter and albedo uncertainties of the analytical uncertainty model introduced in Section B.2.3 and the MC method (Mueller et al. 2011, see also Section 3.3).

of the MC method of Mueller et al. (2011) are listed in Table B.1 and discussed in the following.

As expected, the diameter uncertainties are constantly underestimated, on average by a factor of 5. The low diameter uncertainties are due to the simplification that assumes all flux density measurements have the same fractional uncertainty, which is chosen to be the lowest fractional uncertainty of all flux density measurements (σ_d/d, as defined in Equation B.5, provides an absolute lower limit on the diameter uncertainty). The estimation of the most likely diameter uncertainty is a complex task and the aim of future work. Such a method must take into account the individual fractional flux density uncertainties, their relative locations in the model SED, and the impact of the beaming parameter η. The relative locations of the flux density measurements in the model SED are important to assess their ability to constrain the SED. η directly impacts the surface temperature distribution of the model body, and hence influences both the diameter and the albedo.

The comparison of the albedo uncertainties provided by the analytical uncertainty model and the MC method shows that in the case of the fixed–η fits the analytical model underestimates the albedo uncertainties, whereas in the case of the floating–η fits the overall agreement is good, despite a slight overestimation of the albedo uncertainties. Floating–η fits use per definition the best–fit value of η, which is not necessarily the case in fixed–η fits. Hence, the impact of η, which is not yet regarded in the analytical uncertainty model, on the albedo uncertainties is smaller for floating–η fits, providing a reasonable estimate of the uncertainties. The estimation of the albedo uncertainties can be significantly improved by including η into the model, which will be the subject of future work.

The comparison shows that the analytical uncertainty model provides reasonable estimates of the lower limit uncertainties in diameter. Albedo uncertainties derived with

the model roughly agree with those derived by the MC method for floating–η fits, and are underestimated in the case of fixed–η fits. A proper accounting of η as part of the model will be the subject of future work.

Given its overall applicability, the model can also be applied in reverse, for instance to estimate the signal–to–noise ratio of thermal–infrared observations necessary to provide a lower limit precision in the diameter. The same applies for the necessary precision in the absolute magnitude for robust albedo determinations.

B.2.4 Conclusions

- The absolute lower limit diameter uncertainty (σ_d) can be analytically estimated from the fractional uncertainties of the thermal–infrared flux densities ($\sigma_{F,i}/F_i$) as

$$\frac{\sigma_d}{d} \geq \frac{1}{2}\frac{\min(\sigma_{F,i}/F_i)}{\sqrt{N}}. \tag{B.6}$$

  The distribution of the diameter uncertainties follows a standard normal distribution.

- The distribution of the albedo uncertainties is well–described by a log–normal distribution,

$$f(p_V, \bar{\mu}, \bar{\sigma}) = \frac{1}{p_V \cdot \bar{\sigma}\sqrt{2\pi}} \exp\left(-\frac{1}{2}\frac{(\log(p_V) - \bar{\mu})^2}{\bar{\sigma}^2}\right), \tag{B.7}$$

  with its location and scale parameters, $\bar{\mu} = \log(p_V)$ and $\bar{\sigma} = \log((p_V + \sigma_{pV}^{+})/p_V)$, where p_V and σ_{pV}^{+} are the median and upper 1σ uncertainty (as defined in Mueller et al. (2011) or Section 3.3) of the albedo, respectively.

- The log–normal distribution of the albedo uncertainties implies that the intuitive way of citing albedo uncertainties ($p_V \pm \sigma_{pV}^{\pm}$) is somewhat misleading. The more correct log–normal formulation describes the $n\sigma$ confidence interval of the albedo distribution as $p_V \times \exp(\pm n \times \bar{\sigma})$. The 1σ confidence interval of the log–normal and standard normal distributions are identical by definition. I propose that in future work in addition to the standard notation for the 1σ confidence interval the log–normal scale parameter, $\bar{\sigma}$, is given to enable a correct computation of the $n\sigma$ intervals.

- Combining the results of the investigation of the diameter and albedo uncertainties, I constructed a simple analytical uncertainty model that allows for an estimation of the lower limit diameter uncertainty and the albedo uncertainty as a function of the model input parameters.

B.3 The "MIPSKBOs" Project

In its cold mission phase, the MIPS instrument onboard the Spitzer Space Telescope (cf. Section 2.2) was utilized for observations of TNOs and Centaurs in its 24, 70 and 160 μm bands by different observers. In the course of the "MIPSKBOs" project, all existing Spitzer TNO and Centaur observations have been collected to reprocess them in a consistent manner, allowing for a better compatibility of the individual observations, and improving their accuracy. Results of the MIPSKBOs project are used in Sections 5.2 and 5.3 of this work.
In the following sections, the MIPSKBOs project, the MIPS instrument, and my contributions to the project are briefly described.

B.3.1 "MIPSKBOs": MIPS Observations of TNOs and Centaurs

During Spitzer's cryogenic lifetime, 105 different TNOs and Centaurs were observed by the Spitzer MIPS instrument in a total of 651 individual observations. Observations were planned and conducted by a number of different observers, and are now publicly available from the Spitzer Heritage Archive (also see Section 2.2). The "*MIPSKBOs*" project aims to reprocess these observational data in a consistent manner in support of the Herschel *TNOs are Cool!* program, using the latest reduction techniques and target positions. The *MIPSKBOs* project was initiated by John Stansberry (University of Arizona) and Michael Mueller (SRON, University of Arizona at that time), setting up an automated data processing pipeline. The work described here was performed during a four months stay at the University of Arizona, Tucson, on the invitation of Dr. Stansberry.

In the observations, all three bands of the MIPS instrument (24, 70 and 160 μm) were used in the point–source photometry mode; due to a lack in sensitivity, all 160 μm observations have failed. Most objects were visited multiple times to obtain follow–up observations, using the "moving cluster" mode (see Section B.3.2). The detailed description of the data reduction and analysis routines will be the subject of Section B.3.3.

The work on the revision of the *MIPSKBOs* data reduction and analysis pipeline has been completed. Final flux densities, or upper limit estimates, are available for all targets, and have been passed on to the *TNOs are Cool!* program. It is noteworthy that the observed flux densities of the *MIPSKBOs* project agree well with the Herschel PACS flux densities from the *TNOs are Cool!* program, despite the fact that observations are years apart. The *MIPSKBOs* flux densities have been used for preliminary thermal modeling in the course of this work, as presented in Section B.3.3. The final results of the *MIPSKBOs* project will be published in a future publication (Mueller et al. 2013) and as a database website.

B.3.2 The Multiband Imaging Photometer for Spitzer (MIPS)

The MIPS photometer instrument consists of three different detector arrays: a Si:As (Silicon Arsenic) array for imaging at 24 μm as well as unstressed and stressed Ge:Ga (Germanium Gallium) arrays for imaging at 70 and 160 μm, respectively. The 70 μm detector offers wide and narrow field of view imaging mode, the latter at higher spatial resolution. Due to problems with the cables and connectors linking the actively cooled 70 and 160 μm arrays ($\leq$10 K) to the warm electronics, the output from half of the 70 μm arrays suffers from very high noise and is unusable, and a contiguous 5–pixel block of the 160 μm arrays is dead.

The MIPS detectors simultaneously view non–overlapping patches of the sky. The telescope beam is picked up from the telescope focal plane by pick–off mirrors. The beams are separated and directed to the individual detectors using a number of mirrors, passing through bandpass filters. A detailed explanation of the MIPS instrument setup can be found in the MIPS Instrument Handbook (2011).

Both the elevated dark current and the high background noise from the "warm" mirror prevents a further use of MIPS in the warm mission phase. In the following, I introduce some of the basic characteristics of the MIPS instruments, some of which are listed in Table B.2, with a focus on imaging, which was used in the *MIPSKBOs* project for observations of TNOs (see Section B.3):

- The 24 and 160 μm detectors sample the telescope's PSF according to the Nyquist theorem (see Section A.2.1.1). The 70 μm pixels are somewhat larger than one PSF FWHM, trading off image resolution for a better detector sensitivity.

- The spectral response of the MIPS filters and detectors is shown in Figure B.5. Note that calibrated MIPS flux densities are based on a nominal spectrum that is equal to that of a 10000 K black body, which is a different approach compared to IRAC (see Sections A.2.2.2 and 2.2.2.1). Resulting color correction coefficients for typical TNO surface temperatures are listed in Table B.2. Proper color correction is crucial for 24 μm flux densities for temperatures below 50 K.

- The calibration of the MIPS 24, 70, and 160 μm bands is accurate to within 4%, 7%, 12%, respectively (see the MIPS Instrument Handbook 2011).

- Some images taken with MIPS suffer from image artifacts. In 24 μm observations, the pick–off mirror produces regular patterns of dark spots, which is well–known and usually removed by the MIPS pipeline. At 24 and 70 μm latency effects exist that are caused by bright sources or stimulator flashes. The 160 μm detector suffers from a short–wavelength stray–light leak, which affects measurements of blue sources, such as hot stars.

Table B.2. MIPS Detector Characteristics.

Parameter	24μm	70μm	160μm
Effective Wavelength (μm)	23.68	71.42	155.9
Filter Bandpass (μm)	20.8–26.1	61–80	140–174
Field of View ($'$)	5.4×5.4	5.2×2.6[(1)]	5.4×0.75
Array Size (pixel)	128×128	32×16	2×20
Projected Pixel Size ($''$)	2.49×2.60	9.85×10.06	15.96×18.04
PSF Mean FWHM ($''$)	6	18	40
Color Correction Coefficient for $T = 70$ K	0.986	0.914	0.979
$T = 50$ K	1.119	0.893	0.971
$T = 30$ K	2.031	0.901	0.954
$T = 20$ K	7.005	1.052	0.944
Point–Source Sensitivity (5σ/500 s, mJy)	0.11	6	15
Point–Source Saturation Level in 1 s (Jy)	4.1	23	3

Note. — All values were extracted from the MIPS Instrument Handbook (2011) and Rieke et al. (2004).

[1]The measures of the field of view are in-flight measures, i.e., taken into account the compromising of the detector.

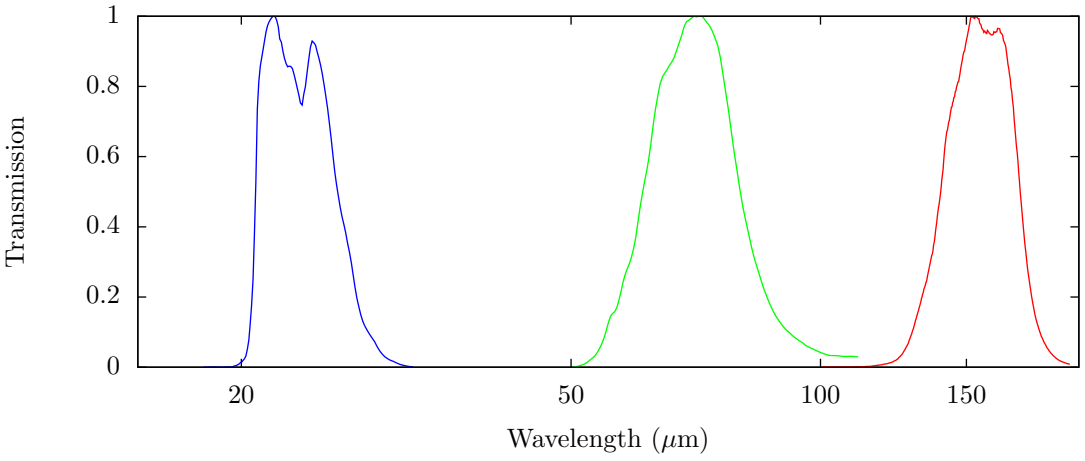

Figure B.5 Spectral response of the MIPS 24 (blue), 70 (green), and 160 μm (red) filters and detectors (MIPS Instrument Handbook 2011).

MIPS Observing Modes

MIPS provides four observation modes, which are

- a photometry mode for point–source observations, offering nominal and high–resolution imaging at 70 and 160 μm; combined with the "moving–cluster" option, the photometry mode can be used to obtain multiple images in a row using a dithering pattern,
- a scan–map mode for imaging of large–scale structures,
- a SED mode for spectroscopy in the 70 μm band, and
- a Total Power mode, which is used to obtain absolute brightness measurements for highly extended sources.

Each of the observing modes obtains multiple individual exposures ("Data Collection Event", DCE) that are combined to a single map in the image processing. DCE data correspond to Level–0 raw data. Dithering between the DCE's is done by a combination of motions of the MIPS scan mirror and spacecraft repositioning.

B.3.3 The *MIPSKBOs* Pipeline

The *MIPSKBOs* "pipeline" is a combination of software routines that includes all data reduction and analysis steps that are necessary to derive flux density measurements from the observations. The pipeline was designed by Michael Mueller and John Stansberry in such a way as to require human interaction only where absolutely necessary. In the following, I give a brief outline of the pipeline and then present my contributions to it in more detail. Due to the failing of the 160 μm observations, I focus onthe discussion of the 24 and 70 μm observations.

The *MIPSKBOs* pipeline is implemented in the Integrated Data Language (IDL), making use of existing astronomical (e.g., NASA's IDL astronomy user's library) and instrument–specific libraries. The data reduction starts from Level–0 raw data (see Section 2.2.1.3) that were retrieved from the Spitzer Heritage Archive. The raw data of each observation, comprising a number of individual DCEs, are reduced into single flux–calibrated FITS files using the MIPS Data Analysis Tool (Gordon et al. 2005). The tool corrects for image artifacts like cosmic rays (impacting high–energy particles) and detector–specific effects. The reduction of the 24 μm data is entirely automated, whereas the 70 μm band data requires manual masking of the object and other bright sources: the 70 μm detector uses a stimulator flash for proper flux calibration (Gordon et al. 2007) between the individual DCEs, causing latency effects in the detector response. The correction of the latency effects includes the subtraction of the median value of each pixel

column; in order to minimize the impact of bright objects on the median, those have to be masked manually.

In the next step, the observation mid–times are determined for each observation, which in turn are used to obtain the latest ephemeris position prediction of the object at the time of the observation from the JPL Horizons Systems; this updated position is in the following referred to as the "Horizons position". Observations of objects for which multiple observations are available are combined to improve the data quality, resulting in different image map products. If the object moved a sufficient distance between the individual observations, precluding an overlap of its positions, the sky background is determined by stacking the observations in the rest frame of the background, producing a "sky" map, showing the sky background only. In order to properly remove the target, it has to be masked in the production of the sky map using the median. Similarly, the individual observations are stacked to match their Horizons positions in the moving object frame and added, resulting in a "comove" map (see Section A.2.1.1), which has an improved SNR compared to the individual observations. Subtraction of the sky map from the individual observations prior to the production of the comove map results in a "sky–subtracted comove" map, which only shows the object with the sky background mostly removed and usually provides the best SNR of all map types.

Aperture photometry (see Section A.2.2.1) is applied on all three types of maps (individual observations, comoves, and sky–subtracted comoves), using a centroiding algorithm that refines the object's position by determining the object's photo–center (see discussion below for details). Measured flux densities and respective uncertainties for each observation, comove and sky–subtracted comove map are finally stored into a database from where they can be accessed via a website[5]

My Contributions to the *MIPSKBOs* Pipeline include, but are not limited to:

- I have *improved the masking in the production of the 70 μm FITS files* in such a way as to use masks of fixed size that are positioned on the Horizons position, instead of the often inaccurate telescope pointing position. Furthermore, I have investigated the signal–to–noise ratio (SNR) as a function of the size of the masks (see Figure B.7, left panel). The best SNR is obtained for a mask diameter of 9 pixels, which agrees with the results of Gordon et al. (2007).

- Some observations suffer from large positional uncertainties, due to insufficiently constrained orbits at the time of the observations. Latest orbit determinations from the NASA Horizons system (see above) are used to *refine the target position on the individual maps*. Furthermore, positional uncertainties and the observation geometries for each observation are obtained from NASA Horizons. The extraction

[5]As of this writing, the *MIPSKBOs* website is still unpublished and only accessible to team members. It will be made public with the publication of Mueller et al. (2013).

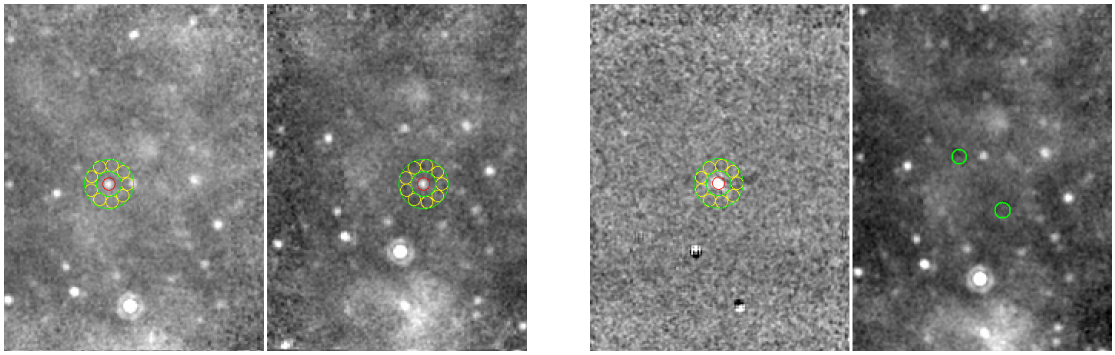

Individual Observations | Sky–Subtracted Comove / Sky Background

Figure B.6 Sky–subtracted comove map example showing TNO 2002 MS4. **Left.** The object was observed twice; each of the two maps shows the position of 2002 MS4 indicated by the photometry aperture (red circle). The green circles indicate the annulus in which the sky background is measured, and the yellow circles are additional apertures in which the sky background is measured, as well. The movement of the object in both maps that are ∼2 days apart, is obvious. **Right.** The left image shows the sky–subtracted comove map (see text), the right one shows the sky background. The sky background has been completely removed in the comove map. The two features near the bottom are image artifacts caused by the imperfect subtraction of the bright background source near the bottom of the field of view. The positions of 2002 MS4 in the sky background image are indicated by the green circles (compare to the left panel). The misty impression in the sky background map is caused by galactic cirrus (see Section 2.1.2).

is performed using a Python script that was adapted from A. Hagen (Pennsylvania State University, private communications). The residuals between the telescope pointing (i.e., the predicted) position and the position according to the refined orbits (Horizons) in most of the targets are smaller than 3″, some have residuals of 100″ and larger (see Figure B.7, right panel).

- The aperture photometry process was *improved by implementing a centroiding algorithm* that places the aperture on the photometric center of light of the object's image if the deviation from the Horizons position is smaller than the 3σ positional uncertainty[6] and the signal–to–noise ratio of the photometric measurement at the centroid position is higher than 5.

- The results of the *MIPSKBOs* pipeline are integrated into a *MySQL database with a website interface*, from which all object information, photometry results, and image data are easily accessible.

[6]In cases in which no positional uncertainty is provided, the centroid algorithm is not used and the aperture is always placed on the updated Horizons position.

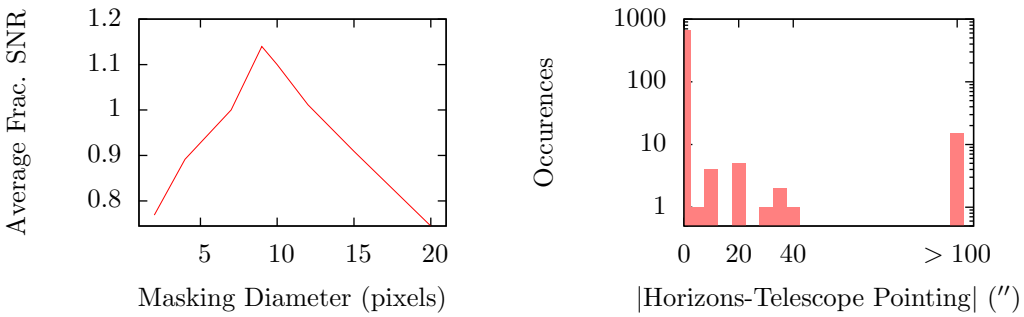

Figure B.7 **Left.** Average fractional SNR as a function of the masking diameter in the production of the flux calibrated FITS files. The analysis is based on a sample of 40 arbitrarily selected observations; fractional SNRs are relative to that obtained when using a 7 pixel diameter mask (the previously used value). The plot shows that the maximum average SNR for the sample is obtained by using a masking diameter of 9 pixels, the same value that is proposed by Gordon et al. (2007). **Right.** Positional residual between the originally predicted target position at the time of the observation (telescope pointing position) and the updated Horizons position. The majority of the targets have residuals smaller than 3″, few have larger residuals. Some of those objects with residuals >100″ have been found to be off the observed field. Large residuals are caused by large orbital uncertainties at the time of the observations.

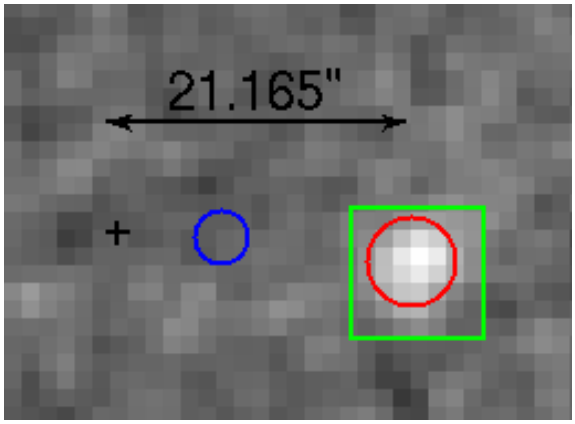

Figure B.8 The visual inspection of the two available observations of 2000 EE173, one of which is shown here, shows that the telescope pointing (black cross) and even the updated Horizons position (blue circle) both miss the target. Visual identification (green box) was necessary in this case. The red circle shows the final photometry position as derived by the centroiding algorithm.

B.3.4 Discussion and Preliminary Results

The *MIPSKBOs* project sample includes 651 individual observations from which 137 sky–subtracted comove and 8 non–sky–subtracted comove maps were produced. The non–sky–subtracted comove maps were only generated for observations where no sky subtraction was possible.

All comove maps were visually inspected in order to check the target identification. Two objects, 2000 GM137 and 2000 EE173, have been found to be off their individual Horizons position by 53″and 13″, respectively. In both cases the target could be recovered and the photometry aperture was placed manually (see Figure B.8). 2002 VR130 and (66652) Borasisi were off by 5″ and their positions were improved manually, as well. Furthermore, all individual observations that are processed into comove maps are checked for contamination by bright background sources. In the case of contaminations, the contaminated individual observations are excluded from the production of the comove map. This is discussed in all detail in Mueller et al. (2013).

The *MIPSKBOs* pipeline was also applied to MIPS observations of icy moons of Jupiter and Saturn. Results are discussed by Grav (2013).

Preliminary Thermal Modeling Results

In this work, namely in Sections 5.2 and 5.3, preliminary results from the *MIPSKBOs* project are utilized. These results were derived using thermal modeling from the final flux density estimates of the *MIPSKBOs* pipeline. H magnitudes were extracted from NASA Horizons. In the final modeling of the data, improved H magnitudes from refereed publications will be used. The NEATM (see Section 3.2.4) has been applied in the thermal modeling, using both the fixed–η and the floating–η mode; $\eta = 1.2$ (Stansberry et al. 2008) has been used in the fixed–η fits. Uncertainties on the diameters and albedos were derived using the Monte–Carlo method presented by Mueller et al. (2011) (also see Section 3.3).

The adopted results of the individual objects are selected based on the following scheme:

1. floating–η results are preferred over fixed–η results;

2. results derived from sky–subtracted comove maps are prioritized if available; if sky–subtracted comove maps are not available, the results from non–sky–subtracted comove maps and individual observations are adopted, in this order;

3. in cases in which multiple observations of the same object with the same image type are available, that observation with the highest SNR is prioritized.

The preliminary results derived here (see Tables 5.4 on page 162 and 5.6 on page 178) will be superseded by those by Mueller et al. (2013).

Appendix C

Publications

C.1 List of Publications

In the following, I list peer–reviewed publications to which I have contributed and selected conference contributions in the framework of the ExploreNEOs and TNOs are Cool! programs. Abstracts are reproduced, where available.

"ExploreNEOs"–Publications

Peer–Reviewed Publications

- *"ExploreNEOs. II. The Accuracy of the Warm Spitzer Near-Earth Object Survey"*
  Harris, A. W., **Mommert**, **M.**, Hora, J. L., Mueller, M., Trilling, D. E., Bhattacharya, B., Bottke, W. F., Chesley, S., Delbo, M., Emery, J. P., Fazio, G., Mainzer, A., Penprase, B., Smith, H. A., Spahr, T. B., Stansberry, J. A., and Thomas, C. A.
  2011, *The Astronomical Journal* **141**, 75
  We report on results of observations of near-Earth objects (NEOs) performed with the NASA Spitzer Space Telescope as part of our ongoing (2009-2011) Warm Spitzer NEO survey ("ExploreNEOs"), the primary aim of which is to provide sizes and albedos of some 700 NEOs. The emphasis of the work described here is an assessment of the overall accuracy of our survey results, which are based on a semi-empirical generalized model of asteroid thermal emission. The NASA Spitzer Space Telescope has been operated in the so-called Warm Spitzer mission phase since the cryogen was depleted in 2009 May, with the two shortest-wavelength channels, centered at 3.6 μm and 4.5 μm, of the Infrared Array Camera continuing to provide valuable data. The set of some 170 NEOs in our current Warm Spitzer results catalog contains 28 for which published taxonomic classifications are available, and 14 for which relatively reliable published diameters and albedos are available. A comparison of the Warm Spitzer results with previously published results ("ground truth"), complemented by a Monte Carlo error analysis, indicates that the rms Warm Spitzer diameter and albedo errors are $\pm$20% and $\pm$50%, respectively. Cases in which agreement with results from the literature is worse than expected are highlighted and discussed; these include the potential spacecraft target 138911 2001 AE2. We confirm that 1.4 appears to be an appropriate overall default value for the relative reflectance between the V band and the Warm Spitzer wavelengths, for use in correction of the Warm Spitzer fluxes for reflected solar radiation.
  My contribution to this work is presented in Section B.1.

- *"ExploreNEOs. III. Physical Characterization of 65 Potential Spacecraft Target Asteroids"*
  Mueller, M., Delbo', M., Hora, J. L., Trilling, D. E., Bhattacharya, B., Bottke, W. F., Chesley, S., Emery, J. P., Fazio, G., Harris, A. W., Mainzer, A., **Mommert**, **M.**, Penprase, B., Smith, H. A., Spahr, T. B., Stansberry, J. A., and Thomas, C. A.
  2011, *The Astronomical Journal* **141**, 109
  Space missions to near-Earth objects (NEOs) are being planned at all major space agencies,

and recently a manned mission to an NEO was announced as a NASA goal. Efforts to find and select suitable targets (plus backup targets) are severely hampered by our lack of knowledge of the physical properties of dynamically favorable NEOs. In particular, current mission scenarios tend to favor primitive low-albedo objects. For the vast majority of NEOs, the albedo is unknown. Here we report new constraints on the size and albedo of 65 NEOs with rendezvous $\Delta v < 7$ km s^{-1}. Our results are based on thermal-IR flux data obtained in the framework of our ongoing (2009-2011) ExploreNEOs survey using NASA's "Warm-Spitzer" space telescope. As of 2010 July 14, we have results for 293 objects in hand (including the 65 low-Δv NEOs presented here); before the end of 2011, we expect to have measured the size and albedo of $\sim$700 NEOs (including probably $\sim$160 low-Δv NEOs). While there are reasons to believe that primitive volatile-rich materials are universally low in albedo, the converse need not be true: the orbital evolution of some dark objects likely has caused them to lose their volatiles by coming too close to the Sun. For all our targets, we give the closest perihelion distance they are likely to have reached (using orbital integrations from Marchi et al. 2009) and corresponding upper limits on the past surface temperature. Low-Δv objects for which both albedo and thermal history may suggest a primitive composition include (162998) 2001 SK162, (68372) 2001 PM9, and (100085) 1992 UY4.

- *"ExploreNEOs. V. Average Albedo by Taxonomic Complex in the Near–Earth Asteroid Population"*

  Thomas, C. A., Trilling, D. E., Emery, J. P., Mueller, M., Hora, J. L., Benner, L. A. M., Bhattacharya, B., Bottke, W. F., Chesley, S., Delbó, M., Fazio, G., Harris, A. W., Mainzer, A., **Mommert**, **M.**, Morbidelli, A., Penprase, B., Smith, H. A., Spahr, T. B., and Stansberry, J. A.

  2011, *The Astronomical Journal* **142**, 85

  Examining the albedo distribution of the near-Earth object (NEO) population allows for a better understanding of the relationship between absolute (H) magnitude and size, which impacts calculations of the size frequency distribution and impact hazards. Examining NEO albedos also sheds light on the differences between the NEO and Main Belt populations. We combine albedo results from the ExploreNEOs Warm Spitzer Exploration Science program with taxonomic classifications from the literature, publicly available data sets, and new observations from our concurrent spectral survey to derive the average albedos for C-, D-, Q-, S-, V-, and X-complex NEOs. Using a sample size of 118 NEOs, we calculate average albedos of $0.29^{+0.05}_{-0.04}$, $0.26^{+0.04}_{-0.03}$, and $0.42^{+0.13}_{-0.11}$ for the Q-, S-, and V-complexes, respectively. The averages for the C- and D-complexes are $0.13^{+0.06}_{-0.05}$ and $0.02^{+0.02}_{-0.01}$, but these averages are based on a small number of objects (five and two, respectively) and will improve with additional observations. We use albedos to assign X-complex asteroids to one of the E-, M-, or P-types. Our results demonstrate that the average albedos for the C-, S-, V-, and X-complexes are higher for NEOs than the corresponding averages observed in the Main Belt.

- *"ExploreNEOs. VI. Second Data Release and Preliminary Size Distribution of Near–Earth Objects"*
  Trilling, D. E., **Mommert**, **M.**, Mueller, M., Spahr, T. B., Hora, J. L., Harris, A. W., Thomas, C. A., and Benner, L., Bhattacharya, B., Bottke, W. F., Delbo, M., Emery, J. P., Fazio, G., Mainzer, A., Penprase, B., and Smith, H. A.
  submitted to *The Astronomical Journal*

- *"ExploreNEOs. VII. Accurate H-magnitudes for 87 Near Earth Objects and New Albedos & Diameters for 72 Near Earth Objects"*
  Hagen, A. R., Trilling, D. E., Penprase, B. E., Thomas, C. A., Jones, S. L., Hickey, D., Fitzgerald, C., Kistler, J. L., Burt, B. J., Hagen, L. M. Z., Wilka, C. A., Mueller, M., Harris, A. W., **Mommert**, **M.**, Benner, L. A. M., Bhattacharya, B., Bottke, W. F., Chesley, S., Delbo, M., Emery, J. P., Fazio, G., Hora, J. L., Mainzer, A., Morbidelli, A., Smith, H. A., Spahr, T. B., and Stansberry, J. A.
  in preparation

- *"ExploreNEOs. VIII. A Search for Near–Earth Objects of Cometary Origin"*
  Mommert, **M.**, Harris, A. W., Mueller, M., Hora, J. L., Trilling, D. E., Bottke, W. F., Thomas, C. A., Delbo, M., Emery, J. P., Fazio, G., and Smith, H. A.
  submitted to *The Astronomical Journal*
  Parts of this work are presented in Section 4.2.

Selected Conference Contributions

- *"ExploreNEOs: A Search for Near-Earth Objects of Cometary Origin"*
  Mommert, **M.**, Harris, A. W., Trilling, D. E., Mueller, M., Hora, J. L., Delbo, M., Bottke, W. F., Emery, J. P., Fazio, G., Hagen, A. R., Morbidelli, A., Smith, H. A., and Thomas, C. A.
  DPS 2012, Reno NV, oral presentation
  The short dynamical lifetime of near-Earth objects (NEOs) compared to the age of the Solar System implies the existence of sources of replenishment in order to maintain the observed population of NEOs. Main belt asteroids and Jupiter family comets (JFCs), which can end up in typical NEO orbits via planetary perturbations and non-gravitational forces, are the most important sources of replenishment of NEOs. JFCs that become NEOs suffer accelerated loss of their near-surface volatiles, evolving into inactive "dormant" or "extinct" comets that are observationally indistinguishable from low albedo asteroids. Dynamically, however, they retain "comet-like" orbital characteristics. Knowledge of the fraction of extinct comets in the NEO population is important for assessing the amount of cometary material that has been transported to Earth. Furthermore, identifying inactive comet candidates facilitates detailed investigations of the final phase of comet evolution. We present an independent analysis of the fraction of former cometary objects in the NEO population. Due to the

large number of NEOs we use a statistical approach to identify dormant or extinct comets based on dynamical and physical properties. We utilize (1) the Tisserand parameter with respect to Jupiter, (2) the minimum orbit intersection distance with respect to Jupiter and (3) albedo measurements. Our albedos are determined from thermal-IR observations made by the Warm Spitzer Space Telescope Exploration Science project "ExploreNEOs", using thermal modeling. The main goal of this work is to estimate the fraction of dormant or extinct comets in the NEO population. We will further provide a list of former comet candidate objects and assess their accessibility with spacecraft via the delta-V parameter. We enhance our investigation by adding data from the literature to our sample and compare our results to earlier published works based on independent analyses. MM acknowledges support by the DFG SPP 1385.

"TNOs are Cool!"–Publications

Peer–Reviewed Publications

- *"TNOs are Cool": A survey of the trans-Neptunian region. I. Results from the Herschel science demonstration phase (SDP)*
  Müller, T. G. and Lellouch, E. and Stansberry, J. and Kiss, C. and Santos-Sanz, P. and Vilenius, E. and Protopapa, S. and Moreno, R. and Mueller, M. and Delsanti, A. and Duffard, R. and Fornasier, S. and Groussin, O. and Harris, A. W. and Henry, F. and Horner, J. and Lacerda, P. and Lim, T. and **Mommert**, **M.** and Ortiz, J. L. and Rengel, M. and Thirouin, A. and Trilling, D. and Barucci, A. and Crovisier, J. and Doressoundiram, A. and Dotto, E. and Gutiérrez, P. J. and Hainaut, O. R. and Hartogh, P. and Hestroffer, D. and Kidger, M. and Lara, L. and Swinyard, B. and Thomas, N.
  2010, *Astronomy and Astrophysics* **518**, L146
  The goal of the Herschel open time key programme "TNOs are Cool!" is to derive the physical and thermal properties for a large sample of Centaurs and trans-Neptunian objects (TNOs), including resonant, classical, detached and scattered disk objects. We present results for seven targets either observed in PACS point-source, or in mini scan-map mode. Spitzer-MIPS observations were included for three objects. The sizes of these targets range from 100 km to almost 1000 km, five have low geometric albedos below 10%, (145480) 2005 TB190 has a higher albedo above 15%. Classical thermal models driven by an intermediate beaming factor of $\eta = 1.2$ or η-values adjusted to the observed colour temperature fit the multi-band observations well in most cases. More sophisticated thermophysical models give very similar diameter and albedo values for thermal inertias in the range 0-25 J m^{-2} s$^{-0.5}$ K^{-1}, consistent with very low heat conductivities at temperatures far away from the Sun. The early experience with observing and model strategies will allow us to derive physical and thermal properties for our complete Herschel TNO sample of 140 targets as a benchmark for understanding the solar system debris disk, and extra-solar ones as well. Herschel is an ESA

space observatory with science instruments provided by European-led Principal Investigator consortia and with important participation from NASA.

- *"TNOs are cool": A survey of the trans-Neptunian region. II. The thermal lightcurve of (136108) Haumea*
  Lellouch, E. and Kiss, C. and Santos-Sanz, P. and Müller, T. G. and Fornasier, S. and Groussin, O. and Lacerda, P. and Ortiz, J. L. and Thirouin, A. and Delsanti, A. and Duffard, R. and Harris, A. W. and Henry, F. and Lim, T. and Moreno, R. and **Mommert**, **M.** and Mueller, M. and Protopapa, S. and Stansberry, J. and Trilling, D. and Vilenius, E. and Barucci, A. and Crovisier, J. and Doressoundiram, A. and Dotto, E. and Gutiérrez, P. J. and Hainaut, O. and Hartogh, P. and Hestroffer, D. and Horner, J. and Jorda, L. and Kidger, M. and Lara, L. and Rengel, M. and Swinyard, B. and Thomas, N.
  2010, *Astronomy and Astrophysics* **518**, L147
  Thermal emission from Kuiper belt object (136108) Haumea was measured with Herschel-PACS at 100 μm and 160 μm for almost a full rotation period. Observations clearly indicate a 100 μm thermal lightcurve with an amplitude of a factor of $\sim$2, which is positively correlated with the optical lightcurve. This confirms that both are primarily due to shape effects. A 160 μm lightcurve is marginally detected. Radiometric fits of the mean Herschel- and Spitzer- fluxes indicate an equivalent diameter $D \sim 1300$ km and a geometric albedo pv $\sim$0.70-0.75. These values agree with inferences from the optical lightcurve, supporting the hydrostatic equilibrium hypothesis. The large amplitude of the 100 μmlightcurve suggests that the object has a high projected a/b axis ratio ($\sim$1.3) and a low thermal inertia as well as possible variable infrared beaming. This may point to fine regolith on the surface, with a lunar-type photometric behavior. The quality of the thermal data is not sufficient to clearly detect the effects of a surface dark spot. Herschel is an ESA space observatory with science instruments provided by European-led Principal Investigator consortia and with important participation from NASA.

- *"TNOs are Cool": A survey of the trans-Neptunian region . III. Thermophysical properties of 90482 Orcus and 136472 Makemake*
  Lim, T. L. and Stansberry, J. and Müller, T. G. and Mueller, M. and Lellouch, E. and Kiss, C. and Santos-Sanz, P. and Vilenius, E. and Protopapa, S. and Moreno, R. and Delsanti, A. and Duffard, R. and Fornasier, S. and Groussin, O. and Harris, A. W. and Henry, F. and Horner, J. and Lacerda, P. and **Mommert**, **M.** and Ortiz, J. L. and Rengel, M. and Thirouin, A. and Trilling, D. and Barucci, A. and Crovisier, J. and Doressoundiram, A. and Dotto, E. and Gutiérrez Buenestado, P. J. and Hainaut, O. and Hartogh, P. and Hestroffer, D. and Kidger, M. and Lara, L. and Swinyard, B. M. and Thomas, N.
  2010, *Astronomy and Astrophysics* **518**, L148
  Context. The goal of the Herschel open time programme TNOs are Cool! is to derive the physical and thermal properties for a large sample of Centaurs, and trans-Neptunian objects

(TNOs), including resonant, classical, detached and scattered disk objects.
Aims: Based on observations of two targets we tried (i) to optimise the SPIRE observing technique for faint (close to the background confusion noise), slowly moving targets; (ii) to test different thermal model techniques; (iii) to determine radiometric diameter and albedo values; (iv) to compare with Spitzer results whenever possible.
Methods: We obtained SPIRE photometry on two targets and PACS photometry on one of the targets.
Results: We present results for the two targets, (90482) Orcus and (136472) Makemake, observed with SPIRE and for one of those targets, Makemake, observed with PACS. We adopt $p_V = 0.27$ and $D = 850$ km as our best estimate of the albedo and diameter of Orcus using single terrain models. With two-terrain models for Makemake, the bright terrain is fitted by, $0.78 < p_V < 0.90$, and the dark terrain $0.02 < p_V < 0.12$, giving $1360 < D < 1480$ km.
Conclusions: A single terrain model was derived for Orcus through the SPIRE photometry combined with MIPS data. The Makemake data from MIPS, PACS and SPIRE combined are not compatible with a single terrain model, but can be modelled with a two-terrain fit. These science demonstration observations have shown that the scanning technique, which allows us to judge the influence of background structures, has proved to be a good basis for this key programme. Herschel is an ESA space observatory with science instruments provided by European-led Principal Investigator consortia and with important participation from NASA.

- *"TNOs are Cool": A survey of the trans-Neptunian region. IV. Size/albedo characterization of 15 scattered disk and detached objects observed with Herschel-PACS*
Santos-Sanz, P. and Lellouch, E. and Fornasier, S. and Kiss, C. and Pal, A. and Müller, T. G. and Vilenius, E. and Stansberry, J. and **Mommert**, **M.** and Delsanti, A. and Mueller, M. and Peixinho, N. and Henry, F. and Ortiz, J. L. and Thirouin, A. and Protopapa, S. and Duffard, R. and Szalai, N. and Lim, T. and Ejeta, C. and Hartogh, P. and Harris, A. W. and Rengel, M.
2012, *Astronomy and Astrophysics* **541**, A92
Context. Physical characterization of trans-Neptunian objects, a primitive population of the outer solar system, may provide constraints on their formation and evolution.
Aims: The goal of this work is to characterize a set of 15 scattered disk (SDOs) and detached objects, in terms of their size, albedo, and thermal properties.
Methods: Thermal flux measurements obtained with the Herschel-PACS instrument at 70, 100 and 160 μm, and whenever applicable, with Spitzer-MIPS at 24 and 70 μm, are modeled with radiometric techniques, in order to derive the objects' individual size, albedo and when possible beaming factor. Error bars are obtained from a Monte-Carlo approach. We look for correlations between these and other physical and orbital parameters.
Results: Diameters obtained for our sample range from 100 to 2400 km, and the geomet-

ric albedos (in V band) vary from 3.8% to 84.5%. The unweighted mean V geometric albedo for the whole sample is 11.2% (excluding Eris); 6.9% for the SDOs, and 17.0% for the detached objects (excluding Eris). We obtain new bulk densities for three binary systems: Ceto/Phorcys, Typhon/Echidna and Eris/Dysnomia. Apart from correlations clearly due to observational bias, we find significant correlations between albedo and diameter (more reflective objects being bigger), and between albedo, diameter and perihelion distance (brighter and bigger objects having larger perihelia). We discuss possible explanations for these correlations. Herschel is an ESA space observatory with science instruments provided by European-led Principal Investigator consortia and with important participation from NASA. PACS: The Photodetector Array Camera and Spectrometer is one of Herschel's instruments.Appendices are available in electronic form at http://www.aanda.org

- *TNOs are cool: A survey of the trans-Neptunian region. V. Physical characterization of 18 Plutinos using Herschel-PACS observations*

  Mommert, **M.** and Harris, A. W. and Kiss, C. and Pál, A. and Santos-Sanz, P. and Stansberry, J. and Delsanti, A. and Vilenius, E. and Müller, T. G. and Peixinho, N. and Lellouch, E. and Szalai, N. and Henry, F. and Duffard, R. and Fornasier, S. and Hartogh, P. and Mueller, M. and Ortiz, J. L. and Protopapa, S. and Rengel, M. and Thirouin, A.
  2012, *Astronomy and Astrophysics* **541**, A93

  Context. The Herschel open time key programme TNOs are Cool: A survey of the trans-Neptunian region aims to derive physical and thermal properties for a set of ∼140 Centaurs and trans-Neptunian objects (TNOs), including resonant, classical, detached and scattered disk objects. One goal of the project is to determine albedo and size distributions for specific classes and the overall population of TNOs.

  Aims: We present Herschel-PACS photometry of 18 Plutinos and determine sizes and albedos for these objects using thermal modeling. We analyze our results for correlations, draw conclusions on the Plutino size distribution, and compare to earlier results.

  Methods: Flux densities are derived from PACS mini scan-maps using specialized data reduction and photometry methods. In order to improve the quality of our results, we combine our PACS data with existing Spitzer MIPS data where possible, and refine existing absolute magnitudes for the targets. The physical characterization of our sample is done using a thermal model. Uncertainties of the physical parameters are derived using customized Monte Carlo methods. The correlation analysis is performed using a bootstrap Spearman rank analysis.

  Results: We find the sizes of our Plutinos to range from 150 to 730 km and geometric albedos to vary between 0.04 and 0.28. The average albedo of the sample is 0.08±0.03, which is comparable to the mean albedo of Centaurs, Jupiter family comets and other TNOs. We were able to calibrate the Plutino size scale for the first time and find the cumulative Plutino size distribution to be best fit using a cumulative power law with q = 2 at sizes ranging from 120-400 km and q = 3 at larger sizes. We revise the bulk density of 1999

TC36 and find $\rho = 0.64^{+0.15}_{-0.11}$ g cm^{-3}. On the basis of a modified Spearman rank analysis technique our Plutino sample appears to be biased with respect to object size but unbiased with respect to albedo. Furthermore, we find biases based on geometrical aspects and color in our sample. There is qualitative evidence that icy Plutinos have higher albedos than the average of the sample. Herschel is an ESA space observatory with science instruments provided by European-led Principal Investigator consortia and with important participation from NASA. The Photodetector Array Camera and Spectrometer (PACS) is one of Herschel's instruments. PACS has been developed by a consortium of institutes led by MPE (Germany) and including UVIE (Austria); KU Leuven, CSL, IMEC (Belgium); CEA, LAM (France); MPIA (Germany); INAF-IFSI/OAA/OAP/OAT, LENS, SISSA (Italy); IAC (Spain). This development has been supported by the funding agencies BMVIT (Austria), ESA-PRODEX (Belgium), CEA/CNES (France), DLR (Germany), ASI/INAF (Italy), and CICYT/MCYT (Spain).

This work is brief presented in Section 5.1 and reproduces in its entirety in Section C.2.

- *"TNOs are Cool": A survey of the trans-Neptunian region. VI. Herschel/PACS observations and thermal modeling of 19 classical Kuiper belt objects*

  Vilenius, E. and Kiss, C. and **Mommert**, **M.** and Müller, T. and Santos-Sanz, P. and Pal, A. and Stansberry, J. and Mueller, M. and Peixinho, N. and Fornasier, S. and Lellouch, E. and Delsanti, A. and Thirouin, A. and Ortiz, J. L. and Duffard, R. and Perna, D. and Szalai, N. and Protopapa, S. and Henry, F. and Hestroffer, D. and Rengel, M. and Dotto, E. and Hartogh, P.

  2012, *Astronomy and Astrophysics* **541**, A94

  Context. Trans-Neptunian objects (TNO) represent the leftovers of the formation of the solar system. Their physical properties provide constraints to the models of formation and evolution of the various dynamical classes of objects in the outer solar system.

  Aims: Based on a sample of 19 classical TNOs we determine radiometric sizes, geometric albedos and beaming parameters. Our sample is composed of both dynamically hot and cold classicals. We study the correlations of diameter and albedo of these two subsamples with each other and with orbital parameters, spectral slopes and colors.

  Methods: We have done three-band photometric observations with Herschel/PACS and we use a consistent method for data reduction and aperture photometry of this sample to obtain monochromatic flux densities at 70.0, 100.0 and 160.0 μm. Additionally, we use Spitzer/MIPS flux densities at 23.68 and 71.42 μm when available, and we present new Spitzer flux densities of eight targets. We derive diameters and albedos with the near-Earth asteroid thermal model (NEATM). As auxiliary data we use reexamined absolute visual magnitudes from the literature and data bases, part of which have been obtained by ground based programs in support of our Herschel key program.

  Results: We have determined for the first time radiometric sizes and albedos of eight classical

TNOs, and refined previous size and albedo estimates or limits of 11 other classicals. The new size estimates of 2002 MS4 and 120347 Salacia indicate that they are among the 10 largest TNOs known. Our new results confirm the recent findings that there are very diverse albedos among the classical TNOs and that cold classicals possess a high average albedo (0.17±0.04). Diameters of classical TNOs strongly correlate with orbital inclination in our sample. We also determine the bulk densities of six binary TNOs. Herschel is an ESA space observatory with science instruments provided by European-led Principal Investigator consortia and with important participation from NASA.

- *"TNOs are Cool": A survey of the trans-Neptunian region. VII. Size and surface characteristics of (90377) Sedna and 2010 EK$_{139}$*
  Pál, A. and Kiss, C. and Müller, T. G. and Santos-Sanz, P. and Vilenius, E. and Szalai, N. and **Mommert**, **M.** and Lellouch, E. and Rengel, M. and Hartogh, P. and Protopapa, S. and Stansberry, J. and Ortiz, J.-L. and Duffard, R. and Thirouin, A. and Henry, F. and Delsanti, A.
  2012, *Astronomy and Astrophysics* **541**, L6
  We present estimates of the basic physical properties (size and albedo) of (90377) Sedna, a prominent member of the detached trans-Neptunian object population and the recently discovered scattered disk object 2010 EK139, based on the recent observations acquired with the Herschel Space Observatory, within the "TNOs are Cool!" key programme. Our modeling of the thermal measurements shows that both objects have larger albedos and smaller sizes than the previous expectations, thus their surfaces might be covered by ices in a significantly larger fraction. The derived diameter of Sedna and 2010 EK139 are 995±80 km and 470^{+35}_{-10} km, while the respective geometric albedos are $p_V = 0.32\pm0.06$ and $0.25^{+0.02}_{-0.05}$. These estimates are based on thermophysical model techniques.

- *"The extra red plutino (55638) 2002 VE95"*
  Barucci, M. A. and Merlin, F. and Perna, D. and Alvarez-Candal, A. and Müller, T. and **Mommert**, **M.** and Kiss, C. and Fornasier, S. and Santos-Sanz, P. and Dotto, E.
  2012, *Astronomy and Astrophysics* **539**, A152
  Aims: In the framework of a large program, we observed (55638) 2002 VE95 with the ESO-VLT telescope to better constrain its surface composition and to investigate the possible heterogeneity of the surface.
  Methods: We report new near-infrared observations performed in 2007 and 2008. Using the new constraints of the albedo obtained by Herschel Space Observatory observations, a surface model was computed using the complete set of spectra (from visible to the near-infrared) as well as those of the previous published data to investigate the surface composition properties of (55638) 2002 VE95.
  Results: The surface is heterogeneous. This red object is covered by different icy compounds, such as water (4-19%) and methanol (10-12%). Different organic compounds, such as titan

and triton tholins seem also to be present in the surface. The amount of the components is different depending on the observed area. That methanol ice seems to be present mainly on very red surface favors the hypothesis that surfaces of very red objects are more primordial. Based on observations made with ESO Very Large Telescope at the La Silla-Paranal Observatory under program ID 178.C-0036 (PI: A. Barucci) and the Herschel Space Observatory. Herschel is an ESA space observatory with science instruments provided by European-led Principal Investigator consortia and with important participation from NASA.

- *"TNOs are Cool: A survey of the trans–Neptunian region. VIII. Combined Herschel PACS and SPIRE observations of 9 bright targets at 70–500 μm"*
  Fornasier, S., Lellouch, E., Müller, T., Santos-Sanz, P., Panuzzo, P., Kiss, C., Lim, T., **Mommert**, **M.**, Bockelee-Morvan, D., Vilenius, E., Stansberry, J., Tozzi, G. P., Mottola, S., Duffard, R., Delsanti, A., Henry, F., Lacerda, P., Barucci, A., Crovisier, J. and Gicquel, A.
  submitted to *Astronomy and Astrophysics*

Selected Conference Contributions

- *"TNO Modelling Aspects and First Radiometric Results from the TNOs are Cool! Project"*
  Mommert, **M.** and Müller, G. and Böhnhardt, H. and Lellouch, E. and Stansberry, J. and Barucci, A. and Crovisier, J. and Delsanti, A. and Doressoundiram, A. and Dotto, E. and Duffard, R. and Fornasier, S. and Groussin, O. and Gutiérrez Buenestado, P. and Hainaut, O. and Harris, A. and Hartogh, P. and Henry, F. and Hestroffer, D. and Horner, J. and Jewitt, D. and Kidger, M. and Kiss, C. and Lacerda, P. and López, L. L. and Lim, T. and Müller, M. and Moreno, R. and Ortiz Moreno, J. L. and Protopapa, S. and Rengel, M. and Santos Sanz, P. and Swinyard, B. and Thomas, N. and Thirouin, A. and Trilling, D.
  TNO 2010, Philadelphia, oral presentation
  The 'TNOs are Cool: A Survey of the Trans-Neptunian Region' project is a Herschel Open Time Key Program awarded some 370 h of Herschel observing time. The observations include PACS and SPIRE point-source photometry on about 140 trans-Neptunian objects with known orbits. The goal is to characterize the individual objects and the full sample using radiometric techniques, in order to probe formation and evolution processes in the Solar System and to establish a benchmark for understanding the Solar System debris disk as well as extra-solar ones. In order to derive effective sizes and geometric albedos from radiometric data we use different thermal and thermophysical model approaches. The former are represented by the Standard Thermal Model (STM, Lebofsky et al. 1986), the Fast-Rotating Model (FRM, Lebofsky Spencer 1989) and the Near-Earth Asteroid Thermal Model (NEATM, Harris 1998), which is - despite its name - applicable to all types of atmosphereless bodies in the Solar System, which is fitted to the multi-band data using the beaming parameter η. The thermophysical model uses an approach by Lagerros (1996,

1997, 1998) where the temperature distribution is calculated for the given illumination and observing geometry, rotation axis and period have to be assumed if not available. The 'free' parameter is the thermal inertia, a physical property of the surface material. All modelling results are compared among each other, results and relevant issues are discussed and refereed in respect to TNO observations. We present results on a set of TNOs which were selected for the Science Demonstration and early mission phases and report on progress in deriving effective sizes, geometric albedos, thermal characteristics, and model depending issues.

- *"TNOs are Cool: A Survey of the Trans-Neptunian Region: Radiometric properties of Trans-Neptunian Objects"*
  Mommert, **M.** and Müller, G. and Böhnhardt, H. and Lellouch, E. and Stansberry, J. and Barucci, A. and Crovisier, J. and Delsanti, A. and Doressoundiram, A. and Dotto, E. and Duffard, R. and Fornasier, S. and Groussin, O. and Gutiérrez Buenestado, P. and Hainaut, O. and Harris, A. and Hartogh, P. and Henry, F. and Hestroffer, D. and Horner, J. and Jewitt, D. and Kidger, M. and Kiss, C. and Lacerda, P. and López, L. L. and Lim, T. and Müller, M. and Moreno, R. and Ortiz Moreno, J. L. and Protopapa, S. and Rengel, M. and Santos Sanz, P. and Swinyard, B. and Thomas, N. and Thirouin, A. and Trilling, D.
  Cospar 2011, Bremen, poster presentation
  The "TNOs are Cool: A Survey of the Trans-Neptunian Region" project is a Herschel Open Time Key Program awarded some 370 h of Herschel observing time. The observations include PACS and SPIRE point-source photometry on about 140 trans-Neptunian objects with known orbits. The goal is to characterize the individual objects and the full sample using radiometric techniques, in order to probe formation and evolution processes in the Solar System and to establish a benchmark for understanding the Solar System debris disk as well as extra-solar ones. We present results on a set of TNOs which were selected for the Science Demonstration and early mission phases and report on progress in deriving effective sizes, geometric albedos, and thermal characteristics. Our early sample also includes binary objects for which density estimates can be made on the basis of the derived diameters. TNO densities can provide insight into Solar-System formation scenarios.

- *"TNOs are Cool: A Survey of the Transneptunian Region - Physical Characterization of 16 Plutinos using PACS observations"*
  Mommert, **M.** and Harris, A. W. and Müller, T. G. and Stansberry, J. and Lellouch, E. and Böhnhardt, H. and Delsanti, A. and Duffard, R. and Fornasier, S. and Hartogh, P. and Henry, F. and Kiss, C. and Mueller, M. and Pal, A. and Protopapa, S. and Santos-Sanz, P. and Szalai, N. and Rengel, M. and Vilenius, E.
  EPSC/DPS 2011, Nantes, oral presentation
  We present the physical characterization of a set of 16 Plutinos, which were observed by the PACS instrument onboard Herschel. The characterization was performed using a thermal model and results in diameter and albedo estimations including uncertainties. We discuss

our results and compare them to other TNO subpopulations.

C.2 Physical Characterization of 18 Plutinos using PACS Observations

The following work has been published as Mommert et al. (2012) in the framework of the TNOs are Cool! program. Its results are briefly outlined in Section 5.1.

Credit:
Michael Mommert, A&A, 541, A93, 2012, `http://dx.doi.org/10.1051/0004-6361/201118562`, *reproduced with permission* © *ESO.*

A&A 541, A93 (2012)
DOI: 10.1051/0004-6361/201118562

Astronomy & Astrophysics

TNOs are cool: A survey of the trans-Neptunian region

V. Physical characterization of 18 Plutinos using *Herschel*-PACS observations⋆

M. Mommert[1], A. W. Harris[1], C. Kiss[2], A. Pál[2], P. Santos-Sanz[3], J. Stansberry[5], A. Delsanti[3,13], E. Vilenius[6], T. G. Müller[6], N. Peixinho[7,8], E. Lellouch[3], N. Szalai[2], F. Henry[3], R. Duffard[9], S. Fornasier[3,12], P. Hartogh[4], M. Mueller[10,11], J. L. Ortiz[9], S. Protopapa[4,14], M. Rengel[4], and A. Thirouin[9]

[1] Deutsches Zentrum für Luft- und Raumfahrt (DLR), Institut für Planetenforschung, Rutherfordstraße 2, 12489 Berlin, Germany
e-mail: michael.mommert@dlr.de
[2] Konkoly Observatory of the Hungarian Academy of Sciences, 1525 Budapest, PO Box 67, Hungary
[3] LESIA-Observatoire de Paris, CNRS, UPMC Univ Paris 06, Univ. Paris-Diderot, 5 place J. Janssen, 92195 Meudon Principal Cedex, France
[4] Max-Planck-Institut für Sonnensystemforschung (MPS), Max-Planck-Straße 2, 37191 Katlenburg-Lindau, Germany
[5] The University of Arizona, Tucson, AZ 85721, USA
[6] Max-Planck-Institut für extraterrestrische Physik (MPE), Postfach 1312, Giessenbachstr., 85741 Garching, Germany
[7] Center for Geophysics of the University of Coimbra, Av. Dr. Dias da Silva, 3000-134 Coimbra, Portugal
[8] Astronomical Observatory of the University of Coimbra, Almas de Freire, 3040-04 Coimbra, Portugal
[9] Instituto de Astrofísica de Andalucía (CSIC) C/ Bajo de Huétor, 50, 18008 Granada, Spain
[10] SRON Netherlands Institute for Space Research, Postbus 800, 9700 AV Groningen, The Netherlands
[11] UNS-CNRS-Observatoire de la Côte d'Azur, Laboratoire Cassiopée, BP 4229, 06304 Nice Cedex 04, France
[12] Univ. Paris Diderot, Sorbonne Paris Cité, 4 rue Elsa Morante, 75205 Paris, France
[13] Laboratoire d'Astrophysique de Marseille, CNRS & Université de Provence, 38 rue Frédéric Joliot-Curie, 13388 Marseille Cedex 13, France
[14] Department of Astronomy, University of Maryland, College Park, MD 20742, USA

Received 1 December 2011 / Accepted 31 January 2012

ABSTRACT

Context. The *Herschel* open time key programme *TNOs are Cool: A survey of the trans-Neptunian region* aims to derive physical and thermal properties for a set of ∼140 Centaurs and trans-Neptunian objects (TNOs), including resonant, classical, detached and scattered disk objects. One goal of the project is to determine albedo and size distributions for specific classes and the overall population of TNOs.
Aims. We present *Herschel*-PACS photometry of 18 Plutinos and determine sizes and albedos for these objects using thermal modeling. We analyze our results for correlations, draw conclusions on the Plutino size distribution, and compare to earlier results.
Methods. Flux densities are derived from PACS mini scan-maps using specialized data reduction and photometry methods. In order to improve the quality of our results, we combine our PACS data with existing *Spitzer* MIPS data where possible, and refine existing absolute magnitudes for the targets. The physical characterization of our sample is done using a thermal model. Uncertainties of the physical parameters are derived using customized Monte Carlo methods. The correlation analysis is performed using a bootstrap Spearman rank analysis.
Results. We find the sizes of our Plutinos to range from 150 to 730 km and geometric albedos to vary between 0.04 and 0.28. The average albedo of the sample is 0.08 ± 0.03, which is comparable to the mean albedo of Centaurs, Jupiter family comets and other TNOs. We were able to calibrate the Plutino size scale for the first time and find the cumulative Plutino size distribution to be best fit using a cumulative power law with $q = 2$ at sizes ranging from 120–400 km and $q = 3$ at larger sizes. We revise the bulk density of 1999 TC36 and find $\varrho = 0.64^{+0.15}_{-0.11}$ g cm^{-3}. On the basis of a modified Spearman rank analysis technique our Plutino sample appears to be biased with respect to object size but unbiased with respect to albedo. Furthermore, we find biases based on geometrical aspects and color in our sample. There is qualitative evidence that icy Plutinos have higher albedos than the average of the sample.

Key words. Kuiper belt: general – infrared: planetary systems – methods: observational – techniques: photometric

1. Introduction

Since its discovery in 1930, Pluto has been a unique object not only for being the only rocky planet-sized object not bound to a planet outside the orbit of Mars, but also for having the most eccentric and inclined orbit of all the planets, which even overlaps the orbit of Neptune. Cohen & Hubbard (1965) were the first to show that, despite that overlap, close approaches between the planets are prevented by the 2:3 mean motion resonance: Pluto's revolution period equals 3/2 of Neptune's period, ensuring that conjunctions always occur near Pluto's aphelion. This leads to a

⋆ *Herschel* is an ESA space observatory with science instruments provided by European-led Principal Investigator consortia and with important participation from NASA. The Photodetector Array Camera and Spectrometer (PACS) is one of *Herschel*'s instruments. PACS has been developed by a consortium of institutes led by MPE (Germany) and including UVIE (Austria); KU Leuven, CSL, IMEC (Belgium); CEA, LAM (France); MPIA (Germany); INAF-IFSI/OAA/OAP/OAT, LENS, SISSA (Italy); IAC (Spain). This development has been supported by the funding agencies BMVIT (Austria), ESA-PRODEX (Belgium), CEA/CNES (France), DLR (Germany), ASI/INAF (Italy), and CICYT/MCYT (Spain).

high degree of stability of the orbit. The origin of Pluto's peculiar orbit ($e = 0.25$ and $i = 17°$) was first explained by Malhotra (1993), who showed that encounters of the Jovian planets with residual planetesimals during the late stages of the formation of the solar system could lead to a radial migration of the former. As a result of Neptune's outward migration, a Pluto-like body could have been captured in the 2:3 resonance, excited to its highly inclined and eccentric orbit and transported outward.

In the meantime, the discovery of 1992 QB1 by Jewitt & Luu (1993) showed that Pluto is not the only object beyond the orbit of Neptune. The following years revealed a large population of trans-Neptunian objects (TNOs), presumably a population of residual planetesimals from the age of the formation of the solar system, as previously proposed by Edgeworth (1949) and Kuiper (1951). The population shows dynamical complexity and recurring orbital characteristics allowing the classification of TNOs in different dynamical groups (cf. Elliot et al. 2005; Gladman et al. 2008). Many of the newly discovered objects show a dynamical behaviour similar to that of Pluto, which led Jewitt & Luu (1996) to dub them *Plutinos*.

Plutinos reside in Neptune's 2:3 resonance (Gladman et al. 2008) and are the most numerous resonant population. This observation agrees with dynamical studies by Melita & Brunini (2000), which reveal that the 2:3 resonance is much more stable than other resonances, particularly at low inclinations. While the semi-major axes of Plutinos are strongly concentrated around 39.5 AU, their eccentricities and inclinations vary significantly from Pluto's ($0.03 \leq e \leq 0.88$ and $0.4° \leq i \leq 40.2°$ with a mean eccentricity and inclination of 0.21 and 12.1°, respectively)[1]. The origin of the Plutino population is ascribed to the same resonance capture mechanism which is responsible for Pluto's peculiar orbit (Malhotra 1995). Based on numerical simulations, Duncan et al. (1995) find that the 2:3 mean motion resonance interferes with secular resonances leading to a severe instability for high inclination orbits and a longterm leakage for low inclination orbits of Plutinos, making them a possible source region of Jupiter family comets (JFCs). Morbidelli (1997) found that a slow chaotic diffusion of Plutinos can be provided, which is necessary to explain the observed continuous flux of JFCs. Their results were recently confirmed by di Sisto et al. (2010), who found that Plutinos may also be a secondary source of the Centaur population. A collisional analysis of the 2:3 resonance carried out by de Elía et al. (2008) shows that the Plutino population larger than a few kilometers in diameter is not significantly altered by catastrophic collisions over the age of the solar system. They also pointed out the importance of specifying the number of Pluto-sized objects among the Plutino population, since the escape frequency of Plutinos strongly depends on this number.

Our sample of 18 Plutinos is selected based on the object classification scheme of Gladman et al. (2008) and represents ~7.5% of the known Plutino population as of 27 October, 2011 (data from MPC). 14 of our 18 sample targets have been classified in Gladman et al. (2008). For the remaining ones dynamical simulations performed by Ch. Ejeta show that their Plutino-type orbits are stable for at least 10^7 years, which suggests, but does not prove, orbital stability over the lifetime of the solar system. We give the numbers and preliminary designations of the sample objects in Table 1. In order to avoid confusion, we will refer to specific objects in this work only by their preliminary designation or name, where available. In Fig. 1 we plot our dataset in comparison to the sample of all known Plutinos in e–i phase space. We neglect a here, since it is very well confined around 39.5 AU. The plot shows the spread of both samples in e–i space, whereas the means of the two samples show a good agreement. Therefore, we assume that our sample well represents the dynamical variety of the whole Plutino population.

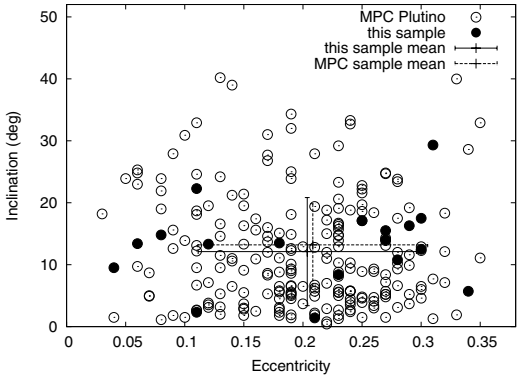

Fig. 1. Our Plutino sample (filled circles) compared to the known Plutino population (open circles, data from MPC, as of 18 Nov. 2011) in e–i phase space. The crosses with solid and dashed error bars refer to the mean and the standard deviation of our sample and the known Plutino population, respectively. This plot demonstrates that our sample is heterogenous and reflects the dynamical spread of the complete Plutino population. (The plot omits 3 known Plutinos, due to their high eccentricities, which are not part of our sample; however, these objects are included in the determination of the mean.)

Table 1. Plutino target sample.

(15875)	1996 TP66	(144897)	2004 UX10
(38628)	2000 EB173 Huya	(175113)	2004 PF115
(47171)	1999 TC36	(208996)	2003 AZ84
(47932)	2000 GN171		2001 KD77
(55638)	2002 VE95		2001 QF298
(84719)	2002 VR128		2002 VU130
(84922)	2003 VS2		2002 XV93
(120216)	2004 EW95		2003 UT292
(134340)	Pluto		2006 HJ123

Notes. We list numbers and preliminary designations or object names, where allocated. In order to avoid confusion, we will refer to specific objects in this work only by their preliminary designation or name.

Our Plutino sample is selected solely on the basis of *Herschel* observability in the sense of observation geometry and detector sensitivity. *Herschel* observations presented here are conducted over a time span of more than 7 months. In this time span, *Herschel* is able to observe at all ecliptical longitudes, despite its restrictions on the solar aspect angle, which must not be lower than 60.8° and not be larger than 119.2°. Hence, no bias is introduced based on preferred ecliptical longitudes. Since the target objects of the "TNOs are Cool" project are selected on the basis of optical discoveries, the most important bias in our sample is presumably the optical detection bias, favoring large objects and objects with high albedos. The detectional bias impact on our results will be discussed in Sect. 4.5.

Our target sample includes 3 known multiple systems, which are Pluto, 1999 TC36 and 2003 AZ84 and the expected

[1] Statistical data are based on Minor Planet Center data as of 18 Nov. 2011 (http://minorplanetcenter.net/iau/MPCORB.html).

Table 2. PACS observations summary.

Object	ObsIDs	Dur. (min)	Mid-time (UT)	r (AU)	Δ (AU)	α (°)	PACS flux densities (mJy) 70 μm	100 μm	160 μm
1996 TP66	1342202289/...2310	113.3	08-08 03:28	27.3175	27.6467	2.0	≤0.8	≤1.1	≤1.5
1999 TC36	1342199491/...9630	75.7	07-01 10:10	30.6722	30.8956	1.9	27.2 ± 1.4	22.3 ± 1.9	11.0 ± 1.6
2000 GN171	1342202906/...2971	150.9	08-12 18:19	28.2876	28.4320	2.0	3.2 ± 0.7	5.8 ± 1.1	3.2 ± 1.3
2001 KD77	1342205966/...6009	150.9	10-07 05:54	35.7854	36.1111	1.5	5.4 ± 0.6	1.0 ± 1.1	4.1 ± 1.8
2001 QF298	1342197661/...7681	113.3	06-03 06:43	43.1037	43.3727	1.3	7.2 ± 0.8	6.5 ± 1.7	5.0 ± 1.3
2002 VE95	1342202901/...2953	113.3	08-12 15:17	28.5372	28.8990	1.9	10.6 ± 0.8	8.6 ± 1.1	6.8 ± 1.6
2002 VR128	1342190929/...0990	109.3	02-22 11:57	37.4636	37.7851	1.4	15.8 ± 0.9	13.1 ± 1.2	8.8 ± 1.3
2002 VU130	1342192762/...2783	112.8	03-26 05:04	41.6877	42.1392	1.2	3.2 ± 0.8	2.4 ± 1.0	2.1 ± 1.3
2002 XV93	1342193126/...3175	112.8	03-31 22:35	39.7152	40.0645	1.4	17.3 ± 1.1	17.4 ± 1.2	10.8 ± 2.1
2003 AZ84[a]	1342187054	cf. (Müller et al. 2010)		45.376	44.889	1.1	27.0 ± 2.8	–	19.7 ± 5.2
2003 AZ84[b]	cf. Footnote *b*	484.5	09-27 13:42	45.3025	45.6666	1.2	–	25.7 ± 0.3	14.6 ± 0.8
2003 UT292	1342190949/...1025	145.6	02-22 22:33	29.4217	29.4484	1.9	6.3 ± 0.8	4.7 ± 1.4	3.6 ± 1.2
2003 VS2	1342191937/...1977	75.7	03-10 07:22	36.4694	36.7093	1.5	17.8 ± 1.1	16.5 ± 1.5	10.2 ± 3.0
2003 VS2[c]	cf. Footnote *c*	508.0	08-11 18:23	36.4760	36.8017	1.5	14.4 ± 0.3	–	14.0 ± 0.6
2004 EW95	1342199483/...9712	113.3	07-01 22:42	27.4708	27.1723	2.1	19.5 ± 0.9	18.7 ± 1.2	9.6 ± 1.8
2004 PF115	1342208462/...8841	113.3	11-11 10:53	41.4271	41.2712	1.4	10.7 ± 0.9	10.6 ± 1.0	8.8 ± 2.1
2004 UX10	1342199495/...9626	75.7	07-01 11:12	38.9500	39.3307	1.4	8.7 ± 1.1	10.9 ± 1.6	5.2 ± 1.8
2006 HJ123	1342204150/...4200	113.3	09-09 05:52	36.5383	36.9867	1.4	3.0 ± 1.2	3.5 ± 1.6	3.2 ± 2.1
Huya	1342202873/...2914	75.7	08-12 03:37	28.6648	28.7665	2.0	41.4 ± 1.6	37.6 ± 1.8	22.5 ± 2.2
Pluto/Charon	1342191953/...1988	75.7	03-10 12:46	31.7985	32.0470	1.7	283.9 ± 8.6	354.8 ± 11.2	289.2 ± 17.2

Notes. Column headings are: object name; *Herschel* ObsID of the first AOR of a sequence of four AORs of two consecutive observations (first visit/follow-on observation), respectively; total duration of all AORs in minutes; observation mid-time of all observations (MM-DD UT) in 2010; r: heliocentric distance; Δ: *Herschel*-target distance; α: solar phase angle; color-corrected flux density values at PACS photometer reference wavelengths 70, 100 and 160 μm, uncertainties include photometric and calibration uncertainties. Upper limits are 1σ. Geometric data were extracted from NASA Horizons (`http://ssd.jpl.nasa.gov/horizons.cgi`) for the indicated mid-time of the observations; [(a)] chop/nod observations (Müller et al. 2010); [(b)] averaged lightcurve observations using ObsIDs 1342205152/...5222–5225 sampling the 100 and 160 μm bands; [(c)] averaged lightcurve observations using ObsIDs 1342202371/...2574–2577 sampling the 70 and 160 μm bands.

binary 2002 GN171. We emphasize, that the spatial resolution of PACS is not sufficient to separate any multiple system. Flux densities measured for one object therefore consist of contributions from fluxes of all system components. Diameter and albedo determined with our models refer to respective parameters of an object with the area equivalent diameter of the whole system. We discuss these objects in detail in Sect. 4.2.

The "TNOs are Cool: A Survey of the trans-Neptunian region" project is a *Herschel* open time key programme awarded some 370 h of *Herschel* observing time for investigating about 140 TNOs with known orbits (Müller et al. 2009). The observations include PACS (Poglitsch et al. 2010) and SPIRE (Griffin et al. 2010) point-source photometry. The goal is to characterize the diameter and albedo for the individual objects and the full sample using radiometric techniques, in order to probe formation and evolution processes in the solar system. Using thermal modeling we determine sizes and albedos of the 18 Plutino members. The "TNOs are Cool" sample includes data of 7 more Plutinos, which have not been processed by the time of writing this.

2. Observations and data reduction

2.1. Herschel observations

Photometric measurements using the Photometer Array Camera and Spectrometer (PACS, Poglitsch et al. 2010) onboard the *Herschel* Space Observatory (Pilbratt et al. 2010) have been taken in mini scan map mode covering homogeneously a field of roughly 1′ in diameter. This mode turned out to be best suited for our needs and offers more sensitivity than other observation modes (Müller et al. 2010).

According to the "TNOs are Cool!" open time key programme observation strategy a target is observed at two epochs, separated by a time interval that corresponds to a movement of 30–50″ of the target, allowing for an optimal background subtraction, to eliminate confusion noise and background sources. At each epoch the target is observed in the "blue" (nominal wavelength of 70 μm) and "green" (100 μm) band twice, using two different scan position angles. "Red" (160 μm) band data are taken in parallel when sampling one of the other bands. This forms a series of 4 measurements in the blue and green bands, and a series of 8 measurements in the red band for a specific target. The maps are taken in the medium scan speed (20″/s) mode, using a scan-leg length of 3′ and 2–4 repetitions. In the case of 2002 VR128 a scan-leg length of 2.5′ was used. More details on the observation planning can be found in Vilenius et al. (2012).

Observational circumstances and PACS flux densities are summarized in Table 2. Additional information on the targets is given in Table 3.

2.2. Herschel-PACS data processing

The raw PACS measurements were used to produce individual scan maps (level-2) using an optimized version of the standard PACS mini scan map pipeline in HIPE (Ott 2010). The individual scan maps of the same epoch and band were mosaicked using the MosaicTask(). In the production of the final maps background-matching and source stacking techniques are applied to correct for the possible relative astrometric uncertainties between the two visits. We created two sorts of background-eliminated products from the "per-visit" mosaics: "background-subtracted" (see Stansberry et al. 2008; Santos-Sanz et al. 2012)

Table 3. Absolute magnitude H, lightcurve information, information on the presence of ices and color indices.

Object	α (°)	N	β (mag/°)	H_V (mag)	Photometry References	Δ_{mag} (mag)	Ice?	LC & Ice Ref.
1996 TP66	0.90–1.86	3	0.10 ± 0.04	7.51 ± 0.09	1, 2, 3	<0.04	no	4, 36
1999 TC36	0.28–1.71	47	0.08 ± 0.04	5.41 ± 0.10^a	1, 8–13	0.20 ± 0.04	H_2O	12, 16, 36, 41, 42, 43
2000 GN171	0.02–2.04	40	0.14 ± 0.03^c	6.45 ± 0.34^a	10, 13, 14	0.61 ± 0.03	no	17, 36, 39, 40, 42
2001 KD77	1.54–1.56	6	0.10 ± 0.04	6.42 ± 0.08	20, 21	<0.07		22
2001 QF298	0.68–1.02	3	0.10 ± 0.04	5.43 ± 0.07	21, 24, 25	<0.12		22
2002 VE95	0.57–2.07	40	0.16 ± 0.04	5.70 ± 0.06	13, 26	0.08 ± 0.04	H_2O	26, 27, 36
2002 VR128	0.31–0.58	6	0.10 ± 0.04	5.58 ± 0.37	MPC	–		–
2002 VU130	1.28–1.37	3	0.10 ± 0.04	5.47 ± 0.83	MPC	–		–
2002 XV93	1.11	3	0.10 ± 0.04	5.42 ± 0.46	MPC	–		–
2003 AZ84	0.33–1.17	4	0.15 ± 0.05	3.74 ± 0.08^a	14, 24, 28, 29	0.14 ± 0.03	H_2O	27, 36, 42, 48
2003 UT292	0.35–1.75	13	0.10 ± 0.04	6.85 ± 0.68^b	MPC	–		–
2003 VS2	0.53–0.59	7	0.10 ± 0.04	4.11 ± 0.38	MPC	0.21 ± 0.01	H_2O	30, 36, 44
2004 EW95	0.45–0.80	20	0.10 ± 0.04	6.69 ± 0.35	MPC	–		–
2004 PF115	0.31–0.93	13	0.10 ± 0.04	4.54 ± 0.25^b	MPC	–		–
2004 UX10	0.75–1.06	4	0.10 ± 0.04	4.75 ± 0.16	28, 30	0.08 ± 0.01	(H_2O)	30, 48
2006 HJ123	0.22–1.49	5	0.10 ± 0.04	5.32 ± 0.66^b	MPC	–		–
Huya	0.49–1.80	13	0.09 ± 0.04	5.14 ± 0.07	8, 10, 32	<0.1	(H_2O)	16, 36, 37, 38, 39, 40
Pluto/Charon	0.18–1.87	277	0.037 ± 0.002^d	-0.67 ± 0.34	MPC	0.33	CH_4, CO, N_2	33, 45, 46, 47
Object	$B-V$	$V-R$	$B-R$	$R-I$	$V-I$	$B-I$	s	Ref.
1996 TP66	1.03 ± 0.11	0.66 ± 0.07	1.68 ± 0.12	0.66 ± 0.10	1.29 ± 0.11	2.25 ± 0.15	30.4 ± 4.7	1, 3, 5, 6, 7, 21
1999 TC36	1.00 ± 0.13	0.70 ± 0.03	1.74 ± 0.05	0.62 ± 0.05	1.30 ± 0.13	2.35 ± 0.14	32.1 ± 2.3	1, 8, 9, 11–13, 15
2000 GN171	0.96 ± 0.06	0.60 ± 0.04	1.56 ± 0.07	0.62 ± 0.05	1.14 ± 0.17	2.16 ± 0.09	23.9 ± 2.9	13, 14, 18, 19
2001 KD77	1.12 ± 0.05	0.62 ± 0.07	1.76 ± 0.06	0.57 ± 0.07	1.20 ± 0.07	2.31 ± 0.09	23.5 ± 4.1	20, 21, 23
2001 QF298	0.67 ± 0.07	0.39 ± 0.06	1.05 ± 0.09	0.57 ± 0.19	0.89 ± 0.19	1.35 ± 0.09	4.6 ± 4.6	19, 21, 24, 25
2002 VE95	1.07 ± 0.14	0.72 ± 0.05	1.79 ± 0.04	0.76 ± 0.12	1.38 ± 0.15	2.47 ± 0.13	37.8 ± 3.7	13, 19, 28
2002 VR128	0.94 ± 0.03	0.60 ± 0.02	1.54 ± 0.04	–	–	–	22.76 ± 2.1	19
2002 XV93	0.72 ± 0.02	0.37 ± 0.02	1.09 ± 0.03	–	–	–	0.9 ± 2.1	19
2003 AZ84	0.67 ± 0.05	0.38 ± 0.04	1.05 ± 0.06	0.55 ± 0.15	0.92 ± 0.14	1.68 ± 0.19	3.6 ± 3.5	19, 24, 28, 29, 34
2003 VS2	0.93 ± 0.02	0.59 ± 0.02	1.52 ± 0.03	–	–	–	21.7 ± 2.1	19
2004 EW95	0.70 ± 0.02	0.38 ± 0.02	1.08 ± 0.03	–	–	–	1.7 ± 2.1	19
2004 UX10	0.95 ± 0.02	0.58 ± 0.05	1.53 ± 0.02	–	–	–	20.2 ± 4.4	28, 31
Huya	0.95 ± 0.05	0.57 ± 0.09	1.54 ± 0.06	0.61 ± 0.05	1.19 ± 0.06	2.14 ± 0.07	21.9 ± 4.6	7, 8, 10, 18, 32
Sample av.	0.84 ± 0.13	0.51 ± 0.12	1.43 ± 0.25	0.62 ± 0.05	1.19 ± 0.11	2.07 ± 0.35	17 ± 12	
Sun	0.64	0.36	–	–	0.69	–	–	35

Notes. The top part of the table shows: object name; α: phase angle range of observations utilized in the determination of H; N: number of available observations; β: linear phase coefficient; H_V: absolute magnitude in the V band with respective uncertainty; photometry references; Δ_{mag}: optical lightcurve amplitude (peak-to-peak); Ice?: information on the presence of ices, if available (discoveries in parentheses are tentative); LC & Ice Ref.: lightcurve and ice references. The lower part of the table shows different color indices for our sample objects, where available, including uncertainties, and the spectral slope s in percent of reddening per 100 nm as determined from the given color information following Hainaut & Delsanti (2002), and references. The weighted sample mean (cf. Table 3) of each color index is given for comparison, as well as some color indices of the Sun. We determine the weighted mean $\langle x \rangle$ of quantities x_i using the absolute uncertainties σ_i as weighting parameter. The uncertainty of $\langle x \rangle$, σ, is calculated as $\sigma^2 = (1 + \sum_i [(x_i - \langle x \rangle)^2 / \sigma_i^2]) / \sum_i (1/\sigma_i^2)$. Defined this way, σ is a combination of the weighted root mean square and the weighted standard deviation of the uncertainties. [(a)] Original photometric uncertainty is smaller than the half peak-to-peak lightcurve amplitude: new value is $(\sigma_H^2 + (0.5\Delta_{mag})^2)^{1/2}$; [(b)] converted R band data; [(c)] regression analysis leads to an unrealistic phase coefficient, adopt instead phase coefficient from Belskaya et al. (2008); [(d)] phase coefficient adopted from Buie et al. (1997).

References. MPC: photometric data were provided by the Minor Planet Center observations database (http://minorplanetcenter.net/iau/ECS/MPCOBS/MPCOBS.html); (1): Boehnhardt et al. (2001); (2): Davies et al. (2000); (3): Jewitt & Luu (1998); (4): Collander-Brown et al. (1999); (5): Tegler & Romanishin (1998); (6): Barucci et al. (1999); (7): Jewitt & Luu (2001); (8): Doressoundiram et al. (2001); (9): Delsanti et al. (2001); (10): McBride et al. (2003); (11): Tegler et al. (2003); (12): Dotto et al. (2003); (13): Rabinowitz et al. (2007); (14): DeMeo et al. (2009); (15): Benecchi et al. (2009); (16): Ortiz et al. (2003); (17): Sheppard & Jewitt (2002); (18): Boehnhardt et al. (2001); (19): Tegler (priv. comm.); (20): Doressoundiram et al. (2002); (21): Doressoundiram et al. (2007); (22): Sheppard & Jewitt (2003); (23): Peixinho et al. (2004); (24): Fornasier et al. (2004); (25): Doressoundiram et al. (2005); (26): Barucci et al. (2006); (27): Ortiz et al. (2006); (28): Perna et al. (2010); (29): Santos-Sanz et al. (2009); (30): Thirouin et al. (2010); (31): Romanishin et al. (2010); (32): Ferrin et al. (2001); (33): Buie et al. (1997); (34): Rabinowitz et al. (2008); (35): Doressoundiram et al. (2008); (36): Barkume et al. (2008); (37): Licandro et al. (2001); (38): Brown (2000); (39): de Bergh et al. (2004); (40): Alvarez-Candal et al. (2007); (41): Merlin et al. (2005); (42): Guilbert et al. (2009); (43): Protopapa et al. (2009); (44): Barucci et al. (2012); (45): Owen et al. (1993); (46): DeMeo et al. (2010); (47): Merlin et al. (2010); (48): Barucci et al. (2011).

and "double-differential" maps[2]. The latter are generated by subtracting the maps of the two visits, yielding a positive and a negative beam of the object on the differential map with all background structures eliminated. A duplicate of this map is then shifted in such a way as to match the positive beam of the original map with the negative one of the duplicate map. In the last step the original and shifted mosaics are subtracted again and av-

[2] Background-subtracted mosaics were used in the cases of 1996 TP66, 2001 KD77, 2002 VE95, 2002 XV93, 2003 AZ84, 2003 VS2, 2004 PF115 and Pluto/Charon; double-differential mosaics for the other targets.

eraged, resulting in a double-differential mosaic with a positive beam showing the full target flux, and two negative beams on either side showing half the target flux. The final photometry is performed on the central, positive beam. The advantage of this technique is the nearly complete elimination of the sky background that makes it favorable for faint targets. Full details can be found in Kiss et al. (in prep.).

Photometry is performed on the final background-subtracted and/or double-differential maps, which are both background-eliminated. Flux densities are derived via aperture photometry using either IRAF/Daophot or IDL/Astrolib routines, both producing identical results. We extract the flux at the photocenter position of the target and apply an aperture correction technique (Howell 1989) for each aperture radius based on the encircled energy fraction for the PACS point spread function (Müller et al. 2011a). We construct an aperture-corrected curve of growth from which we derive the optimum synthetic aperture, which usually lies in the "plateau" region of the curve of growth.

Photometric uncertainties are estimated by random implantation of 200 artificial sources in the nearby sky background of the target. The 1σ photometric uncertainty of the target flux is derived as the standard deviation of these artificial source fluxes (Santos-Sanz et al. 2012). This 1σ limit is also given as an upper limit in the case of non-detections.

The absolute calibration of our data is based on mini scan maps of 5 fiducial stars and 18 large main belt asteroids (Müller et al. 2011a). The absolute calibration uncertainties of the PACS bands are 3% for the 70 and 100 μm bands and 5% for the 160 μm band, respectively. This additional uncertainty adds quadratically to the photometric error and is included in the flux densities given in Table 2. The absolute accuracy of the photometry was checked against the predicted standard star flux densities. In the bright regime (above 30 mJy) the relative accuracy was found to be ~5%, while in the faint regime (below 30 mJy) the accuracy is driven by the uncertainties in the maps and is about or below 2 mJy in all bands, on the individual maps.

A general description of the PACS data reduction steps (including photometry) will be given in Kiss et al. (in prep.).

The flux densities given in Table 2 have been color corrected and therefore are monochromatic. The measured flux density is determined by the response function of the PACS band filters convolved with the spectral energy distribution (SED) of the source (Müller et al. 2011b). The SED of TNOs resembles a black body spectrum of a certain temperature; the resulting color-correction factors depend weakly on the emission temperature. The black body temperature is approximated by the mean surface temperature, which is given by $2^{-0.25}T_{\rm SS}$, where $T_{\rm SS}$ is the subsolar temperature, defined in Eq. (3). We determine the color correction factors based on the mean surface temperature in an iterative process during the modeling. The mean color correction factors for all objects in this sample are 0.9810 ± 0.0003, 0.988 ± 0.003 and 1.015 ± 0.005 for the 70, 100 and 160 μm band, respectively: the size of the color corrections are smaller than the uncertainty of the individual flux density measurements (cf. Table 2), which justifies the use of the mean surface temperature as an approximation of the best fit black body temperature.

We have obtained time-resolved lightcurve observations of 2003 AZ84 and 2003 VS2, covering 110% and 106% of the respective lightcurve using 99 and 100 observations, respectively. A detailed analysis of both lightcurves will be subject of an upcoming publication (Santos-Sanz et al., in prep.). In this work, we make use of the averaged fluxes, which are more precise than single measurements, due to the larger number of observations and the cancelling of lightcurve effects.

2.3. Spitzer MIPS observations

Whenever possible, the *Herschel* flux densities were combined with existing flux density measurements of the Multiband Imaging Photometer for *Spitzer* (MIPS, Rieke et al. 2004) onboard the *Spitzer* Space Telescope (Werner et al. 2004) to improve the results. Useful data were obtained in the MIPS 24 and 70 μm bands, which have effective wavelengths of 23.68 and 71.42 μm. The MIPS 70 μm band overlaps with the *Herschel* 70 μm channel, providing a consistency check between data from the two observatories. A comparison of the PACS and MIPS 70 μm band flux densities shows that most measurements are consistent within a 1σ range. Significant deviations occur for 2003 AZ84 and Huya, which might have been caused by lightcurve effects or statistical noise.

The reduction of MIPS observations of TNOs has been described in detail in Stansberry et al. (2008) and Brucker et al. (2009), details on the calibration can be found in Gordon et al. (2007) and Engelbracht et al. (2007). We adopt absolute calibration uncertainties of 3% and 6% for the 24 and 70 μm observations (50% larger than the uncertainties derived for observations of stellar calibrators), respectively. The larger uncertainties account for effects from the sky-subtraction technique, the faintness of the targets, and uncertainties in the color corrections.

The sky subtraction techniques introduced in Sect. 2.2 are derived from techniques originally developed for the MIPS data reductions. Reprocessed fluxes presented here are based on new reductions of the MIPS data, utilizing updated ephemeris positions for the targets. This allows for more precise masking of the target when generating the image of the sky background, and for more precise placement of the photometric aperture. In most cases the new fluxes are very similar to the previously published values for any given target, but in a few cases significant improvements in the measured flux density and SNR were achieved.

The standard color correction routine (Stansberry et al. 2007) resulting in monochromatic flux densities for the 24 and 70 μm bands requires the measurement of both bands and assumes the temperature of a black body which fits the 24:70 flux density ratio best. However, the two previously unpublished flux densities of 2002 VE95 and 2002 XV93 are for the 24 μm band only, which precludes the application of the standard method. In order to provide approximate color correction to these flux densities, we apply a method similar to the *Herschel*-PACS color correction routine.

2.4. Optical Photometry

In order to derive diameter and albedo estimates, we combine thermal infrared measurements with optical data in the form of the absolute magnitude H, which is the object's magnitude if it was observed at 1 AU heliocentric distance and 1 AU distance from the observer at a phase angle $\alpha = 0$. H, albedo p_V and diameter d are related via

$$d = 2\delta \times 10^{V_\odot/5} \times 10^{-H/5} / \sqrt{p_V}, \quad (1)$$

with the magnitude of the Sun $V_\odot = -26.76 \pm 0.02$ (Bessell et al. 1998) in the Johnson-Cousins-Glass system and δ a numerical constant. The relation returns d in km, if δ equals 1 AU expressed in km. In order to derive reliable albedo estimates, H and its uncertainty have to be well known (Harris & Harris 1997). This is not the case for most small bodies in the solar system, including Plutinos, for which reliable data are usually sparse. We determine H magnitudes from observed magnitudes

Table 4. *Spitzer* observations summary.

Object	AORKEY	Dur. (min)	Mid-time (UT)	r (AU)	Δ (AU)	α (°)	MIPS flux densities (mJy) 24 μm	70 μm	Ref.
1996 TP66	8805632	38.4	04-01-23 03:31	26.4913	26.2500	2.1	0.689 ± 0.038	<5.87	1
	12659456	40.8	05-09-24 15:54	26.6292	26.1132	1.9	0.426 ± 0.029	<2.30	1
1999 TC36	9039104	62.4	04-07-12 11:04	31.0977	30.9436	1.9	1.233 ± 0.022	25.30 ± 2.53	1
2000 GN171	9027840	25.1	04-06-21 00:01	28.5040	28.0070	1.8	0.258 ± 0.031	5.60 ± 4.00	2
2002 VE95	17766912/...7168	18.0	07-09-18 21:28	28.2291	28.2962	2.1	0.476 ± 0.044	–	3
2002 XV93	17768704/...8960	227.4	07-10-28 04:30	40.0092	39.6962	1.4	0.321 ± 0.018	–	3
2003 AZ84	10679040	28.9	06-03-30 09:22	45.6674	45.218	1.1	0.291 ± 0.023	17.8 ± 2.66	1
2003 VS2	10680064	11.7	05-08-27 10:08	36.4298	36.5344	1.6	0.304 ± 0.051	25.7 ± 7.34	1
Huya	8808192	21.3	04-01-27 09:40	29.3261	29.2503	1.9	3.630 ± 0.052	57.2 ± 5.25	1
	8937216	43.1	04-01-29 17:55	29.3252	29.2100	1.9	3.400 ± 0.050	52.9 ± 1.86	1

Notes. Column headings are: object name; *Spitzer* AORKEY identification; total duration of all AORs; observation mid-time of the 24 and 70 μm measurements (20YY-MM-DD UT); r: heliocentric distance; Δ: *Spitzer*-target distance; α: solar phase angle; color-corrected flux density values at MIPS photometer reference wavelengths 23.68 and 71.42 μm, upper limits are 1σ; references. Geometric data were extracted from NASA Horizons (`http://ssd.jpl.nasa.gov/horizons.cgi`) for the indicated mid-time of the observations.

References. (1) Stansberry et al. (2008), uncertainties derived as flux density/SNR; (2) revised 70 μm data from Stansberry et al. (2008); (3) previously unpublished data.

in literature and observational data from the Minor Planet Center (MPC) (cf. Table 3). We deliberately do not use the H magnitudes provided by the MPC, since there is no uncertainty estimate given for these values and the reliability of these magnitudes is questionable (for instance, Romanishin & Tegler 2005, have determined a systematic uncertainty of MPC H magnitudes of 0.3 mag). Our results include uncertainty assessments and are reasonably close other estimates (for instance Doressoundiram et al. 2007).

H and the geometric albedo are defined at zero phase angle (α). However, existing photometric data were taken at $\alpha \neq 0$, which is corrected for by assuming a linear approximation of the phase angle dependence: $H_V = m_V(1,1) - \alpha \cdot \beta$, in which $m_V(1,1)$ is the apparent V band magnitude normalized to unity heliocentric and geocentric distance, and β is the linear phase coefficient. Since we want to derive the geometric albedo p_V, we use V band photometry when available, otherwise we use R band photometry and convert to V band magnitudes using an averaged $\langle V-R\rangle = 0.567 \pm 0.118$ color index[3], and a correction for the intrinsic solar color index of $(V-R)_\odot = 0.36$ (Doressoundiram et al. 2008). $\langle V-R\rangle$ is based on observations of 41 Plutinos and is adopted from Hainaut & Delsanti (2002, data as of July 13, 2010).

If available, we give priority to data drawn from refereed publications, due to the existence of photometric uncertainties and the better calibration. All available apparent magnitudes for a target are converted to $m_V(1,1)$ magnitudes and plotted as a function of the phase angle. For targets where the data show a clear trend of $m_V(1,1)$ vs. α, we use a weighted linear regression analysis to fit a line to the data, yielding the linear phase coefficient. In the case of high scatter, a canonical $\beta = 0.10 \pm 0.04$ mag/° is assumed, based on data given by Belskaya et al. (2008) (V and R band data, excluding Pluto). H then represents the average of the values determined from each $m_V(1,1)$. MPC photometric data are usually highly scattered due to the coarse photometry, so the fixed-β technique is always applied if only MPC data are available. The results of all computations are given in Table 3, which also gives lightcurve amplitude information and color indices, as far as available. Due to the usage of a two-visit observation strategy, the determined *Herschel* flux densities are a combination of flux densities taken at two different points in time. Hence, it is not trivial to correct both *Herschel* measurements for lightcurve effects. However, lightcurve effects are already included in the uncertainty of the absolute magnitude H, assuming that the optical measurements are randomly sampled with respect to the individual lightcurve. In cases where the uncertainty of H is smaller than half the peak-to-peak lightcurve amplitude, we account for lightcurve effects by a quadratic addition of the latter value to the uncertainty of H. This was only necessary in three cases (cf. Table 3).

[3] The applied Plutino $V-R$ color agrees within 1σ with our sample mean of 0.51 ± 0.12 (cf. Table 3).

3. Thermal modeling

By combining thermal-infrared and optical data, the physical properties of an object can be estimated using a thermal model. The disk-integrated thermal emission at wavelength λ of a spherical model asteroid is calculated from the surface temperature distribution $T(\theta,\varphi)$ as

$$F(\lambda) = \epsilon d^2/\Delta^2 \iint B(\lambda, T(\theta,\varphi)) \cos^2\theta \, \cos(\varphi-\alpha)\, \mathrm{d}\varphi\, \mathrm{d}\theta, \qquad (2)$$

where ϵ is the emissivity, d the object's diameter, Δ its distance from the observer, α is the solar phase angle and θ and φ are surface latitude and longitude measured from the subsolar point, respectively. $B(\lambda,T)$ is the Planck equation, $B(\lambda,T) = 2hc^2/\lambda^5\ [\exp(hc/(\lambda k_\mathrm{B}T)) - 1]^{-1}$, where T is the temperature, h Planck's constant, c the velocity of light and k_B Boltzmann's constant. The disk-integrated thermal emission is then fitted to the thermal-infrared data by variation of the model surface temperature distribution T. The body's temperature distribution depends on parameters such as albedo, thermal inertia, surface roughness, observation geometry, spin axis orientation and rotation period. In the modeling process, we take into account the individual observation geometries of each flux density measurement.

One of the first and most simple models is the standard thermal model (STM, cf. Lebofsky & Spencer 1989, and references therein), which assumes the model body to be of spherical shape, non-rotating and/or having zero thermal inertia, with a smooth surface and observed at phase angle $\alpha = 0$. The surface temperature distribution is described by an instantaneous thermal equilibrium between emitted thermal radiation and absorbed sunlight.

In this work we make use of the near-Earth asteroid thermal model (NEATM, Harris 1998), which is, despite its name, applicable to atmosphereless TNOs (Müller et al. 2010; Stansberry et al. 2008, the latter use a similar approach with their hybrid STM). The main difference of the NEATM compared to the STM is the use of a variable beaming factor η, which adjusts the subsolar temperature

$$T_{\rm SS} = [(1-A)S_\odot/(\epsilon\sigma\eta r^2)]^{1/4}, \quad (3)$$

where A is the Bond albedo, $S_\odot$ the solar constant, σ the Stefan-Boltzmann constant and r the object's heliocentric distance. A is related to the geometric albedo, p_V, via $A \sim A_V = qp_V$ (Lebofsky & Spencer 1989). We use a phase integral $q = 0.336\ p_V + 0.479$ (Brucker et al. 2009). η accounts for thermal inertia and surface roughness in a first-order approximation and can serve as a free parameter being derived as part of the fitting process, which usually provides better results than assuming a fixed value of η. Small values of η ($\eta < 1$) imply higher surface temperatures compared to that of a Lambertian surface, for instance due to surface roughness or porosity. High values of η ($\eta > 1$) lead to a reduction of the model surface temperature, mimicking the effect of thermal inertia. In contrast to the STM, the NEATM accounts for phase angles $\neq 0$ (as shown in Eq. (2)). In the case of TNOs, however, this aspect is unimportant, since these objects are always observed at very low phase angles, due to their large heliocentric distances.

Whenever *Spitzer* data are available we combine them with PACS data. The combination of the data has a large impact on the reliability and accuracy of the model output. The peak emission wavelength in flux density units (Jy) of typical Plutino orbits ranges from 80 μm to 100 μm (compare model SEDs in Fig. 3). Hence, PACS band wavelengths (70 μm, 100 μm and 160 μm) are located in the flat peak plateau and the shallow Rayleigh-Jeans tail of the Planck function, respectively, and therefore constrain the model SED and η insufficiently. Adding a *Spitzer* 24 μm band measurement, which is located in the steeper Wien-slope, improves the ability to constrain the model SED and allows for the determination of reliable estimates of η. Therefore, we adopt floating-η fits if additional *Spitzer* data are available and rely on floating-η fits if only *Herschel* data are available. However, in some cases of poor data quality or whenever data from different parts of the lightcurve or from very different observation geometries are combined, the floating-η method leads to η values which are too high or too low and therefore unphysical (the range of physically meaningful η values is $0.6 \leq \eta \leq 2.6$[4]). In such cases, we also apply the fixed-η method, which makes use of a canonical value of $\eta = 1.20 \pm 0.35$ derived by Stansberry et al. (2008) from *Spitzer* observations of a sample of Centaurs and TNOs. The validity of this approach is discussed in Sect. 4.1. We treat non-detections with a 1σ uncertainty as $0 \pm \sigma$ detections in our models.

Throughout this work we assume the surface emissivity ϵ to be constant at a value of 0.9 for all wavelengths, which is based on laboratory measurements of silicate powder (Hovis & Callahan 1966) and a commonly adopted approximation for small bodies in the solar system.

[4] The physical range of η values were probed by using NEATM to model the two extreme cases of (1) a fast rotating object of high thermal inertia with low surface roughness and (2) a slow rotating object of low thermal inertia with high surface roughness, which yield the upper and lower η limit, respectively. Fluxes for both cases were determined using a full thermophysical model (Lagerros 1996, 1997, 1998; Mueller 2007), in which surface roughness is implemented via spherical cratering. The degree of surface roughness is determined via the opening angle (0°–180°) and surface density (0.0–1.0) of the craters.

3.1. Uncertainty assessment

In order to derive uncertainty estimates for diameter and albedo, we make use of a Monte Carlo (MC) simulation in which a sample of 1000 randomized synthetic bodies is created by variation of the observed flux density, the η value, and the absolute magnitude H. The randomized parameters follow a normal distribution centered on the nominal value, within the limits of the respective uncertainties. The uncertainties in flux density and H are taken from Tables 2 and 3, respectively. In the case of floating-η fits, η follows as a result of the modeling process, whereas in the case of fixed-η fits, the value of $\eta \pm 0.35$, determined by Stansberry et al. (2008) is applied.

Uncertainties of a specific parameter are derived from the ensemble of modeled synthetic bodies as the upper and lower values that include 68.2% of the ensemble (centered on the median), respectively. The uncertainties are usually aligned asymmetrically around the median, since most diameter and albedo distributions do not strictly follow a normal distribution. This method was introduced by Mueller et al. (2011). Finally, we combine the uncertainties determined through the MC method with the respective parameter values provided by the best model fit.

In order to improve uncertainty estimates, we make use of the rescaled uncertainties approach, introduced by Santos-Sanz et al. (2012). The motivation for this technique is the fact, that uncertainty estimates resulting from the MC method might be unrealistically small in cases in which the model fits the observational data only poorly. As a measure for the fit quality we use the reduced χ^2, which is a result of the fitting process. It is defined as

$$\chi^2_{\rm red} = \frac{1}{\text{n.d.f.}} \sum_i \left[\frac{F_{{\rm obs},i} - F_{{\rm model},i}}{\sigma_{{\rm obs},i}} \right]^2, \quad (4)$$

with $F_{{\rm obs},i}$ and $F_{{\rm model},i}$ being the observed and modeled flux densities of the different observations i, respectively, and $\sigma_{{\rm obs},i}$ being the respective observational flux density uncertainty. $\chi^2_{\rm red}$ is normalized by the number of degrees of freedom (n.d.f.), which equals the number of datapoints -2 in the case of a floating-η fit and the number of datapoints -1 in the case of a fixed-η method, respectively. A poor fit results in $\chi^2_{\rm red} \gg 1$.

The idea is to increase the flux density uncertainties uniformly by a factor S, which leads to an increase in variation of the flux densities of the synthetic bodies. The value of S is determined in such a way as to provide by definition the best possible model fit, i.e. $\chi^2_{\rm red} = 1$, which is achieved by choosing $S = \sqrt{\chi^2_{\rm red,\,min}}$, with $\chi^2_{\rm red,\,min}$ being the minimum $\chi^2_{\rm red}$ resulting from fitting the unaltered observational data. Hence, the rescaled flux density uncertainties are $\hat{\sigma}_{\rm obs} = S\,\sigma_{\rm obs}$ and the resulting $\hat{\chi}^2_{\rm red,\,min}$, which is obtained by replacing $\sigma_{\rm obs}$ with $\hat{\sigma}_{\rm obs}$ in Eq. (4), is by definition unity. Diameter uncertainties are dominated by flux uncertainties and the quality of the fit, whereas albedo uncertainties are dominated by the uncertainty of H. The rescaled uncertainties are used only in the MC method to determine the uncertainties of the physical parameters. In order to obtain the best fit, the original uncertainties are applied.

The method is illustrated in Fig. 2 using synthetic data. Figure 2a shows the original flux densities with error bars of the size of the original uncertainties. The dark line represents

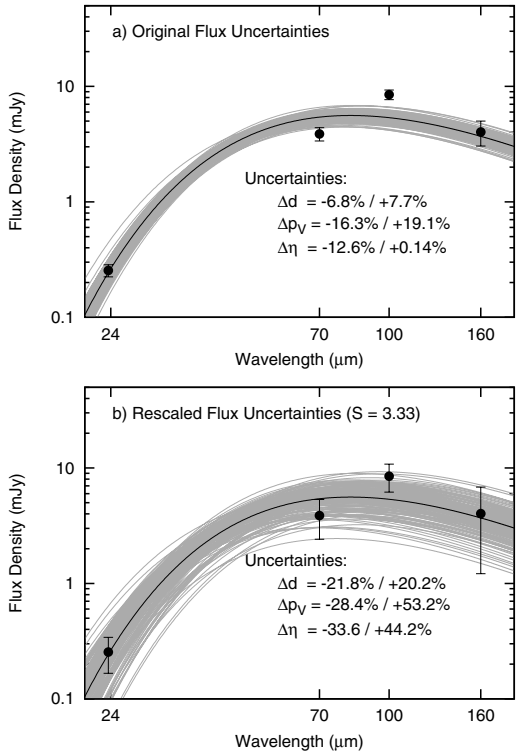

Fig. 2. Illustration of the rescaled flux density uncertainties technique using synthetic data. **a)** Filled circles represent the flux densities at the different wavelengths with original flux density uncertainties. The dark line represents the best fit line ($\chi^2_{\rm red}$ = 11.09); the grey lines are fit lines of 100 out of 1000 synthetical bodies generated for the MC method. The bad quality of the fit is obvious, since the 70 and 100 μm datapoints are hardly fit by any of the single fit lines. Therefore, the reliability of the uncertainties of the output parameters is questionable. **b)** By rescaling the error bars by a factor of 3.33 = $\sqrt{11.09}$, the broadness of the distribution of single fit lines is increased, which covers now all datapoints. As a result, the output parameter fractional uncertainties are increased and therefore more realistic.

the best NEATM fit (floating-η method) of the dataset, whereas each grey line symbolizes the best fit SED of one of 100 of the 1000 randomized synthetic bodies. It is obvious that the distribution of single fit curves misses the 100 μm PACS band completely and hardly fits the 70 μm datapoint. Hence, the fit quality is bad, which results in an underestimation of the model output uncertainties. By rescaling the uncertainties of the flux densities, the broadness of the distribution of single fit lines increases, as depicted in Fig. 2b. As a consequence of the rescaling, all datapoints are covered by the set of lines and the derived uncertainties are significantly increased, leading to much more realistic uncertainty estimates.

4. Results and discussion

An overview of all modeling results is given in Table 5. Where possible, floating and fixed-η modeling approaches were applied based on *Herschel*-only and combined *Herschel* and *Spitzer* datasets, in order to test the consistency of the results. The objects' SEDs determined by the different models are plotted in Fig. 3.

Table 5. Modeling results sorted by modeling technique.

Object	Data	d [km]	p_V	η
floating-η fits:				
1999 TC36	HS	$393.1^{+25.2}_{-26.8}$	$0.079^{+0.013}_{-0.011}$	$1.10^{+0.07}_{-0.08}$
2000 GN171	HS	$147.1^{+20.7}_{-17.8}$	$0.215^{+0.093}_{-0.070}$	$1.11^{+0.24}_{-0.21}$
2002 VE95	HS	$249.8^{+13.5}_{-13.1}$	$0.149^{+0.019}_{-0.016}$	$1.40^{+0.12}_{-0.11}$
2002 XV93	H	$451.3^{+61.7}_{-64.4}$	$0.060^{+0.042}_{-0.025}$	$0.72^{+0.30}_{-0.24}$
2002 XV93	HS	$549.2^{+21.7}_{-23.0}$	$0.040^{+0.020}_{-0.015}$	$1.24^{+0.06}_{-0.06}$
2003 AZ84[a]	HS	$727.0^{+61.9}_{-66.5}$	$0.107^{+0.023}_{-0.016}$	$1.05^{+0.19}_{-0.15}$
2003 VS2[a]	HS	$523.0^{+35.1}_{-34.4}$	$0.147^{+0.063}_{-0.043}$	$1.57^{+0.30}_{-0.23}$
2004 EW95	H	$265.9^{+48.3}_{-45.2}$	$0.053^{+0.035}_{-0.022}$	$0.93^{+0.55}_{-0.42}$
2004 PF115	H	$406.3^{+97.6}_{-85.3}$	$0.113^{+0.082}_{-0.042}$	$0.84^{+0.61}_{-0.40}$
2004 UX10	H	$361.0^{+124.2}_{-93.5}$	$0.172^{+0.141}_{-0.078}$	$0.96^{+0.98}_{-0.56}$
2006 HJ123	H	$283.1^{+142.3}_{-110.8}$	$0.136^{+0.308}_{-0.089}$	$2.48^{+3.92}_{-1.91}$
Huya	H	$395.7^{+35.7}_{-34.7}$	$0.100^{+0.022}_{-0.018}$	$0.75^{+0.22}_{-0.19}$
Huya	HS	$438.7^{+26.5}_{-25.2}$	$0.081^{+0.011}_{-0.011}$	$0.89^{+0.06}_{-0.06}$
fixed-η fits:				
1996 TP66	HS	$154.0^{+28.8}_{-33.7}$	$0.074^{+0.063}_{-0.031}$	
1999 TC36	H	$407.5^{+38.9}_{-38.7}$	$0.073^{+0.019}_{-0.014}$	
1999 TC36	HS	$428.3^{+81.7}_{-112.2}$	$0.066^{+0.064}_{-0.023}$	
2000 GN171	H	$150.0^{+19.7}_{-19.1}$	$0.207^{+0.105}_{-0.070}$	
2000 GN171	HS	$155.1^{+20.4}_{-27.3}$	$0.193^{+0.141}_{-0.075}$	
2001 KD77	H	$232.3^{+40.5}_{-39.4}$	$0.089^{+0.044}_{-0.027}$	
2001 QF298	H	$408.2^{+40.2}_{-44.9}$	$0.071^{+0.020}_{-0.014}$	
2002 VE95	H	$237.0^{+18.2}_{-21.4}$	$0.165^{+0.037}_{-0.027}$	
2002 VE95	HS	$226.3^{+27.6}_{-42.5}$	$0.181^{+0.113}_{-0.042}$	
2002 VR128	H	$448.5^{+42.1}_{-43.2}$	$0.052^{+0.027}_{-0.018}$	
2002 VU130	H	$252.9^{+33.6}_{-31.3}$	$0.179^{+0.202}_{-0.103}$	
2002 XV93	H	$544.1^{+47.8}_{-55.6}$	$0.041^{+0.026}_{-0.017}$	
2002 XV93	HS	$534.3^{+69.6}_{-124.2}$	$0.042^{+0.048}_{-0.021}$	
2003 AZ84[a]	H	$771.0^{+78.9}_{-77.9}$	$0.095^{+0.026}_{-0.019}$	
2003 AZ84[a]	HS	$766.8^{+58.9}_{-97.8}$	$0.096^{+0.035}_{-0.016}$	
2003 UT292	H	$186.6^{+17.3}_{-20.3}$	$0.092^{+0.091}_{-0.049}$	
2003 VS2	H	$483.1^{+37.0}_{-50.0}$	$0.172^{+0.092}_{-0.056}$	
2003 VS2[a]	H	$465.7^{+45.7}_{-51.0}$	$0.185^{+0.091}_{-0.062}$	
2003 VS2[a]	HS	$466.9^{+38.6}_{-49.9}$	$0.184^{+0.110}_{-0.065}$	
2004 EW95	H	$291.1^{+20.3}_{-25.9}$	$0.044^{+0.021}_{-0.015}$	
2004 PF115	H	$468.2^{+38.6}_{-49.1}$	$0.123^{+0.043}_{-0.033}$	
2004 UX10	H	$398.1^{+32.6}_{-39.3}$	$0.141^{+0.044}_{-0.031}$	
2006 HJ123	H	$216.4^{+29.7}_{-34.2}$	$0.281^{+0.259}_{-0.152}$	
Huya	H	$461.1^{+31.2}_{-41.4}$	$0.073^{+0.017}_{-0.011}$	
Huya	HS	$561.5^{+82.8}_{-111.4}$	$0.049^{+0.041}_{-0.017}$	
Pluto/Charon	H	$2119.9^{+164.5}_{-182.2}$	$0.730^{+0.162}_{-0.153}$	

Notes. "Data" denotes the dataset on which the modeling results are based: "H" equals *Herschel* data, "HS" equals *Herschel* and *Spitzer* data, respectively; diameter, geometric albedo and η are given including respective upper and lower uncertainties. We show all succesful model fit results in order to allow for a comparison of the reliability of the techniques and the data sets. In the case of all fixed-η modeling approaches, $\eta = 1.20 \pm 0.35$ was applied. [(a)] Using averaged lightcurve observations.

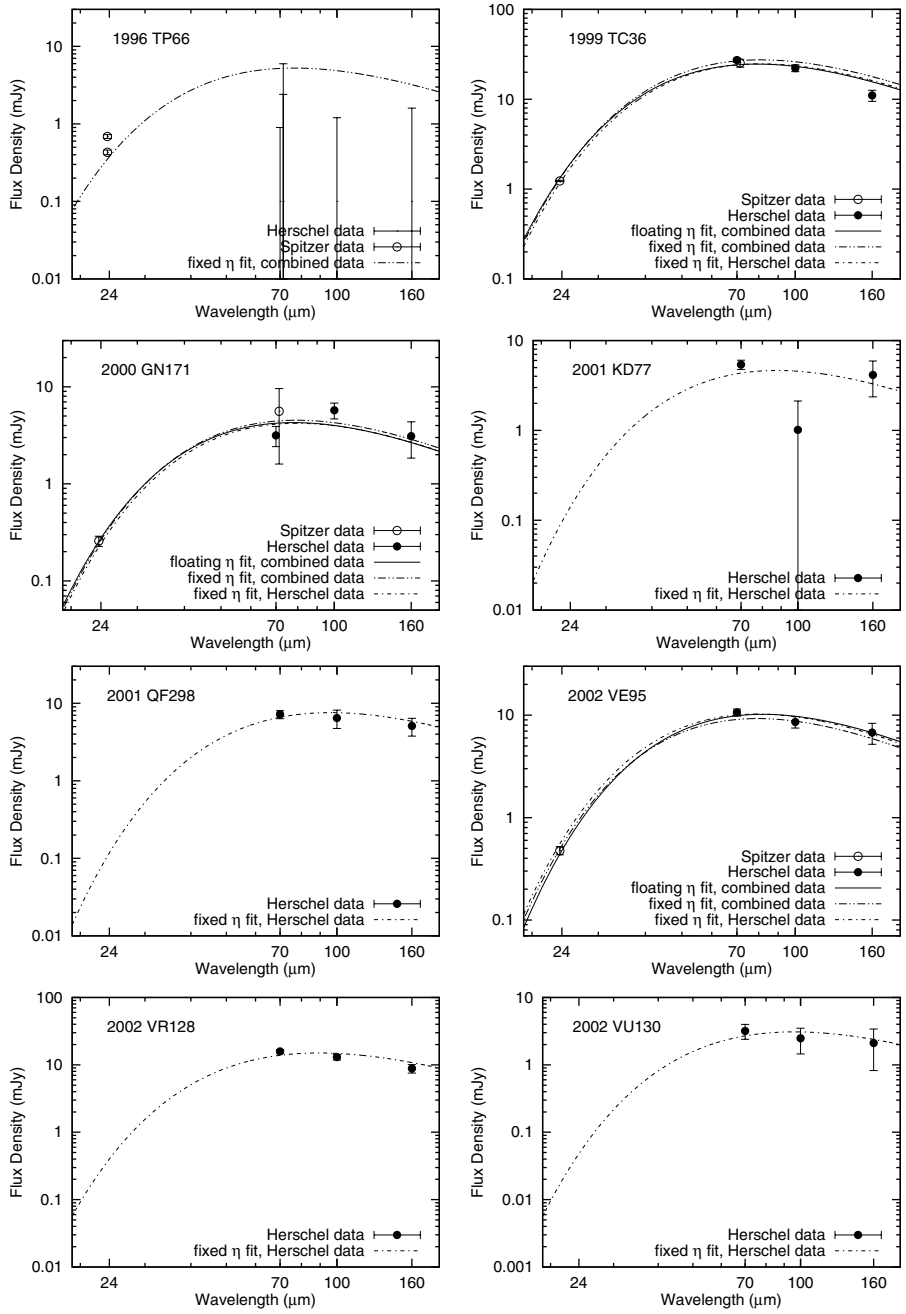

Fig. 3. Model fits of the Plutino sample using different modeling approaches and different data samples: the solid and dashed lines are floating-η fits based on combined *Herschel* and *Spitzer* and *Herschel*-only data, respectively; the dash-dotted and dash-dot-dotted lines represent fixed-η fits of combined *Herschel* and *Spitzer* and *Herschel*-only data samples, respectively; datapoints at 23.68 μm and 71.42 μm are *Spitzer* MIPS data (open circles), those at 70 μm, 100 μm and 160 μm are *Herschel*-PACS data (filled circles). The model is fit to each flux measurement using the circumstances appropriate for the epoch of that observation. In order to simplify the figures, we have normalized the *Spitzer* flux densities to the epoch of the *Herschel* observations using the ratio of the best-fit model flux densities for the *Herschel* and *Spitzer* epoch, and then plotted the measured value times this ratio. Uncertainties are rescaled similarly, preserving the SNR for the *Spitzer* data.

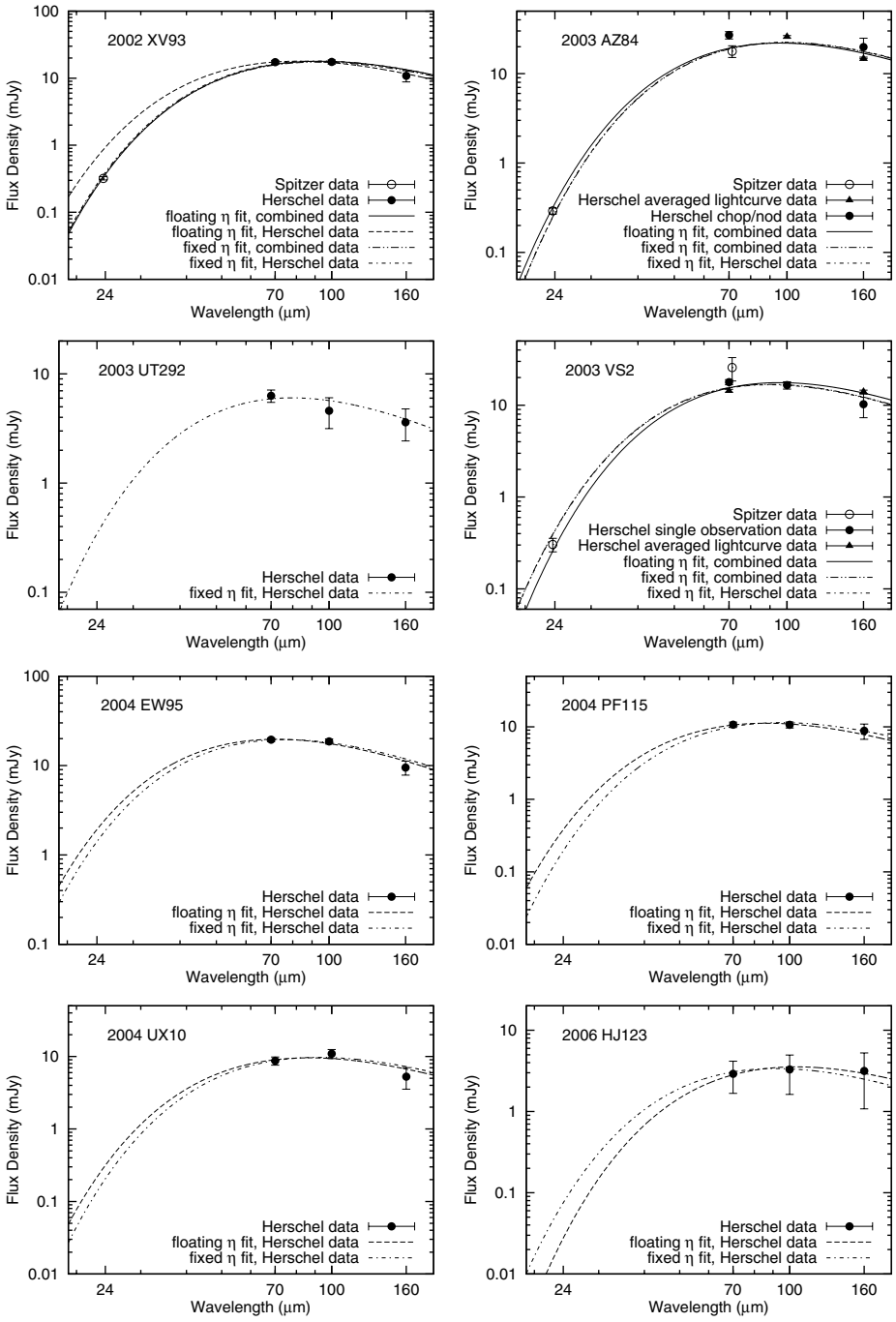

Fig. 3. continued.

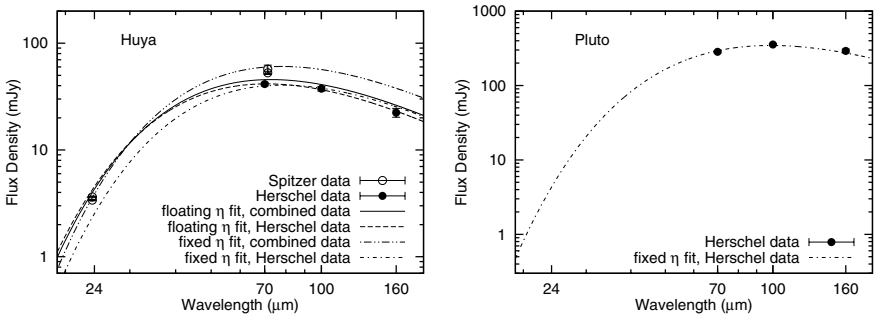

Fig. 3. continued.

In the following sections we test the validity of the $\eta = 1.2$ assumption for the Plutino sample, and discuss the modeling results of the individual objects. After that, the results of the sample as a whole are discussed and used to determine a cumulative size distribution of the Plutino population. Finally, correlations between the different physical, photometric and dynamical parameters and the presence of ices are examined.

4.1. Test of the fixed-η assumption

We were able to derive floating-η fits for 12 targets; we adopted the 7 which are based on combined *Herschel* and *Spitzer* data. The top section of Table 5 gives the results of all converged floating-η fits. The weighted mean[5] η determined from the 7 adopted floating-η model fits yields $\langle\eta\rangle = 1.11^{+0.18}_{-0.19}$, which is consistent with the adopted value of $\eta = 1.20 \pm 0.35$ (Stansberry et al. 2008) applied in the fixed-η approach. The root mean square fractional residuals in the results of the fixed-η method between using $\eta = 1.20$ and $\langle\eta\rangle = 1.11$ is 5% and 10% for diameter and albedo, respectively. However, the average fractional uncertainties in diameter and albedo of all adopted results are ±10% and +49/−31%, respectively, which is larger than the residuals. Therefore, we continue to adopt $\eta = 1.20$ for the fixed-η approach.

4.2. Discussion of individual targets

1996 TP66: Despite the availability of both *Herschel* and *Spitzer* data, the floating-η approach was not applicable for 1996 TP66, because of the non-detections in the PACS 70, 100 and 160 μm bands. The best fit fixed-η solution is largely constrained by the two 24 μm MIPS flux densities. Therefore, our results ($d = 154.0^{+28.8}_{-33.7}$ km, $p_V = 0.074^{+0.063}_{-0.031}$, based on $\eta = 1.20$) barely differ from those of Stansberry et al. (2008), who find $d = 160^{+45}_{-45}$ km and $p_V = 0.074^{+0.07}_{-0.03}$ using $\eta = 1.20^{+0.35}_{-0.35}$, solely based on the 24 μm MIPS flux densities. The reason for the non-detections is unclear. However, the fact that no clear detection was possible in the wavelength regime of 70 μm and above using two different instruments (PACS and MIPS) and at different epochs points to a real effect. We based the observation planning on $p_V = 0.07$, which agrees well with the best fit model.

1999 TC36: This target was well detected in all three PACS bands. In combination with MIPS flux densities, a good floating-η fit was possible here, which misses the PACS 160 μm band flux density. This might hint to a more complex surface albedo distribution or a wavelength-dependency of the emissivity. Our adopted diameter and albedo estimates, $393.1^{+25.2}_{-26.8}$ km and $0.079^{+0.013}_{-0.011}$, respectively, agree with earlier estimates by Stansberry et al. (2008): $d = 414.6^{+38.8}_{-38.2}$ km and $p_V = 0.072^{+0.015}_{-0.012}$. 1999 TC36 is a triple component system (Trujillo & Brown 2002; Jacobson & Margot 2007; Benecchi et al. 2010), consisting of two similarly sized central components A_1 and A_2 and a more distant secondary component, B. The nature of this system makes it possible to determine the mean density of the system and, using optical flux differences between the single components, the sizes of the components. We revisit the calculations performed by Stansberry et al. (2006) and Benecchi et al. (2010). Our newly derived estimates of the sizes, based on the flux differences found by Benecchi et al. (2010), are: $d_{A1} = 272^{+17}_{-19}$ km, $d_{A2} = 251^{+16}_{-17}$ km and $d_B = 132^{+8}_{-9}$ km. Using these diameters, we are able to improve the mean system density $\varrho = 0.64^{+0.15}_{-0.11}$ g cm^{-3}, which is somewhat higher than the earlier estimate $\varrho = 0.54^{+0.32}_{-0.21}$ g cm^{-3} (Benecchi et al. 2010). Assuming material densities of $1.0 \leq \varrho_0 \leq 2.0$ g cm^{-3}, we find porosities or fractional void space of 36–68%. Our calculations are based on the assumptions of spherical shape of each component and the same albedo for each component.

2000 GN171: Both fixed and floating-η model fits based on the combined *Herschel* and *Spitzer* datasets were possible, leading to good fits with similar outcomes. We adopt the floating-η result $d = 147.1^{+20.7}_{-17.8}$ km, $p_V = 0.215^{+0.093}_{-0.070}$, and $\eta = 1.11^{+0.24}_{-0.21}$, which differs significantly from an earlier estimate by Stansberry et al. (2008), who determined $d = 321^{+57.4}_{-54.2}$ km, $p_V = 0.057^{+0.025}_{-0.016}$ and $\eta = 2.32^{+0.46}_{-0.43}$. The large discrepancy stems from an overestimated MIPS 70 μm band flux density in the Stansberry et al. (2008) data, which has been revised for this work. By adding the *Herschel*-PACS data, the SED is better constrained, leading to a more reliable result. 2000 GN171 is either a Roche binary or a Jacobi ellipsoid (Lacerda & Jewitt 2007). With a lightcurve amplitude of 0.61 mag (Sheppard & Jewitt 2002), the size of the companion or the ellipticity of the body is significant. Hence, the real diameter of 2000 GN171, the smallest Plutino in our sample, might be even smaller.

2001 KD77: We modeled this target solely on the basis of PACS data, since existing MIPS flux density measurements suffer from a large positional uncertainty. For this faint target, the fixed-η fit mainly relies on the 70 μm band measurement, which has the highest SNR of all bands. Figure 3 clearly shows the mismatch of the 100 μm band measurement, which is scarcely detectable on the sky subtracted maps. Due to its large uncertainty, this

[5] The weighted mean and its uncertainties were determined using the equation given in Table 3.

datapoint is nearly neglected by the fixed-η fit, and therefore scarcely impacts the modeling results. The reason for the low 100 μm flux density is unknown.

2002 VE95, *2002 XV93*, *2003 AZ84*, *2003 VS2* and *Huya*: These objects show a good to excellent agreement of both the different model technique fits compared to each other, as well as the model SED compared with the different measured flux densities. For all five targets combined *Herschel* and *Spitzer* flux densities are available and we adopt the floating-η modeling results. 2003 AZ84 and 2003 VS2 data include averaged lightcurve data, which strongly constrain the respective SEDs, due to their small uncertainties. Earlier estimates of 2003 VS2 by Stansberry et al. (2008) based on *Spitzer* data suggested $d = 725.2^{+199.0}_{-187.6}$ km and $p_V = 0.058^{+0.048}_{-0.022}$ using $\eta = 2.00^{+0.54}_{-0.51}$, which is significantly different from our results $d = 523.0^{+35.1}_{-34.4}$ km, $p_V = 0.147^{+0.063}_{-0.043}$, based on $\eta = 1.57^{+0.30}_{-0.23}$. The discrepancy might stem from the high 70 μm MIPS flux density value, which, together with the 24 μm MIPS data point, suggests a steeper Wien slope of the spectral energy distribution compared to the combined *Herschel* and *Spitzer* data set. 2003 AZ84 was observed before by *Herschel* during the Science Demonstration Phase using the chop/nod technique (Müller et al. 2010), yielding $d = 896 \pm 55$ and $p_V = 0.065 \pm 0.008$, using $\eta = 1.31 \pm 0.08$, which differs from our results $d = 727.0^{+61.9}_{-66.5}$ km, $p_V = 0.107^{+0.023}_{-0.016}$, based on $\eta = 1.05^{+0.19}_{-0.15}$. Despite the smaller diameter determined using the averaged lightcurve data, 2003 AZ84 is still the largest Plutino in our sample, apart from Pluto. 2003 AZ84 has a moon, which is 5.0 ± 0.3 mag fainter than the primary (Brown & Suer 2007). This large difference in magnitude suggests that the thermal flux of the companion is negligible. The modeling results of Huya vary significantly depending on the model technique and the dataset. A visual inspection of the model fits shows that the floating-η approach based on the combined data set matches the measured SED best and results in $d = 438.7^{+26.5}_{-25.2}$ and $p_V = 0.081^{+0.011}_{-0.011}$, based on $\eta = 0.89^{+0.06}_{-0.06}$. Earlier estimates by Stansberry et al. (2008) based on *Spitzer* data suggest $d = 532.6^{+25.1}_{-24.4}$ and $p_V = 0.050^{+0.005}_{-0.004}$, based on $\eta = 1.09^{+0.07}_{-0.06}$. 2002 XV93 has the lowest albedo in the sample.

2001 QF298, *2002 VR128*, *2002 VU130*, *2003 UT292*, *2004 EW95*, *2004 PF115*, *2004 UX10* and *2006 HJ123*: For these targets we have to rely on *Herschel*-only data and therefore adopt the results of the fixed-η technique. We were able to succesfully apply the floating-η method to 2004 EW95, 2004 PF115, 2004 UX10 and 2006 HJ123 as well. Modeling results in Table 5 and the plots in Fig. 3 of the SEDs show a good agreement between the results of the different techniques, supporting the validity of the fixed-η approach and the reliability of the *Herschel* flux measurements. Differences in the fit quality are induced by the different SNR values of the respective measurements. Both 2002 VU130 and 2006 HJ123 suffer from large albedo uncertainties, which is a result of the large uncertainty of their absolute magnitude H. 2006 HJ123 shows the highest albedo of our sample, excluding Pluto.

Pluto: Paradoxically, Pluto is a clear outlier from the Plutino population, being by far the largest and having the brightest surface. Besides that, Pluto was the first TNO discovered to have an atmosphere (Hubbard et al. 1988; Brosch 1995), has a pronounced optical lightcurve caused by albedo variations, and has a moon half its own size. An additional complication is the effect of N_2 ice on Pluto's surface: sublimation and deposition of N_2 is accompanied by latent heat transport that results in much lower (higher) dayside (nightside) temperatures than would be expected on an airless body (e.g. Spencer et al. 1997). Despite these facts, we attempt to treat Pluto like any other Plutino and compare our modeling results to the known properties of Pluto and Charon, and discuss the reasons for discrepancies that emerge.

The Pluto system has been subject to detailed study via, for instance, direct imaging, stellar occultation observations and thermal radiometry in the past. Mean hemispheric albedo ranges are 0.49 to 0.66 for Pluto and 0.36 to 0.39 for Charon (Buie et al. 1997). Charon's diameter is well determined to be 1208 km (Gulbis et al. 2006; Sicardy et al. 2006). Pluto's diameter estimates suffer from uncertainties related to the presence of the atmosphere and range from about 2290–2400 km (Tholen & Buie 1997). For the purpose of comparing with the results of our thermal models, we adopt a diameter of 2322 km (Young et al. 2007). These numbers lead to an equivalent diameter and albedo of the combined system of 2617 km and 0.44–0.73, respectively.

We deliberately refrain from combining our *Herschel* data set with existing *Spitzer* measurements (for instance Lellouch et al. 2011), due to the so far unexplained secular fading of the Pluto/Charon system (Stansberry et al. 2009). Instead, we rely on our original *Herschel* measurements only, and so we adopt the fixed-η results: $d = 2119.9^{+164.5}_{-182.2}$ km and $p_V = 0.730^{+0.162}_{-0.153}$ (cf. Fig. 3). Our thermal estimate of the effective system diameter deviates by 3σ from the known effective system diameter given above; the albedo derived from our thermal modeling is only barely consistent with the maximum allowable albedo given above. Our attempt to apply a simple thermal model to Pluto shows the susceptibility of such models to violations of the model assumptions. We discuss effects, which may explain the discrepancy of our adopted values with the equivalent values:

- By replacing the Pluto/Charon system with a single equivalent body, we had to assume a single average albedo for both objects, which is a coarse simplification, in order to apply our models. Furthermore, surface albedo variations of Pluto (Buie et al. 2010) lead to a more complex spectral energy distribution and affect the model results significantly. Our model results would be improved by using a two-terrain model, which was used to model the thermal emission of Makemake (Lim et al. 2010), in which Pluto and Charon would each be represented by one terrain, or applying more sophisticated albedo surface distributions: Lellouch et al. (2011) applied a 3-terrain model to model the thermal emission of Pluto and an additional terrain to model Charon's contribution.
- Former thermal infrared measurements of Pluto revealed its thermal lightcurve in different wavelength ranges (Lellouch et al. 2000, 2011), which was not accounted for in our modeling. Given the time lags between the individual observations, this might have introduced a perceptible distortion of the SED, which affects the modeling results.
- Millimeter wavelength observations of Pluto (Gurwell & Butler 2005; Gurwell et al. 2010) revealed a lower surface brightness temperature than assumed from thermal equilibrium, which is due to the combination of two effects: (1) the mixing of SEDs at different temperatures, and in particular the increased contribution of the N_2-dominated areas, whose temperature is ~37 K due to the dominance of sublimation cooling in the thermal budget of N_2 ice, and (2) the fact that emissivities are expected to decrease at long wavelengths as a result of sub-surface sounding in a progressively more transparent medium. Lellouch et al. (2011) find in particular that the emissivity of CH_4 ice, one of the terrains in their

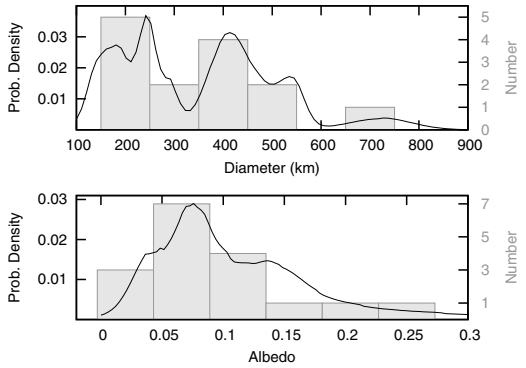

Fig. 4. Diameter and albedo probability density functions and histograms. The probability density functions describe the probability to find an object of a specific diameter or albedo, when picking a random object. The functions were derived by summing up the probability density functions of each object, being represented by a non-symmetric normal distribution taking into account the different upper and lower uncertainties of each result. This approach returns a more detailed picture than the histogram. Pluto was excluded from the sample.

3-terrain Pluto model, shows a steady decrease with increasing wavelength (their Fig. 8). Without additional assumptions, our thermal model is not capable of taking such effects into account.

Due to the failed model fit and Pluto's uniqueness among the Plutinos, we exclude it from the following discussion of the properties of our Plutino sample.

4.3. Sample statistics

Figure 4 shows diameter and albedo probability density functions and histograms based on the results compiled in Table 6. The size distribution ranges from 150 km to 730 km and the albedo distribution from 0.04 to 0.28 with a clear peak around 0.08. The low probability density at high albedos is caused by the large uncertainties of such albedos. Excluding Pluto, the weighted mean[6] of the albedo, weighted by absolute uncertainties, yields 0.08 ± 0.03, which agrees well with the range of typical geometric albedos of the TNO and Centaur sample of Stansberry et al. (2008). Table 7 shows a comparison of the mean albedos of our Plutino sample with different TNO sub-population and JFCs. It turns out that the average albedo of the Plutinos agrees well with that of the scattered disk, Centaur, hot classical and JFC population. Through dynamical studies Duncan et al. (1995), Yu & Tremaine (1999) and di Sisto et al. (2010) suggested the Plutino population to be a source of JFCs and/or Centaurs, which is compatible with our results. Furthermore, most of the Plutinos appear to have darker surfaces than the cold classical TNOs and detached objects.

[6] Upper and lower uncertainties were calculated corresponding to the calculations applied in Table 3. The calculation of the weighted mean albedo based on fractional uncertainties yields 0.11. However, we prefer to adopt the weighted mean albedo based on absolute errors, since it better agrees with the low albedo of the bulk of the Plutinos and is enforced from our results in Sect. 4.4.

Table 6. Adopted modeling results.

Object	Data	d [km]	p_V	η
1996 TP66	HS	$154.0^{+28.8}_{-33.7}$	$0.074^{+0.063}_{-0.031}$	$1.20^{+0.35}_{-0.35}$
1999 TC36	HS	$393.1^{+25.2}_{-26.8}$	$0.079^{+0.013}_{-0.011}$	$\mathbf{1.10^{+0.07}_{-0.08}}$
2000 GN171	HS	$147.1^{+20.7}_{-17.8}$	$0.215^{+0.093}_{-0.070}$	$\mathbf{1.11^{+0.24}_{-0.21}}$
2001 KD77	H	$232.3^{+40.5}_{-39.4}$	$0.089^{+0.044}_{-0.027}$	$1.20^{+0.35}_{-0.35}$
2001 QF298	H	$408.2^{+40.2}_{-44.9}$	$0.071^{+0.020}_{-0.014}$	$1.20^{+0.35}_{-0.35}$
2002 VE95	HS	$249.8^{+13.5}_{-13.1}$	$0.149^{+0.019}_{-0.016}$	$\mathbf{1.40^{+0.12}_{-0.11}}$
2002 VR128	H	$448.5^{+42.1}_{-43.2}$	$0.052^{+0.027}_{-0.018}$	$1.20^{+0.35}_{-0.35}$
2002 VU130	H	$252.9^{+33.6}_{-31.3}$	$0.179^{+0.202}_{-0.103}$	$1.20^{+0.35}_{-0.35}$
2002 XV93	HS	$549.2^{+21.7}_{-23.0}$	$0.040^{+0.020}_{-0.015}$	$\mathbf{1.24^{+0.06}_{-0.06}}$
2003 AZ84[a]	HS	$727.0^{+61.9}_{-66.5}$	$0.107^{+0.023}_{-0.016}$	$\mathbf{1.05^{+0.19}_{-0.15}}$
2003 UT292	H	$185.6^{+17.9}_{-18.0}$	$0.067^{+0.068}_{-0.034}$	$1.20^{+0.35}_{-0.35}$
2003 VS2[a]	HS	$523.0^{+35.1}_{-34.4}$	$0.147^{+0.063}_{-0.043}$	$\mathbf{1.57^{+0.30}_{-0.23}}$
2004 EW95	H	$291.1^{+20.3}_{-25.9}$	$0.044^{+0.021}_{-0.015}$	$1.20^{+0.35}_{-0.35}$
2004 PF115	H	$468.2^{+38.6}_{-49.1}$	$0.123^{+0.043}_{-0.033}$	$1.20^{+0.35}_{-0.35}$
2004 UX10	H	$398.1^{+32.6}_{-39.3}$	$0.141^{+0.044}_{-0.031}$	$1.20^{+0.35}_{-0.35}$
2006 HJ123	H	$216.4^{+29.7}_{-34.2}$	$0.281^{+0.259}_{-0.152}$	$1.20^{+0.35}_{-0.35}$
Huya	HS	$438.7^{+26.5}_{-25.2}$	$0.081^{+0.011}_{-0.011}$	$\mathbf{0.89^{+0.06}_{-0.06}}$

Notes. Columns as in Table 5. η values of floating-η modeling results are in bold. No adopted values are given for Pluto/Charon, since our model approaches are not applicable to these objects (cf. Sect. 4.2). [(a)] Using averaged lightcurve observations.

Table 7. Average albedos of Centaurs, different TNO sub-populations and JFCs.

Population	Average Albedo	N	Reference
Centaurs	0.06	21	1
Plutinos	0.08 ± 0.03	17	2
Cold Classicals[a]	0.16 ± 0.05	6	3
Hot Classicals[a]	0.09 ± 0.05	12	3
Scattered Disk Objects[b]	0.07/0.05	8	4
Detached Objects[b]	0.17/0.12[c]	6[c]	4
TNOs and Centaurs	0.07−0.08	47	1
JFCs	$<0.075^R$	32	5

Notes. N denotes the number of datapoints. [(a)] Unweighted mean; [(b)] unweighted/weighted mean, based on relative uncertainties; [(c)] excluding Eris; [(R)] means the geometric albedo in R band, which is comparable to p_V for small values.

References. (1): Stansberry et al. (2008); (2): this work; (3): Vilenius et al. (2012); (4): Santos-Sanz et al. (2012); (5): Fernández et al. (2005).

4.4. Plutino size distribution

Using the absolute magnitude estimates for all known Plutinos from the MPC and our measured albedos we are able to calibrate the Plutino size scale for the first time and to determine a cumulative size distribution of the known Plutino population. We use two different approaches to determine the cumulative size distribution $N(\geq d)$. Firstly, we assume monochromatic albedo distributions based on the two average albedos determined in Sect. 4.3. This approach enables the direct conversion of H magnitudes into diameter but neglects the measured diversity in albedo. The second approach makes use of a Monte Carlo method to determine the size distribution based on the

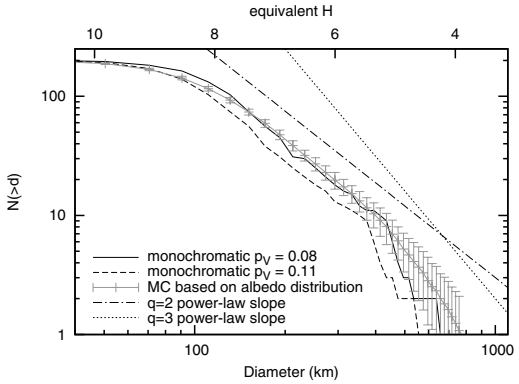

Fig. 5. Cumulative Plutino size distributions $N(\geq d)$ based on MPC H magnitudes and different assumptions: the solid and dashed line represent monochromatic albedo distributions using $p_V = 0.08$ and $p_V = 0.11$, respectively. The grey line shows the result of an averaged Monte Carlo simulations based on 100 runs and the measured albedo distribution with corresponding 1σ standard deviations. It is obvious that the monochromatic $p_V = 0.08$ size distribution agrees better with the result of the Monte Carlo simulation. Furthermore, we show two cumulative power laws $N(\geq d) \sim d^{-q}$ with $q = 2$ and $q = 3$ and arbitrary interceptions for comparison. A $q = 2$ cumulative power law better fits the measured size distribution in the size range 120–450 km, whereas the distribution of larger objects is better fit by a $q = 3$ cumulative power law. We can give an upper size limit for the kink at the small-sized end around 120 km. The upper abscissa gives the equivalent H magnitude based on a monochromatic albedo distribution of $p_V = 0.08$.

actually measured albedo distribution. For this purpose, each MPC H magnitude is assigned to a randomly generated albedo, which is used to determine the diameter. Hence, we assume that H is not correlated to the albedo, which is supported by our findings in Sect. 4.5. The distribution of the randomly generated albedos follows the determined probability density function (Fig. 4). Hence, this approach takes into account the measured albedo diversity. Figure 5 shows a comparison of the two different methods. It is clearly visible that the averaged Monte Carlo approach agrees well with the monochromatic $p_V = 0.08$ model, which supports our assumption that this value better represents the average Plutino albedo compared to the value of 0.11.

For comparison, we plot in Fig. 5 the slopes of different cumulative power laws $N(\geq d) \sim d^{-q}$. We find that the distribution of intermediate-sized Plutinos (120–450 km) is well-described by $q = 2$, which is smaller than the presumed value of $q \sim 3$ (Trujillo et al. 2001; Kenyon & Bromley 2004). The large diameter tail ($d \geq 450$ km) seems to be better described by $q = 3$. However, this region suffers from uncertainties due to small number statistics. A change in the cumulative power law slope at the small-sized tail seems to occur at diameters of 80−120 km, which is larger than the proposed range of 40−80 km (Bernstein et al. 2004; Kenyon et al. 2008; de Elía et al. 2008). However, the number of intrinsically fainter, and therefore smaller Plutinos is likely to be underrepresented, since the MPC sample suffers from an optical discovery bias. A proper debiasing of the size and albedo distributions is planned as part of future work. However, we suppose that a larger number of small-sized Plutinos would shift the kink to smaller diameters. Hence, we are only able to give an upper size limit of the location of the kink, which is 120 km. Furthermore, we note that our size distribution is based on albedo measurements derived from objects of the size range 150−730 km, which might be different from the albedo distribution of smaller Plutinos.

4.5. Correlations

The Plutino sample was checked for correlations of the physical parameters, orbital properties and intrinsic optical colors, using a modified Spearman rank correlation analysis technique. The technique is based on a bootstrap method and takes into account the uncertainties (error bars) of the parameters (data points), and computes the confidence interval of the corresponding correlation coefficient. Since we are taking into account data error bars, the results are estimates of the most probable correlation coefficient $\langle\rho\rangle$ accompanied by the probability P (p-value) of that $\langle\rho\rangle$ value to occur given no relationship in the sample, i.e. to occur by pure chance. The lower the value of P the higher the significance level of the correlation. We present the 68% confidence interval for the correlation value $\langle\rho\rangle$, i.e. the interval which includes 68% of the bootstrapped values. This confidence interval equals the canonical 1σ interval of a Gaussian distribution. As an additional aid in reading the P values we also compute its Gaussian-σ equivalent significance P_σ. The details of the technique are described in Santos-Sanz et al. (2012). Following Efron & Tibshirani (1993), we define a weak correlation by $0.3 < |\langle\rho\rangle| < 0.6$ and a strong correlation by $|\langle\rho\rangle| > 0.6$. $P < 0.05$ indicates reasonably strong evidence of correlation, $P < 0.025$ indicates strong evidence of correlation and $P < 0.003$ describes a clear (3σ) correlation.

It turns out that most parameters are uncorrelated. Only very few parameter pairs show reasonably strong evidence of correlation. Those and a few other interesting results are listed in Table 8 and discussed here. Other parameter pairs lack sufficient evidence for correlation or possess weak correlation values.

- We do not detect any strong and significant trend between diameter d and albedo p_V (cf. Fig. 6). Although we cannot rule out the possibility of some correlation between these two parameters given our sample size, it is very unlikely that a strong correlation between the two parameters might exist. On the other hand, both diameter and albedo seem to be clearly uncorrelated with the η value.
- The absolute magnitude H is not correlated with diameter, albedo, or η. This shows that our sample is not biased towards large and high (or low) albedo objects, which supports our approach to randomly assign albedos to H magnitudes in Sect. 4.4. This finding, however, does not exclude a discovery bias on smaller diameters than those examined here or a discovery bias based on geometrical aspects.
- We find a significant anti-correlation between eccentricity e and diameter d (cf. Fig. 6), showing that in our sample highly eccentric objects tend to be smaller. This anti-correlation is precisely the opposite of the correlation between perihelion distance q and diameter d, and also the opposite of the correlation between diameter d and the heliocentric distance of each object at the time of its discovery $r^\star$. We consider that these relationships are merely caused by the fact that objects on more eccentric orbits come closer to the Sun, which significantly improved their detectability. Hence, the observed relation between an object's diameter and its eccentricity (and perihelion distance) is very likely to be caused by a discovery bias.
- The correlation between diameter d and the heliocentric distance of each object at the time of its discovery $r^\star$, compared to the lack of correlation between albedo p_V and $r^\star$, shows

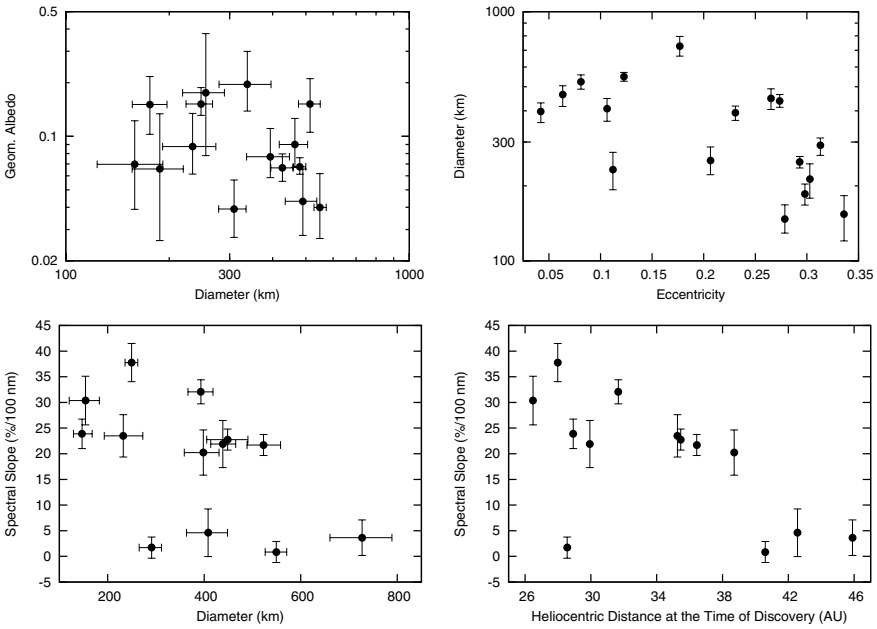

Fig. 6. Plots of some correlations. *Upper left*: we find no correlation between diameter and albedo; *upper right*: a clear anti-correlation between eccentricity and diameter is the result of a detection bias; *lower left*: we find smaller Plutinos to be redder than larger ones, which contradicts what was previously suggested by Peixinho et al. (2004) based on the intrinsical brightness H of a different Plutino sample; *lower right*: we find that the color of Plutinos is correlated to the heliocentric distance at the time of their discovery, which hints to a color bias.

that the likelihood of detection solely depends on size, and is rather independent of the object's albedo. This follows because the brightness of an object scales as $d^2 p_V$: the measured range of diameters translates into a brightness change factor of 24, whereas the total effect of the albedo can only account for a factor of 6. We can rule out a bias towards high (and low) albedos as a result of the nature of discovery of our sample targets. This supports the representativeness of the measured albedo distribution for the Plutino population and shows that the nature of the discovery bias is size-dependent.

– Most color indices and the spectral slope are anti-correlated with heliocentric distance at the time of an object's discovery $r^\star$ (Fig. 6). The farther an object is, the less red it seems to be. This points to a probable color bias in our sample, maybe induced by the common use of R band filters and the improved sensitivity in red bands of state-of-the-art detectors, which are used in TNO surveys. However, we find a lack of bluer objects at shorter heliocentric distances, which should be detectable, despite their color. This might suggest that such objects do not exist, at least within our sample.
– We can not confirm a trend found by Hainaut & Delsanti (2002) and Peixinho et al. (2004) of bluer Plutinos being intrinsically fainter using the spectral slope s as a measure of color. The correlation analysis of $B-R$ and H leads to similar results: $\langle\rho\rangle = 0.25^{+0.35}_{-0.43}$ and $P = 0.420$. Our sample suggests precisely the opposite, with a trend between spectral slope s and the diameter d showing smaller Plutinos to be redder (Fig. 6). We note however, that Peixinho et al. (2004) find their trend due to a "cluster" of blue Plutinos with $H_R > 7.5$, i.e. $H \gtrsim 8$, objects at magnitude/size ranges we do not have in our sample. Hence, both effects might be the result of selection effects.

It is also interesting to ask if the presence of water ice on our targets (see Table 3) is correlated with albedo or diameter. Only 6 of our targets (other than Pluto) are known to definitely have ice, while two definitely do not. Because we do not have a quantitative and consistently defined measure of how much ice is present on these objects, a formal correlation analysis is not possible. Qualitatively speaking, we can say that 5 of the objects with ice have high albedos (>0.11), with 1999 TC36 being the only icy object with a typical (0.07) Plutino albedo. Thus there is qualitative evidence that icy Plutinos have higher albedos than is typical. 1996 TP66 and 2000 GN171 are the only objects with good spectra indicating the lack of water ice. Their albedos (0.07 and 0.22, respectively) span most of the range of our measured albedos. This seems to indicate that Plutinos lacking water ice can have almost any albedo (although the lack of a detection of 70 μm emission from 1996 TP66 by either *Spitzer* or *Herschel* casts considerable doubt on the accuracy of its albedo determination). It seems remarkable that these two objects, which are free of ices, are also the two smallest objects (~150 km) of our sample. However, the small number of spectroscopically examined objects does not allow for a conclusion, whether the presence of ices is correlated to the object diameter.

5. Summary

The analysis of the diameters and albedos of 18 Plutinos using PACS photometry, leads us to the following conclusions:

– The diameter and albedo range of our Plutino sample yields 150–730 km and 0.04–0.28, respectively. Excluding Pluto, the weighted mean of the Plutino albedo distribution is 0.08 ± 0.03 and agrees with the average albedos observed for

Table 8. Results of the modified Spearman rank correlation analysis of the Plutino sample.

Parameters	N	$\langle\rho\rangle$	P	(P_σ)
physical parameters:				
d/p_V	17	$-0.32^{+0.29}_{-0.24}$	0.217	(1.24)
d/η	7	$-0.12^{+0.61}_{-0.54}$	0.806	(0.25)
p_V/η	7	$0.08^{+0.61}_{-0.67}$	0.870	(0.16)
H/d	17	$-0.30^{+0.37}_{-0.30}$	0.234	(1.19)
H/p_V	17	$-0.19^{+0.30}_{-0.27}$	0.468	(0.73)
H/η	7	$0.08^{+0.72}_{-0.81}$	0.868	(0.17)
orbital and physical parameters:				
e/d	17	$-0.62^{+0.18}_{-0.13}$	0.008	(2.67)
d/q	17	$0.62^{+0.13}_{-0.17}$	0.008	(2.67)
$d/r^\star$	17	$0.58^{+0.16}_{-0.22}$	0.015	(2.43)
$p_V/r^\star$	17	$0.10^{+0.30}_{-0.32}$	0.711	(0.37)
color information, orbital and physical parameters:				
$s/r^\star$	13	$-0.58^{+0.46}_{-0.26}$	0.038	(2.07)
s/d	13	$-0.62^{+0.32}_{-0.20}$	0.025	(2.24)
s/H	13	$0.20^{+0.36}_{-0.42}$	0.523	(0.64)
$(B-R)/d$	13	$-0.50^{+0.29}_{-0.21}$	0.082	(1.74)

Notes. N is the number of sample datapoints; $\langle\rho\rangle$ and P are the most probable correlation coefficient and the probability of the most probable correlation coefficient to occur given no relationship in the sample (cf. text), respectively. The uncertainty of $\langle\rho\rangle$ denotes its 68 % confidence level. P_σ is the significance expressed in terms of σ. We show only the results of parameter pairs which meet the following criteria: $|\langle\rho\rangle| \geq 0.3$ and $P \leq 0.1$, or which are of special interest. Parameter pairs are sorted by parameter type. All correlation coefficients were calculated excluding Pluto. Correlation analyses taking η into account are based solely on the 7 floating-η fit solutions. In order to assess the effects of discovery bias, we include the heliocentric distance at the time of discovery $r^\star$ in our analysis. To improve the readability we refrain from listing all correlation values of the color indices with $r^\star$ and d. Instead we only show the correlation values of spectral slope with $r^\star$ and d, which gives similar results.

the scattered disk, Centaur and JFC population. This agreement is compatible with the idea that Plutinos are a source population of Centaurs and JFCs.

- The floating-η fits yield a weighted mean η for the Plutino sample of $1.11^{+0.18}_{-0.19}$, which agrees with the canonical $\eta = 1.20 \pm 0.35$ (Stansberry et al. 2008) utilized in the fixed-η fits.
- We refine the size estimates of the components of 1999 TC36: $d_{A1} = 272^{+17}_{-19}$ km, $d_{A2} = 251^{+16}_{-17}$ km and $d_B = 132^{+8}_{-9}$ km; we estimate the bulk density of the multiple system to be $\varrho = 0.64^{+0.15}_{-0.11}$ g cm^{-3}.
- Pluto is the clear outlier of the Plutino population, being by far the largest object with the brightest surface. We have shown, that canonical simple thermal modeling of Pluto data leads to inadequate results, probably mainly due to its multi-component nature, thermal lightcurve and atmosphere.
- Using our measured albedos we calibrated the Plutino size scale for the first time and determined a cumulative size distribution of the known Plutinos. We find that intermediate sized Plutinos (120 km $\leq D \leq$ 400 km) follow a cumulative power-law distribution with $q = 2$, whereas the distribution of larger objects is better described by $q = 3$. We are able to give an upper size limit for the kink at the small-sized end of the distribution, which is 120 km.
- We find no correlations between albedo and diameter, as well as H, and diameter, albedo and η, respectively. This shows that our sample is not biased towards large and high (or low) albedo objects. Furthermore, we find a correlation between diameter and the heliocentric distance at the time of discovery, but not between the albedo and the heliocentric distance at the time of discovery. This leads us to the conclusion that the nature of the discovery bias is mainly size-dependent.
- A significant correlation between diameter and eccentricity (and perihelion distance) is very likely to be caused by a detectional bias based on geometrical aspects.
- We find hints to color biases in our sample: Plutinos, which have been farther from Sun at the time of their discovery seem to be bluer and smaller sized Plutinos tend to be redder, which contradicts previous finding by Peixinho et al. (2004).
- There is qualitative evidence that icy Plutinos have higher albedos than the average of the sample. We are not able to conclude on a correlation between the diameter and the presence of ices.

Acknowledgements. We would like to thank Alain Doressoundiram for his useful suggestions as a referee. Furthermore, we thank Chemeda Ejeta (MPS, Katlenburg-Lindau, Germany) for performing dynamical simulations on some of our targets. M. Mommert acknowledges support through the DFG Special Priority Program 1385: *The First 10 Million Years of the solar system – a Planetary Materials Approach*. C. Kiss and A. Pal acknowledge the support of the Bolyai Research Fellowship of the Hungarian Academy of Sciences. P. Santos-Sanz would like to acknowledge financial support by the Centre National de la Recherche Scientifique (CNRS). J. Stansberry acknowledges support for this work provided by NASA through an award issued by JPL/Caltech. R. Duffard acknowledges financial support from the MICINN (contract Ramón y Cajal). Part of this work was supported by the German *Deutsches Zentrum für Luft- und Raumfahrt* (DLR) project numbers 50 OR 0903, 50 OFO 0903 and 50 OR 1108, and the PECS program of the European Space Agency (ESA) and the Hungarian Space Office, PECS-98073. J.L. Ortiz acknowledges support from spanish grants AYA2008-06202-C03-01, AYA2011-30106-C02-01 and 2007-FQM2998.

References

Alvarez-Candal, A., Barucci, M. A., Merlin, F., Guilbert, A., & de Bergh, C. 2007, A&A, 475, 369
Barkume, K. M., Brown, M. E., & Schaller, E. L. 2008, AJ, 135, 55
Barucci, M. A., Doressoundiram, A., Tholen, D., Fulchignoni, M., & Lazzarin, M. 1999, Icarus, 142, 476
Barucci, M. A., Merlin, F., Dotto, E., Doressoundiram, A., & de Bergh, C. 2006, A&A, 455, 725
Barucci, M. A., Alvarez-Candal, A., Merlin, F., et al. 2011, Icarus, 214, 297
Barucci, M. A., Merlin, F., Perna, D., et al. 2012, A&A, 539, A152
Belskaya, I. N., Levasseur-Regourd, A., Shkuratov, Y. G., & Muinonen, K. 2008, Surface Properties of Kuiper Belt Objects and Centaurs from Photometry and Polarimetry, ed. M. A. Barucci, H. Boehnhardt, D. P. Cruikshank, A. Morbidelli, & R. Dotson, 115
Benecchi, S. D., Noll, K. S., Grundy, W. M., et al. 2009, Icarus, 200, 292
Benecchi, S. D., Noll, K. S., Grundy, W. M., & Levison, H. F. 2010, Icarus, 207, 978
Bernstein, G. M., Trilling, D. E., Allen, R. L., et al. 2004, AJ, 128, 1364
Bessell, M. S., Castelli, F., & Plez, B. 1998, A&A, 333, 231
Boehnhardt, H., Tozzi, G. P., Birkle, K., et al. 2001, A&A, 378, 653
Brosch, N. 1995, MNRAS, 276, 571
Brown, M. E. 2000, AJ, 119, 977
Brown, M. E., & Suer, T.-A. 2007, IAU Circ., 8812, 1
Brucker, M. J., Grundy, W. M., Stansberry, J. A., et al. 2009, Icarus, 201, 284
Buie, M. W., Tholen, D. J., & Wasserman, L. H. 1997, Icarus, 125, 233
Buie, M. W., Grundy, W. M., Young, E. F., Young, L. A., & Stern, S. A. 2010, ApJ, 139, 1128
Cohen, C. J., & Hubbard, E. C. 1965, AJ, 70, 10
Collander-Brown, S. J., Fitzsimmons, A., Fletcher, E., Irwin, M. J., & Williams, I. P. 1999, MNRAS, 308, 588
Davies, J. K., Green, S., McBride, N., et al. 2000, Icarus, 146, 253
de Bergh, C., Boehnhardt, H., Barucci, M. A., et al. 2004, A&A, 416, 791

de Elía, G. C., Brunini, A., & di Sisto, R. P. 2008, A&A, 490, 835
Delsanti, A. C., Boehnhardt, H., Barrera, L., et al. 2001, A&A, 380, 347
DeMeo, F. E., Fornasier, S., Barucci, M. A., et al. 2009, A&A, 493, 283
DeMeo, F. E., Dumas, C., de Bergh, C., et al. 2010, Icarus, 208, 412
di Sisto, R. P., Brunini, A., & de Elía, G. C. 2010, A&A, 519, A112
Doressoundiram, A., Barucci, M. A., Romon, J., & Veillet, C. 2001, Icarus, 154, 277
Doressoundiram, A., Peixinho, N., de Bergh, C., et al. 2002, AJ, 124, 2279
Doressoundiram, A., Peixinho, N., Doucet, C., et al. 2005, Icarus, 174, 90
Doressoundiram, A., Peixinho, N., Moullet, A., et al. 2007, AJ, 134, 2186
Doressoundiram, A., Boehnhardt, H., Tegler, S. C., & Trujillo, C. 2008, Color Properties and Trends of the Transneptunian Objects, ed. M. A. Barucci, H. Boehnhardt, D. P. Cruikshank, A. Morbidelli, & R. Dotson, 91
Dotto, E., Barucci, M. A., Boehnhardt, H., et al. 2003, Icarus, 162, 408
Duncan, M. J., Levison, H. F., & Budd, S. M. 1995, AJ, 110, 3073
Edgeworth, K. E. 1949, MNRAS, 109, 600
Efron, B., & Tibshirani, R. 1993, An introduction to the bootstrap, Monographs on Statistics and Applied Probability (New York: Chapman and Hall/CRC), 57
Elliot, J. L., Kern, S. D., Clancy, K. B., et al. 2005, ApJ, 129, 1117
Engelbracht, C. W., Blaylock, M., Su, K. Y. L., et al. 2007, PASP, 119, 994
Fernández, Y. R., Jewitt, D. C., & Sheppard, S. S. 2005, AJ, 130, 308
Ferrin, I., Rabinowitz, D., Schaefer, B., et al. 2001, ApJ, 548, L243
Fornasier, S., Doressoundiram, A., Tozzi, G. P., et al. 2004, A&A, 421, 353
Gladman, B., Marsden, B. G., & Vanlaerhoven, C. 2008, in Nomenclature in the Outer Solar System, ed. M. A. Barucci, H. Boehnhardt, D. P. Cruikshank, & A. Morbidelli, 43
Gordon, K. D., Engelbracht, C. W., Fadda, D., et al. 2007, PASP, 119, 1019
Griffin, M. J., Abergel, A., Abreu, A., et al. 2010, A&A, 518, L3
Guilbert, A., Alvarez-Candal, A., Merlin, F., et al. 2009, Icarus, 201, 272
Gulbis, A. A. S., Elliot, J. L., Person, M. J., et al. 2006, Nature, 439, 48
Gurwell, M. A., & Butler, B. J. 2005, in AAS/Division for Planetary Sciences Meeting Abstracts, BAAS, 37, 743
Gurwell, M. A., Butler, B. J., & Moullet, A. 2010, in AAS/Division for Planetary Sciences Meeting Abstracts, BAAS, 42, 1014
Hainaut, O. R., & Delsanti, A. C. 2002, A&A, 389, 641
Harris, A. W. 1998, Icarus, 131, 291
Harris, A. W., & Harris, A. W. 1997, Icarus, 126, 450
Hovis, W. A., & Callahan, W. R. 1966, J. Opt. Soc. Amer., 56, 639
Howell, S. B. 1989, PASP, 101, 616
Hubbard, W. B., Hunten, D. M., Dieters, S. W., Hill, K. M., & Watson, R. D. 1988, Nature, 336, 452
Jacobson, S., & Margot, J. L. 2007, in AAS/Division for Planetary Sciences Meeting Abstracts, BAAS, 38, 519
Jewitt, D., & Luu, J. 1993, Nature, 362, 730
Jewitt, D., & Luu, J. 1996, in Completing the Inventory of the Solar System, ed. T. Rettig, & J. M. Hahn, ASP Conf. Ser., 107, 255
Jewitt, D., & Luu, J. 1998, AJ, 115, 1667
Jewitt, D. C., & Luu, J. X. 2001, AJ, 122, 2099
Kenyon, S. J., & Bromley, B. C. 2004, AJ, 128, 1916
Kenyon, S. J., Bromley, B. C., O'Brien, D. P., & Davis, D. R. 2008, in Formation and Collisional Evolution of Kuiper Belt Objects, ed. M. A. Barucci, H. Boehnhardt, D. P. Cruikshank, A. Morbidelli, & R. Dotson, 293
Kuiper, G. P. 1951, Proc. National Academy of Science, 37, 1
Lacerda, P., & Jewitt, D. C. 2007, ApJ, 133, 1393
Lagerros, J. S. V. 1996, A&A, 310, 1011
Lagerros, J. S. V. 1997, A&A, 325, 1226
Lagerros, J. S. V. 1998, A&A, 332, 1123
Lebofsky, L. A., & Spencer, J. R. 1989, in Asteroids II, ed. R. P. Binzel, T. Gehrels, & M. S. Matthews, 128
Lellouch, E., Laureijs, R., Schmitt, B., et al. 2000, Icarus, 147, 220
Lellouch, E., Stansberry, J., Emery, J., Grundy, W., & Cruikshank, D. P. 2011, Icarus, 214, 701
Licandro, J., Oliva, E., & Di Martino, M. 2001, A&A, 373, L29
Lim, T. L., Stansberry, J., Müller, T. G., et al. 2010, A&A, 518, L148
Malhotra, R. 1993, Nature, 365, 819
Malhotra, R. 1995, AJ, 110, 420
McBride, N., Green, S. F., Davies, J. K., et al. 2003, Icarus, 161, 501
Melita, M. D., & Brunini, A. 2000, Icarus, 147, 205
Merlin, F., Barucci, M. A., Dotto, E., de Bergh, C., & Lo Curto, G. 2005, A&A, 444, 977
Merlin, F., Barucci, M. A., de Bergh, C., et al. 2010, Icarus, 210, 930
Morbidelli, A. 1997, Icarus, 127, 1
Mueller, M. 2007, Ph.D. Thesis, FU Berlin, Germany
Mueller, M., Delbo', M., Hora, J. L., et al. 2011, AJ, 141, 109
Müller, T. G., Lellouch, E., Böhnhardt, H., et al. 2009, Earth Moon and Planets, 105, 209
Müller, T. G., Lellouch, E., Stansberry, J., et al. 2010, A&A, 518, L146
Müller, T. G., Nielbock, M., Balog, Z., Klaas, U., & Vilenius, E. 2011a, PACS Photometer – Point-Source Flux Calibration, Document: PICC-ME-TN-037, Tech. Rep.
Müller, T. G., Okumura, K., & Klaas, U. 2011b, PACS Photometer Passbands and Colour Correction Factors for Various Source SEDs, Document: PICC-ME-TN-038, Tech. Rep.
Ortiz, J. L., Gutiérrez, P. J., Casanova, V., & Sota, A. 2003, A&A, 407, 1149
Ortiz, J. L., Gutiérrez, P. J., Santos-Sanz, P., Casanova, V., & Sota, A. 2006, A&A, 447, 1131
Ott, S. 2010, in Astronomical Data Analysis Software and Systems XIX, ed. Y. Mizumoto, K.-I. Morita, & M. Ohishi, ASP Conf. Ser., 434, 139
Owen, T. C., Roush, T. L., Cruikshank, D. P., et al. 1993, Science, 261, 745
Peixinho, N., Boehnhardt, H., Belskaya, I., et al. 2004, Icarus, 170, 153
Perna, D., Barucci, M. A., Fornasier, S., et al. 2010, A&A, 510, A53
Pilbratt, G. L., Riedinger, J. R., Passvogel, T., et al. 2010, A&A, 518, L1
Poglitsch, A., Waelkens, C., Geis, N., et al. 2010, A&A, 518, L2
Protopapa, S., Alvarez-Candal, A., Barucci, M. A., et al. 2009, A&A, 501, 375
Rabinowitz, D. L., Schaefer, B. E., & Tourtellotte, S. W. 2007, AJ, 133, 26
Rabinowitz, D. L., Schaefer, B. E., Schaefer, M., & Tourtellotte, S. W. 2008, AJ, 136, 1502
Rieke, G. H., Young, E. T., Engelbracht, C. W., et al. 2004, ApJS, 154, 25
Romanishin, W., & Tegler, S. C. 2005, Icarus, 179, 523
Romanishin, W., Tegler, S. C., & Consolmagno, G. J. 2010, AJ, 140, 29
Santos-Sanz, P., Ortiz, J. L., Barrera, L., & Boehnhardt, H. 2009, A&A, 494, 693
Santos-Sanz, P., Lellouch, E., Fornasier, S., et al. 2012, A&A, 541, A92
Sheppard, S. S., & Jewitt, D. C. 2002, AJ, 124, 1757
Sheppard, S. S., & Jewitt, D. C. 2003, Earth Moon and Planets, 92, 207
Sicardy, B., Bellucci, A., Gendron, E., et al. 2006, Nature, 439, 52
Spencer, J. R., Stansberry, J. A., Trafton, L. M., et al. 1997, in Volatile Transport, Seasonal Cycles, and Atmospheric Dynamics on Pluto, ed. S. A. Stern, & D. J. Tholen, 435
Stansberry, J. A., Grundy, W. M., Margot, J. L., et al. 2006, ApJ, 643, 556
Stansberry, J. A., Gordon, K. D., Bhattacharya, B., et al. 2007, PASP, 119, 1038
Stansberry, J., Grundy, W., Brown, M., et al. 2008, in Physical Properties of Kuiper Belt and Centaur Objects: Constraints from the Spitzer Space Telescope, ed. M. A. Barucci, H. Boehnhardt, D. P. Cruikshank, & A. Morbidelli, 161
Stansberry, J. A., Lellouch, E., Grundy, W., et al. 2009, in AAS/Division for Planetary Sciences Meeting Abstracts, 41, 06.02
Tegler, S. C., & Romanishin, W. 1998, Nature, 392, 49
Tegler, S. C., Romanishin, W., & Consolmagno, G. J. 2003, ApJ, 599, L49
Thirouin, A., Ortiz, J. L., Duffard, R., et al. 2010, A&A, 522, A93
Tholen, D. J., & Buie, M. W. 1997, in Bulk Properties of Pluto and Charon, ed. S. A. Stern, & D. J. Tholen, 193
Trujillo, C. A., & Brown, M. E. 2002, IAU Circ., 7787, 1
Trujillo, C. A., Luu, J. X., Bosh, A. S., & Elliot, J. L. 2001, AJ, 122, 2740
Vilenius, E., Kiss, C., Mommert, M., et al. 2012, A&A, submitted
Werner, M. W., Roellig, T. L., Low, F. J., et al. 2004, ApJS, 154, 1
Young, E. F., Young, L. A., & Buie, M. 2007, in BAAS, 38, 541
Yu, Q., & Tremaine, S. 1999, AJ, 118, 1873

Appendix D

Curriculum Vitae

For reasons of personal data protection, the curriculum vitae is not included in the online version.